From cells to tissues:

Remodeling and polarity reorientation in epithelial tissues

DISSERTATION

zur Erlangung des akademischen Grades

Doctor rerum naturalium
(Dr. rer. nat.)

vorgelegt

der Fakultät Mathematik und Naturwissenschaften
der Technischen Universität Dresden

von

Dipl.-Phys. Matthias Merkel
geboren am 11. November 1984 in Cottbus

MAX-PLANCK-INSTITUT FÜR PHYSIK KOMPLEXER SYSTEME

Dresden, 2014

Eingereicht am 2. Juli 2014.
Verteidigt am 21. November 2014.

1. Gutachter: Prof. Dr. Frank Jülicher
2. Gutachter: Prof. Dr. Jens-Uwe Sommer

Acknowledgments

First of all, I thank Frank Jülicher for giving me the opportunity to work as a PhD student under his supervision. He contributed many of the key ideas for this work, and he guided me through my projects with his invaluable advice. I have learned a lot from him. Furthermore, I thank him and Jens-Uwe Sommer for reviewing this thesis. In this context, I also want to express my deep gratitude for Benjamin Lindner, who was my supervisor during my time as a diploma student. He paved me the way to the field of biological physics. I owe him a lot.

This work could not exist without all the experimental input provided by our collaborators from the Max Planck Institute of Molecular Cell Biology and Genetics. I want to thank Suzanne Eaton, Andreas Sagner, Benoît Aigouy, Raphaël Etournay, Franz Gruber, and Corinna Blasse for the always interesting, fruitful, and stimulating discussions in our Friday meetings. Thanks for explaining all the biology to me. In particular, with Andreas, Raphaël, Benoît, and Franz, we worked together hand in hand on all the details of our projects. Along with that, most of the biological image data used for this thesis stem from experiments by Andreas and Raphaël.

I also want to thank my collaborators on the theoretical side. The following persons contributed directly or indirectly to this work: Douglas Stable, Marko Popovic, Guillaume Salbreux, Amitabha Nandi, Reza Farhadifar, Silvanus Alt, Benjamin Friedrich, Peer Mumcu, Maryam Aliee, Sebastian Fürthauer, Jonas Ranft, and Johannes Baumgart. Thank you for the productive, rich, and inspiring work atmosphere. It has always been enjoyable discussing with you. Also, I thank Marko Popovic, Silvanus Alt, and Jens Karschau for critical comments on the manuscript. My time here at the institute would not have been was it was without all the nice chats, lunch breaks, and coffee breaks with Silvanus Alt, Gary Klindt, Andre Scholich, Helge Aufderheide, Christoph Weber, Jonas Ranft, Amitabha Nandi, Marko Popovic, Jochen Schneider, Tilo Schwalger, Johannes Baumgart, Steffen Werner, David Zwicker, Pablo Sartori, Lucas Wetzel, David Jörg, Rui Ma, Masud Haque, and, last but certainly not least, my office mate Johannes Knolle.

Finally, I want to thank my family and my friends for their support. In particular, I thank my WG mates, Ron Dockhorn, Christiane Falkenberg, Michael Körner, Manuela Lipinsky, and Christoph Schünemann. Maybe, I was not always on time with my WG service. Also, I thank Manuela Lipinsky for her precious love and her constant support during all this time. Moreover, I explicitly want to thank Juliane Döring and Christian Bruchatz for their help during the last weeks.

Abstract

An essential prerequisite for the existence of multi-cellular life is the organization of cells into tissues. In this thesis, we theoretically study how large-scale tissue properties can emerge from the collective behavior of individual cells. To this end, we focus on the properties of epithelial tissue, which is one of the major tissue types in animals. We study how rheological properties of epithelia emerge from cellular processes, and we develop a physical description for the dynamics of an epithelial cell polarity. We apply our theoretical studies to observations in the developing wing of the fruit fly, *Drosophila melanogaster*.

In order to study epithelial mechanics, we first develop a geometrical framework that rigorously describes the deformation of two-dimensional cellular networks. Our framework decomposes large-scale deformation into cellular contributions. For instance, we show how large-scale tissue shear decomposes into contributions by cell shape changes and into contributions by different kinds of topological transitions. We apply this framework in order to quantify the time-dependent deformation of the fruit fly wing, and to decompose it into cellular contributions.

We also use this framework as a basis to study large-scale rheological properties of epithelia and their dependence on cellular fluctuations. To this end, we represent epithelial tissues by a vertex model, which describes cells as elastic polygons. We extend the vertex model by introducing fluctuations on the cellular scale, and we develop a method to perform perpetual simple shear simulations. Analyzing the steady state of such simple shear simulations, we find that the rheological behavior of vertex model tissue depends on the fluctuation amplitude. For small fluctuation amplitude, it behaves like a plastic material, and for high fluctuation amplitude, it behaves like a visco-elastic fluid.

In addition to analyzing mechanical properties, we study the reorientation of an epithelial cell polarity. To this end, we develop a simple hydrodynamic description for polarity reorientation. In particular, we account for polarity reorientation by tissue shear, by another polarity field, and by local polarity alignment. Furthermore, we develop methods to quantify polarity patterns based on microscopical images of the fly wing. We find that our hydrodynamic description does not only account for polarity reorientation in wild type fly wings. Moreover, it is for the first time possible to also account for the observed polarity patterns in a number of genetically altered flies.

Kurzzusammenfassung

Eine wesentliche Voraussetzung für die Existenz mehrzelligen Lebens ist, dass sich einzelne Zellen sinnvoll zu Geweben ergänzen können. In dieser Dissertation untersuchen wir, wie großskalige Eigenschaften von Geweben aus dem kollektiven Verhalten einzelner Zellen hervorgehen. Dazu konzentrieren wir uns auf Epitheliengewebe, welches eine der Grundgewebearten in Tieren darstellt. Wir stellen theoretische Untersuchungen zu rheologischen Eigenschaften und zu zellulärer Polarität von Epithelien an. Diese theoretischen Untersuchungen vergleichen wir mit experimentellen Beobachtungen am sich entwickelnden Flügel der schwarzbäuchigen Taufliege (*Drosophila melanogaster*).

Um die Mechanik von Epithelien zu untersuchen, entwickeln wir zunächst eine geometrische Beschreibung für die Verformung von zweidimensionalen zellulären Netzwerken. Unsere Beschreibung zerlegt die mittlere Verformung des gesamten Netzwerks in zelluläre Beitrage. Zum Beispiel wird eine Scherverformung des gesamten Netzwerks auf der zellulären Ebene exakt repräsentiert: einerseits durch die Verformung einzelner Zellen und andererseits durch topologische Veränderungen des zellulären Netzwerks. Mit Hilfe dieser Beschreibung quantifizieren wir die Verformung des Fliegenflügels während des Puppenstadiums. Des Weiteren führen wir die Verformung des Flügels auf ihre zellulären Beiträge zurück.

Wir nutzen diese Beschreibung auch als Ausgangspunkt, um effektive rheologische Eigenschaften von Epithelien in Abhängigkeit von zellulären Fluktuationen zu untersuchen. Dazu simulieren wir Epithelgewebe mittels eines Vertex Modells, welches einzelne Zellen als elastische Polygone abstrahiert. Wir erweitern dieses Vertex Modell um zelluläre Fluktuationen und um die Möglichkeit, Schersimulationen beliebiger Dauer durchzuführen. Die Analyse des stationären Zustands dieser Simulationen ergibt plastisches Verhalten bei kleiner Fluktuationsamplitude und visko-elastisches Verhalten bei großer Fluktuationsamplitude.

Neben mechanischen Eigenschaften untersuchen wir auch die Umorientierung einer Zellpolarität in Epithelien. Dazu entwickeln wir eine einfache hydrodynamische Beschreibung für die Umorientierung eines Polaritätsfeldes. Wir berücksichtigen dabei insbesondere Effekte durch Scherung, durch ein anderes Polaritätsfeld und durch einen lokalen Gleichrichtungseffekt. Um unsere theoretische Beschreibung mit experimentellen Daten zu vergleichen, entwickeln wir Methoden um Polaritätsmuster im Fliegenflügel zu quantifizieren. Schließlich stellen wir fest, dass unsere hydrodynamische Beschreibung in der Tat beobachtete Polaritätsmuster reproduziert. Das gilt nicht nur im Wildtypen, sondern auch in genetisch veränderten Tieren.

Contents

1 Introduction **1**
1.1 The development of multi-cellular organisms 1
1.2 Biology of epithelial tissues 2
1.3 The model system *Drosophila melanogaster* 3
1.3.1 Development of the fruit fly 3
1.3.2 Development of the fruit fly wing 5
1.4 Planar cell polarity 6
1.4.1 The Core polarity system 6
1.4.2 The Fat polarity system 9
1.4.3 Planar cell polarity in the fruit fly wing 10
1.5 Physical description of biological tissues 10
1.5.1 Continuum descriptions for biological tissues 11
1.5.2 Cell-based models for epithelial mechanics 12
1.5.3 Models for planar cell polarity 14
1.6 Overview over this thesis 15

2 Tissue shear in cellular networks **17**
2.1 Geometry of tissue deformation on the cellular scale 17
2.1.1 Cellular networks and their triangle-based description 17
2.1.2 Characterization of triangle shapes 20
2.1.3 Characterization of triangle deformation 23
2.1.4 Coarse-graining: deformation of triangle groups 29
2.1.5 Characterization of shear induced by topological transitions . . 33
2.2 Decomposition of the large-scale flow field into cellular contributions . . 37
2.2.1 The velocity gradient describes large-scale deformations 37
2.2.2 Large-scale divergence of the flow field 38
2.2.3 Large-scale shear of the flow field 38
2.3 Cellular contributions to the flow field in the fruit fly wing 40
2.3.1 Extraction of the large-scale flow field and its components from experimental movies 40
2.3.2 Components of the flow field in a wild type wing 41
2.3.3 Comparison of different wild type wings 46
2.4 Discussion 46

3 Rheological behavior of vertex model tissue under external shear 51
3.1 A vertex model to describe epithelial mechanics 51
3.1.1 Force-balanced states 52
3.1.2 Line tension fluctuations 53
3.1.3 Influence of line tension fluctuations on tissue growth 54
3.1.4 Simple shear simulations using skewed periodic boundary conditions 54
3.2 Fluctuation-induced fluidization of tissue 57
3.2.1 Cellular shear elasticity 58
3.2.2 Fluctuation-dependent elongation relaxation 58
3.3 Discussion 64

4 Quantitative study of polarity reorientation in the fruit fly wing 65
4.1 Experimentally quantified polarity patterns 65
4.1.1 Genetic conditions 66
4.1.2 Effects of Sple over-expression 68
4.2 Effective hydrodynamic theory for polarity reorientation 72
4.2.1 Effective free energy 73
4.2.2 Generic dynamics of the polarity field 74
4.2.3 Stationary solutions 75
4.3 Comparison of theory and experiment 78
4.3.1 Fits of wing hair profiles to stationary solutions 80
4.3.2 Numerical solution of the polarity reorientation dynamics 83
4.4 Discussion 91

5 Conclusions and outlook 93

Appendices 99

A Algebra of real 2×2 matrices 101
A.1 Sum decomposition into scaling rotations and nematics 101
A.1.1 Sum decomposition 101
A.1.2 Scaling rotations 101
A.1.3 Determinant 102
A.2 Properties of nematics 102
A.2.1 Components of a nematic 102
A.2.2 Norm and angle of a nematic 102
A.2.3 Orthonormal basis in the formal vector space of nematics 103
A.2.4 Infinitesimal changes of norm and angle 104
A.3 Products between scaling rotations and nematics 104
A.3.1 Two scaling rotations 105
A.3.2 A scaling rotation and a nematic 105

A.3.3 Two nematics . . . 105
A.4 Exponentials of real 2×2 matrices . . . 106
A.4.1 Definition . . . 106
A.4.2 General properties . . . 106
A.4.3 Exponentials of antisymmetric matrices . . . 107
A.4.4 Exponentials of symmetric matrices . . . 107
A.4.5 Exponentials of nematics . . . 107
A.5 Product decomposition of real 2×2 matrices . . . 108
A.5.1 Existence of the decomposition . . . 108
A.5.2 Uniqueness of the decomposition . . . 110

B Deformation of triangle networks 111
B.1 Equivalence of two definitions for the displacement gradient . . . 111
B.2 Triangle transformation parameters in terms of triangle state change . . 113
B.2.1 Finite transformations . . . 113
B.2.2 Infinitesimal transformations . . . 116
B.2.3 Shear-induced rotation of a single triangle . . . 117
B.3 Components of the displacement gradient for groups of triangles 119
B.3.1 Shear of a group of triangles in the absence of topological transitions . . . 119
B.3.2 Rotation of a group of triangles . . . 120
B.4 Integrated shear depends on the deformation protocol . . . 123
B.4.1 Single triangle . . . 125
B.4.2 General proof . . . 126
B.5 Shear contributions by single topological transitions . . . 131
B.5.1 Cell divisions . . . 131
B.5.2 T2 transitions . . . 132
B.6 Topological transitions at the network margin . . . 133
B.6.1 T1 transitions . . . 134
B.6.2 Cell divisions . . . 134
B.6.3 T2 transitions . . . 136
B.7 Alternative triangulation . . . 136
B.8 Application to experimental data . . . 138
B.8.1 Introduction of artificial intermediate network states . . . 138
B.8.2 Computation of the large-scale quantities . . . 138
B.8.3 Triangulation for vertices with more than three bonds . . . 142

C Simple shear simulations using the vertex model 143
C.1 Implementation of the vertex model . . . 143
C.1.1 Boundary conditions . . . 143
C.1.2 Numerical minimization of the work function . . . 146
C.1.3 T1 and T2 transitions . . . 147

C.2 Growth simulation details 149
C.3 Simple shear simulations 150
  C.3.1 Simulation details 150
  C.3.2 Fluctuations inhibit shear banding 151
  C.3.3 Average flow field 154
  C.3.4 Steady state axis of the elongation nematic 156
C.4 Quantification of observables 157
  C.4.1 Definition of stress 157
  C.4.2 Shear components 159
  C.4.3 Quantification of uncertainties 162

D Coarse-graining of a cellular Core PCP model 163
D.1 Core PCP vertex model 163
D.2 Fourier transformation on a hexagonal grid 165
  D.2.1 Hexagonal grid 165
  D.2.2 Discrete Fourier transformation with respect to angle and position 166
  D.2.3 Core PCP model in Fourier space 167
D.3 Continuous degeneracy of the homogeneous ground state 170
D.4 Relaxation of hydrodynamic modes 171
D.5 Comparison to a generic first order polarity dynamics 175
  D.5.1 Generic first order polarity dynamics 175
  D.5.2 Effective relaxation rates of bend and splay modes in the cellular Core PCP model 176

E Quantification of polarity patterns in the fruit fly wing 179
E.1 Hair polarity in the adult fly wing 179
  E.1.1 Quantification of the wing hair direction pattern 179
  E.1.2 Profiles of wing hair direction angles 183
  E.1.3 Profiles of bristle direction angles 185
E.2 Quantification of polarity from images with a clonal staining 185
  E.2.1 From segmented image data 186
  E.2.2 From unsegmented image data 187
E.3 Quantification of PCP and cell elongation nematics 188
  E.3.1 Cell elongation nematics 189
  E.3.2 PCP nematics 189
E.4 Experimental procedures 190

F Theory for polarity reorientation in the fruit fly wing 193
F.1 Derivation of stationary solutions 193
  F.1.1 Inhomogeneous stationary solutions 193
F.2 Fits of stationary states to wing hair angle profiles 200
  F.2.1 Fit function 200

F.2.2 Fitting procedure 201
F.2.3 Fit parameter values for Sple over-expression 201
F.3 Numerical solution of the polarity reorientation dynamics 204
F.3.1 Initial conditions 204
F.4 Comparison to an observed PCP reorientation after 36 hAPF 205
F.5 Comparison to the turnover rate of Core PCP clusters 207
F.6 Possible additional effects 208
F.6.1 Variants of the polarity angle bulk dynamics 208
F.6.2 Effect of wing veins 210
F.6.3 Effect of gradients in Sple protein concentration 212

G Boundary conditions for the polarity field in the fruit fly wing 215
G.1 Quantification of wing margin bristle directions 215
G.2 Physical theory for the direction of wing margin bristles 217
G.2.1 Effective potential describing the boundary conditions 217
G.2.2 Effective thermodynamic equilibrium at the boundary 218
G.3 Determination of parameter values 219
G.4 Comparison of theory and experiment 222

Table of symbols 225

Bibliography 229

Chapter 1

Introduction

1.1 The development of multi-cellular organisms

The development from a fertilized egg cell to a complex, multi-cellular organism is a fascinating process. Besides environmental factors, it is mainly controlled by the genetic material, the DNA [1, 2]. The huge amount of information encoded in the DNA allows for the broad diversity of living beings that we see in nature (Fig. 1.1). There are about 10 . . . 100 million different species on earth today. What mechanisms transform the linear information stored in the DNA into this huge variety of complex organisms?

Genetic studies alone are by far not sufficient to answer this question [3–8]. This becomes clear when considering how the DNA influences development. In the first place, the DNA merely controls the behavior of the individual cells by defining the rules for cellular protein expression [1, 2]. From this perspective, development is even more fascinating: it is a self-organized process, which arises from the collective behavior of up to $\sim 10^{13}$ single cells. This immediately leads to the following question: How can the development of an organism arise from the collective behavior of individual cells?

Any answer to this question needs to link processes occurring at the cellular scale ($\sim 1 \ldots 30\,\mu\text{m}$) to processes at the scale of an organism ($\sim 1\,\text{mm} \ldots 1\text{m}$). A common

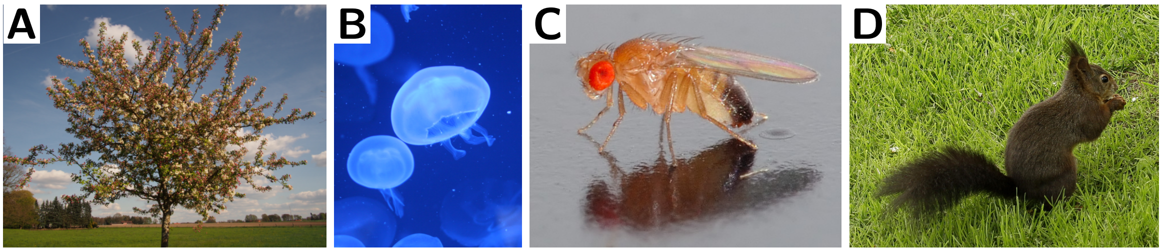

Figure 1.1: The diversity of multi-cellular life forms on earth. **(A)** An apple tree (genus: *malus*). **(B)** Jellyfishes (phylum: *cnidaria*). **(C)** A fruit fly (species: *Drosophila melanogaster*). **(D)** A red squirrel (genus: *Sciurus*). (Image sources: (A,D) Uschi Dreiucker/`pixelio.de`, (B) Caroline Lang/`pixelio.de`, (C) André Karwath/`commons.wikimedia.org`.)

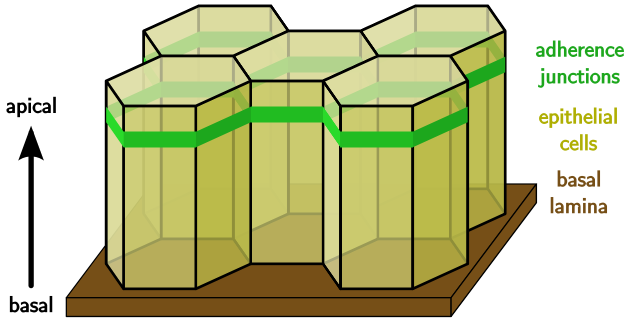

Figure 1.2: Layered organization of cells within epithelial tissue. All epithelia show an apical-basal polarity. They are supported by a basal lamina. The individual cells adhere via adherens junctions.

approach introduces intermediate length scales: The development of an organism can be understood by the behavior of the different organs and tissues it is made of; and the behavior of tissues can be understood in terms of cellular processes.

Interestingly, developmental processes on the tissue scale are fairly reproducible among different organisms of a given species [1, 2]. However, this is mostly not true on the single cell scale [9].[1] Thus, in order to create an understanding for the development of an entire organism, one strives to describe tissue behavior by simple effective properties, leaving out fluctuations on the cellular scale.

In this work, we develop and apply physical tools to study how cells organize into tissues. To this end, we focus on two-dimensional tissues, called *epithelia*. We study mechanical properties of epithelia and the reorientation of a cellular polarity within epithelia, which is called *Planar Cell Polarity* (PCP). Our research compares theoretical results to observations in the developing wing of the fruit fly, *Drosophila melanogaster* (Fig. 1.1C).

In the remaining parts of this chapter, we first introduce fundamental biological concepts (Sections 1.2, 1.3, and 1.4). Then, in Section 1.5, we discuss physical descriptions of biological tissues. Finally, in Section 1.6, we outline how this thesis contributes to the physical understanding of epithelial tissues.

1.2 Biology of epithelial tissues

Besides connective tissue, muscle tissue, and nerve tissue, *epithelial tissue* is among the major tissue types in animals [2, 10, 11]. Epithelial tissues are organized into layers of densely adhering cells (Fig. 1.2) [2, 12]. An epithelium is supported by a thin layer of extracellular material called the *basal lamina*. Epithelia surround all cavities within the body like the gut lumen, the airway lumen, or blood vessels. Also the skin is an epithelium.

Epithelia are classified with respect to the number of cell layers they are made of [10]. They range from unilayered or *simple* epithelia to multilayered or *stratified* epithelia. In this work, we focus on simple epithelia.

---

[1] However surprisingly, in more primitive organisms like the nematode *Caenorhabditis elegans*, development is reproducible even down to the single cell level [2].

Epithelia fulfill many different functions [2, 13]. For instance, they provide mechanical protection, and they act as barriers for fluids of different chemical composition. Also, they allow for active directed transport of molecules across themselves.

These functions are mainly provided by two properties of epithelia. First, the individual cells of an epithelium are mechanically linked to each other by so-called *adherens junctions* (Fig. 1.2) [2, 12, 14]. Intracellularly, adherens junctions are linked to cytoskeletal actin filaments.[2] Besides adherens junctions, there are junctions that are responsible for sealing the intercellular space in order to prevent molecules from passing across the epithelium.

Second, all epithelia are characterized by a transverse polarity, which is called *apical-basal* polarity (Fig. 1.2). The basal lamina is always on the basal side of an epithelium and is typically in contact to connective tissue. In contrast to that, the apical side is a free surface that is in contact with a cavity or the outside of the body.

Another kind of epithelial polarity is called Planar Cell Polarity (PCP). It is presented in Section 1.4.

1.3 The model system *Drosophila melanogaster*

In this work, we apply physical methods to experimental data obtained from the fruit fly, *Drosophila melanogaster*. The fruit fly has been studied as a biological model system for over 100 years now. Back then, Thomas Hunt Morgan carried out first inheritance experiments on it [15]. With these experiments, he and his students subsequently laid foundations for today's genetics.

Today, the fruit fly is one of the best understood developmental systems [1]. In between, its entire genome with $\sim$ 13600 genes has been sequenced [16]. After all, there is a wealth of genetic and experimental tools available, which makes the fruit fly an attractive model system to study developmental processes.

1.3.1 Development of the fruit fly

Another reason for the popularity of the fruit fly as a model system is its comparably short development time. It develops from a fertilized egg into an adult fly within only about 10 days (Fig. 1.3A) [1, 2, 17]. About three hours after fertilization, the animal is made up of a single spherical epithelium [1]. All later tissues of the fly are derived from this epithelium. It subsequently develops into an embryo, passes three larval stages, and becomes a pupa. Before it becomes a pupa, it forms a pupal case called the *puparium*. Finally, after the pupal stage, the adult fly emerges from the puparium.

---

[2] In addition to adherens junctions, epithelial cells are mechanically linked to each other by so-called *desmosomes*, which are intracellularly linked to intermediate filaments.

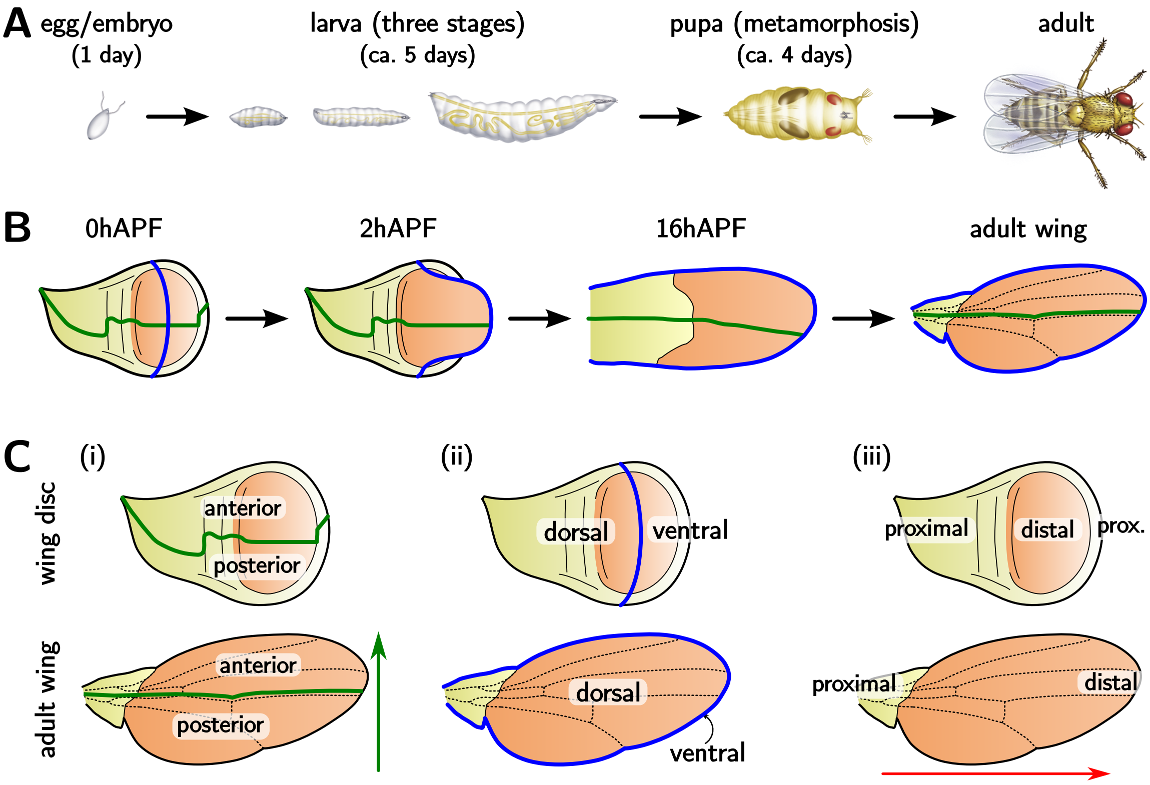
A
egg/embryo
(1 day)
larva (three stages)
(ca. 5 days)
pupa (metamorphosis)
(ca. 4 days)
adult
B
0hAPF
2hAPF
16hAPF
adult wing
C
(i)
(ii)
(iii)
wing disc
adult wing
anterior
posterior
dorsal
ventral
proximal
distal
prox.
anterior
posterior
dorsal
ventral
proximal
distal

Figure 1.3: **(A)** Developmental phases of the fruit fly. The fly develops from an egg via an embryo through three larval stages. Afterwards, it becomes a pupa by forming a pupal case around it, which is called *puparium*. During pupal stages, we denote developmental times in *hours after puparium formation* (hAPF). Finally, the adult fly emerges from the pupal case. **(B)** Development of the fly wing during the pupal stage, starting from the larval precursor structure, which is called *wing disc*. Note that during the pupal stage, the wing folds along the DV boundary (blue solid line, see panel Cii), such that dorsal and ventral layers lie on top of each other. In the wings, the yellow region is the *wing hinge* and orange region is the *wing blade*. In the wing disc, the orange region is called *wing pouch*. **(C)** Compartment boundaries and organ axes in the wing disc and in the adult wing. (i) The boundary between *anterior* and *posterior* compartments is indicated by a green solid line, respectively. (ii) The boundary between *dorsal* and *ventral* compartments (DV boundary) is indicated by a blue solid line, respectively. (iii) In the wing disc, the *proximo-distal axis* runs radially from the margin of the wing disc into the middle of the wing pouch. In the wing, the proximo-distal axis runs laterally away from the fly body. (Image sources: (A) adapted from ref. [17], (B,C) adapted from ref. [18].)

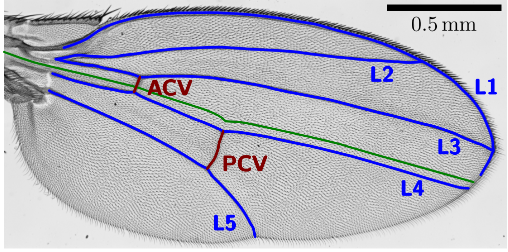

Figure 1.4: The stereotypical vein pattern of a fruit fly wing. There are five so-called *longitudinal veins* (blue solid lines), denoted by L1, ..., L5, and two so-called *cross veins* (red solid lines). These are the *anterior cross vein* (ACV) and the *posterior cross vein* (PCV). The approximate position of the AP boundary is indicated by the green solid line.

In this work, we focus on the fly development during the pupal stage. Times during the pupal stage are measured in *hours after puparium formation* (hAPF). For instance, the pupal stage starts at 0 hAPF. For technical reasons, all developmental times given in hAPF in this thesis have a precision of $\sim \pm 0.5\,\mathrm{h}$.

Note that the developmental speed of the fly is temperature-dependent [17, 19]. The development at high temperatures is faster than at low temperatures. Throughout this work, we refer to the fly development at a temperature of 25°C.

1.3.2 Development of the fruit fly wing

In this thesis, we focus on the development of the fruit fly wing during the pupal stage. During this time, it develops from a larval precursor structure, which is called the *wing disc*, through a series of complex deformations into the adult wing (Fig. 1.3B) [1, 20]. The wing disc consists of a single epithelial layer. During pupal stages, it folds along the blue solid line (the DV boundary, see below) such that the wing ultimately consists of two epithelial layers. When the fly finally emerges from the pupal case, nearly all wing cells die. Thus, the adult wing is mainly made of stiff, dead cuticle material, which had been secreted from the wing cells during pupal stages [20]. The wing divides into the *hinge region* (yellow region) and the *blade region* (orange region). During late pupal stages, each of the two epithelial layers of the blade region is made up of $\sim 10^4$ cells.

Directions and positions within the wing can be characterized by three organ axes (Fig. 1.3C). First, there are two subpopulations of wing cells, which are clearly separated by a nearly straight line. These subpopulations are the anterior and posterior wing compartments with a compartment boundary between them (the AP boundary, Fig. 1.3Ci) [18]. Cells of each compartment always keep their compartmental identity and inherit it to their daughter cells. The AP boundary gives rise to a direction which points from the posterior compartment to the anterior compartment (green arrow). Second, the wing consists of a dorsal layer, which is oriented towards the top of the fly, and a ventral layer, which is oriented towards the bottom of the fly (Fig. 1.3Cii). Similar to the AP boundary, the dorso-ventral boundary (DV boundary) is also a compartment boundary. Third, the so-called proximo-distal direction points from the hinge towards the tip of the wing (Fig. 1.3Ciii, red arrow). In the following, if not stated differently, we will always show wings or parts of wings such that distal is to the right and anterior is up.

The adult fruit fly wing is characterized by a stereotypical pattern of wing veins (Fig. 1.4) [20]. There are five so-called *longitudinal veins*, denoted by L1, . . . , L5, and two *cross veins*. The first longitudinal vein, L1, corresponds to the anterior wing margin. Interestingly, among different animals with the same genotype, the variability of wing vein positions is on the order of a single cell diameter [21].

1.4 Planar cell polarity

One fascinating aspect about biological tissues is that the individual cells typically behave in a coordinated manner. Such coordination is not trivial. This is because typically, each individual cell within a tissue only behaves according to locally available cues [1]. Such locally available cues could for instance be local stresses, local protein concentrations, or interactions with neighboring cells. Thus, in order to coordinate cells within a tissue, global information has to be made available locally.

One kind of global information that plays a role during development is directional information, such as body or organ axes. That global axes of an organism are reflected locally can be observed in everyday life: For instance, the fur of mammals usually shows a clear directional order with respect to body or organ axes (Fig. 1.5A) [22]. Similarly, hairs on the surface of the fruit fly wing are ordered with respect to the long axis of the wing (Fig. 1.5B). How should a single cell “know” the axis of the entire organ or even the entire organism? Nature has invented several mechanisms to provide global directional information at the level of individual cells. Here, we study one such mechanism, which is called *Planar Cell Polarity* (PCP).

PCP typically appears in epithelia and in contrast to apical-basal polarity, PCP is defined in the plane of the epithelium. Thus, it is oriented perpendicular to the apial-basal polarity. PCP is defined by an anisotropic intracellular distribution of so-called PCP proteins [23, 24]. These proteins typically localize to the lateral membrane of epithelial cells, close to the adherens junctions. On the tissue scale, PCP often shows large-scale directional order reflecting organ or body axes.

Different sets of PCP proteins give rise to different PCP systems. In this work, we discuss two prominent PCP systems: the *Core PCP* system and the *Fat PCP* system. In the following, both PCP systems are presented in detail. Afterwards, we discuss PCP patterns in the fruit fly wing.

1.4.1 The Core polarity system

The Core PCP system is a genetic pathway that is highly conserved during evolution [25]. It is involved in many developmental processes in invertebrates and in vertebrates (Fig. 1.6). For instance, it controls the direction of hairs and bristles on the body surface of insects, in particular on the wing of the fruit fly (Figs. 1.5B, 1.6A,D, and

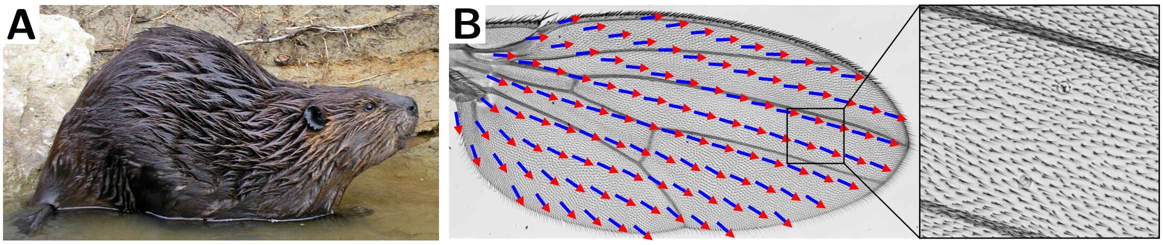

Figure 1.5: Hairs on the body surface often show directional order that corresponds to body or organ axes. **(A)** Fur of the North American beaver (*Castor canadensis*). **(B)** Wing of the fruit fly *Drosophila melanogaster*. The arrows indicate the local direction of hairs on the wing surface (see also Fig. 1.6A; local hair direction was quantified as described in Appendix E.1.1). (Image source: (A) Laszlo Ilyes/`flickr.com`)

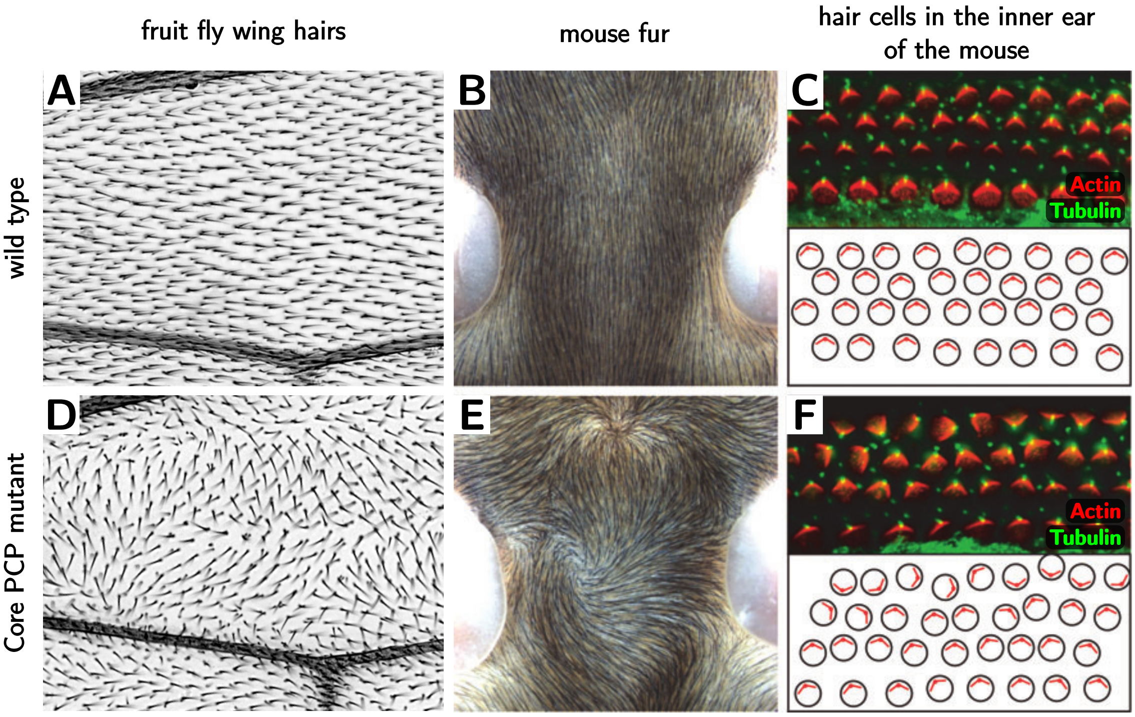
fruit fly wing hairs
mouse fur
hair cells in the inner ear of the mouse
wild type
Core PCP mutant
A
B
C
Actin
Tubulin
D
E
F
Actin
Tubulin

Figure 1.6: Mutations of Core PCP proteins perturb polar order in invertebrate and in vertebrate tissues. **(A,B,C)** Wild type tissues. **(D,E,F)** Core PCP mutant tissues. **(A,D)** Hairs on the fruit fly wing. **(B,E)** Skin hair on the dorsal mouse neck. **(C,F)** Sensory hair cells in the mouse inner ear. (Image source: (B,C,E,F) adopted from ref. [25].)

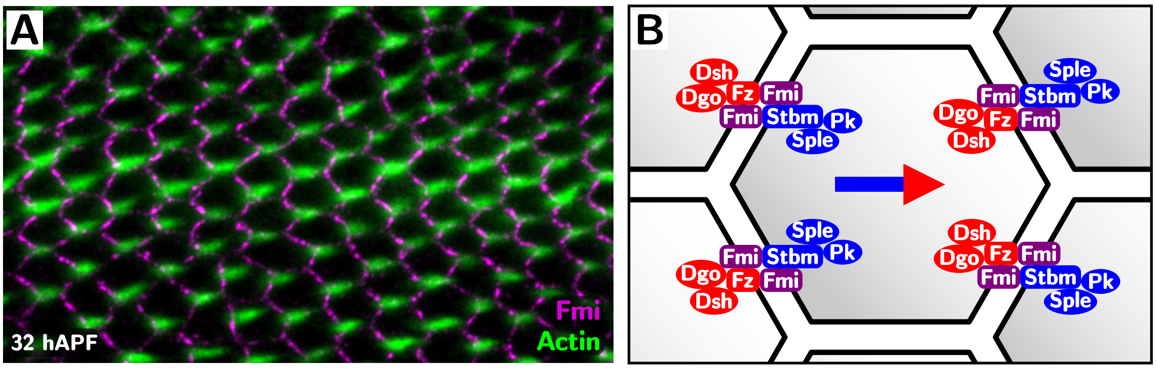

Figure 1.7: Organization of Core PCP proteins into polarized clusters. **(A)** Part of a developing fruit fly wing at 32 hAPF. The Core PCP protein Fmi is shown in magenta and wing hair precursors, which are rich in actin, are marked in green. **(B)** Schematic illustration of the spatial organization of the Core PCP proteins. The two protein classes are shown in blue and red, respectively. A cellular Core PCP vector is defined by the angular distribution of PCP proteins within a given cell (blue-red arrow).

1.7A) [26, 27]. In vertebrates, Core PCP controls the direction of mammalian skin hairs (Fig. 1.6B,E) [28] and of hair cells in the inner ear (Fig. 1.6C,F) [29, 30]. Also, Core PCP is believed to be involved in anisotropic tissue deformation during the early developmental stages of gastrulation and neurulation [22, 31], it controls the orientation of ridges on the fly wing [32], it influences cell packing in the fly wing [33], it controls cell differentiation in the compound eye of insects [34], and it may direct the orientation of cell divisions [35]. Furthermore, it is suspected to play a role in many other processes as for instance the development of the central nervous system and cardiovascular development in vertebrates [22, 25].

The molecular details of Core PCP have been studied for more than 30 years, now [26]. Although the precise interactions between the Core PCP proteins are not yet fully understood, much has already been learned. Here, we focus on the Core PCP proteins as they appear in invertebrates.

The Core PCP proteins organize into polarized clusters, where each cluster spans the membranes of two abutting cells (Fig. 1.7A,B) [36, 37]. The polarization of a given cluster is reflected in the anisotropic distribution of two classes of Core PCP proteins within the cluster (Fig. 1.7B) [25, 38]. One class, which is shown in red in Fig. 1.7B, comprises the transmembrabne protein *Frizzled* (Fz) and the cytoplasmic proteins *Dishevelled* (Dsh) and *Diego* (Dgo). The other class, shown in blue, comprises the transmembrane protein *Strabismus* (Stbm) and the cytoplasmic proteins *Prickle* (Pk) and *Spiny legs* (Sple).[3] The proteins Pk and Sple are different isoforms of the same

---

[3] Note that the intracellular localization of the Sple protein is still subject of an ongoing debate [39].

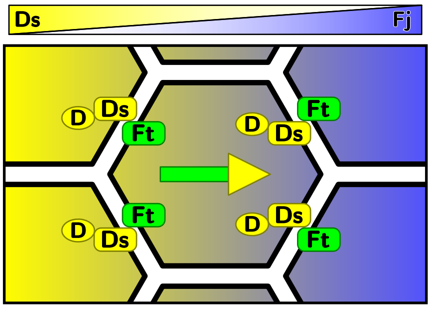

Figure 1.8: PCP proteins of the Fat polarity system. Also indicated are large-scale gradients of Ds and Fj, which are believed to locally induce large-scale order of Fat PCP. A cellular Fat PCP vector is defined by the angular distribution of Fat PCP proteins within a given cell (green-yellow arrow).

gene [40].[4] In addition, the transmembrane protein *Flamingo* (Fmi) is considered to mediate intercellular interactions between Fz and Stbm, which is essential for the formation of the polarized clusters [37].

Besides *inter*cellular interactions between the Core PCP proteins, it is believed that there are also *intra*cellular interactions [37, 38]. In particular, the cytoplasmic proteins (Pk, Sple, Dsh, and Dgo) are supposed to mediate an intracellular repulsion of the two protein classes. Also, the cytoplasmic proteins are supposed to promote the clustered organization of the PCP proteins. In this work, we define a cellular Core PCP vector such that it points towards high concentrations of Fz within a given cell (blue-red arrow in Fig. 1.7B).

1.4.2 The Fat polarity system

Like for the Core PCP system, the most important molecular details of the Fat PCP system have already been clarified in the past [41–43]. The two Fat PCP proteins *Fat* (Ft) and *Dachsous* (Ds) can bind to each other across cell membranes (Fig. 1.8). Their binding affinity is believed to be modulated by the protein *Four jointed* (Fj) [41]. In addition, the Ft-Ds dimers lead to the intracellular polarization of the myosin *Dachs* (D) towards the Ds side. Moreover, it has been shown that large-scale order of Fat PCP can be induced by gradients of Ds and Fj (Fig. 1.8) [44, 45]. In this thesis, we define a cellular Fat PCP vector such that it points towards high concentrations of Ds and D within a given cell (green-yellow arrow in Fig. 1.8).

Fat PCP influences tissue morphogenesis in different ways. First, the Fat PCP proteins have been shown to be involved in growth control [46–48]. Also, it guides anisotropies in cellular stresses, in cell shape, in cell rearrangements, and in cell divisions [49–51]. In addition, it has been shown that Fat PCP couples to Core PCP in some tissues [25, 38, 52]. However, the precise interactions between both PCP systems are subject of an ongoing debate [39, 42, 43, 53–57]. In this thesis, we study the interactions between Fat PCP and Core PCP using physical tools.

---

[4] This means that there are different ways to express the so-called *pk-sple* gene resulting in different proteins, Pk and Sple, that have some parts of their amino acid sequence in common.

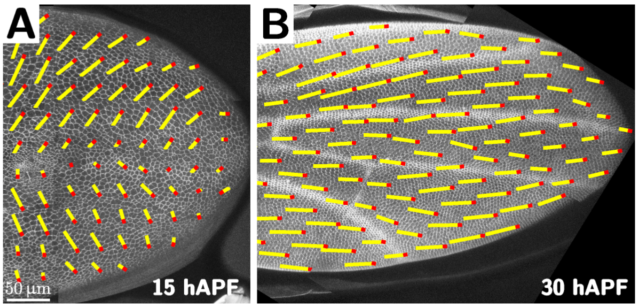

Figure 1.9: Reorientation of Core PCP in the fruit fly wing between 15 hAPF **(A)** and 30 hAPF **(B)**. The yellow bars indicate the local axis of Core PCP. The red dots indicate the direction of Core PCP (corresponding to the arrowheads of the blue-red arrows in Figs. 1.5B and 1.7B). (Image source: adopted from ref. [54].)

1.4.3 Planar cell polarity in the fruit fly wing

The fruit fly wing is the classical model system for studying PCP. It is the first system where Core PCP was discussed and much is known about PCP in the fly wing [23–27, 38]. Also, the comparably flat geometry makes it an attractive system for the study of PCP.

Another advantage of the fly wing as a PCP model is the following. There is a simple read-out of the local Core PCP vector: Each cell of the wing epithelium gives rise to a single hair, the direction of which is determined by the local direction of Core PCP (Figs. 1.5B and 1.6A). In particular, the direction of the hair corresponds to the direction where the intracellular Fz intensity is highest. Put differently, the blue-red arrows in Figs. 1.5B and 1.7B correspond to each other. The hairs start to grow during pupal stages, around 32 hAPF (green structures in Fig. 1.7A). Ultimately, the hairs become part of the cuticle that remains after the wing cells die. Note that both wing layers, dorsal and ventral, give rise to wing hairs. Correspondingly, one sees pairs of hairs rather than single hairs in Figs. 1.5B and 1.6A.

It has recently been shown that in the fruit fly wing, Core PCP reorients during pupal stages (Fig. 1.9) [54, 58]. In wild type wings around 15 hAPF, the Core PCP vector field is oriented towards the margin of the wing with angles of ca. $\pi/4$ with respect to the proximo-distal wing axis (Fig. 1.9A). This polarity pattern reorients continuously to point distally at 30 hAPF, reflecting the wild type wing hair pattern (Fig. 1.9B; compare Figs. 1.5B, 1.6A, and 1.7A). Another recent study has shown that both, Core PCP and Fat PCP, already show large-scale order in the wing disc during larval stages [55]. To our knowledge, Fat PCP has not been systematically quantified in the pupal wing before our work.

1.5 Physical description of biological tissues

From the physical point of view, biological tissues are complex materials. They are highly heterogeneous, being composed of cells, which are in turn composed of various cell organelles of different chemical composition [2]. Moreover, biological tissues are living matter.

Living matter is fundamentally different from most dead matter in one central property: it continuously transforms chemically stored free energy into systematic motion. It is thus called *active matter* [59–64]. On the scale of an organism, chemical free energy is typically taken up in the form of food or sunlight. Within the individual cells of an organism, this free energy is stored by phosphorylation of molecules like *adenosine diphosphate* into *adenosine triphosphate*. Because of the continuous transformation of this free energy into mechanical energy, for instance by molecular motors [65], living matter is permanently out of thermodynamic equilibrium [66]. This is different from most dead matter, which eventually reaches thermodynamic equilibrium in the absence of external driving.[5]

In the following, we discuss physical descriptions for different aspects of biological tissues. First, we present continuum descriptions of the large-scale rheological behavior of tissues. Then, we list models that describe mechanical behavior of epithelial tissues at the cellular scale. Finally, we present theoretical models describing PCP.

1.5.1 Continuum descriptions for biological tissues

The precise rheological properties of biological tissues typically depend on the type of tissue studied [11, 67]. For instance, blood is mainly liquid and bones are mainly solid. However, practically all tissues show a combination of viscous, elastic, and plastic behavior [3, 68]. In particular, even blood shows a yield stress like plastic materials [11, 68, 69] and bones have a finite viscosity [67].

Systematic studies of mechanical tissue properties started in the first half of the 20th century. Around 1940, Johannes Holtfreter observed the sorting of dissociated embryonic cells into distinctly layered aggregates [70, 71]. A similar kind of sorting occurs for instance during the early developmental stage of gastrulation, which nearly all multi-cellular animals undergo. In 1963, Malcom Steinberg put forward his *differential adhesion hypothesis*, which explains these cell sorting experiments by the unmixing of liquids with different surface tensions [72–75]. His work resulted in an ongoing discussion about the roles of cellular adhesion and interfacial tension in creating an effective tissue surface tension [76–79]. Nowadays, similar ideas are applied to study for instance the comparmentalization of the fruit fly wing [18, 80–82]. In these latter works, the morphology of compartment boundaries is explained by an increased tension at the interface between different cell populations.

Besides interfacial properties, there is an ongoing discussion about the bulk properties of biological tissues. A classical physical model for cellular materials is foam, which typically shows elastic and plastic behavior [83–85]. In contrast to that, Steinberg and co-workers usually described cell aggregates as viscous fluids [86] or visco-elastic fluids

---

[5] From a different point of view, one could also consider the take up of food as an external driving for living organisms – like a car is driven by fuel. However, in living tissues, the externally supplied free energy is stored and consumed throughout the whole material, which is in contrast to most man-made materials.

[87–89]. Other work describes the same data using models for visco-elastic solids [90] or using combined elastic-plastic-viscous models [91, 92]. More recently, descriptions of complex active visco-elastic fluids have emerged [59, 60, 62–64]. Such descriptions have also been applied to biological tissues [93–97].

Clearly, the rheological properties of tissues result from the rheological properties of single cells. However, cellular interactions like topological changes of the cellular network also play a role. For instance, cell divisions have been shown to fluidify otherwise purely elastic biological tissues [95, 96]. In this thesis, we contribute to this discussion by studying how the stress relaxation behavior of tissues depends on cell-scale fluctuations.

The physical description of biological tissues has to deal with fundamental difficulties, which also appear when describing plastic deformations of solids [98–101]. We will shortly outline these difficulties. For elastic materials, deformation or strain can be described with respect to a fixed reference state, which is typically stress-free. In the absence of external forces the system always returns to this stress-free reference state. However in plastic materials, deformations may change the microscopic topological structure of the material, for instance by rewiring links between the microscopic elements. Typically, whenever the topological structure of the material is changed, the stress-free state changes. Thus, plastic deformations can not be described with respect to a single reference state. Often, the total deformation of the material is then decomposed into an *elastic strain* and a *plastic strain* [85, 92, 98, 102]. The elastic strain describes the deformation with respect to a varying reference state, and the plastic strain describes the change of the reference state.

Taking such reference changes into account is also necessary for the description of biological tissues [68, 90, 91, 103]. In biological tissues, the topology of the cellular network changes continuously, for instance due to cell divisions and cell rearrangements. In this thesis, we develop a theoretical framework that decomposes the deformation of two-dimensional biological tissues into several contributions. More precisely, we decompose tissue deformation into contributions by cellular shape changes, which are related to elastic strain, and into contributions by topological changes, which are related to plastic strain.

1.5.2 Cell-based models for epithelial mechanics

There is a large variety of different cell-based models used to describe biological tissues. Here, we merely present a selection. For a more complete overview, see refs. [104, 105].

One class of models describes individual cells by point-like particles, where each cell is represented by either a single particle [93, 94, 106–110] or by a particle pair [95, 111]. Interactions between the individual cells are described by mechanical potentials depending on the particle distances. To simulate time-dependent tissue behavior, the Metropolis algorithm [106, 107, 109], simple friction dynamics [93, 94, 110], Langevin dynamics [108], or Dissipative Particle Dynamics [95, 111] have been used. Such

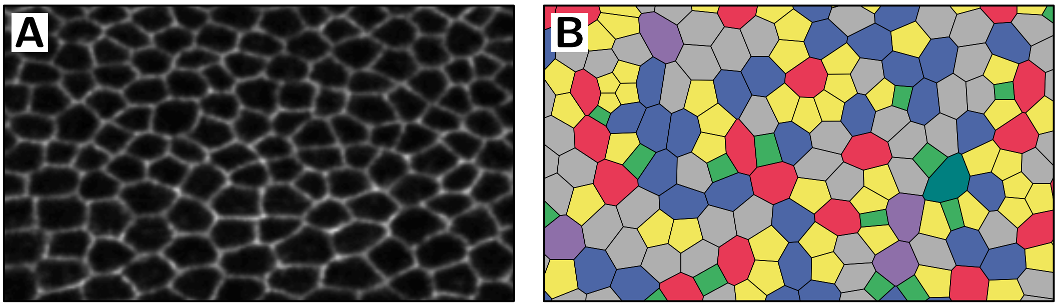

Figure 1.10: In a vertex model, each cell is represented by a polygon. **(A)** Membrane staining of a fruit fly wing epithelium at 25 hAPF. **(B)** Force-equilibrated state of the vertex model from ref. [118]. The cells are colored according to their neighbor number (see Table 3.1 on page 55).

methods have been applied to study tissue growth, cell sorting, tissue surface tension, tissue rheology, wound healing, and tumor growth [93–95, 106–111].

Another class of models are the *Cellular Potts Models* (CPMs), which also take cell shapes into account [104, 112–115]. Like many physical models for biological tissue, they start from an effective tissue energy to describe mechanical cell properties and cell interactions. In particular, these models mostly include effective cell-cell interfacial tensions and a cell area elasticity. The CPMs are based on the so-called Potts model, which generalizes the Ising model to more than two possible values for the spin [116, 117]. In the CPMs, each cell corresponds to a single spin value. CPMs are lattice-based, where each lattice site is characterized by a spin, i.e. may belong to one of the cells. To simulate dynamics, the Metropolis algorithm is used. Such models have been applied in a broad range of contexts [104, 105], for instance to study cell sorting [112, 113], growth, division, apoptosis, differentiation [114], and tissue rheology [92].

Finally, there is the class of so-called *vertex models*, which describe epithelia as networks of polygons, where each cell is represented by a single polygon (Fig. 1.10) [50, 58, 78, 80–82, 118–127]. Like CPMs, most vertex models also start from an effective energy describing elastic properties of single cells. Practically all vertex models assume a cell-cell interfacial tension, and most vertex models assume some kind of area elasticity. The time-evolution of the cellular network is simulated using a quasi-static description of subsequent energy minima [80–82, 118, 120–126, 128] or actual friction dynamics [50, 58, 119, 125]. The vertex model has been applied to study local epithelial topology [118, 121, 122], growth control [120, 123, 124], morphology of interfaces [80–82], anisotropic tissue growth [50], the emergence of ordered cellular patterns [125], and PCP [50, 54, 121, 125]. Currently, the first complex three-dimensional vertex models are being established [126]. In this thesis, we use the vertex model from ref. [118] to study epithelial rheology.

1.5.3 Models for planar cell polarity

In many tissues, the Core PCP pattern shows large-scale polar order that typically correlates with organ or body axes (see for instance Fig. 1.6A-C). It is a long-standing puzzle in the field, how such large-scale order could be created [24, 38, 52, 129]. One class of approaches assumes for instance a large-scale gradient of an unknown protein called "factor X" [130–133]. According to these models, such a gradient would be locally read out by the Core PCP system. However, despite intense research, the protein corresponding to the postulated "factor X" could not be identified.

Another, more recent work suggests that Core PCP is reoriented by shear deformations of tissue [54]. There, it was shown that a coupling to shear could explain the observed reorientation of Core PCP in the pupal fruit fly wing (see Section 1.4.3). To this end, a simple hydrodynamic description from liquid crystal theory was used [134]. From this point of view, large-scale order of Core PCP could be led back to global tissue deformations.

Such a reorientation of Core PCP by tissue shear could be based on different microscopic mechanisms. One such mechanism could be mediated by cell elongation: Shear could guide cell elongation, which in turn affects microtuble orientation [135–137], which finally reorients Core PCP. Indeed, it has been shown that in the fruit fly wing, the shear axis coincides with the cell elongation axis [54], which coincides with the axis of microtubles [138]. Furthermore, it was shown that Core PCP proteins are actively transported along microtubles [139]. In this thesis, we provide further evidence for a coupling of Core PCP reorientation to an effective shear field, which encompasses tissue shear and cell elongation. Interestingly, it has recently been suggested that also the Fat polarity system may affect the orientation of microtubles depending on the balance of the proteins Prickle and Sple [57, 140, 141].

During the past ten years, a number of models describing Core PCP on the cellular and sub-cellular level have emerged [54, 58, 121, 125, 131, 132, 142–147]. In this and the following paragraph, we present a few of them. Two prominent models successfully described the wing hair phenotypes in many genetic experiments [131, 132, 142]. However, the used reaction-diffusion type models are very involved, and include for instance ten coupled non-linear partial differential equations. This clearly hinders a true physical understanding. In ref. [143], the authors propose a much simpler model. Using an analogy to ferromagnetism, they conclude that some external directional bulk cue is needed to create long-range Core PCP order.

Two other cellular Core PCP models have been created by building them on top of vertex models [54, 58, 121, 125]. In these models, scalar variables describe the net amount of PCP proteins on each side of a cell-cell interface. Then, cellular Core PCP vectors or nematics are defined from anisotropies in the distribution of these proteins. Interactions across cell-cell interfaces and within cells are described using an effective energy function. Such models have been used to explain the emergence of large scale directional Core PCP order [54, 121] and large-scale positional order of cells [125]. In this thesis, we use the Core PCP model defined in [54, 121].

1.6 Overview over this thesis

In this thesis, we theoretically study the behavior of epithelial tissues. To this end, we aim at an effective description of tissue properties at large scales. Also, we are interested in understanding how these properties result from cellular processes. We compare our theoretical concepts to experimental data from the developing fruit fly wing. These experimental data were provided through a close collaboration with the group of Suzanne Eaton at the Max Planck Institute of Molecular Cell Biology and Genetics in Dresden.

The remaining parts of this thesis are organized as follows. In the next two chapters, we study the mechanical properties of two-dimensional tissues. As a prerequisite for that, in Chapter 2, we study how tissue deformation arises from cellular processes. More precisely, we develop an exact theoretical framework that decomposes tissue deformation into cellular contributions, which comprise cellular shape changes and contributions by topological transitions. Then, in Chapter 3, we study large-scale rheological properties of two-dimensional tissues using a vertex model. We show that small-scale fluctuations may turn plastic tissue behavior into visco-elastic behavior.

In Chapter 4, we study the dynamics of PCP in the pupal fly wing. To this end, we create a hydrodynamic description for the reorientation of Core PCP. This description includes couplings to an effective tissue shear and to Fat PCP. We find that our theoretical description successfully reproduces not only the wild type wing hair pattern, but also the wing hair patterns of genetically modified flies. In Chapter 5, we conclude this thesis with a summary and an outlook.

Chapter 2

Tissue shear in cellular networks

During development of an organism, epithelia may undergo large-scale deformations. For example, the wing epithelium of a fruit fly deforms significantly during pupal stages (Fig. 2.1A). On the cellular scale, such deformations are reflected by cell shape changes, T1 transitions (cell rearrangements), T2 transitions (cell extrusion events), and cell divisions (Fig. 2.1B). In this chapter, we propose a formalism to quantify large-scale tissue deformations and to decompose them into cellular contributions.

To this end, we first discuss deformations on the cellular scale (Section 2.1). We use rigorous geometric arguments to relate local deformations to cellular shape changes. Also, we discuss the local effect of individual topological transitions of the cellular network. Then, we derive the central relations that exactly decompose large-scale tissue deformations into contributions by cell shape changes and by topological transitions (Section 2.2). Afterwards, we use this theoretical framework in order to quantitatively describe the large-scale deformation of the pupal fruit fly wing (Section 2.3, Fig. 2.1A). Finally, we summarize our results and compare to the existing literature (Section 2.4).

In this chapter, we have to introduce an appreciable number of quantities. On pages 225f., we list the most important among them.

2.1 Geometry of tissue deformation on the cellular scale

2.1.1 Cellular networks and their triangle-based description

Tissue as a cellular network

In this thesis, we describe epithelia as planar networks of cells (Fig. 2.2A). For simplicity, we describe cells as polygons (green solid outline).[1] The shape of each cell is defined by the positions of its corners, which we call vertices (red dot). A vertex that lies on the network margin is called margin vertex. All other vertices are called inner vertices. Two vertices may be connected by a bond (blue solid line), which corresponds to the side of a polygon. The connections between cells, vertices, and bonds define the

---

[1] However, note that this chapter applies as well to cells with curved boundaries.

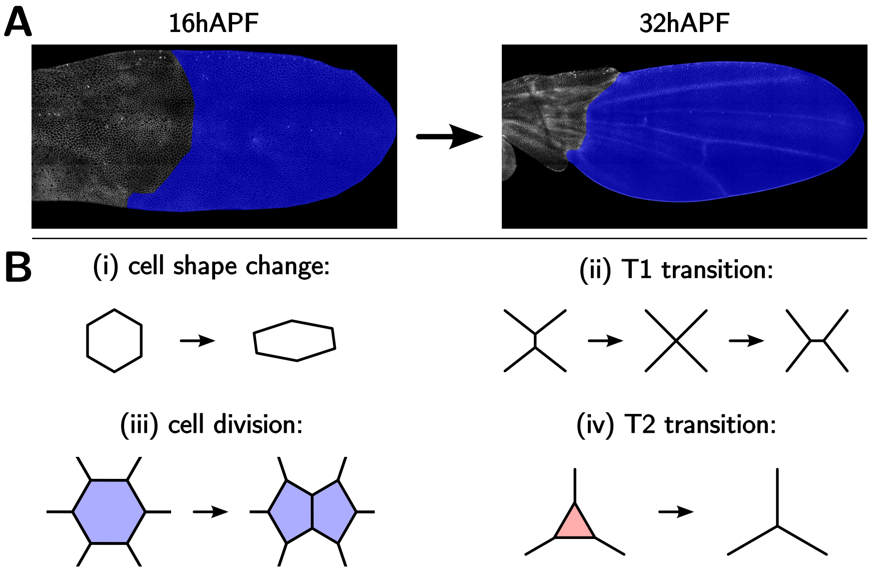
A
16hAPF
32hAPF
B
(i) cell shape change:
(ii) T1 transition:
(iii) cell division:
(iv) T2 transition:

Figure 2.1: Large-scale deformations of epithelia correspond to cellular events. **(A)** Deformation of the wing blade (blue region) of a wild type fruit fly between the developmental times of 16 hAPF and 32 hAPF. **(B)** Cellular events considered in this chapter.

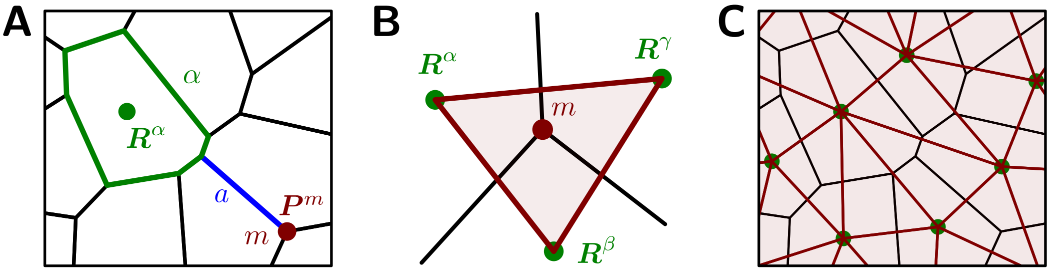
A
α
R^α
a
P^m
m
B
R^α
R^γ
m
R^β
C

Figure 2.2: Planar cellular network and tiling into triangles. **(A)** Planar cellular network, where black lines mark cell-cell interfaces (bonds). A cell α is marked with its center position $\boldsymbol{R}^\alpha$ (green solid outline and green dot). Also marked is a vertex m (red dot) and a bond a (blue solid line). **(B)** Definition of a single triangle. Bonds are marked by black lines. For each vertex m (red dot), we define a single triangle (red solid lines). The corners of this triangle are defined by the centers $\boldsymbol{R}^\alpha$, $\boldsymbol{R}^\beta$, and $\boldsymbol{R}^\gamma$ (green dots) of the three cells touching vertex m. **(C)** The so-defined triangles tile the whole cellular network.

topology of the cellular network. Throughout this thesis, cells are labeled by lowercase Greek letters starting with α, vertices are labeled by lowercase Latin letters starting with m, and bonds are labeled by lowercase Latin letters starting with a.

A vertex that is connected to N bonds is called N-fold. For simplicity, in this and the following section, we restrict to the case where all inner vertices are threefold.[2] In Section 2.3, we generalize our ideas allowing for the existence of N-fold inner vertices with $N \geq 3$. In all following chapters, we also allow for $N \geq 3$.

In order to describe the geometry of the network, we introduce a two-dimensional Cartesian coordinate system and denote the axes by x and y. Then, the whole geometric information of the network is given by the set of all vertex positions $\boldsymbol{P}^m$. Throughout this work, boldface symbols denote vectors. For a given vertex m, the components of its position vector $\boldsymbol{P}^m$ are given by

$$\boldsymbol{P}^m = \begin{pmatrix} P_x^m \\ P_y^m \end{pmatrix}. \tag{2.1}$$

From the vertex positions, we can define cellular properties. For a given M-sided cell α, the area is given by:

$$A^\alpha = \frac{1}{2} \sum_{m=1}^{M} \Big(P_x^m P_y^{m+1} - P_x^{m+1} P_y^m \Big). \tag{2.2}$$

For the summation on the right hand side, the vertex indices m are sorted in counter-clockwise order and the vertex $M+1$ corresponds to the vertex 1. Furthermore, we define the center of area $\boldsymbol{R}^\alpha$ of cell α by:[3]

$$R_i^\alpha = \frac{1}{6A^\alpha} \sum_{m=1}^{M} \Big(P_x^m P_y^{m+1} - P_x^{m+1} P_y^m \Big) \big(P_i^m + P_i^{m+1} \big). \tag{2.4}$$

Like above, vertex indices m are sorted in counter-clockwise order. Our description of tissue deformation will be based on the displacements of the cell centers $\boldsymbol{R}^\alpha$.

Triangle-based description of cellular networks

In order to describe deformations of the cellular network, we tile the network into triangles. We choose a tiling into triangles because it allows for an exact description of network deformation. In particular, for each triangle, we can define a 2 × 2 tensor

---

[2] We do not restrict N for margin vertices. Note that in general, margin vertices may also be twofold.

[3] Eq. (2.4) is equivalent to the following integral over the polygon area:

$$\boldsymbol{R}^\alpha = \frac{1}{A^\alpha} \int_{A^\alpha} \boldsymbol{r} \, \mathrm{d}^2 r. \tag{2.3}$$

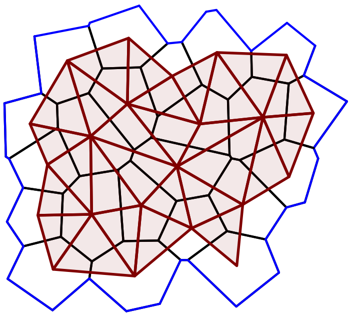

Figure 2.3: A cellular network (black lines are bonds) with its margin (blue lines). The triangulation is shown by red triangles. The triangulation does not cover the margin of the cellular network.

that uniquely describes its deformation (see Section 2.1.3). This is not possible for polygons with more than three sides.

We propose the following procedure to triangulate the network (Fig. 2.2B). Each inner vertex m gives rise to a single triangle, which we also label by m. Since the vertex m is threefold, it touches three cells, which we denote by α, β, and γ. Then, the corners of the triangle m are defined by the respective cell centers $\boldsymbol{R}^\alpha$, $\boldsymbol{R}^\beta$, and $\boldsymbol{R}^\gamma$. These rules uniquely define a tiling of the cellular network into triangles, without gaps or overlaps between the triangles (Fig. 2.2C).[4] However, because only inner vertices give rise to triangles, the margin region of the network is not covered by triangles (Fig. 2.3).

In the following, we first discuss the deformation of single triangles. To this end, we define triangle state properties (Section 2.1.2) and relate them to components of triangle deformation (Section 2.1.3). Then, we coarse grain the obtained relations in order to study the deformation of triangle groups in the absence of topological transitions (Section 2.1.4). Afterwards, we discuss the effect of individual topological transitions (Section 2.1.5). Finally, we provide a decomposition of large-scale deformations into contributions by cellular shape changes and topological transitions (Section 2.2).

2.1.2 Characterization of triangle shapes

Triangle state tensor S_{ij}

Here, we introduce a tensor S_{ij}^m describing the shape of a given triangle m. Note that in this and the next section, we introduce a number of triangle-related quantities. To this end, we will focus on a single triangle, and thus, we omit the superscript m on all triangle-related quantities in this and the next section.

The state tensor S_{ij} of the triangle m is defined by a linear transformation, which maps a reference triangle to the triangle m (Fig. 2.4A). The corner positions of the triangle m are given by the respective centers of the three abutting cells $\boldsymbol{R}^1$, $\boldsymbol{R}^2$, and $\boldsymbol{R}^3$.

---

[4] Note that one could also choose another method to triangulate the cellular network and much of our formalism to quantify deformation does not depend on the triangulation method. In Appendix B.7, we shortly discuss one alternative triangulation method.

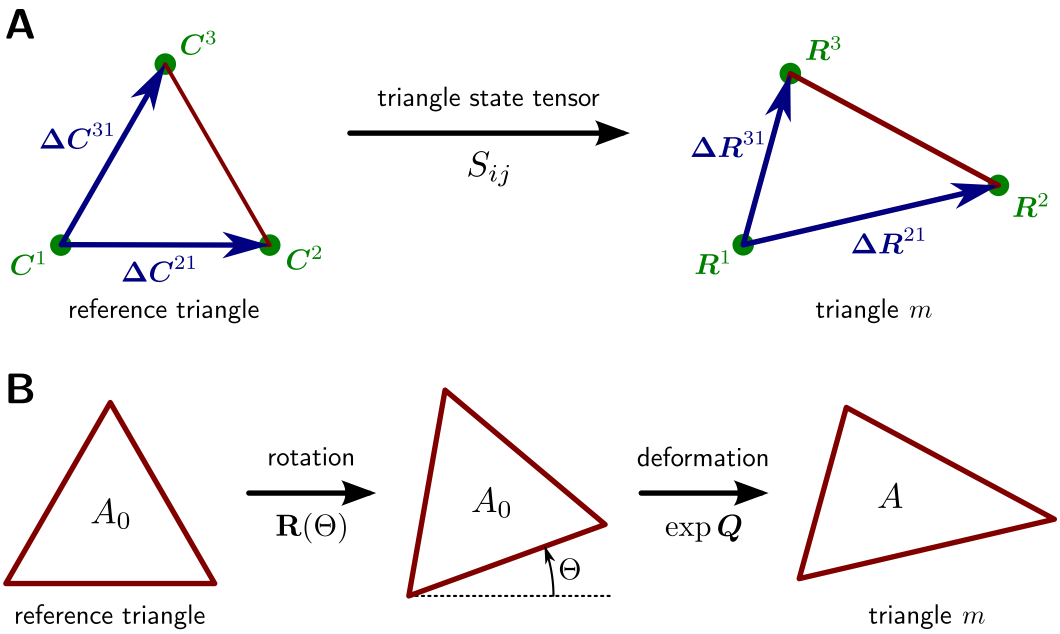
A
C^3
ΔC^{31}
C^1
ΔC^{21}
C^2
reference triangle
triangle state tensor
S_{ij}
R^3
ΔR^{31}
R^2
R^1
ΔR^{21}
triangle m
B
A_0
reference triangle
rotation
$\mathbf{R}(\Theta)$
A_0
Θ
deformation
$\exp \boldsymbol{Q}$
A
triangle m

Figure 2.4: Definition of triangle state properties. **(A)** Definition of the state tensor S_{ij} for a triangle m. The tensor S_{ij} is defined by a linear transformation mapping the sides of an equilateral reference triangle to the sides of triangle m (Eq. (2.5)). **(B)** The state tensor S_{ij} is decomposed into a rotation by the orientation angle Θ, followed by a deformation characterized by the shape tensor Q_{ij} (Eq. (2.7)). The scalars A_0 and A denote the respective areas of the reference triangle and of the triangle m.

As reference triangle, we choose an equilateral triangle with area A_0. Furthermore, the reference triangle is rotated such that one side is parallel to the x axis of the coordinate system. The corner positions of the reference triangle are denoted by $\boldsymbol{C}^1$, $\boldsymbol{C}^2$, and $\boldsymbol{C}^3$.[5]

We define the state tensor S_{ij} such that it maps the sides of the reference triangle to the corresponding sides of triangle m. Thus, for any choice of $\alpha, \beta \in \{1, 2, 3\}$:

$$\Delta R_i^{\beta\alpha} = S_{ij} \Delta C_j^{\beta\alpha}. \tag{2.5}$$

Here, we defined the vector $\boldsymbol{\Delta C}^{\beta\alpha} = \boldsymbol{C}^\beta - \boldsymbol{C}^\alpha$ describing a side of the reference triangle and the vector $\boldsymbol{\Delta R}^{\beta\alpha} = \boldsymbol{R}^\beta - \boldsymbol{R}^\alpha$ describing the corresponding side of triangle m. Because of Eq. (2.5), the tensor S_{ij} contains the same geometrical information as all difference vectors $\boldsymbol{\Delta R}^{\beta\alpha}$ describing the sides of triangle m.

---

[5] There is a freedom of choice in how the corners of triangle m are associated to the corners of the reference triangle. We choose the convention the corners of both triangles should be sorted in counter-clockwise order. However, there is still a discrete gauge freedom in choosing which corner of the reference triangle should correspond to the center of cell 1.

There is a unique tensor S_{ij} that fulfills Eq. (2.5) for any choice of $\alpha, \beta \in \{1, 2, 3\}$. It is given by the following matrix product:

$$\boldsymbol{S} = \left(\boldsymbol{\Delta R}^{21} \;\; \boldsymbol{\Delta R}^{31}\right) \cdot \left(\boldsymbol{\Delta C}^{21} \;\; \boldsymbol{\Delta C}^{31}\right)^{-1}. \tag{2.6}$$

Here, the vectors $\boldsymbol{\Delta R}^{\beta\alpha}$ and $\boldsymbol{\Delta C}^{\beta\alpha}$ denote column vectors and the dot denotes the matrix product. [6]

Decomposition of the triangle state tensor

We parametrize the state tensor S_{ij} by an orientation angle Θ and a symmetric tensor Q_{ij} describing the shape of triangle m. More precisely, we decompose the linear transformation defined by S_{ij} into a rotation by the angle Θ, followed by a deformation characterized by Q_{ij} (Fig. 2.4B):

$$\boldsymbol{S} = \exp\left(\boldsymbol{Q}\right) \cdot \mathbf{R}\left(\Theta\right). \tag{2.7}$$

In Appendix A.5, we show that Θ and Q_{ij} are uniquely defined by this relation. Here, the dot denotes the matrix product and the exponential of a matrix is defined by the Taylor series of the exponential function (Appendix A.4). The rotation matrix $\mathrm{R}_{ij}\left(\Theta\right)$ is defined by

$$\mathbf{R}\left(\Theta\right) = \exp\left(\Theta\boldsymbol{\epsilon}\right) \tag{2.8}$$

with the generator of rotations

$$\boldsymbol{\epsilon} = \begin{pmatrix} 0 & -1 \\ 1 & 0 \end{pmatrix}. \tag{2.9}$$

Note that Eq. (2.7) corresponds to a polar decomposition of the tensor S_{ij} [148]. Also note that the shape tensor Q_{ij} corresponds most closely to what is often called elastic strain.

We further decompose the shape tensor Q_{ij} into a contribution by the trace Q_{kk} and into a symmetric, traceless part $\tilde{Q}_{ij}$:

$$Q_{ij} = \frac{1}{2} Q_{kk}\delta_{ij} + \tilde{Q}_{ij}. \tag{2.10}$$

The trace Q_{kk} characterizes the triangle area A in the following way (Eq. (A.23) in Appendix A.4.2):

$$A = A_0 \exp\left(Q_{kk}\right). \tag{2.11}$$

Thus, the trace Q_{kk} characterizes an isotropic area scaling factor.

---

[6] Note that one may permute the cell indices $(1, 2, 3)$ in Eq. (2.6) without changing S_{ij}.

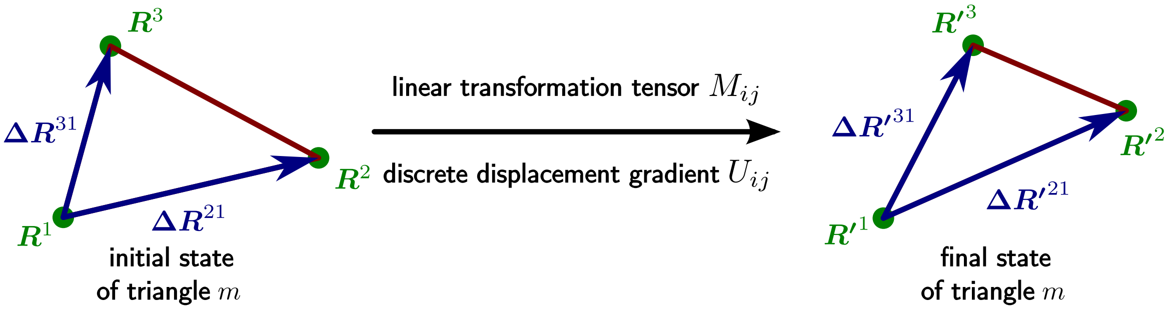

Figure 2.5: Definition of the tensors M_{ij} and U_{ij} describing triangle deformation. The tensor M_{ij} defines a linear transformation mapping the initial state of the triangle to its final state. The tensor U_{ij} is defined by the corresponding displacement gradient (compare Eq. (2.17)).

The symmetric, traceless part $\tilde{Q}_{ij}$ characterizes triangle elongation. We use it as a measure for local cell shape anisotropy. According to Eq. (2.7), the pure shear deformation defined by the tensor $\exp(\tilde{\boldsymbol{Q}})$ corresponds to the nematic anisotropy of the triangle shape (Appendices A.4.4 and A.4.5). In the following, we call symmetric, traceless tensors *nematic tensors* or just *nematics* (Appendix A.2). The norm of the nematic $\tilde{Q}_{ij}$ is defined by

$$|\tilde{Q}| = \left(\tilde{Q}_{xx}^2 + \tilde{Q}_{xy}^2\right)^{1/2}. \tag{2.12}$$

Furthermore, the angle of $\tilde{Q}_{ij}$, which we denote by Φ, is defined by the two equations $\tilde{Q}_{xx} = |\tilde{Q}| \cos(2\Phi)$ and $\tilde{Q}_{xy} = |\tilde{Q}| \sin(2\Phi)$.

2.1.3 Characterization of triangle deformation

Linear transformation tensor M_{ij}

In the last section, we described state properties of triangles. Here, we describe the deformation of a triangle m from an initial to a final state (Fig. 2.5). The corners of triangle m are defined by the centers of the cells 1, 2, and 3. The initial positions of the cell centers are denoted by $\boldsymbol{R}^\alpha$ and the final positions are denoted by $\boldsymbol{R}'^\alpha$ with $\alpha \in \{1, 2, 3\}$.

To describe the deformation of triangle m, we introduce a tensor M_{ij} that defines a linear transformation mapping the initial triangle to final triangle. Similarly to Eq. (2.5), we require for any choice of $\alpha, \beta \in \{1, 2, 3\}$ that:

$$\Delta R'^{\beta\alpha}_i = M_{ij} \Delta R^{\beta\alpha}_j. \tag{2.13}$$

Here, the vectors $\boldsymbol{\Delta R}^{\beta\alpha} = \boldsymbol{R}^\beta - \boldsymbol{R}^\alpha$ and $\boldsymbol{\Delta R}'^{\beta\alpha} = \boldsymbol{R}'^\beta - \boldsymbol{R}'^\alpha$ describe the sides of the triangle m in the initial and in the final state, respectively. Eq. (2.13) is uniquely fulfilled by the following definition for M_{ij}:

$$\boldsymbol{M} = \left(\boldsymbol{\Delta R'}^{21} \;\; \boldsymbol{\Delta R'}^{31}\right) \cdot \left(\boldsymbol{\Delta R}^{21} \;\; \boldsymbol{\Delta R}^{31}\right)^{-1}. \tag{2.14}$$

Here, the vectors $\boldsymbol{\Delta R'}^{\beta\alpha}$ and $\boldsymbol{\Delta R}^{\beta\alpha}$ denote column vectors and the dot denotes the matrix product.

Discrete displacement gradient U_{ij}

Now, based on the transformation tensor M_{ij}, we introduce a discretely defined displacement gradient tensor U_{ij}. To this end, we first extend the linear transformation defined by M_{ij} to all points within the triangle. A linear transformation that maps all points $\boldsymbol{r}$ of the initial triangle to points $\boldsymbol{r'}$ of the final triangle reads

$$r'_i = R'^1_i + M_{ij}\big(r_j - R^1_j\big). \tag{2.15}$$

Note that indeed, this transformation maps the initial triangle corners $\boldsymbol{R}^\alpha$ to the respective final triangle corners $\boldsymbol{R'}^\alpha$, where $\alpha \in \{1, 2, 3\}$.

The linear transformation in Eq. (2.15) defines the displacement field $\boldsymbol{u}(\boldsymbol{r})$:

$$\boldsymbol{u}(\boldsymbol{r}) = \boldsymbol{r'}(\boldsymbol{r}) - \boldsymbol{r}. \tag{2.16}$$

Then, the displacement gradient tensor U_{ij} reads:

$$U_{ij} = \frac{\partial u_j}{\partial r_i}. \tag{2.17}$$

With Eqs. (2.15) and (2.16), we obtain

$$U_{ij} = M_{ji} - \delta_{ij}. \tag{2.18}$$

Here, δ_{ij} denotes the Kronecker symbol. We use this equation as the discrete definition of the triangle displacement gradient U_{ij}. It contains the same information as the linear transformation tensor M_{ij}. However, for infinitesimal deformations, U_{ij} becomes infinitesimally small, whereas M_{ij} converges to the identity tensor. Note that Eq. (2.18) involves the transposition of matrix M_{ij}.

Decomposition of the triangle transformation tensor

We parametrize the linear transformation tensor M_{ij} by a rotation angle $\Delta\Psi$ and a symmetric deformation tensor ΔN_{ij}. Therefore, similarly to the state tensor S_{ij}, we write (compare Eq. (2.7) and Fig. 2.4B):

$$\boldsymbol{M} = \exp\left(\boldsymbol{\Delta N}\right) \cdot \mathbf{R}(\Delta\Psi). \tag{2.19}$$

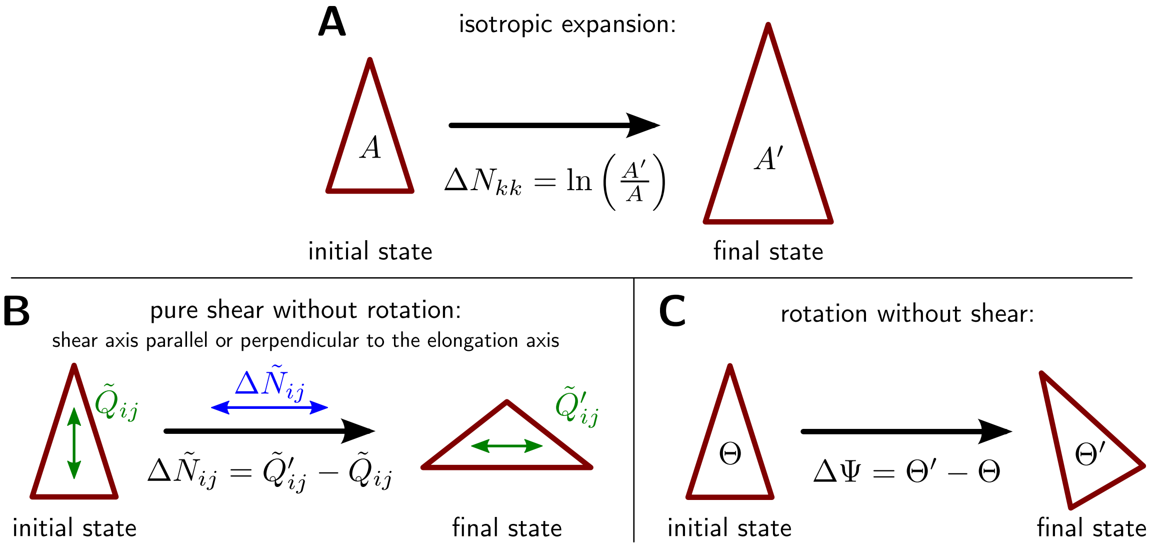
A
isotropic expansion:
A
$\Delta N_{kk} = \ln\left(\frac{A'}{A}\right)$
A'
initial state
final state
B
pure shear without rotation:
shear axis parallel or perpendicular to the elongation axis
$\tilde{Q}_{ij}$
$\Delta\tilde{N}_{ij}$
$\Delta\tilde{N}_{ij} = \tilde{Q}'_{ij} - \tilde{Q}_{ij}$
$\tilde{Q}'_{ij}$
initial state
final state
C
rotation without shear:
Θ
$\Delta\Psi = \Theta' - \Theta$
Θ'
initial state
final state

Figure 2.6: Transformation parameters $\Delta\Psi$ and ΔN_{ij} in terms of changes of triangle state properties for finite deformations. **(A)** Isotropic expansion. **(B)** Pure shear deformation without rotation and with a shear nematic $\Delta\tilde{N}_{ij}$ that is proportional to the elongation nematic $\tilde{Q}_{ij}$. **(C)** Rotation without shear. Note that isotropic expansion may be combined with either pure shear or rotation and the equations given in the respective panels still hold. However, the combination of pure shear deformations with rotations yields additional terms (see Eqs. (2.27) and (2.28) below).

In Appendix A.5, we show that this relation uniquely defines ΔN_{ij} and $\Delta\Psi$.

Similarly, the discrete displacement gradient tensor U_{ij} is parametrized as follows (using Eq. (2.18)):

$$\boldsymbol{U} = \mathbf{R}(-\Delta\Psi) \cdot \exp\left(\boldsymbol{\Delta N}\right) - \boldsymbol{I}. \tag{2.20}$$

Here, $\boldsymbol{I}$ denotes the identity tensor with $I_{ij} = \delta_{ij}$.

Like the shape tensor Q_{ij}, the deformation tensor ΔN_{ij} divides into a trace ΔN_{kk} and a symmetric, traceless part $\Delta\tilde{N}_{ij}$:

$$\Delta N_{ij} = \frac{1}{2}\Delta N_{kk}\delta_{ij} + \Delta\tilde{N}_{ij}. \tag{2.21}$$

Taken together, we decomposed the tensors M_{ij} and U_{ij} into three parts. The scalar ΔN_{kk} describes an isotropic area scaling factor (Fig. 2.6A), the nematic tensor $\Delta\tilde{N}_{ij}$ describes a pure shear deformation along its axis (Fig. 2.6B, see also Appendix A.4.5), and the angle $\Delta\Psi$ describes tissue rotation (Fig. 2.6C).

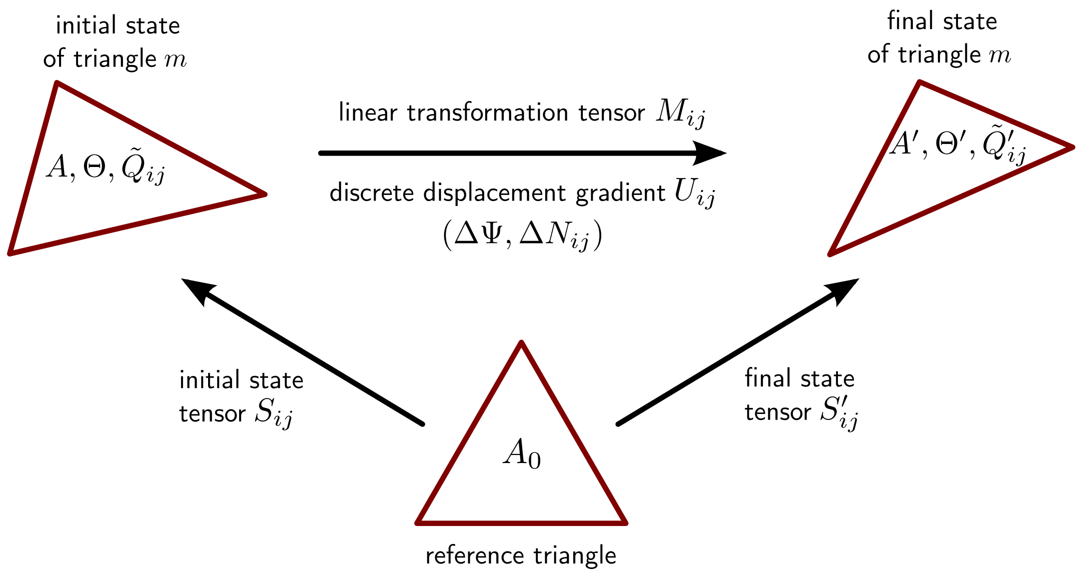
initial state
of triangle m
$A, \Theta, \tilde{Q}_{ij}$
linear transformation tensor M_{ij}
discrete displacement gradient U_{ij}
$(\Delta\Psi, \Delta N_{ij})$
final state
of triangle m
$A', \Theta', \tilde{Q}'_{ij}$
initial state
tensor S_{ij}
final state
tensor S'_{ij}
A_0
reference triangle

Figure 2.7: Connection between triangle transformation and triangle state. The tensors S_{ij} and S'_{ij} describe the initial and final triangle state, respectively. They are parametrized by the respective triangle state properties $A, \Theta, \tilde{Q}_{ij}$ and $A', \Theta', \tilde{Q}'_{ij}$. Both state tensors, S_{ij} and S'_{ij}, are defined by linear transformations with respect to the same reference triangle. Therefore, they can be linked to the linear transformation tensor M_{ij} via Eq. (2.22).

Triangle transformation corresponds to the change of triangle state

Now, we relate the triangle transformation tensor M_{ij} to the change of the triangle state tensor S_{ij} (Fig. 2.7). We denote the initial triangle state tensor by S_{ij} and the final state tensor by S'_{ij}. Then, from Eqs. (2.5) and (2.13) follows:

$$S'_{ik} = M_{ij} S_{jk}. \tag{2.22}$$

Thus, the linear transformation matrix M_{ij} also maps the initial state tensor S_{ij} to the final state tensor S'_{ij}.

Now, we relate the components of the transformation tensor M_{ij} to changes of components of the state tensor S_{ij}. We denote the initial and final components of the state tensor by A, Θ, $\tilde{Q}_{ij}$, and A', Θ', $\tilde{Q}'_{ij}$, respectively. We obtain (Appendix B.2.1):

$$\Delta N_{kk} = \ln\left(\frac{A'}{A}\right) \tag{2.23}$$

$$\exp\left(\boldsymbol{\Delta\tilde{N}}\right) \cdot \mathbf{R}(\Delta\Psi) = \exp\left(\boldsymbol{\tilde{Q}'}\right) \cdot \mathbf{R}(\Delta\Theta) \cdot \exp\left(-\boldsymbol{\tilde{Q}}\right), \tag{2.24}$$

where $\Delta\Theta = \Theta' - \Theta$.

We shortly discuss both equations, which are valid for arbitrary finite transformations. First, according to Eq. (2.23), the isotropic part of the deformation tensor ΔN_{ij} corresponds to area changes (Fig. 2.6A).

Second, in Eq. (2.24), the pure shear part and the rotation part are still entangled. In Appendix B.2.1, we disentangle both and present explicit analytical expressions for $\Delta\tilde{N}_{ij}$ and $\Delta\Psi$. Here, we just discuss two special cases. First, without rotation $\Delta\Psi = 0$ and for a shear nematic $\Delta\tilde{N}_{ij}$ that is proportional to the elongation nematic $\tilde{Q}_{ij}$,[7] we obtain $\Delta\tilde{N}_{ij} = \Delta\tilde{Q}_{ij}$ with $\Delta\tilde{Q}_{ij} = \tilde{Q}'_{ij} - \tilde{Q}_{ij}$ (Fig. 2.6B). Thus, in this case, the shear nematic corresponds exactly to the change of the elongation nematic. Second, without shear $\Delta\tilde{N}_{ij} = 0$, we obtain $\Delta\Psi = \Delta\Theta$ (Fig. 2.6C).[8] Thus, in this case, the rotation angle corresponds to the change in triangle orientation.

In the following, we discuss the general case where shear and rotation occur at the same time. To this end, we consider the limit of infinitesimal transformations.

Infinitesimal transformations

Here, we relate the components of the displacement gradient U_{ij} to changes of the state properties A, $\tilde{Q}_{ij}$, and Θ for the limit of infinitesimal transformations. To this end, we first simplify Eq. (2.20) relating U_{ij} to the deformation parameters ΔN_{ij} and $\Delta\Psi$. In a second step, we simplify Eqs. (2.23) and (2.24).

Introducing the infinitesimal quantities $\delta U_{ij} = U_{ij}$, $\delta N_{ij} = \Delta N_{ij}$, and $\delta\Psi = \Delta\Psi$, we obtain from Eq. (2.20) to linear order:

$$\delta U_{ij} = \delta N_{ij} - \delta\Psi\epsilon_{ij}. \tag{2.25}$$

This equation helps us to interpret the components of the displacement gradient δU_{ij} for infinitesimal transformations. First, the trace $\delta U_{kk} = \delta N_{kk}$ describes isotropic expansion of the triangle. Second, the symmetric, traceless part $\delta\tilde{U}_{ij} = \delta\tilde{N}_{ij}$ describes pure shear deformations. Finally, the antisymmetric part of δU_{ij}, which is given by $\delta\Psi$, describes rotations.

Now, we simplify Eqs. (2.23) and (2.24) in order to express the components of δU_{ij} by changes of the triangle state properties A, $\tilde{Q}_{ij}$, and Θ. For the trace δU_{kk} we obtain from Eq. (2.23):

$$\delta U_{kk} = \frac{1}{A}\delta A \qquad \text{(isotropic expansion).} \tag{2.26}$$

Here, $\delta A = A' - A$ denotes the triangle area change. Thus, the trace of the discrete displacement gradient δU_{kk} corresponds to the relative area change.

For the other components of δU_{ij}, we obtain from Eq. (2.24) to linear order (Appendix B.2.2):

---

[7] Put differently, the respective axes of the shear nematic and the elongation nematic are parallel or perpendicular to each other.

[8] Note that in this case, also the elongation nematic $\tilde{Q}_{ij}$ is being rotated.

$$\delta\tilde{U}_{ij} = \delta\tilde{Q}_{ij} + \delta\tilde{J}_{ij} \qquad \text{(pure shear deformation)} \tag{2.27}$$

$$\delta\Psi = \delta\Theta - \delta\Xi \qquad \text{(rotation).} \tag{2.28}$$

Here, we defined $\delta\tilde{Q}_{ij} = \tilde{Q}'_{ij} - \tilde{Q}_{ij}$ and $\delta\Theta = \Theta' - \Theta$. Also, in Eq. (2.27), we defined:

$$\delta\tilde{J}_{ij} = -2\Big[c\delta\Psi + (1-c)\delta\Phi\Big]\epsilon_{ik}\tilde{Q}_{kj}, \tag{2.29}$$

with $c = \tanh(2|\tilde{Q}|)/2|\tilde{Q}|$ and $\delta\Phi = \Phi' - \Phi$. Norm $|\tilde{Q}|$ and angle Φ of the elongation nematic $\tilde{Q}_{ij}$ are defined in Eq. (2.12) and below. The tensor ϵ_{ij} is defined in Eq. (2.9). In Eq. (2.28), we defined:

$$\delta\Xi = \delta\tilde{U}_{ij}\epsilon_{jk}\tilde{Q}_{ki}\frac{\cosh(2|\tilde{Q}|) - 1}{2|\tilde{Q}|\sinh(2|\tilde{Q}|)}. \tag{2.30}$$

In the following, we discuss Eqs. (2.27)-(2.30) in more detail.

Pure shear deformations Eq. (2.27) states that the shear $\delta\tilde{U}_{ij}$ does not only correspond to the change of the elongation nematic $\tilde{Q}_{ij}$, but also includes a corotational contribution $\delta\tilde{J}_{ij}$. In particular, the corotational contribution $\delta\tilde{J}_{ij}$ represents the amount of shear that is necessary to maintain the elongation nematic $\tilde{Q}_{ij}$ constant in the presence of local tissue rotation.

In order to discuss the corotational contribution to shear, we decompose the elongation change $\delta\tilde{Q}_{ij}$ and the shear $\delta\tilde{U}_{ij}$ into components proportional to $\tilde{Q}_{ij}$ and into components proportional to $\epsilon_{ik}\tilde{Q}_{kj}$ (Appendix A.2.3). Nematic tensors proportional to the elongation $\tilde{Q}_{ij}$ have an axis parallel or perpendicular to the elongation axis, whereas nematic tensors proportional to $\epsilon_{ik}\tilde{Q}_{kj}$ have an axis at an angle of $\pi/4$ with respect to the elongation axis.

We first decompose the elongation change $\delta\tilde{Q}_{ij}$ (Appendix A.2.4):

$$\delta\tilde{Q}_{ij} = \delta|\tilde{Q}|\frac{1}{|\tilde{Q}|}\tilde{Q}_{ij} + 2\delta\Phi\epsilon_{ik}\tilde{Q}_{kj}. \tag{2.31}$$

Here, $\delta|\tilde{Q}|$ denotes the change of the elongation norm $|\tilde{Q}|$. Thus, the component of $\delta\tilde{Q}_{ij}$ that is proportional to $\tilde{Q}_{ij}$ changes the elongation norm, whereas the component that is proportional to $\epsilon_{ik}\tilde{Q}_{kj}$ changes the angle of the elongation axis Φ (Fig. 2.8A,B).

To obtain the shear $\delta\tilde{U}_{ij}$ from $\delta\tilde{Q}_{ij}$, we add the corotational contribution $\delta\tilde{J}_{ij}$ (using Eqs. (2.27) and (2.29)):

$$\delta\tilde{U}_{ij} = \delta|\tilde{Q}|\frac{1}{|\tilde{Q}|}\tilde{Q}_{ij} + 2c(\delta\Phi - \delta\Psi)\epsilon_{ik}\tilde{Q}_{kj}. \tag{2.32}$$

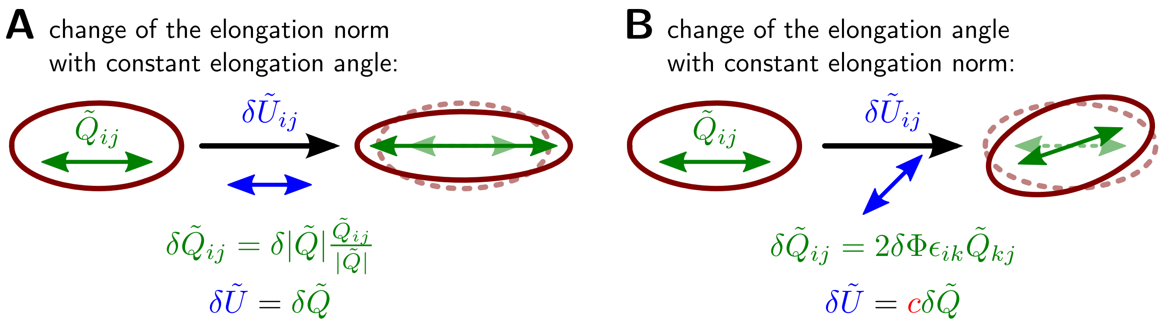
A
change of the elongation norm
with constant elongation angle:
$\tilde{Q}_{ij}$
$\delta\tilde{U}_{ij}$
$\delta\tilde{Q}_{ij} = \delta|\tilde{Q}|\frac{\tilde{Q}_{ij}}{|\tilde{Q}|}$
$\delta\tilde{U} = \delta\tilde{Q}$
B
change of the elongation angle
with constant elongation norm:
$\tilde{Q}_{ij}$
$\delta\tilde{U}_{ij}$
$\delta\tilde{Q}_{ij} = 2\delta\Phi\epsilon_{ik}\tilde{Q}_{kj}$
$\delta\tilde{U} = c\delta\tilde{Q}$

Figure 2.8: Changes of the elongation nematic $\tilde{Q}_{ij}$ correspond to pure shear deformations $\delta\tilde{U}_{ij}$. **(A)** A change of the elongation norm $\delta|\tilde{Q}| \neq 0$, where the elongation angle is constant $\delta\Phi = 0$. Then, the change of the elongation nematic $\delta\tilde{Q}_{ij}$ is proportional to $\tilde{Q}_{ij}$. Furthermore, the shear equals the change in elongation. **(B)** A change of the elongation angle $\delta\Phi \neq 0$, where the elongation norm is constant $\delta|\tilde{Q}| = 0$. Then, the change of the elongation nematic $\delta\tilde{Q}_{ij}$ is proportional to $\epsilon_{ik}\tilde{Q}_{kj}$. Put differently, there is an angle of $\pi/4$ between the axes of $\delta\tilde{Q}_{ij}$ and of $\tilde{Q}_{ij}$. Furthermore, the shear corresponds to the change in elongation attenuated by the factor $c = \tanh(2|\tilde{Q}|)/2|\tilde{Q}|$. In both panels, we set $\delta\Psi = 0$.

In order to discuss the additional contributions by $\delta\tilde{J}_{ij}$, we compare $\delta\tilde{U}_{ij}$ to a *corotational elongation change* $\delta\tilde{Q}^{\text{cr}}_{ij}$ that is observed in a reference frame rotating with $\delta\Psi$ with respect to the coordinate system. Thus, we modify Eq. (2.31) by substituting the rotation of the elongation axis $\delta\Phi$ by its relative rotation $\delta\Phi - \delta\Psi$:

$$\delta\tilde{Q}^{\text{cr}}_{ij} = \delta|\tilde{Q}|\frac{1}{|\tilde{Q}|}\tilde{Q}_{ij} + 2(\delta\Phi - \delta\Psi)\epsilon_{ik}\tilde{Q}_{kj}. \tag{2.33}$$

We find that the equation for the shear $\delta\tilde{U}_{ij}$ is similar to the equation for the corotational elongation change $\delta\tilde{Q}^{\text{cr}}_{ij}$. The only difference is that the angular part in $\delta\tilde{U}_{ij}$ is attenuated by the factor c defined below Eq. (2.29). Thus, there are two contributions combined in $\delta\tilde{J}_{ij}$: one accounts for local rotations, i.e. the difference between $\delta\tilde{Q}^{\text{cr}}_{ij}$ and $\delta\tilde{Q}_{ij}$; and the other one tells us that the angular part of the elongation change does not fully contribute to shear, but is attenuated by the factor c (Fig. 2.8B).

Rotations Eq. (2.28) states that triangle rotation $\delta\Psi$ corresponds to the change in the triangle orientation angle Θ. However strikingly, an additional shear-induced contribution to triangle rotation $\delta\Xi$ arises. It is discussed in detail in Appendix B.2.3.

2.1.4 Coarse-graining: deformation of triangle groups

Eqs. (2.26) and (2.27) relate the deformation of a single triangle to the change of its shape. Here, we coarse-grain these relations in order to study the deformation of

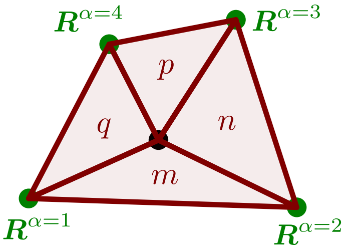
$\boldsymbol{R}^{\alpha=4}$
$\boldsymbol{R}^{\alpha=3}$
p
q
n
m
$\boldsymbol{R}^{\alpha=1}$
$\boldsymbol{R}^{\alpha=2}$

Figure 2.9: A triangle group G consisting of the triangles m, n, p, and q. The discrete displacement gradient of the group U_{ij}^G is defined by the average of the triangle displacement gradients (Eq. (2.35)). However, the same quantity can be obtained from the displacements of the margin corners alone (green dots) using Eq. (2.36).

groups of connected triangles (Fig. 2.9).

Average of triangle-related quantities

In order to define deformation and state quantities for a group of triangles G, we introduce an area-weighted average over all triangles in G. For any triangle-related quantity q^m, we define:

$$\langle q^m \rangle = \frac{1}{A^G} \sum_{m \in G} A^m q^m. \tag{2.34}$$

Here, we defined the total area of the group by $A^G = \sum_{m \in G} A^m$. Both sums run over all triangles m of group G.

Coarse-grained displacement gradient

Now, we can define the discrete displacement gradient U_{ij}^G for the triangle group G. In the absence of topological transitions, it is defined as follows:

$$U_{ij}^G = \langle U_{ij}^m \rangle. \tag{2.35}$$

In this equation, the average $\langle U_{ij}^m \rangle$ is not yet uniquely defined, because during a finite deformation, the individual triangle areas may change. We define that the triangle areas in the initial state should be used as weights for the average.

In order to allow for topological transitions within the group G, we generalize the definition of U_{ij}^G. A definition of U_{ij}^G that is only based on the deformation of the group margin reads:

$$U_{ij}^G = \frac{\epsilon_{ik}}{2A^G} \sum_{\alpha=1}^{n} \left(R_k^\alpha - R_k^{\alpha+1} \right) \left(\left[R_j'^\alpha + R_j'^{\alpha+1} \right] - \left[R_j^\alpha + R_j^{\alpha+1} \right] \right). \tag{2.36}$$

Here, the summation runs over all n cell centers $\boldsymbol{R}^\alpha$ that correspond to the margin corners of the group G in counter-clockwise order (green dots in Fig. 2.9). The vectors $\boldsymbol{R}^\alpha$ denote initial positions and the vectors $\boldsymbol{R}'^\alpha$ denote final positions. The tensor ϵ_{ij} is defined in Eq. (2.9) and A^G denotes the total area of the group in the initial state. In Appendix B.1, we show that the definitions in Eqs. (2.35) and (2.36) are equivalent in the absence of topological transitions.

Deformations are related to changes of average shape properties

Now, we relate the coarse-grained displacement gradient U^G_{ij} to changes of average state properties. In this section, we discuss the case where no topological transition occurs. In the next section, the effects of individual topological transitions are discussed.

Like before, we focus on infinitesimal deformations. To this end, we decompose the infinitesimal displacement gradient $\delta U^G_{ij} = U^G_{ij}$ into trace, symmetric, traceless part, and antisymmetric part:

$$\delta U^G_{ij} = \frac{1}{2}\delta U^G_{kk}\delta_{ij} + \delta\tilde{U}^G_{ij} - \delta\Psi^G\epsilon_{ij}. \tag{2.37}$$

In the following, we discuss the trace δU^G_{kk}, corresponding to isotropic expansion, and the traceless, symmetric part $\delta\tilde{U}^G_{ij}$, corresponding to pure shear deformations. The antisymmetric part $\delta\Psi^G$ is discussed in Appendix B.3.2.

Isotropic expansion The area-weighted average of Eq. (2.26) yields:

$$\delta U^G_{kk} = \frac{1}{A^G}\delta A^G \tag{2.38}$$

where δA^G denotes the change of the total group area A^G. Thus, also for groups of triangles, the isotropic part of the displacement gradient corresponds to the relative area change.

Pure shear deformations To discuss the pure shear part, we first introduce the average triangle elongation $\tilde{Q}^G_{ij}$:

$$\tilde{Q}^G_{ij} = \langle \tilde{Q}^m_{ij} \rangle. \tag{2.39}$$

We use this nematic tensor as a measure for cell shape anisotropy.

We obtain the pure shear part of δU^G_{ij} by coarse-graining Eq. (2.27) (Appendix B.3.1):

$$\delta\tilde{U}^G_{ij} = \delta\tilde{Q}^G_{ij} + \delta\tilde{J}^G_{ij} + \delta\tilde{D}^G_{ij}. \tag{2.40}$$

Here, $\delta\tilde{Q}^G_{ij}$ denotes the change of $\tilde{Q}^G_{ij}$, and the corotational contribution to shear $\delta\tilde{J}^G_{ij}$ corresponds to the mean field version of the triangle quantity $\delta\tilde{J}_{ij}$ (compare Eq. (2.29)):

$$\delta\tilde{J}^G_{ij} = -2\Big[c^G\delta\Psi^G + (1-c^G)\delta\Phi^G\Big]\epsilon_{ik}\tilde{Q}^G_{kj}. \tag{2.41}$$

Analogously to above, the factor c^G is given by $c^G = \tanh(2|\tilde{Q}^G|)/2|\tilde{Q}^G|$, and the symbol $\delta\Phi^G$ denotes the change of Φ^G. We defined the scalars $|\tilde{Q}^G|$ and Φ^G to be the norm and the angle of the nematic $\tilde{Q}^G_{ij}$, respectively.[9] The angle $\delta\Psi^G$ denotes the antisymmetric part of δU^G_{ij} defined analogously to Eq. (2.25). In Eq. (2.40), we also defined $\delta\tilde{D}^G_{ij}$ by:

$$\delta\tilde{D}^G_{ij} = -\Big(\langle\delta U^m_{kk}\tilde{Q}^m_{ij}\rangle - \delta U^G_{kk}\tilde{Q}^G_{ij}\Big) + \Big(\langle\delta\tilde{J}^m_{ij}\rangle - \delta\tilde{J}^G_{ij}\Big). \tag{2.42}$$

The term $\delta\tilde{D}^G_{ij}$ thus represents correlation effects contributing to shear. These correlations are created by the averaging over triangles. Correspondingly, they vanish for a single triangle. Taken together, Eq. (2.40) states that local tissue shear is created by changes of local cell shape anisotropy, by a corotational term, and by correlations.

Now, we separately discuss the two contributions to $\delta\tilde{D}^G_{ij}$. The first term (first parenthesis in Eq. (2.42)), which we call growth correlation, is created by spatial fluctuations in the isotropic expansion δU_{kk}. Fig. 2.10A illustrates this term for a deformation without pure shear component $\delta\tilde{U}^G_{ij} = 0$.[10] We show two triangles with different triangle elongations. One triangle contracts isotropically while the other triangle expands isotropically. Thus, the individual elongations are constant. However, the triangle areas change with respect to each other. Thus, the average elongation $\tilde{Q}^G_{ij}$ changes because of the area weighting in Eq. (2.39). Hence, although $\delta\tilde{U}^G_{ij} = 0$ and $\delta\tilde{J}^G_{ij} = 0$ in Eq. (2.40), we have $\delta\tilde{Q}^G_{ij} \neq 0$. This is compensated for by the growth correlation part of $\delta\tilde{D}^G_{ij}$.

The second part, $\langle\delta\tilde{J}_{ij}\rangle - \delta\tilde{J}^G_{ij}$, which we call rotational correlation, represents spatial fluctuations of angular changes. For instance, it may arise from fluctuations of local tissue rotation $\delta\Psi$. Fig. 2.10B shows an example where two elongated triangles with the same area rotate in opposing directions. Thus, the average tissue rotation $\delta\Psi^G$ and the rotation of the average elongation axis $\delta\Phi^G$ are zero: $\delta\Psi^G = \delta\Phi^G = 0$. Therefore, there is no corotational contribution to shear $\delta\tilde{J}^G_{ij} = 0$. However, although there is no pure shear $\delta\tilde{U}^G_{ij} = 0$, the average elongation changes $\delta\tilde{Q}^G_{ij} \neq 0$. In Eq. (2.40), the change in elongation $\delta\tilde{Q}^G_{ij}$ is compensated for by the rotational correlation part of $\delta\tilde{D}^G_{ij}$.

---

[9] Norm and angle of a nematic are defined in Eq. (2.12) and below. See also Appendix A.2.2.

[10] Both panels of Fig. 2.10 show examples of unconnected groups of triangles. This seems to contradict the definition of G to be a *connected* group of triangles (see beginning of this section). In this footnote, we shortly explain why this is not a problem. Any group of unconnected triangles can be transformed into a group of connected triangles by adding a number of connecting triangles. One can always define the connecting triangles such that their areas go to zero. Then, because of the area weighting, the existence of the connecting triangles does not play a role for the discussed effects.

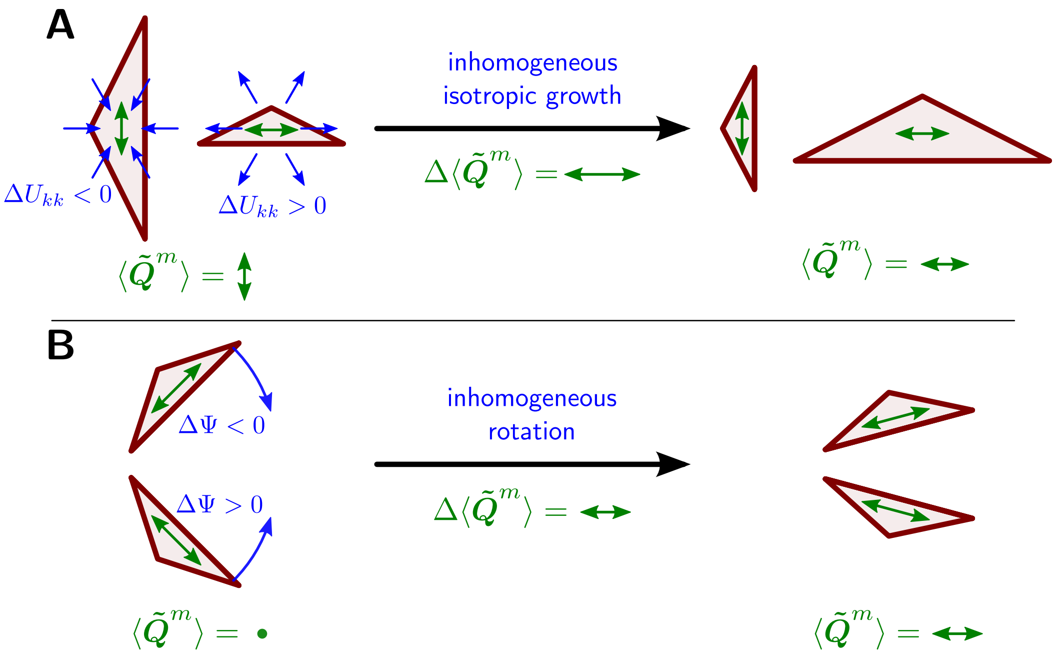
A
$\Delta U_{kk} < 0$
$\Delta U_{kk} > 0$
$\langle \tilde{\boldsymbol{Q}}^m \rangle =$
inhomogeneous
isotropic growth
$\Delta \langle \tilde{\boldsymbol{Q}}^m \rangle =$
$\langle \tilde{\boldsymbol{Q}}^m \rangle =$
B
$\Delta\Psi < 0$
$\Delta\Psi > 0$
inhomogeneous
rotation
$\Delta \langle \tilde{\boldsymbol{Q}}^m \rangle =$
$\langle \tilde{\boldsymbol{Q}}^m \rangle =$
$\langle \tilde{\boldsymbol{Q}}^m \rangle =$

Figure 2.10: Illustration of the two parts of the correlation contribution to shear $\delta\tilde{D}^G_{ij}$. **(A)** The growth correlation part is generated by inhomogeneous isotropic expansion. As an example, we show a deformation without pure shear component. Nevertheless, the average elongation $\tilde{Q}^G_{ij}$ changes because of the area weighting in Eq. (2.39). This change in $\tilde{Q}^G_{ij}$ does not generate shear but is compensated by the growth correlation part of $\delta\tilde{D}^G_{ij}$ in Eq. (2.40). **(B)** The rotational correlation part is generated by inhomogeneous rotation. As an example, we show two elongated triangles with the same area rotating in opposing directions. During this process there is no pure shear occurring. Also, the whole group does not rotate on average. However, there is a change in average elongation $\tilde{Q}^G_{ij}$. This change in $\tilde{Q}^G_{ij}$ is compensated by the rotational correlation part of $\delta\tilde{D}^G_{ij}$ in Eq. (2.40).

2.1.5 Characterization of shear induced by topological transitions

In the previous section, we have shown that in the absence of topological transitions, infinitesimal deformations δU^G_{ij} of triangle groups can be exactly related to changes of average shape properties (Eqs. (2.38) and (2.40)). Here, we discuss the effect of topological transitions on this relationship. Put differently, in the absence of topological transitions, we have exactly related the average displacement gradient to an elastic strain. In this section, we study how topological transitions create plastic strain.

To this end, we discuss the effect of topological transitions on the level of multiple triangles. This is because all three considered types of topological transitions (T1 transitions, cell division, and T2 transitions) have in common that they induce triangulation changes: During a topological transition, individual triangles appear or

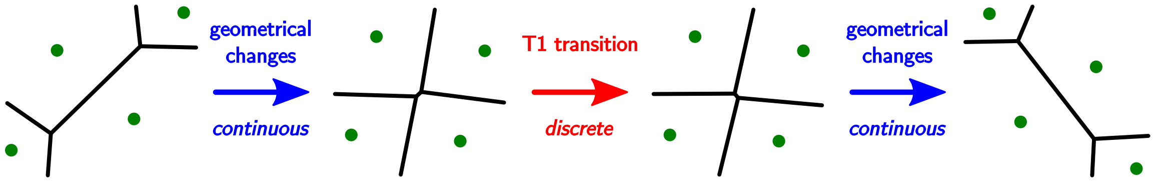

Figure 2.11: Any topological transition (red arrow) switches between two discretely separated topological states of the network. Here, we separate topological transitions from geometrical changes (blue arrows), which are reflected the movement of cell centers (green dots). Geometrical changes in the absence of topological transitions are discussed in Section 2.1.4. Topological transitions in the absence of geometrical changes are discussed in Section 2.1.5. Both are brought together in Section 2.2.

disappear (Figs. 2.12A, Appendix B.5). Therefore, we do not choose a description on the single triangle level, here. Rather, we consider a group G of connected triangles within which a given topological transition occurs.

In the following, we first separate topological transitions from geometrical changes of the network. Then, we discuss how topological transitions affect the isotropic part of the discrete displacement gradient. Finally, we discuss the shear created by a single T1 transition. The shear created by a single cell division and by a single T2 transition are discussed in Appendix B.5.

Separation of topological transitions from geometrical changes

Note that any topological transition occurs instantaneously (Fig. 2.11): it switches between two discretely separated topological states of the system. Therefore, we can separate a given topological transition from any geometrical changes occurring before or after the transition. Thus, cell centers $\boldsymbol{R}^\alpha$ do not move during a topological transition, and the margin of group G does not change its shape. As a consequence, we obtain for the discrete displacement gradient δU_{ij}^G for the triangle group G (using Eq. (2.36)):

$$\delta U_{ij}^G = 0. \tag{2.43}$$

Put differently, there is no local network deformation during a topological transition. However in the following subsections and in Appendix B.5, we explain how topological transitions can nevertheless contribute to tissue shear.

Area changes induced by topological transitions

Before turning to the shear part, we discuss the isotropic part of the displacement gradient for any kind of topological transition. Because the cell centers do not move during the topological transition, the total area of the group A^G does not change:

$$\delta A^G = 0. \tag{2.44}$$

Thus, Eq. (2.38) relating δU^G_{kk} to the relative area change remains fulfilled during topological transitions.

Characterization of the shear induced by a single T1 transition

Here, we study the contribution of a single T1 transition to local shear. First, we discuss the triangulation change induced by a T1 transition (Fig. 2.12A). During the T1 transition, two triangles (m and n) disappear and two other triangles (p and q) appear. Thus, in order to define the shear contribution by the T1 transition, we consider the quadrilateral $\square$, which is defined by the centers of the cells α, β, γ, and δ. Before the T1 transition, this quadrilateral corresponds to the union of the triangles m and n:

$$\boxbslash = \{m, n\}. \tag{2.45}$$

After the T1 transition, it corresponds to the union of the triangles p and q: $\boxslash = \{p, q\}$.

Now, we the discuss the contribution of a single T1 transition to pure shear $\delta\tilde{U}^{\square}_{ij}$. As explained above, we assume no deformations of the quadrilateral $\square$ during the T1 transition. Thus, there is no shear during the T1 transition:

$$\delta\tilde{U}^{\square}_{ij} = 0. \tag{2.46}$$

Nevertheless, the average triangle elongation changes by a finite value (Fig. 2.12B):

$$\Delta\tilde{Q}^{\boxtimes}_{ij} = \tilde{Q}^{\boxslash}_{ij} - \tilde{Q}^{\boxbslash}_{ij}. \tag{2.47}$$

Here, we defined $Q^{\boxbslash}_{ij} = (A^m Q^m_{ij} + A^n Q^n_{ij})/A^{\square}$ and $Q^{\boxslash}_{ij} = (A^p Q^p_{ij} + A^q Q^q_{ij})/A^{\square}$, where $A^{\square}$ denotes the area of the quadrilateral. Thus, although there is no tissue shear, the average triangle elongation changes by a finite amount $\Delta\tilde{Q}^{\boxtimes}_{ij}$, which reflects the change in topology from $\boxbslash$ to $\boxslash$. This seems to contradict Eq. (2.40) relating shear to the change in average elongation. To resolve this, we introduce the nematic tensor $\Delta\tilde{T}^{\boxtimes}_{ij} = -\Delta\tilde{Q}^{\boxtimes}_{ij}$, which we interpret as a contribution to shear created by the T1 transition, corresponding to a plastic strain. We modify Eq. (2.40) accordingly:

$$\delta\tilde{U}^{\square}_{ij} = \Delta\tilde{Q}^{\boxtimes}_{ij} + \delta\tilde{J}^{\boxtimes}_{ij} + \delta\tilde{D}^{\boxtimes}_{ij} + \Delta\tilde{T}^{\boxtimes}_{ij}. \tag{2.48}$$

Here, we define the contributions $\delta\tilde{J}^{\boxtimes}_{ij}$ and $\delta\tilde{D}^{\boxtimes}_{ij}$ to be zero during the T1 transition.

Note that the shear created by a single T1 transition $\Delta\tilde{T}^{\boxtimes}_{ij}$ depends on the shape of the quadrilateral $\square$ at the moment of the T1 transition. Typically, the axis of $\Delta\tilde{T}^{\boxtimes}_{ij}$ is close to the axis of the bond newly created by the T1 transition (compare magenta

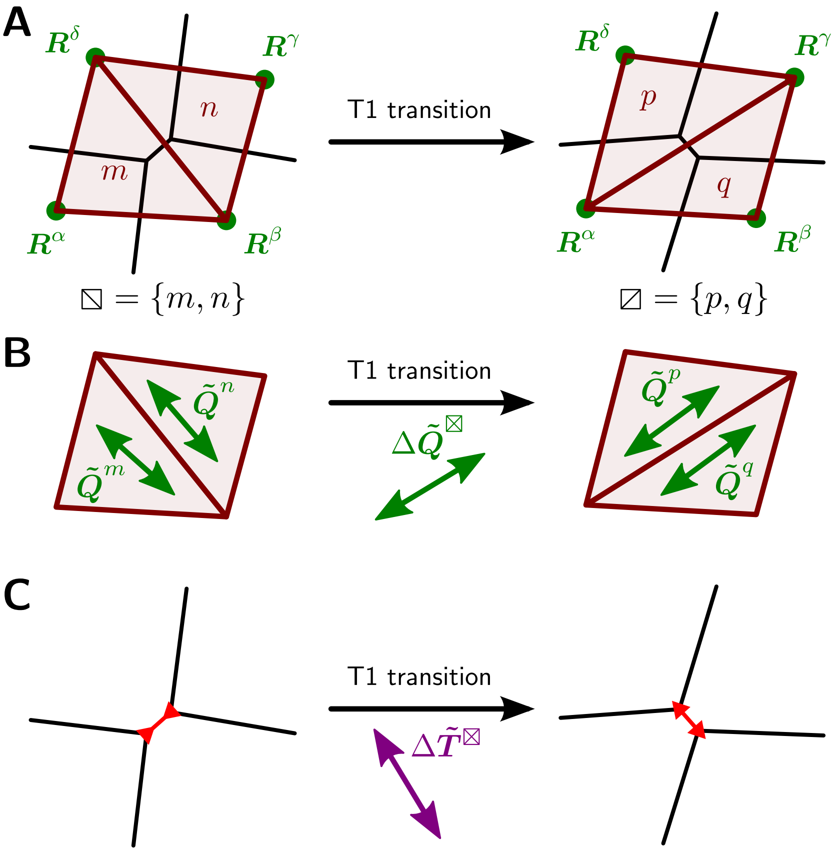
A
R^δ
R^γ
n
m
R^α
R^β
T1 transition
p
q
$\boxbslash = \{m, n\}$
$\boxslash = \{p, q\}$
B
$\tilde{Q}^n$
$\tilde{Q}^m$
$\Delta\tilde{Q}^{\boxtimes}$
$\tilde{Q}^p$
$\tilde{Q}^q$
C
$\Delta\tilde{T}^{\boxtimes}$

Figure 2.12: **(A)** Change of the triangulation due to a single T1 transition. Two triangles (m and n) disappear and two other triangles (p and q) appear. We denote the quadrilateral with corners $\boldsymbol{R}^\alpha$, $\boldsymbol{R}^\beta$, $\boldsymbol{R}^\gamma$, and $\boldsymbol{R}^\delta$ before the transition by $\boxbslash = \{m, n\}$ and after the transition by $\boxslash = \{p, q\}$. **(B)** Although there is no pure shear during the T1 transition, the average elongation nematic of the quadrilateral changes discontinuously by $\Delta\tilde{Q}^{\boxtimes}_{ij}$. **(C)** The axis of the nematic $\Delta\tilde{T}^{\boxtimes}_{ij}$ (magenta double arrow) is typically close to the axis of the bond that is newly created by the T1 transition (red double arrow pointing outwards). However, the axis of $\Delta\tilde{T}^{\boxtimes}_{ij}$ is close to perpendicular to the bond that disappears during the T1 transition (red double arrow pointing inwards).

and red double arrows in Fig. 2.12C). For the special case that the quadrilateral $\square$ is a square, the axis of $\Delta\tilde{T}_{ij}^{\boxtimes}$ is oriented along one of the diagonals of $\square$, and the norm of $\Delta\tilde{T}_{ij}^{\boxtimes}$ turns out to be $|\Delta\tilde{T}^{\boxtimes}| = (\ln 3)/2$.

Analogously to the shear contribution by a single T1 transition $\Delta\tilde{T}_{ij}^{\boxtimes}$, we define the shear contribution by a single cell division $\Delta\tilde{C}_{ij}^{\mathrm{div}}$ and the shear contribution by a single T2 transition $\Delta\tilde{E}_{ij}^{\mathrm{T2}}$ in Appendix B.5.

2.2 Decomposition of the large-scale flow field into cellular contributions

In this section, we consider an infinitesimal deformation of a cellular network from an initial state to a final state. To discuss cellular contributions to large-scale deformation, we use our results from the previous sections.

2.2.1 The velocity gradient describes large-scale deformations

We characterize the deformation of the whole cellular network during the infinitesimal time interval δt by a large-scale velocity gradient v_{ij}. To define this velocity gradient, we first triangulate the network as described in Section 2.1.1, which results in a group G containing all triangles. Then, we define the large-scale velocity gradient by:

$$v_{ij} = \frac{\delta U_{ij}^{G}}{\delta t}. \tag{2.49}$$

Here, the large-scale displacement gradient δU_{ij}^{G} is defined by Eq. (2.36).

According to Appendix B.1, this definition is equivalent to the following contour integral along the triangulation margin:

$$v_{ij} = \frac{1}{A^{G}} \oint n_i \mathrm{v}_j \, \mathrm{d}\ell. \tag{2.50}$$

Here, the symbol A^{G} corresponds to the area of the triangulation and the vector $\boldsymbol{n}$ denotes the unit vector that is locally perpendicular to the triangulation margin and points outside. The vector $\mathbf{v}(\boldsymbol{r})$ denotes the local velocity along the triangulation margin. It is defined as follows. For a cell center that is being displaced from its position in the initial state $\boldsymbol{R}^{\alpha}$ to its position in the final state $\boldsymbol{R'}^{\alpha}$, we define $\mathbf{v}(\boldsymbol{R}^{\alpha}) = (\boldsymbol{R'}^{\alpha} - \boldsymbol{R}^{\alpha})/\delta t$. In points $\boldsymbol{r}$ of the triangulation margin that lie on the line in between two consecutive cell centers $\boldsymbol{R}^{\alpha}$ and $\boldsymbol{R}^{\alpha+1}$, we define the velocity $\mathbf{v}(\boldsymbol{r})$ by the linear interpolation between $\mathbf{v}(\boldsymbol{R}^{\alpha})$ and $\mathbf{v}(\boldsymbol{R}^{\alpha+1})$.

Note that here, we focus on the case where no topological transitions occur at the network margin. More precisely, we focus on the case where the sequences of cell centers $\boldsymbol{R}^\alpha$ along the triangulation margin are the same in the initial and in the final state. This is necessary for the proper definition of δU^G_{ij} and v_{ij}. In Appendix B.6, we discuss the effect of topological transitions at the network margin.

Components of the velocity gradient

Analogously to Eq. (2.37), we decompose the velocity gradient v_{ij} into:

$$v_{ij} = \frac{1}{2} v_{kk}\delta_{ij} + \tilde{v}_{ij} - \omega\epsilon_{ij}. \tag{2.51}$$

The first component $v_{kk} = \delta U^G_{kk}/\delta t$ represents the average divergence of the flow field describing relative area changes. The second component $\tilde{v}_{ij} = \delta\tilde{U}^G_{ij}/\delta t$ represents the average pure shear component of the flow field. Finally, the third component $\omega = \delta\Psi^G/\delta t$ represents the average rotation rate of the flow field. In the following, we separately discuss the divergence v_{kk} and the pure shear component $\tilde{v}_{ij}$. The rotation rate ω is discussed in Appendix B.3.2.

2.2.2 Large-scale divergence of the flow field

For cellular networks with a large number N of cells $N \gg 1$, we obtain for the average divergence v_{kk}:

$$v_{kk} \approx \frac{1}{a}\frac{\mathrm{d}a}{\mathrm{d}t} + k_d - k_a. \tag{2.52}$$

Here, $\mathrm{d}/\mathrm{d}t$ denotes the time derivative, a denotes the average cell area, k_d denotes the average cell division rate, and k_a denotes the average rate of T2 transitions. Thus, the average divergence of the flow field decomposes into the relative growth rate of the average cell area, the division rate, and the negative T2 transition rate.

Eq. (2.52) follows from Eq. (2.38), where the total area of the network is given by $A = aN$. The limit of a large number of cells $N \gg 1$ is necessary, because the area of the triangulation A^G is in general smaller than the total area of the cellular network A. This is because the triangulation does not cover a stripe at the network margin, which is ca. half a cell diameter broad (Fig. 2.3). As a consequence, the velocity gradient v_{ij} describes only the deformation of the triangulated part of the network. However, for networks with a large number of cells $N \gg 1$, we can neglect this effect. Throughout this chapter, equations that assume $N \gg 1$ are denoted by a $\approx$ sign. For instance, $A^G/A \approx 1$. All other equations are exact for infinitesimal deformations.

2.2.3 Large-scale shear of the flow field

In Section 2.1.4, we related the shear to changes of the average triangle elongation. Here, we additionally account for effects by topological transitions. As result, we obtain for the large-scale pure shear rate $\tilde{v}_{ij}$:

$$\tilde{v}_{ij} = \frac{\mathrm{D}\tilde{Q}_{ij}}{\mathrm{D}t} + \tilde{T}_{ij} + \tilde{C}_{ij} + \tilde{E}_{ij} + \tilde{D}_{ij}. \tag{2.53}$$

In the following, we explain all terms on the right hand side of this equation.

The nematic tensor $\tilde{Q}_{ij}$ denotes the average triangle elongation $Q_{ij} = Q^G_{ij}$ defined by Eq. (2.39). Its corotational derivative is defined by

$$\frac{\mathrm{D}\tilde{Q}_{ij}}{\mathrm{D}t} = \frac{\mathrm{d}\tilde{Q}_{ij}}{\mathrm{d}t} + \tilde{J}_{ij}, \tag{2.54}$$

where $\mathrm{d}\tilde{Q}_{ij}/\mathrm{d}t$ denotes the time derivative for each tensor component of $\tilde{Q}_{ij}$. The nematic tensor $\tilde{J}_{ij}$ is defined analogously to Eq. (2.41):

$$\tilde{J}_{ij} = -2\left[c\omega + (1-c)\frac{\mathrm{d}\Phi}{\mathrm{d}t}\right]\epsilon_{ik}\tilde{Q}_{kj}. \tag{2.55}$$

In this equation, we defined $c = \tanh(2|\tilde{Q}|)/2|\tilde{Q}|$, and the scalars $|\tilde{Q}|$ and Φ are norm and angle of the average elongation $\tilde{Q}_{ij}$, respectively.[11] We also defined $\mathrm{d}\Phi/\mathrm{d}t = \delta\Phi/\delta t$, where $\delta\Phi$ denotes the change of Φ.

The nematic $\tilde{D}_{ij}$, summarizes the shear rate contributions by correlation effects:

$$\tilde{D}_{ij} = -\left(\left\langle v^m_{kk}\tilde{Q}^m_{ij}\right\rangle - v_{kk}\tilde{Q}_{ij}\right) + \left(\frac{\left\langle\delta\tilde{J}^m_{ij}\right\rangle}{\delta t} - \tilde{J}_{ij}\right). \tag{2.56}$$

Here, the averaging brackets are defined as in Eq. (2.34).[12] For a discussion of the correlation effects, see Section 2.1.4.

The terms $\tilde{T}_{ij}$, $\tilde{C}_{ij}$, and $\tilde{E}_{ij}$ in Eq. (2.53) denote contributions of T1 transitions, cell divisions, and T2 transitions to the large-scale shear rate, respectively. They are defined by:

$$\tilde{\boldsymbol{T}} = \frac{1}{A^G}\sum_{\text{T1 tr. } k}\delta(t-t_k)A^{\square}_k\boldsymbol{\Delta}\tilde{\boldsymbol{T}}^{\boxtimes}_k \qquad \text{(T1 transitions)} \tag{2.57}$$

$$\tilde{\boldsymbol{C}} = \frac{1}{A^G}\sum_{\text{cell div. } k}\delta(t-t_k)A^{\text{div}}_k\boldsymbol{\Delta}\tilde{\boldsymbol{C}}^{\text{div}}_k \qquad \text{(cell divisions)} \tag{2.58}$$

$$\tilde{\boldsymbol{E}} = \frac{1}{A^G}\sum_{\text{T2 tr. } k}\delta(t-t_k)A^{\text{T2}}_k\boldsymbol{\Delta}\tilde{\boldsymbol{E}}^{\text{T2}}_k \qquad \text{(T2 transitions).} \tag{2.59}$$

---

[11] Norm and angle of a nematic are defined in Eq. (2.12) and below.

[12] Note that the angle Φ of the elongation nematic $\tilde{Q}_{ij}$ may be changed by topological transitions. Such changes would be included in $\tilde{J}_{ij}$ but not in $\langle\delta\tilde{J}^m_{ij}\rangle/\delta t$.

In each of these equations, the sum runs over all topological events k of the respective kind. The symbol t_k denotes the time at which the topological transition k occurs, and δ denotes the Dirac distribution. The nematics $\boldsymbol{\Delta}\tilde{\boldsymbol{T}}_k^{\boxtimes}$, $\boldsymbol{\Delta}\tilde{\boldsymbol{C}}_k^{\mathrm{div}}$, and $\boldsymbol{\Delta}\tilde{\boldsymbol{E}}_k^{\mathrm{T2}}$ denote the respective contribution of a single transition to local shear as defined in Section 2.1.5 and Appendix B.5. Furthermore, the scalars $A_k^{\square}$, A_k^{div}, and A_k^{T2} denote the respective areas of the triangle groups directly involved in the topological transition (Section 2.1.5, Appendix B.5).

The shear contributions by topological transitions follow from our discussion in Section 2.1.5. Each topological transition creates an instantaneous change in $\tilde{Q}_{ij}$. This creates a delta peak in $\mathrm{D}\tilde{Q}_{ij}/\mathrm{D}t$, which is compensated for by a corresponding delta peak in $\tilde{T}_{ij}$, $\tilde{C}_{ij}$, or $\tilde{E}_{ij}$ with an opposite sign.

Note the area weighting in Eqs. (2.57)-(2.59): The contribution of a single topological transition to network shear is inversely proportional to the total area of the triangulation A^G. Moreover, it is directly proportional to the area of the triangle group involved in the topological transition.

2.3 Cellular contributions to the flow field in the fruit fly wing

In this section, we study an experimentally observed deformation of the developing fruit fly wing (Fig. 2.13). To this end, we quantified the time-dependent large-scale flow field between the developmental times of 16 hAPF and 32 hAPF. Furthermore, we show how the average divergence of the flow field and the average shear rate decomposed into cellular contributions according to Eqs. (2.52) and (2.53), respectively.

In the following, we first describe how we extracted the large-scale flow field and its components from experimental movies of the fly wing (Section 2.3.1). Then, we discuss the time-dependent components of the flow field for a single wild type wing (Section 2.3.2). Finally, we test how reproducible our results are by comparing different wild type wings (Section 2.3.3).

2.3.1 Extraction of the large-scale flow field and its components from experimental movies

In order to experimentally quantify the observables appearing in Eqs. (2.52) and (2.53), we recorded in vivo movies of fruit fly wings, where the adherens junctions were stained. The individual images of each movie were registered at discrete time points t_i separated by time intervals of ca. 5 min. For each movie, we ran a segmentation algorithm to extract the time-dependent topology and geometry of the cellular network. For the data shown here, we selected only the cells of the wing blade. Then, in order to characterize a set of cells that represented the same piece of tissue throughout

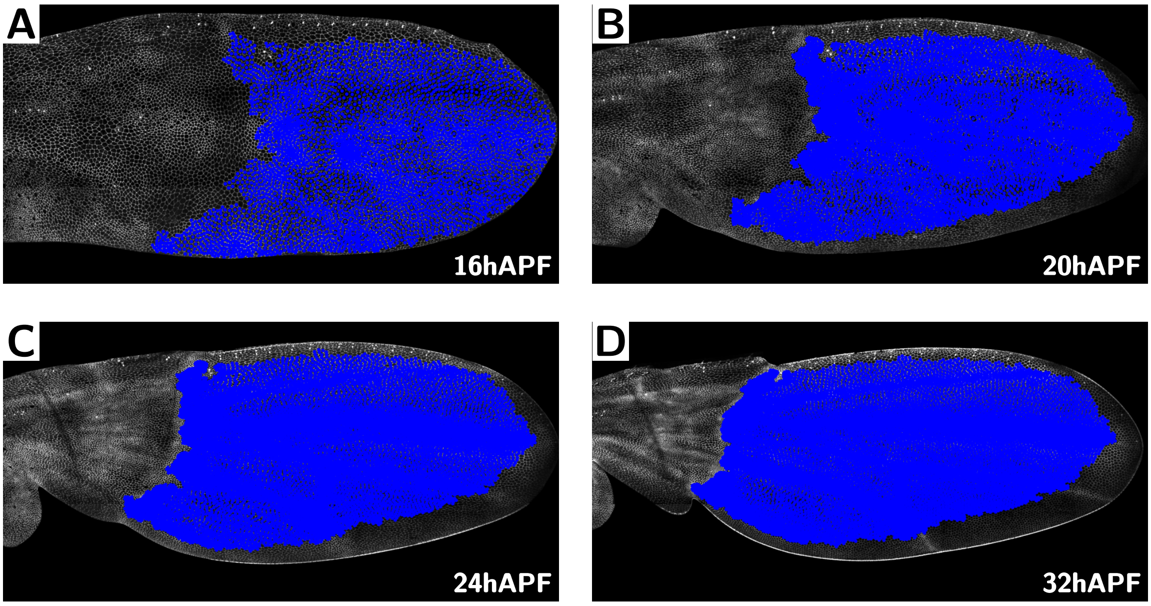

Figure 2.13: Deformation of a fruit fly wing over time. Shown in blue is a network of cells that is tracked over time. Thus, the blue region represents the same piece of tissue throughout the whole movie. In Section 2.3.2, we discuss the time-dependent flow field of this cellular network.

the movie, we removed any cells that disappeared or newly appeared at the network margin. This led to a reduced network of tracked cells, which is shown in Fig. 2.13 (each tracked cell is represented by a blue dot).

Here, we discuss the components of the time-dependent velocity gradient v_{ij}. To this end, we apply Eqs. (2.52) and (2.53) separately to each observed time interval $t_i \dots t_{i+1}$. As opposed to the assumptions made in the previous sections, these time intervals are finite. Therefore, we refine the correlation contribution to shear $\tilde{D}_{ij}$ by introducing higher order terms (Appendix B.8).

In the previous sections, we restricted to the case were all inner vertices are threefold. However, our experimental data also contained N-fold vertices with $N > 3$. Thus, the triangulation defined in Section 2.1.1 could not be implemented in a straightforward way. On page 142 in Appendix B.8.3 , we show how N-fold vertices with $N > 3$ were taken into account.

2.3.2 Components of the flow field in a wild type wing

Here, we study the components of the flow field in a wild type wing and discuss their cellular contributions. To this end, we focus on the average deformation of the region shown in blue in Fig. 2.13. In the following, we discuss the average divergence and the average pure shear part of the flow field separately.

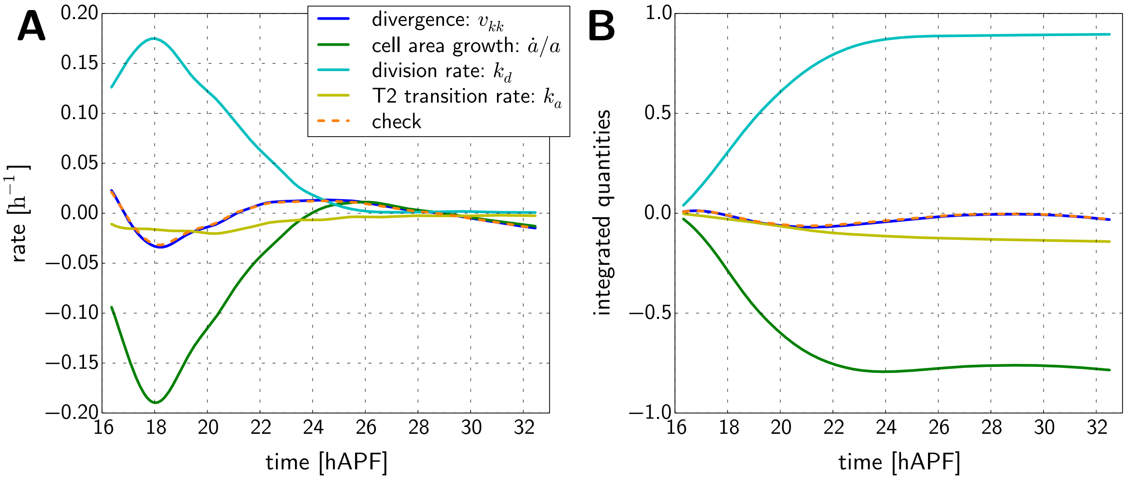

Figure 2.14: (A) Average divergence of the flow field (blue solid line) in the wild type wing blade shown in Fig. 2.13. Also shown is the decomposition into cellular contributions according to Eqs. (2.52) and (2.52). These cellular contributions comprise cell area change (green solid line), cell division rate (cyan solid line), and T2 transition rate (yellow solid line). The orange dashed line corresponds to the sum of these three terms, i.e. they correspond to the right hand side of Eq. (2.52). The deviations between the blue solid line and the orange dashed line are due to the approximation for large networks and to the finite time intervals. **(B)** Integrated versions of the quantities shown in panel A. In both panels, all curves shown are smoothed by convolving with a Gaussian with standard deviation $\sigma \approx 30\,\mathrm{min}$.

Divergence of the flow field

In Fig. 2.14A, the blue solid line shows the time-dependent average divergence of the flow field v_{kk}. According to Eqs. (2.52) and (2.52), it decomposes into the relative cell area growth rate (green solid line), the cell division rate (cyan solid line), and the T2 transition rate (yellow solid line). The orange dashed line corresponds to the sum of these three curves. The fact that it coincides with the v_{kk} curve (blue solid line) shows that Eq. (2.52) holds.

In Fig. 2.14B, we plot the time integrals of each of the curves shown in panel A. For instance, the blue solid line corresponds to the time integral of v_{kk}. Using Eq. (2.38), we obtain for this time integral:

$$\int_{t_0}^{t} v_{kk}(t')\,\mathrm{d}t' = \ln\left(\frac{A^G(t)}{A^G(t_0)}\right). \tag{2.60}$$

Here, the time t_0 is set to 16 hAPF and the upper integration limit t is varied. The function $A^G(t)$ denotes the time-dependent area of the triangulation, which coarsely corresponds to the blue region in Fig. 2.13. Thus, the integrated blue curve corresponds

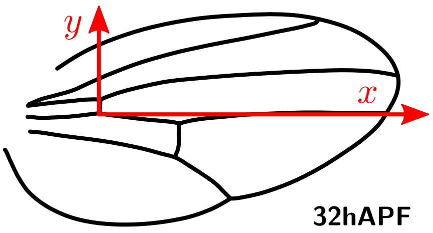

Figure 2.15: Coordinate system based on wing vein positions at 32 hAPF. The origin is the intersection of longitudinal vein 4 and the anterior cross vein. The x axis also passes through the distal end of the longitudinal vein 4. The y axis is perpendicular to the x axis as indicated. For other time points than 32 hAPF, the coordinate system is kept the same with respect to the movie images. The same coordinate system is used in Chapter 4 (compare Fig. 4.9A).

to the absolute change of the logarithm of the total area.

We draw three conclusions from Fig. 2.14. First, the total area of the piece of tissue considered changed only little (blue solid lines). Second, cell divisions alone contributed significantly to an area increase of the piece of tissue (cyan solid lines), whereas the T2 transitions contributed only little (yellow solid lines). Third, the increase in cell number was balanced by a reduction of the average cell area (green solid lines) such that the total area stayed approximately constant.

Pure shear component of the flow field

Here, we discuss the pure shear part of the large-scale flow field and its components according to Eq. (2.53). In order to properly define the components of the corresponding nematic tensors, we introduce the coordinate system explained in Fig. 2.15, which is based on wing vein positions.

For any nematic tensor $\tilde{q}_{ij}$, we plot the first component $q_{xx} = -q_{yy}$ and the second component $\tilde{q}_{xy} = \tilde{q}_{yx}$ separately. As explained in Appendix A.2.2, positive values of the xx component correspond to components parallel to the x axis, which corresponds to the proximo-distal wing axis. Negative values correspond to components parallel to the y axis, which corresponds to the anterior-posterior wing axis. The xy component correspond to components along the two axes that are inclined by $\pi/4$ with respect to the x axis.

Now, we discuss the large-scale shear rate tensor $\tilde{v}_{ij}$. In Fig. 2.16, we plot the time-dependent shear rate $\tilde{v}_{ij}$ (blue solid lines) and its decomposition into cellular contributions. We find that large-scale shear occurred predominantly along the x axis (Fig. 2.16A). Although the wing blade was permanently sheared, the shear rate attained its maximum between 18 hAPF and 19 hAPF and slowly decreased afterwards. The magnitude of the shear rate was on the same order of magnitude as the divergence of the flow field (Fig. 2.14A).

In order to better interpret the cellular contributions to the shear rate, we first discuss the time course of the cell elongation tensor, which is plotted in Fig. 2.17. Initially, at 16 hAPF, cells were on average only little elongated. Then, cell elongation increased mainly along the x axis until ca. 23 hAPF. We call this time interval *phase I*. After that, during *phase II*, cell elongation decreased and leveled off at ca. 0.15.

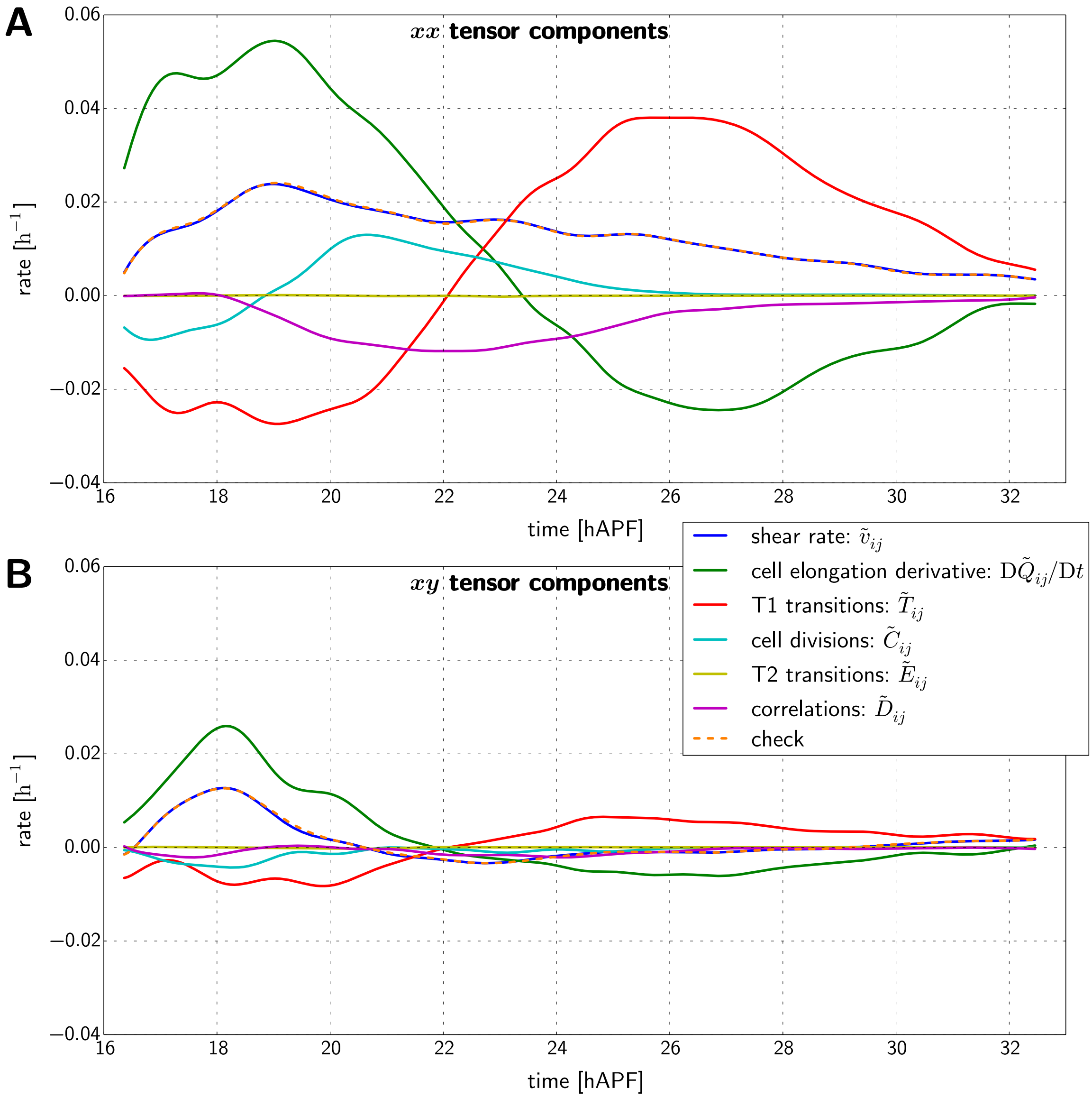

Figure 2.16: Decomposition of the shear rate tensor $\tilde{v}_{ij}$ for the wild type wing blade (Fig. 2.13) according to Eq. (2.53). The shear rate (blue solid lines) is decomposed into the corotational elongation derivative (green solid lines) and contributions by T1 transitions (red solid lines), cell divisions (cyan solid lines), T2 transitions (yellow solid lines), and correlations (magenta solid lines). The orange dashed lines are used to demonstrate the validity of Eq. (2.53). They correspond to the respective sums of all other curves except for the shear rate curve. All curves shown are smoothed by convolving with a Gaussian with standard deviation $\sigma \approx 30\,\mathrm{min}$. **(A)** xx components of the respective nematic tensors. **(B)** xy components of the respective nematic tensors.

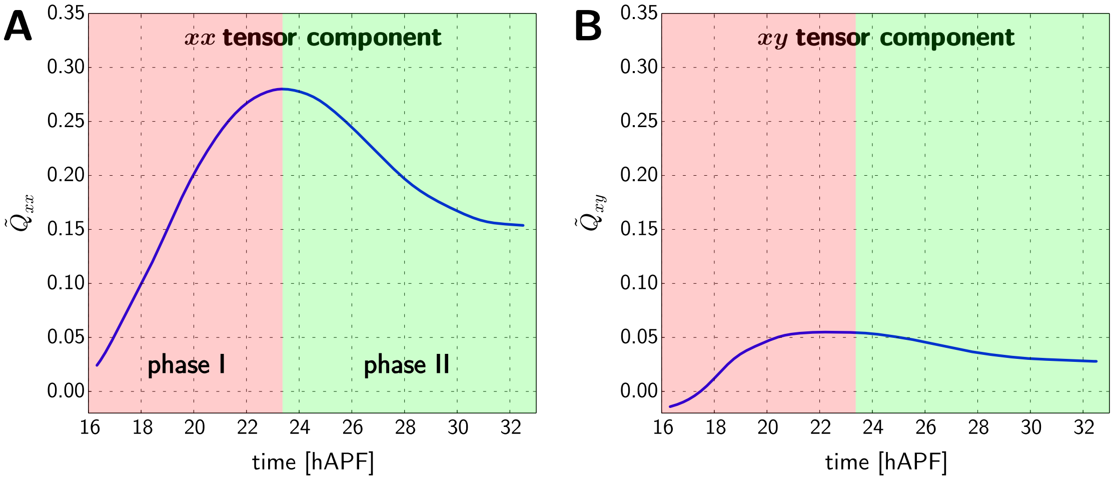

Figure 2.17: Average cell elongation depending on time for the wild type wing blade shown in Fig. 2.13. All curves shown are smoothed by convolving with a Gaussian with standard deviation $\sigma \approx 30\,\mathrm{min}$.

These two phases were also reflected in the cell elongation derivative shown in Fig. 2.16 (green solid lines in Fig. 2.16). It turns out that the derivative of cell elongation (green solid lines) and T1 transitions (red solid lines) were the most important contributions to tissue shear. During phase I, the shear was mainly created by the increase of cell elongation along the x axis. At the same time, T1 transitions occurred along the y axis counteracting the shear by cell shape change. During phase II, cell rearrangements along the x axis allowed for a decrease of cell elongation.

These observations inspire the discussion about the mechanical processes in the wing epithelium. From earlier work [54], we know that the wing blade must be at least partly stretched by external forces from the wing hinge. This stretching of the wing blade would elongate cells during phase I. For elastic cells, this would build up stresses along the x axis. During phase II, such stresses could be relieved by T1 transitions along the x axis allowing the cell elongation to decrease. However, according to our quantifications, during phase I, T1 transitions create shear along the y axis. This is surprising, because in a passive system with elastic cells, the stress would be mostly oriented along the x axis and therefore, T1 transitions should occur along the x axis at all times. This suggests that the T1 transitions occurring along the y axis during phase I could be generated by active anisotropic processes.

Apart from cell shape change and T1 transitions, also cell divisions (cyan solid lines in Fig. 2.16) and correlations (magenta solid lines) contributed to large-scale tissue shear, whereas T2 transitions did not contribute essentially (yellow solid lines). We find that the contribution by cell divisions was mostly oriented along the x axis. However, this contribution was clearly smaller than the shear by cell elongation changes and T1 transitions. The correlations contributing to shear (magenta solid lines) were

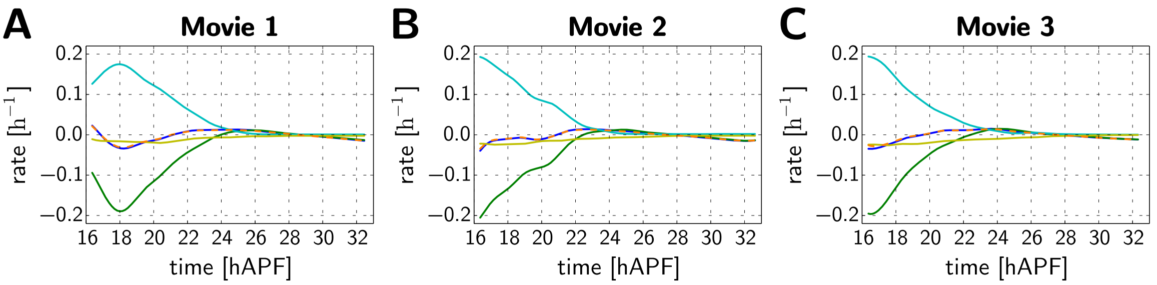

Figure 2.18: Average divergence of the flow field in three different wild type wing blades. Movie 1 (panel A) corresponds to the data presented before (Fig. 2.14A). The caption of Fig. 2.14A applies to all three panels.

on the same order of magnitude as the contribution by cell divisions. However, their contribution was mainly oriented along the y axis reducing the large-scale shear along the x axis.

2.3.3 Comparison of different wild type wings

Here, we study how reproducible the results presented in the previous section are. To this end, we compare three movies of different wild type wings, where the first movie corresponds to the data presented above (Figs. 2.13, 2.14, 2.16, and 2.17). For each movie, we plot the time course of the average divergence of the flow field, the average shear rate, and the average elongation (Figs. 2.18, 2.19, and 2.20, respectively).

We found that the main features discussed above were very reproducible. Differences among the movies were small and occurred on time scales of less than two hours. The main difference between the three movies was that in Movie 1, the development appeared to be delayed by ca. one hour as compared to the other movies. This can be seen most clearly in the direct comparison of the average elongation (Fig. 2.20), but also in the other plots. However, such a delay is on the order of the measurement uncertainty in the developmental times of the flies.

2.4 Discussion

In this chapter, we used rigorous geometric arguments to precisely decompose large-scale deformations of two-dimensional cellular networks into contributions by cellular events. These cellular events comprise cell shape changes, T1 transitions, cell divisions, and T2 transitions. In order to define the respective contributions of these events to deformation, we tiled the network into triangles. Then, cell shape changes correspond

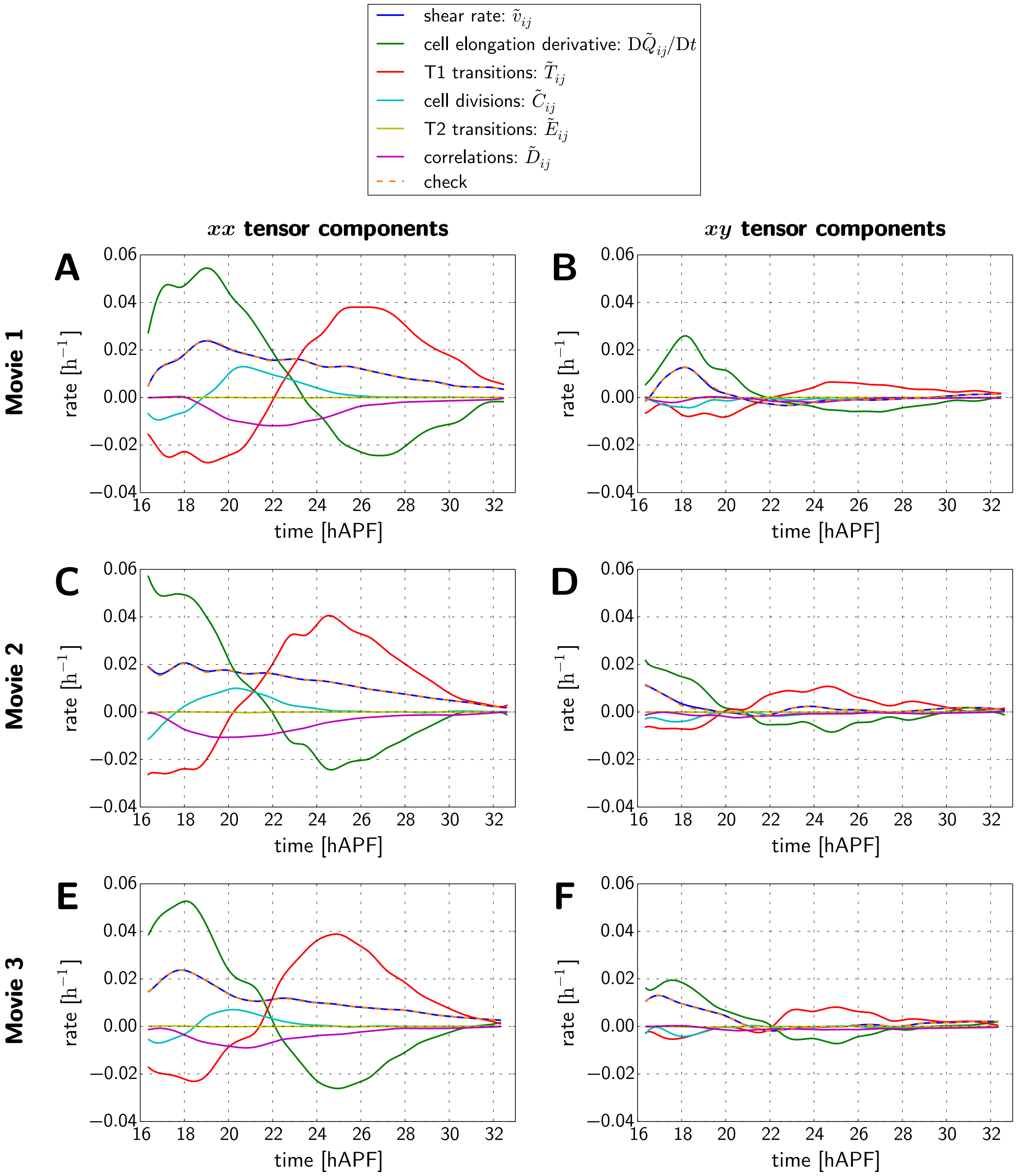

Figure 2.19: Decomposition of the shear rate tensor $\tilde{v}_{ij}$ for three different wild type wing blades. Movie 1 (panels A and B) corresponds to the data presented before (Fig. 2.16). The caption of Fig. 2.16 applies to all six panels.

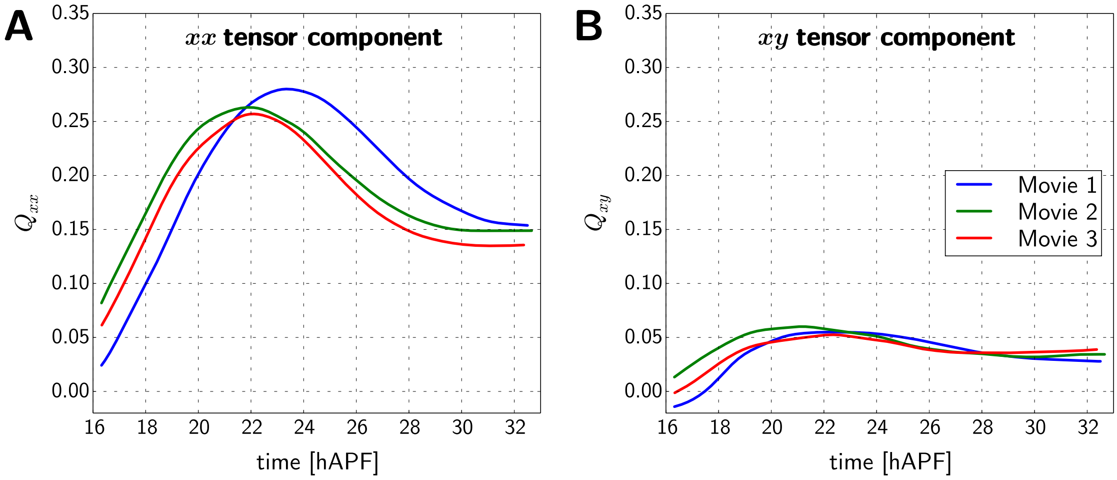

Figure 2.20: Average elongation depending on time for three different wild type wing blades. Movie 1 (blue solid lines) corresponds to the data presented before (Fig. 2.17). All curves shown are smoothed by convolving with a Gaussian with standard deviation $\sigma \approx 30\,\text{min}$.

to triangle shape changes, and topological transitions correspond to the disappearance and appearance of triangles.

We separately discussed the isotropic and anisotropic components of large-scale network deformation. The isotropic component corresponds to an isotropic expansion of the network. It decomposes into relative cell area change, cell division rate, and negative T2 transition rate.

The anisotropic component of network deformation corresponds to pure shear deformations. We showed that large-scale pure shear deformations decompose into contributions by cell shape changes and topological transitions. Furthermore, it turned out that there are correlations that also contribute to pure shear deformations. Such correlations appear whenever the network deforms inhomogeneously.

We applied our theoretical framework in order to study deformations of the fly wing during development. Earlier work [54] qualitatively identified two phases of this deformation process. During the first phase, tissue shear was accompanied by an increase of cell shape anisotropy along the shear axis. Afterwards, during the second phase, cell shape became more isotropic again due to oriented T1 transitions. Here, using our newly developed method, we could quantitatively confirm these observations. Moreover, we newly found that during the first phase, cell rearrangements counteracted the effect of cell shape change, which suggests the existence of active anisotropic terms in the mechanics of the fruit fly wing.

Note that there is a clear distinction between the deformation usually defined in classical elasticity theory and the deformation defined here. In classical elasticity theory, deformation characterizes the state of a solid with respect to a single, clearly defined reference state [101, 149]. In contrast to that, here, we considered infinitesimal deformations relative to some initial state, which corresponds to the reference state. Therefore, for subsequent infinitesimal deformations, the reference state will vary in time. As a consequence, the integrated large-scale shear for a deformation between two given states depends on the precise deformation protocol chosen. This is even true in the absence of topological transitions. In Appendix B.4, we show this in detail and in a more general context.

A crucial ingredient for our theoretical framework to be exact was the triangulation of the cellular network. The deeper reason for this is that for any two triangles in the plane, one always finds a unique linear transformation that maps one triangle to the other. However, note that in principle, other triangulations than that defined in Section 2.1.1 could be chosen. In Appendix B.7, we discussed one example for an alternative triangulation and we found that in particular the contribution of T1 transitions to large-scale shear depends on the method of triangulation.

Other work also derived and applied relations that decompose large-scale deformations of cellular networks into contributions on the cell scale. In a series of papers by the Graner group, deformations of cellular patterns are characterized based on links between cell centers [85, 150–153]. They define a *texture tensor*, which characterizes local shape anisotropies, a local velocity gradient, and a tensor that quantifies creation and removal of links. These tensors are related by an equation similar to Eq. (2.53). They apply this equation in order to study the rheology of two-dimensional foams. However, the authors introduced approximations. One approximation assumes small local shape anisotropies and another one assumes local affinity of deformations. In our work, such assumptions are not necessary because we triangulate the cellular network. Therefore, Eq. (2.53) is exact for infinitesimal deformations.

In ref. [154], the authors describe the deformation of epithelial tissue by introducing a local velocity gradient tensor and a local cell elongation tensor. Then, they define a *cell intercalation strain rate tensor* to be the difference between the local velocity gradient and the local change rate of cell elongation. This cell intercalation strain rate comprises contributions by T1 transitions, but also by sliding of cells past each other. As compared to that work, our approach is more fine-grained revealing fundamental relations between cellular shape changes and large-scale deformations. Moreover, we also describe the deformation by other topological transitions like cell divisions and T2 transitions.

Chapter 3

Rheological behavior of vertex model tissue under external shear

In this chapter, we use a vertex model to study mechanical properties of epithelia. In particular, we discuss the stress relaxation behavior of vertex model tissue depending on cellular fluctuations. To this end, we focus on the steady state of simple shear simulations.

This chapter is organized as follows. In Section 3.1, we present the vertex model that we use, and we introduce model extensions. In Section 3.2, we analyze the stress relaxation behavior of vertex model tissue in simple shear simulations using our results from Chapter 2. We find plastic behavior for small fluctuation amplitude and visco-elastic behavior for large fluctuation amplitude. Finally, in Section 3.3, we discuss our results and compare to previous work. Important symbols appearing in this chapter are listed on pages 226f.

3.1 A vertex model to describe epithelial mechanics

In order to probe the shear stress relaxation behavior of epithelia, we used a vertex model that was developed earlier [118]. In this section, we present this vertex model and we describe how we extended it for our purpose.

The vertex model describes epithelia as planar cellular networks, where each cell is represented by a polygon (as in Section 2.1.1). In the following subsections, we explain different aspects of this model. In Section 3.1.1, we explain how force-balanced states of the cellular network are defined and how they are obtained numerically. In Section 3.1.2, we extend the vertex model by fluctuations of a mechanical tissue property. In Section 3.1.3, we test the effect of these fluctuations on growth. Therefore, we discuss their effect on cell neighbor number distributions during growth. Finally, in Section 3.1.4, we explain the implementation of particular boundary conditions, which allow for continuous simple shear deformations of vertex model tissue. In Section 3.2, these simple shear deformations will be used to probe shear stress relaxation behavior.

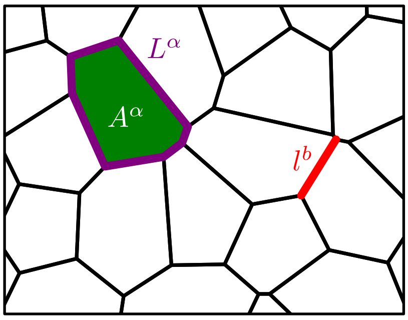

Figure 3.1: Force-balanced state of a cellular network. Force-balanced states are described by minima of the work function W, which depends on the areas A^α and perimeters L^α of all cells α and on the lengths l^b of all bonds b.

3.1.1 Force-balanced states

Here, we first show how force-balanced states of the cellular network are defined in the vertex model. Then, we explain how they were obtained numerically.

Work function

Force-balanced states of the cellular network are described by minima of the following work function [118, 121]:

$$W = \frac{K}{2}\sum_{\alpha}\left(A^\alpha - A_0\right)^2 + \frac{\Gamma}{2}\sum_{\alpha}\left(L^\alpha\right)^2 + \sum_{b}\Lambda^b l^b. \tag{3.1}$$

Here, the first two sums run over all cells α of the network and the third sum runs over all bonds b of the network (Fig. 3.1). The first term describes an elasticity of the area A^α of each cell α, where the parameters A_0 and K denote preferred area and area elasticity, respectively. The second term describes an elasticity of the cell perimeter L^α, where the parameter Γ denotes the perimeter elasticity. In this work, we assume the parameters A_0, K, and Γ to be constant and homogeneous among all cells. The last term describes contributions of bond lengths l^b to the work function, where the coefficients Λ^b denote line tensions. Here, the line tensions may vary in time and among different bonds. Without fluctuations, which are introduced below, we set all line tensions to a baseline value of $\Lambda^b = \Lambda_0$.

Numerical minimization

The work function W depends on the network topology and on vertex positions. In order to numerically obtain a force-balanced state, the work function is minimized with respect to the vertex positions (Appendix C.1.2). For this multidimensional minimization, we use the conjugate gradient method [155].

During minimization, the network topology may change according to the rules defined in Appendix C.1.3. Note that in contrast to earlier vertex model implementations [58, 82, 121, 123], we allow for N-fold vertices with $N > 3$. This considerably simplifies the treatment of topological transitions.

3.1.2 Line tension fluctuations

In the previous subsection, we defined force-balanced states of the cellular network by minima of the work function W. However, the work function alone may only define elasticities, but no time scale and therefore no finite viscosity. In order to introduce a time scale into the tissue mechanics, we extend the vertex model by fluctuations of the line tensions Λ^b.

Definition

We introduce fluctuations into the line tension Λ^b of each bond b by adding colored noise $\eta^b(t)$:

$$\Lambda^b(t) = \Lambda_0 + \Lambda_F \eta^b(t). \tag{3.2}$$

Here, the constant parameter Λ_F denotes the line tension fluctuation amplitude. The colored noise $\eta^b(t)$ is given by a separate Ornstein-Uhlenbeck process for each bond b:

$$\frac{\mathrm{d}\eta^b(t)}{\mathrm{d}t} = -k_\Lambda \eta^b(t) + \sqrt{2k_\Lambda}\, \xi^b(t). \tag{3.3}$$

Here, $\xi^b(t)$ denotes Gaussian white noise with zero average $\langle \xi^b \rangle = 0$ and $\langle \xi^b(t_1)\xi^c(t_2)\rangle = \delta_{bc}\delta(t_2 - t_1)$ for any two bonds b and c. The parameter k_Λ is a rate that corresponds to the characteristic frequency of the Ornstein-Uhlenbeck noise $\eta^b(t)$.

Upon creation of a bond b at time t_0, the initial value of $\eta^b(t_0)$ is drawn from a normal distribution with average zero and variance one. The prefactors in Eq. (3.3) are chosen such that $\langle \eta^b(t)\eta^c(t)\rangle = \delta_{bc}$ remains true for all times $t \geq t_0$. As a consequence, Λ_F corresponds to the standard deviation of the line tension. Also, the line tension fluctuations of different bonds are uncorrelated.

Introduction of dimensionless units

In order to reduce the number of parameters, we introduce dimensionless units choosing k_Λ^{-1} as typical time scale, $A_0^{1/2}$ as typical length scale, and KA_0^2 as typical energy scale [compare 118, 122]. Then, we define dimensionless versions of all quantities, which we denote by a bar, here. For instance:

dimensionless quantity	$\bar{W}$	$\bar{\Lambda}_0$	$\bar{\Lambda}_F$	$\bar{\Gamma}$	$\bar{t}$
definition	$W/(KA_0^2)$	$\Lambda_0/(KA_0^{3/2})$	$\Lambda_F/(KA_0^{3/2})$	$\Gamma/(KA_0)$	tk_Λ

For simplicity of notation, we will omit the bar in the following. Thus, in the following and in Appendix C, all quantities are given in these dimensionless units.

For our study, we choose the parameter values $\Lambda_0 = 0.12$ and $\Gamma = 0.04$. These values have been found to reproduce three independent morphological features of the fruit fly wing disc epithelium [118].

Implementation

Epithelial dynamics including fluctuations were simulated using time steps of length $\Delta t = 0.01$. During each time step, the noise variables $\eta^b(t)$ of all bonds were updated. Therefore, the line tensions $\Lambda^b(t)$ and the work function W changed. Thus, at the end of the time step, the network was relaxed to a new minimum of W.

3.1.3 Influence of line tension fluctuations on tissue growth

In the last subsection, we showed how we introduced line tension fluctuations into the vertex model. Here, we test our implementation by studying their influence on epithelial growth and comparing to earlier work [118].

In ref. [118], the authors showed that growth simulations in the vertex model produce characteristic distributions of cell neighbor numbers. Moreover, in ref. [121], it was shown that line tension fluctuations could increase the fraction of hexagons in the cellular network. This corresponds to an annealing effect, because for the chosen parameter values of Λ_0 and Γ, a packing of regular hexagons corresponds to the ground state of the work function [122].

Here, we study the influence of line tension fluctuations on the cell neighbor number distribution (Fig. 3.2). To this end, we simulated line tension fluctuations together with growth, where the average cell cycle length was given by τ_{div} (Fig. 3.2A, Appendix C.2). Starting from a 6 by 6 hexagonal network, the simulation ran for a time corresponding to τ_{div} such that in the final state, the network consisted of ca. 100 cells.

We found that the neighbor number distribution was strongly biased by line tension fluctuations. In particular, with increasing cell cycle time τ_{div} as compared to the fluctuation time scale, the fraction of hexagons in the final state of the simulations increased significantly (Fig. 3.2B). Furthermore, for fast cell divisions ($\tau_{\text{div}} = 1$), the fraction of hexagons in the final state increased with the line tension fluctuation amplitude Λ_F (Fig. 3.2C). In contrast to that, without line tension fluctuations, we obtained the distribution reported in ref. [118] (blue solid lines in Figs. 3.2B-D). Taken together, this suggests that cell divisions alone drive the neighbor number towards the distributions reported in ref. [118]; whereas line tension fluctuations tend to increase the fraction of hexagons. However surprisingly, for very slow cell divisions and large line tension fluctuation amplitude, the fraction of hexagons decreased again (Fig. 3.2D).

3.1.4 Simple shear simulations using skewed periodic boundary conditions

In order to probe the stress relaxation behavior of vertex model tissue, we carried out simple shear simulations. As compared to pure shear simulations, simple shear simulations bear the advantage that the steady state can be simulated as long as necessary to provide enough statistics. Here, we first show what boundary conditions

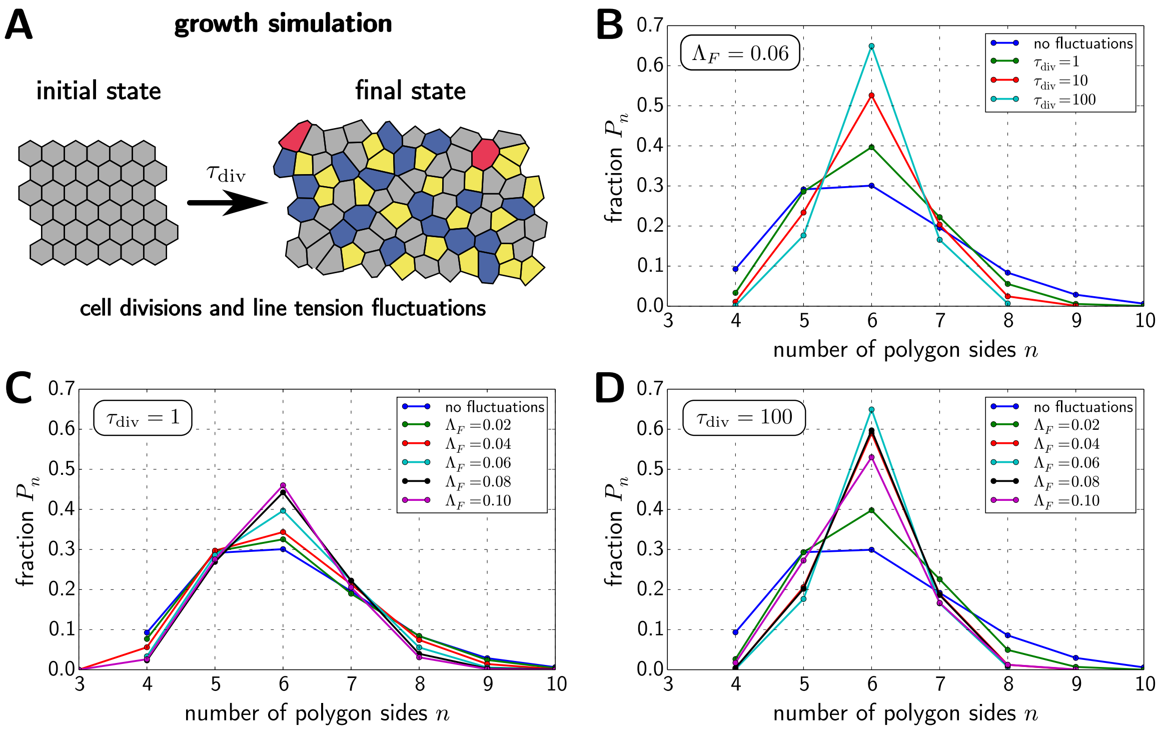

Figure 3.2: Effect of line tension fluctuations on the cell neighbor number distribution in growth simulations. **(A)** The simulations started from a 6×6 hexagonal network and lasted for the average cell cycle time of $\tau_{\rm div}$. Growth and line tension fluctuations were simulated simultaneously. The cells are colored according to their neighbor number (Table 3.1). **(B,C,D)** Cell neighbor number distribution in the final state. Shown are values averaged over 100 individual simulations. Uncertainties were computed as the standard deviation of the respective Bernoulli distribution. They were smaller than the symbol size. **(B)** The fraction of hexagons increased with increasing cell cycle time for the fluctuation amplitude $\Lambda_F = 0.06$. **(C)** The fraction of hexagons increased with increasing fluctuation amplitude Λ_F for $\tau_{\rm div} = 1$. **(D)** For $\tau_{\rm div} = 100$, the fraction of hexagons first increased with the fluctuation amplitude until $\Lambda_F = 0.06$ and then decreased again.

Table 3.1: Cell colors encode neighbor numbers (Figs. 3.2A, 3.3, and 3.5).

neighbor number	4	5	6	7	8
color	green	yellow	gray	blue	red

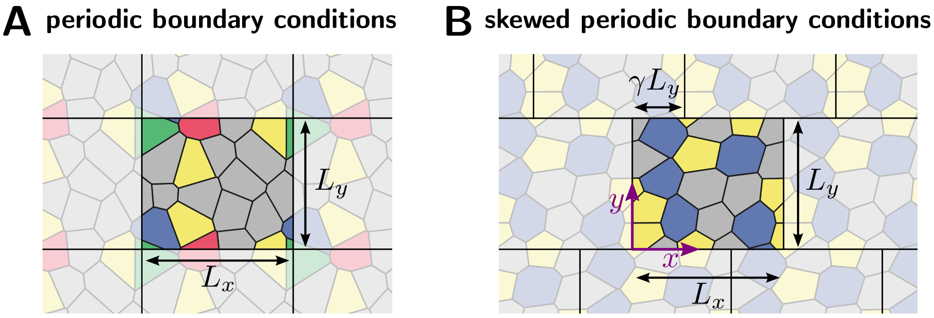
A periodic boundary conditions
L_y
L_x
B skewed periodic boundary conditions
γL_y
L_y
y
x
L_x

Figure 3.3: Illustration of the boundary conditions used. **(A)** Periodic boundary conditions as used in earlier studies. The size of the simulation box is $L_x \times L_y$. **(B)** In this work, continuous simple shear simulations are implemented using periodic boundary conditions with a skew of γL_y. The variable γ denotes the integrated simple shear. The pure periodic boundary conditions (panel A) are recovered for $\gamma = 0$. In order to more clearly illustrate the periodicity in the cellular patterns, the cells in both panels are colored according to Table 3.1.

we used in order to allow for continuous simple shear. Then, we explain how we carried out the simple shear simulations.

Boundary conditions

In order to implement simple shear in the vertex model, we extend the boundary conditions used in earlier studies (Fig. 3.3). In earlier studies, periodic boundary conditions were used, where the simulation box was a rectangle with side lengths $L_x \times L_y$ (Fig. 3.3A) [58, 82, 121, 123]. Here, we define the simple shear variable γ, which introduces an additional skew γL_y in the periodic boundary conditions (Fig. 3.3B, Appendix C.1.1). Such boundary conditions are similar to the so-called Lees-Edwards boundary conditions [156]. Note that the simulation box defines a coordinate system (magenta arrows in Fig. 3.3B), which we use in the following.

Simple shear simulations

For all simple shear simulations in this chapter, we fixed the dimensions of the simulation box (L_x, L_y) and we increased simple shear variable γ with a constant rate, which we denote by $\dot{\gamma}$.

Under these conditions and without fluctuations, we observed the formation of shear bands in our simulations (Fig. 3.4) [121].[1] Here, we prevent shear bands using line tension fluctuations with amplitudes $\Lambda_F \geq 0.02$ (Appendix C.3.2).

---

[1] The term *shear bands* refers to the localization of strain upon deformation of a solid. Put differently, the solid is not sheared homogeneously. Most parts of it may even be deformed only little. Rather, the shear is localized within so-called *shear bands* (red solid line in Fig. 3.4).

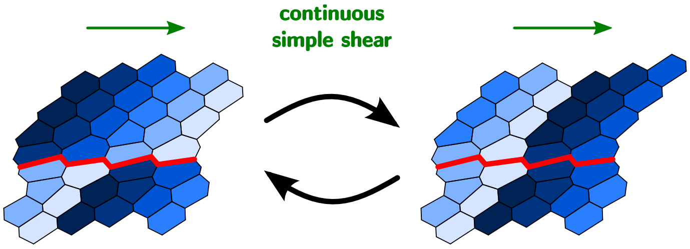

Figure 3.4: A shear band (red solid line) appeared in simple shear simulations without fluctuations. Along this line, cells slid past each other. Two time snapshots are shown, where each cell has the same color in both snapshots.

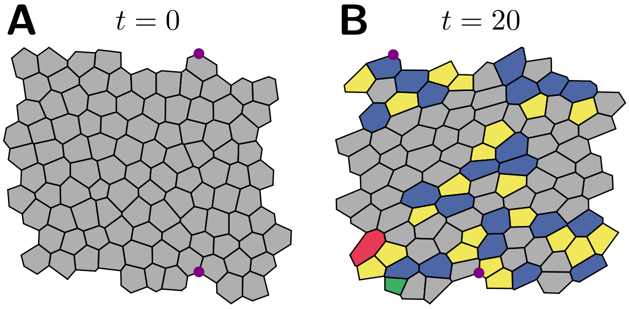

Figure 3.5: Two snapshots at different time points of a simple shear simulation with $\dot{\gamma} = 0.5$ and $\Lambda_F = 0.06$. Cells are colored according to Table 3.1. Pairs of magenta dots within each snapshot indicate the same vertex, respectively. At time $t = 0$, the cellular network is not regular because of the line tension fluctuations.

For large fluctuation amplitudes, cells were occasionally extruded by T2 transitions.[2] To ensure the existence of a steady state with a finite number of cells, we fixed the cell number by forcing a cell division upon each T2 transition (Appendix C.3.1).

3.2 Fluctuation-induced fluidization of tissue

In this section, we study the shear stress relaxation behavior of vertex model tissue and the role of fluctuations. To this end, we use the following set of simple shear simulations. We started from a 10×10 pattern of hexagonal cells (Fig. 3.5A). During the simulation, the simulation box was sheared by the boundary conditions with a constant simple shear rate of $\dot{\gamma}$. Also, line tension fluctuations with amplitude Λ_F were included. We varied the line tension fluctuation amplitude Λ_F within the interval $0.02 \leq \Lambda_F \leq 0.10$ and the shear rate $\dot{\gamma}$ within the interval $0 \leq \dot{\gamma} \leq 1$. For each combination of both parameter values, we performed 100 simulation runs for a total time of $T = 1000$ (for $\Lambda_F \leq 0.04$) or $T = 100$ (for $\Lambda_F > 0.04$). Two snapshots from one of the simulations are shown in Fig. 3.5. For details, see Appendix C.3.1.

In the following, we characterize the shear stress relaxation behavior in the simple shear simulations. We also show how it depended on the fluctuation amplitude Λ_F. To this end, we focus on a mean field description of steady state properties. In Section 3.2.1, we show that cells were characterized by a mainly constant shear modulus. Thus, shear stress was proportional to cell elongation. Then, in Section 3.2.2, we study the relaxation of cell elongation. To this end, we use the theoretical framework developed in Chapter 2.

---

[2] The observed rates of T2 transitions per cell ranged up to 0.016 in dimensionless units (Section 3.1.2, page 53).

3.2.1 Cellular shear elasticity

Here, we are interested in the cellular shear modulus, which connects the shear stress nematic $\tilde{\sigma}_{ij}$ to the cell elongation nematic $\tilde{Q}_{ij}$.[3] We define the nematic $\tilde{\sigma}_{ij}$ as the dimensionless shear stress exerted by the simulation box on the vertex model tissue (Appendix C.4.1).[4] The average cell elongation $\tilde{Q}_{ij}$ is defined as in the preceding chapter (Section 2.2.3).

Focusing on a description of the steady state, we first exclude initial transients. To this end, we study the time-dependence of $\tilde{\sigma}_{ij}$ and $\tilde{Q}_{ij}$. For the fluctuation amplitude $\Lambda_F = 0.06$ and the shear rate $\dot{\gamma} = 0.2$, both quantities are plotted in Fig. 3.6A,B. We find that both nematics were clearly correlated. After initial transients that lasted for a time of ca. 5 in dimensionless units, both nematics appeared to reach steady state values.

We computed the steady state values of the nematics $\tilde{\sigma}_{ij}$ and $\tilde{Q}_{ij}$ for all parameter pairs $(\Lambda_F, \dot{\gamma})$. To this end, for a given parameter pair $(\Lambda_F, \dot{\gamma})$ and a given simulation run, we averaged the respective values for all time points $t \geq t_0$ starting from a manually determined cut off time $t_0 > 0$. For the example shown in Fig. 3.6A,B, we chose $t_0 = 10$. Afterwards, we averaged the steady state values of all 100 simulation runs of the given parameter pair $(\Lambda_F, \dot{\gamma})$.

The so-obtained steady state values of $\tilde{\sigma}_{ij}$ and $\tilde{Q}_{ij}$ are presented in Fig. 3.6C,D for varying parameter values Λ_F and $\dot{\gamma}$. We find that first, $\tilde{\sigma}_{ij}$ and $\tilde{Q}_{ij}$ were largely parallel up to $\sim 0.01\pi$ (Fig. 3.6D). Thus, the shear modulus can be represented by a scalar E with:

$$\tilde{\sigma}_{ij} = E\tilde{Q}_{ij}. \tag{3.4}$$

Second, the cellular shear modulus was largely independent on $\tilde{Q}_{ij}$ and on the fluctuation amplitude Λ_F (Fig. 3.6C). We find $E \approx 0.5$ (black dashed line in Fig. 3.6C). Interestingly, for the chosen parameter values $\Lambda_0 = 0.12$ and $\Gamma = 0.04$, this corresponds to the theoretical elasticity of a hexagonal cell without line tension fluctuations [122].

3.2.2 Fluctuation-dependent elongation relaxation

Here, we study the relaxation of the cell elongation nematic $\tilde{Q}_{ij}$ using the simple shear simulations introduced above. As we have seen in the last section, the shear stress $\tilde{\sigma}_{ij}$ was mainly proportional to the cell elongation $\tilde{Q}_{ij}$. Thus, studying the relaxation of cell elongation corresponds to studying the relaxation of shear stress.

---

[3] Throughout this work, *nematic* or *nematic tensor* denote a symmetric, traceless tensor. For details, see Appendix A.2.

[4] The dimensionless shear stress $\tilde{\sigma}_{ij}$ is given in units of KA_0.

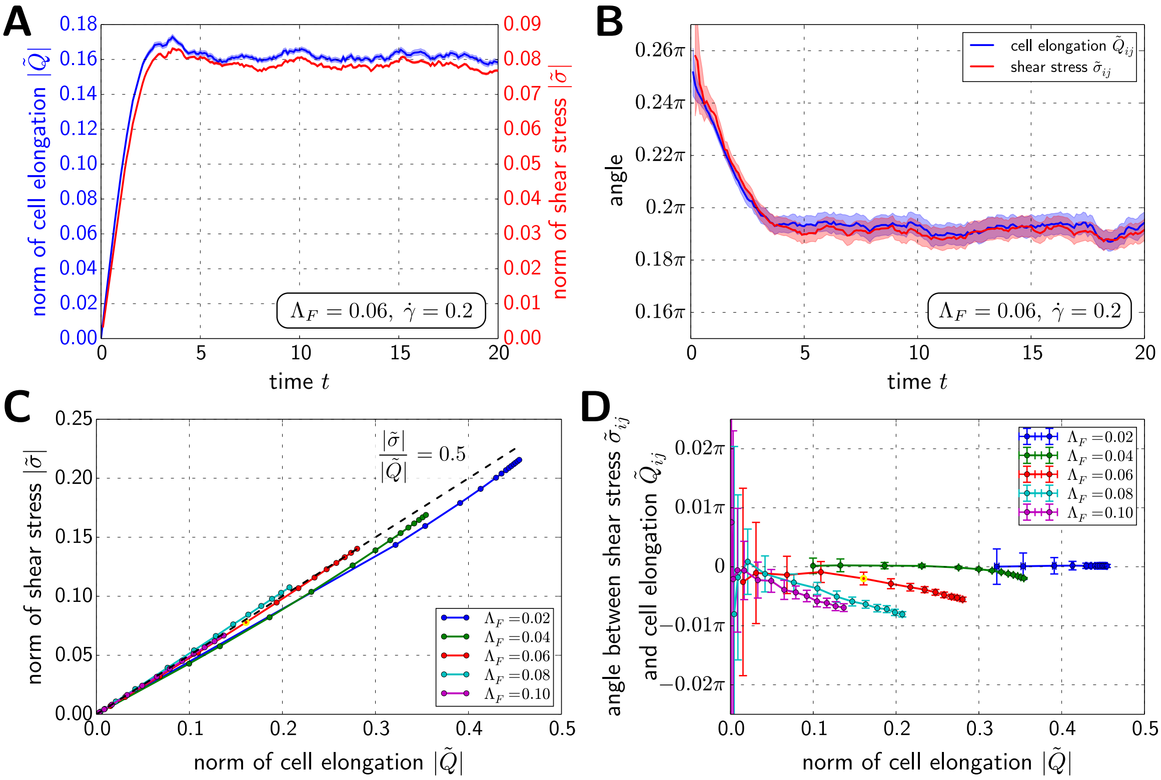

Figure 3.6: The cellular shear modulus is largely independent on the fluctuation amplitude Λ_F and on the shear rate $\dot{\gamma}$. **(A,B)** Comparison of the norms **(A)** and the angles **(B)** of the cell elongation $\tilde{Q}_{ij}$ (blue solid lines) and of the shear stress $\tilde{\sigma}_{ij}$ (red solid lines). Angles are defined with respect to the x axis of the coordinate system defined in Fig. 3.3B. Shown are average values corresponding to 100 independent simulation runs. The hatched regions show the respective uncertainties. Parameter values used: $\Lambda_F = 0.06$ and $\dot{\gamma} = 0.2$. **(C,D)** Comparison of steady state norms and angles of $\tilde{Q}_{ij}$ and of $\tilde{\sigma}_{ij}$ for varying parameter values Λ_F and $\dot{\gamma}$. Each dot represents a parameter pair $(\Lambda_F, \dot{\gamma})$. The yellow dots marks the parameter pair used in panels A and B. **(C)** Norm of the shear stress $|\tilde{\sigma}|$ depending on the norm of the cell elongation $|\tilde{Q}|$. The black dashed line represents a slope of 0.5. **(D)** Angle between the axes of $\tilde{\sigma}_{ij}$ and $\tilde{Q}_{ij}$. The uncertainties in panels A-D were computed as explained in Appendix C.4.3. In panel C, the error bars are not shown, because the uncertainties are smaller than the symbol size.

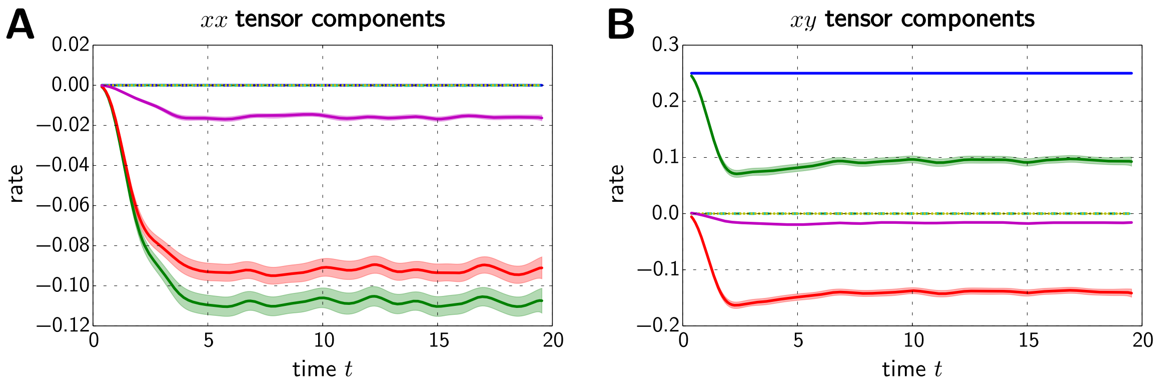

Figure 3.7: Decomposition of the cell elongation derivative $\mathrm{D}\tilde{Q}_{ij}/\mathrm{D}t$ (green solid lines) according to Eq. (3.5) for simple shear simulations. Essentially, only the shaer rate $\tilde{v}_{ij}$ (blue solid lines), the T1 transitions $-\tilde{T}_{ij}$ (red solid lines), and the correlations $-\tilde{D}_{ij}$ (magenta solid lines) contributed. The contributions by cell divisions $-\tilde{C}_{ij}$ (cyan dashed lines) and T2 transitions $-\tilde{E}_{ij}$ (yellow dotted lines) could be neglected. All curves are smoothened by colvolving with a Gaussian with a standard deviation of 0.5 in dimensionless units. The hatched regions reflect the standard error of the mean resulting from averaging the respective quantity over 100 individual simulation runs. Parameter values: $\Lambda_F = 0.04$ and $\dot{\gamma} = 0.5$.

Dynamics of cell elongation

In order to characterize the relaxation behavior of cell elongation $\tilde{Q}_{ij}$, we use our results from Chapter 2. According to Eq. (2.53), the dynamics of $\tilde{Q}_{ij}$ can be described by the following equation:

$$\frac{\mathrm{D}\tilde{Q}_{ij}}{\mathrm{D}t} = \tilde{v}_{ij} - \tilde{T}_{ij} - \tilde{C}_{ij} - \tilde{E}_{ij} - \tilde{D}_{ij}. \tag{3.5}$$

Here, $\mathrm{D}\tilde{Q}_{ij}/\mathrm{D}t$ denotes the corotational derivative of $\tilde{Q}_{ij}$. The nematic $\tilde{v}_{ij}$ denotes the shear rate and the nematics $\tilde{T}_{ij}$, $\tilde{C}_{ij}$, $\tilde{E}_{ij}$, and $\tilde{D}_{ij}$ denote shear contributions by T1 transitions, cell divisions, T2 transitions, and correlations, respectively. All of these quantities are defined in Section 2.2.3. In Appendix C.4.2, we show how they were computed in the vertex model simulations.

In order to illustrate Eq. (3.5), we plot these quantities depending on time for the parameter values $\Lambda_F = 0.04$ and $\dot{\gamma} = 0.5$ in Fig. 3.7. In the following, we discuss the individual terms separately. The corotational derivative $\mathrm{D}\tilde{Q}_{ij}/\mathrm{D}t$ (green solid line) describes the relaxation of cell elongation. After a time of ca. 7 in dimensionless units, the system appears to have reached a steady state. Note that in the steady state, where $\tilde{Q}_{ij}$ is constant, the corotational derivative is still nonzero. According to Eq. (2.54), the steady state value of $\mathrm{D}\tilde{Q}_{ij}/\mathrm{D}t$ reads:

$$\frac{\mathrm{D}\tilde{Q}_{ij}}{\mathrm{D}t} = -\omega \frac{1}{|\tilde{Q}|} \tanh\big(2|\tilde{Q}|\big) \epsilon_{ik} \tilde{Q}_{kj}. \tag{3.6}$$

Here, ω denotes the average vorticity of the flow field. For the simple shear simulations, its value is prescribed by the boundary conditions: $\omega = -\dot{\gamma}/2$ (Appendix C.3.3). The steady state value of $\mathrm{D}\tilde{Q}_{ij}/\mathrm{D}t$ corresponds to the shear rate that is necessary to maintain a constant $\tilde{Q}_{ij}$ in the presence of the vorticity ω.

The average shear rate $\tilde{v}_{ij}$ (blue solid lines) is constant, because it is prescribed by the boundary conditions (Appendix C.3.3). For a given parameter value $\dot{\gamma}$, the shear rate components are given by $\tilde{v}_{xx} = 0$ and $\tilde{v}_{xy} = \dot{\gamma}/2$.

The quantities $\tilde{T}_{ij}$, $\tilde{C}_{ij}$, $\tilde{E}_{ij}$, and $\tilde{D}_{ij}$ depend on the mechanical properties of the tissue. In order to characterize cell elongation relaxation for vertex model tissue, we need to understand their behavior. We found that the contributions by cell divisions $-\tilde{C}_{ij}$ (cyan dashed lines) and T2 transitions $-\tilde{E}_{ij}$ (yellow dotted lines) could be neglected. Indeed, this was true for all parameter pairs $(\Lambda_F, \dot{\gamma})$: we always found $|\tilde{C}| \lesssim 10^{-3}$ and $|\tilde{E}| \lesssim 10^{-4}$. In contrast to that, T1 transitions $-\tilde{T}_{ij}$ (red solid lines) and correlations $-\tilde{D}_{ij}$ (magenta solid lines) contributed significantly to $\mathrm{D}\tilde{Q}_{ij}/\mathrm{D}t$.

A nematic characterizing the relaxation of cell elongation

In order to characterize the relaxation of cell elongation, we need to study the behavior of $\tilde{T}_{ij}$ and $\tilde{D}_{ij}$. For simplicity, we subsume both terms into a single nematic $\tilde{F}_{ij}$:

$$\tilde{F}_{ij} = \tilde{T}_{ij} + \tilde{D}_{ij}. \tag{3.7}$$

Thus, the nematic $\tilde{F}_{ij}$ effectively describes the relaxation of cell elongation.

In the following, we study the behavior of $\tilde{F}_{ij}$. For simplicity, we choose a description where $\tilde{F}_{ij}$ only depends on the cell elongation nematic:

$$\tilde{F}_{ij} = \tilde{F}_{ij}\big(\tilde{\boldsymbol{Q}}\big). \tag{3.8}$$

We use this as the constitutive equation for $\tilde{F}_{ij}$. Consequently, $\tilde{F}_{ij}$ should be parallel or perpendicular to $\tilde{Q}_{ij}$. This is because except for the axis of $\tilde{Q}_{ij}$, there are no other directions in Eq. (3.8) that could determine the axis of $\tilde{F}_{ij}$. Moreover, according to Eq. (3.5), if $\tilde{F}_{ij}$ is parallel to $\tilde{Q}_{ij}$, it basically describes a reduction of $\tilde{Q}_{ij}$. Conversely, if it is perpendicular, it describes an amplification of $\tilde{Q}_{ij}$.

Now, we discuss angle and norm of the relaxation nematic $\tilde{F}_{ij}$ separately. First, we test if $\tilde{F}_{ij}$ and $\tilde{Q}_{ij}$ were indeed parallel or perpendicular in the simple shear simulations (Fig. 3.8A). We find that the angles of both nematics deviated by at most 0.03π from each other. These slight deviations might be due to a more complex constitutive

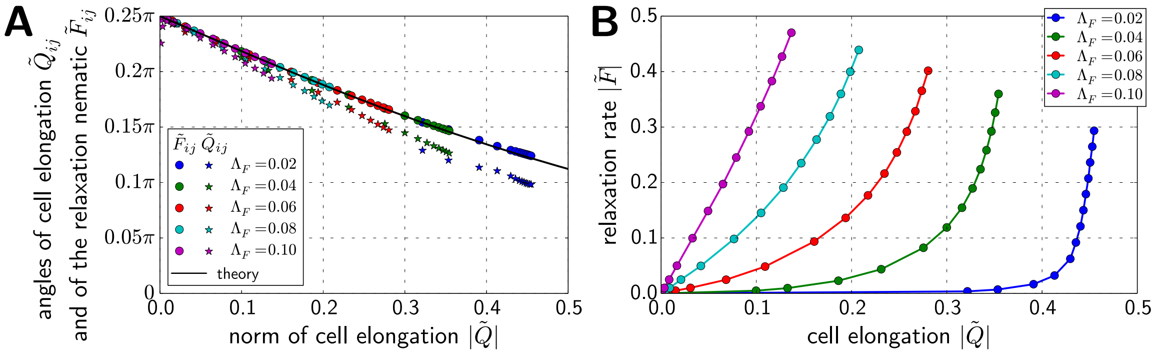

Figure 3.8: Characterization of the nematic $\tilde{F}_{ij}$ describing the relaxation of cell elongation and its dependence on cell elongation $\tilde{Q}_{ij}$. **(A)** Angles of $\tilde{F}_{ij}$ (circles) and $\tilde{Q}_{ij}$ (stars) depending on the norm of cell elongation. Each pair of angles corresponds to a parameter pair (Λ_F, $\dot{\gamma}$) and is computed from the average of 100 individual simulation runs. The black solid line indicates a theoretical curve for the case that $\tilde{F}_{ij}$ and $\tilde{Q}_{ij}$ are exactly parallel or perpendicular to each other (Eq. (3.9)). Angles are defined with respect to the x axis of the coordinate system defined in Fig. 3.3B. **(B)** Norm of $\tilde{F}_{ij}$ depending on the norm of $\tilde{Q}_{ij}$. We observe a smooth transition from plastic behavior for small fluctuation amplitude (blue solid line) to visco-elastic behavior for large fluctuation amplitude (magenta solid line). Each circle corresponds to a parameter pair (Λ_F, $\dot{\gamma}$) and is computed from the average of 100 individual simulation runs. The uncertainties in both panels were computed as explained in Appendix C.4.3. They were smaller than the symbol size.

Table 3.2: Observed time scales of linear visco-elasticity according to Eq. (3.11) for small shear rates $\dot{\gamma} \ll 1$ and varying line tension fluctuation amplitude Λ_F. The time scales listed here were obtained from linear fits of the $|\tilde{F}|(|\tilde{Q}|)$ data for small $|\tilde{Q}|$ (Fig. 3.8B). Dimensionless units are used (see Section 3.1.2, page 53).

Fluctuation amplitude Λ_F	**Visco-elastic time scale** τ
0.06	3.093 ± 0.076
0.08	0.898 ± 0.015
0.10	0.332 ± 0.009

relation for $\tilde{F}_{ij}$ or to the influence of the finite-sized simulation box.

If $\tilde{F}_{ij}$ and $\tilde{Q}_{ij}$ are parallel to each other, one can derive a theoretical expression for the angle Φ of cell elongation $\tilde{Q}_{ij}$. Using Eqs. (3.5), (3.6), and (3.7), we obtain (Appendix C.3.4, Eq. (C.34)):

$$\cos(2\Phi) = \tanh(2|\tilde{Q}|). \tag{3.9}$$

Note that this relation is independent of the norm of $\tilde{F}_{ij}$. This prediction matched the observed angles of $\tilde{F}_{ij}$ in the simulations (black solid lines and circles in Fig. 3.8A).

Because in the simulations, $\tilde{F}_{ij}$ and $\tilde{Q}_{ij}$ were mainly parallel to each other, the relaxation behavior of cell elongation is essentially captured by the norm of $\tilde{F}_{ij}$:

$$|\tilde{F}| = |\tilde{F}|\big(|\tilde{Q}|\big). \tag{3.10}$$

In the simulations, the behavior of cell elongation relaxation $|\tilde{F}|(|\tilde{Q}|)$ depended on the fluctuation amplitude Λ_F (Fig. 3.8B). For small fluctuation amplitude $\Lambda_F = 0.02$, cell elongation relaxation $|\tilde{F}|$ was practically negligible for $|\tilde{Q}| \lesssim 0.4$. Thus, cell elongation and shear stress were not relaxed in this regime and the vertex model tissue showed elastic behavior. For $|\tilde{Q}| \approx 0.45$, there was a sudden and steep onset of cell elongation relaxation $|\tilde{F}|$. Such a behavior corresponds to a plastic behavior with a yield stress corresponding to $|\tilde{\sigma}| \approx 0.22$, where the cell elasticity E measured above was used.

For large fluctuation amplitude $\Lambda_F = 0.10$, cell elongation relaxation $|\tilde{F}|$ was largely proportional to cell elongation $|\tilde{Q}|$. This corresponds to a linear visco-elastic behavior, where the factor of proportionality defines a time scale τ:

$$\tilde{F}_{ij} = \frac{1}{\tau}\tilde{Q}_{ij}. \tag{3.11}$$

Such a behavior results in a Maxwell model for shear stress relaxation [157, 158]. This becomes apparent, when substituting Eqs. (3.5), (3.7), and (3.11) into Eq. (3.4):

$$\left(1 + \tau\frac{\mathrm{D}}{\mathrm{D}t}\right)\tilde{\sigma}_{ij} = 2\eta\tilde{v}_{ij}. \tag{3.12}$$

Here, we defined the viscosity $\eta = \tau E/2$ and we neglected the shear rate contributions by cell divisions $\tilde{C}_{ij}$ and by T2 transitions $\tilde{E}_{ij}$. Note that the corotational derivative is defined analogously to Eq. (2.54), here. For small shear rates, we also observe linear visco-elastic behavior for $\Lambda_F = 0.06$ and $\Lambda_F = 0.08$. The corresponding time scales τ are summarized in Table 3.2.

3.3 Discussion

In this chapter, we used simple shear simulations of a vertex model to study rheological properties of epithelia. In particular, we discussed how the shear stress relaxation behavior depended on fluctuations. To this end, we used our results from Chapter 2. We found that for a small fluctuation amplitude, the vertex model tissue was in a plastic regime. Thus, below a yield stress, it deformed mainly elastically, and at the yield stress, tensions were relaxed. In contrast to that, for large fluctuation amplitude, stresses relaxed with a rate proportional to the stress itself. This corresponds to a visco-elastic behavior according to the Maxwell model.

In our simulations, we also implemented fluctuations in order to allow for a finite viscosity. This is because without fluctuations, the vertex model we used describes elastic tissue properties, but no time scale. Therefore, fluctuations were included by adding independent Ornstein-Uhlenbeck noise sources to the line tensions. Since Ornstein-Uhlenbeck noise possesses a characteristic time scale, a finite viscosity of the vertex model tissue became possible. Also, in our simulations, line tension fluctuations prevented the formation of persistent shear bands (Appendix C.3.2).

In this chapter, we used the quasi-static limit, which assumes that the time scale of mechanical relaxation is much smaller than the time scale of the line tension fluctuations. Alternatively, one could explicitly simulate the mechanical relaxation process. To this end, one could include cellular friction into the vertex model [58]. We suppose that the incorporation of such a friction would affect our results by mainly adding a viscous regime at short time scales.

In ref. [92], the authors also discuss the rheological behavior of biological tissues. To this end, they experimentally deform a cell aggregate and study the response. Then, they compare their results to Potts model simulations. Like us, they find a low fluctuation regime with plastic behavior and a high fluctuation regime with visco-elastic behavior. Here, we showed that also vertex model tissue can be characterized by such a behavior.

Chapter 4

Quantitative study of polarity reorientation in the fruit fly wing

In this chapter, we quantitatively study the experimentally observed reorientation of Planar Cell Polarity (PCP) in the developing wing of the fruit fly between 16 hAPF and 32 hAPF. To this end, we develop an effective hydrodynamic description for polarity reorientation, which is based on non-equilibrium descriptions of polar gels [63] and of liquid crystals [134].

In earlier work [54, 58], a hydrodynamic description for polarity reorientation was developed, which includes a coupling to tissue shear. This description could account for the observed reorientation of Core PCP in wild type wings. Furthermore, since Core PCP is known to guide the direction of wing hairs, the wing hair pattern of wild type flies could be explained as well. Here, we extend this hydrodynamic description by a coupling to a second polarity system, which represents the Fat PCP system. Using this hydrodynamic description, we are able to understand with a single set of parameters not only the wild type wing hair pattern, but also six other wing hair patterns created by genetic modifications of the Core PCP system.

In Section 4.1, we present experimental findings that motivate our study. In Section 4.2, we develop an effective hydrodynamic description for the reorientation of Core PCP and present analytical solutions of it. In Section 4.3, we compare analytical and numerical solutions of our hydrodynamic description to quantified wing hair patterns. Finally, in Section 4.4, we summarize and discuss our results. Note that most of the material presented here is also being published elsewhere [159]. Important symbols appearing in this chapter are listed on page 227.

4.1 Experimentally quantified polarity patterns

In this section, we present experimental data that motivate our theoretical study. It is organized as follows. In Section 4.1.1, we present the genetic modifications discussed in this chapter and the altered wing hair patterns they induce. Then, in Section 4.1.2, we qualitatively discuss the effect of the genetic modifications on Core PCP reorientation.

In order to quantify the wing hair patterns discussed here, we developed an algorithm, which makes use of a local nematic[1] auto-correlation of pixel intensities (Appendix E.1). Furthermore, we developed algorithms to quantify local PCP vectors from images with a clonal staining for a PCP protein, where *clonal staining* refers to a staining applied only to a random subset of cells within a tissue (Appendix E.2). We also apply known methods for the quantification of nematics characterizing PCP and cell shape anisotropy, which we rephrase in Appendix E.3. For details on the biological procedures, please refer to Appendix E.4 and ref. [159].

4.1.1 Genetic conditions

Whenever the Core PCP system is genetically modified in a particular way, the adult wing hair pattern is often altered as compared to the wild type pattern. Mostly, these altered wing hair patterns are largely reproducible. Here, we focus on a genetic modification that causes an over-production of the Core PCP protein Spiny legs (Sple) as compared to wild type production rates. We denote such an over-production by the term *over-expression*. We are interested in the influence of Sple over-expression on the dynamics of the Core PCP system and on the adult wing hair pattern.

By virtue of the large genetic toolbox available for the fruit fly, we can manipulate the over-expression of Sple in a spatio-temporal manner. To study the influence of Sple over-expression on the Core PCP system, we focus on the following conditions of space- and time-dependent Sple over-expression:

1. wild type,
2. early, ubiquitous Sple over-expression,
3. late, ubiquitous Sple over-expression,
4. permanent, ubiquitous Sple over-expression,
5. early, posterior Sple over-expression,
6. late, posterior Sple over-expression, and
7. permanent, posterior Sple over-expression.

Here, *posterior* denotes an over-expression in the posterior compartment only (compare Fig. 1.3Ci) and *ubiquitous* denotes an over-expression in the entire wing.

The terms *early*, *late*, and *permanent* are meant as follows. Throughout the entire chapter, we focus on the reorientation of Core PCP during the developmental time interval between 16 hAPF and 32 hAPF, where 32 hAPF corresponds approximately to the time of wing hair outgrowth. We denote Sple over-expression *permanent*, if it

---

[1] By a *nematic* or a *nematic tensor*, we denote a traceless, symmetric tensor. For details, see Appendix A.2.

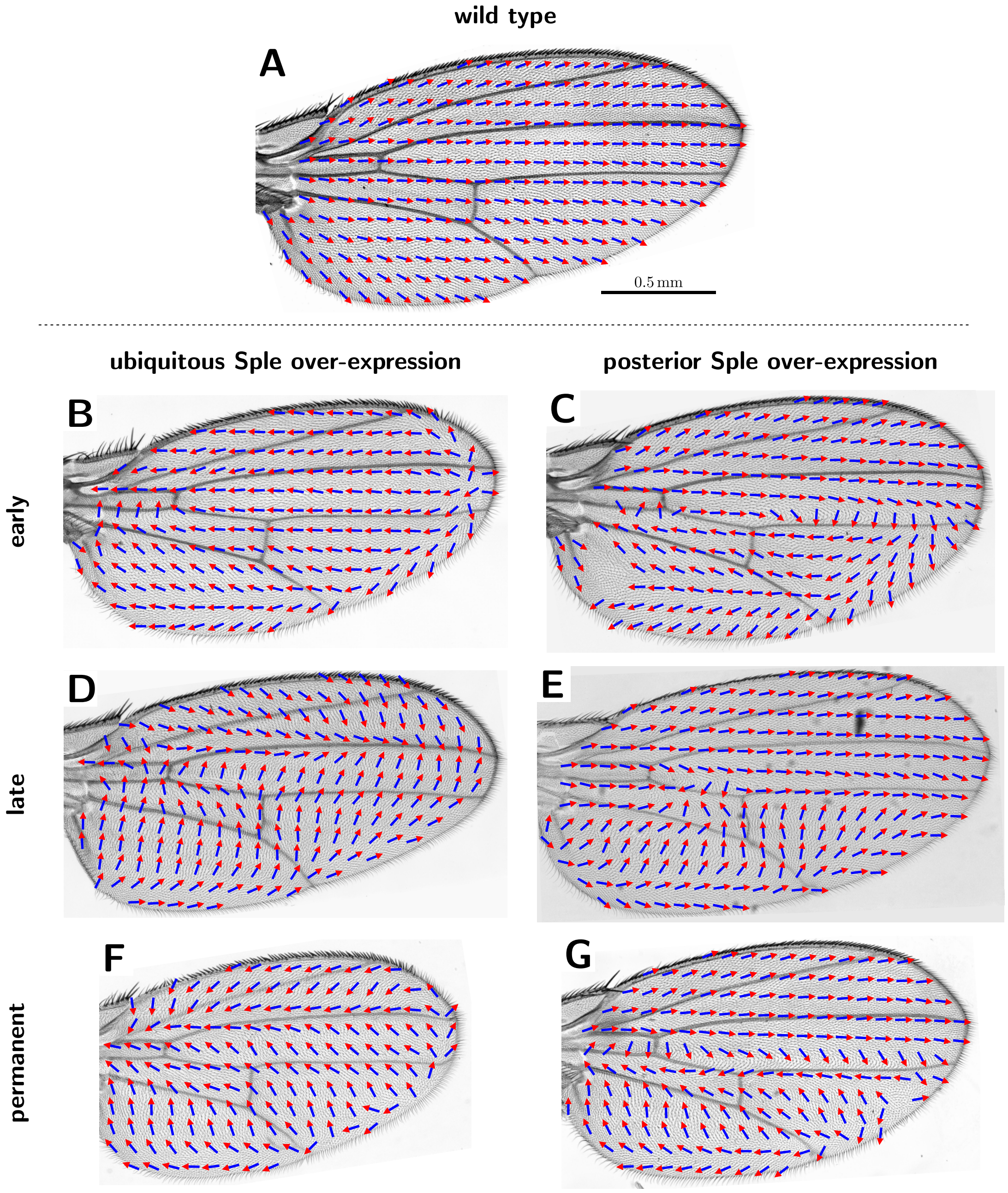
wild type
A
0.5 mm
ubiquitous Sple over-expression
posterior Sple over-expression
early
B
C
late
D
E
permanent
F
G

Figure 4.1: Quantified wing hair patterns for all conditions discussed in this chapter. The arrows indicate the locally averaged direction of wing hairs. **(A)** Wild type (condition 1). **(B)** Early, ubiquitous Sple over-expression (2). **(C)** Early, posterior Sple over-expression (5). **(D)** Late, ubiquitous Sple over-expression (3). **(E)** Late, posterior Sple over-expression (6). **(F)** Permanent, ubiquitous Sple over-expression (4). **(G)** Permanent, posterior Sple over-expression (7). The scale bar in panel A applies to all other panels as well.

occurs throughout the entire development of the fly. An over-expression is denoted *early*, if it coarsely ends with the beginning of the time interval considered. The notion *late* over-expression refers to an over-expression that coarsely starts with the time interval considered. The precise genotypes and experimental protocols for all conditions are explained in Appendix E.4 (Table E.1) and in ref. [159].

Quantified wing hair patterns for all conditions are shown in Fig. 4.1. The wing hair patterns for perturbed conditions (conditions 2-7; Fig. 4.1B-G) were clearly distinct from each other and from the wild type wing hair pattern (condition 1; Fig. 4.1A).

4.1.2 Effects of Sple over-expression

Here, we discuss possible effects of Sple over-expression on the dynamics of Core PCP. To this end, we first compare polarity patterns in wild type wings to polarity patterns in wings permanently and ubiquitously over-expressing Sple (conditions 1 and 4). The wing hair pattern for the over-expression was clearly different from wild type (Fig. 4.2A,B). To test whether this difference is due to an altered Core PCP pattern, we quantified the Core PCP patterns at the time of wing hair outgrowth. However, for technical reasons, we could only quantify the local Core PCP nematic, not the vector (Appendix E.3.2). We found that for both conditions, the Core PCP patterns were well reflected by the respective wing hair patterns (Fig. 4.2A-D). These observations are consistent with the paradigm that Core PCP controls the direction of wing hair outgrowth.

But why was the Core PCP pattern altered by an over-expression of Sple? In order to address this question, we compared the quantified Core PCP patterns to the quantified patterns of cell elongation and Fat PCP nematics at the time of wing hair outgrowth (Fig. 4.2). We found, that in wild type wings, the nematic Core PCP pattern resembled the cell elongation pattern, but not the Fat PCP pattern (Fig. 4.2C,E,G). In contrast to that, in wings over-expressing Sple, the nematic Core PCP pattern resembled the nematic Fat PCP pattern, but not the cell elongation pattern (Fig. 4.2D,F,H).

To further examine these similarities on a single cell level, we plotted histograms of angle differences between the cellular nematics of Core PCP, cell elongation, and Fat PCP (Fig. 4.3). In Fig. 4.3A,B, the cellular angle differences between the nematics of Core PCP and cell elongation are plotted as histograms, where each curve represents the histogram for a different range of the norm of the cell elongation nematic. In wild type wings, there was a clear tendency of Core PCP to be aligned with cell elongation and this alignment was more pronounced for more elongated cells (Fig. 4.3A). However, in wings over-expressing Sple, Core PCP showed no clear correlation with cell elongation (Fig. 4.3B).

In Fig. 4.3C,D, the cellular angle difference between the nematics of Core PCP and Fat PCP are plotted as histograms, where each curve represents the histogram for a different range of the norm of the Fat PCP nematic. In wild type wings, Core PCP showed no clear correlation with Fat PCP (Fig. 4.3C). In contrast to that, in wings

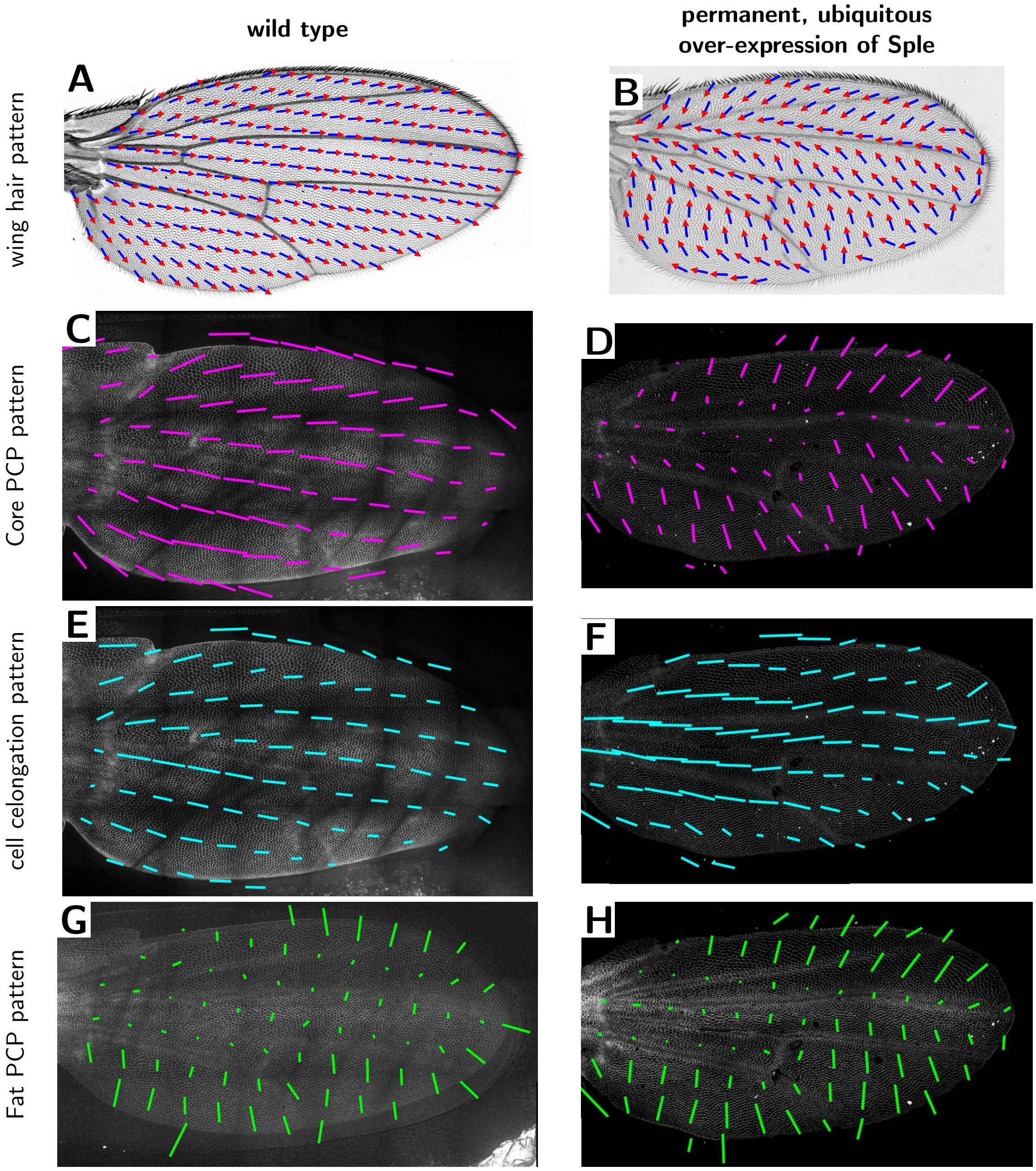
wild type
permanent, ubiquitous over-expression of Sple
wing hair pattern
Core PCP pattern
cell celongation pattern
Fat PCP pattern
A
B
C
D
E
F
G
H

Figure 4.2: Wing hair patterns of adult flies as well as patterns of PCP and cell shape anisotropy at 32 hAPF. **(A,B)** Wing hair patterns of **(A)** wild type wings and **(B)** wings permanently and ubiquitously over-expressing Sple. **(C,D)** Core PCP pattern **(C)** in an in vivo wild type wing, quantified from a Stbm staining, and **(D)** in a dissected wing ubiquitously over-expressing Sple, quantified from a Fmi staining. **(E,F)** Quantified cell elongation pattern in the same wings as in panels C and D, respectively. **(G,H)** Fat PCP patterns quantified from a Ds staining **(G)** in an in vivo wild type wing and **(H)** in the same wing as in panels D and F.

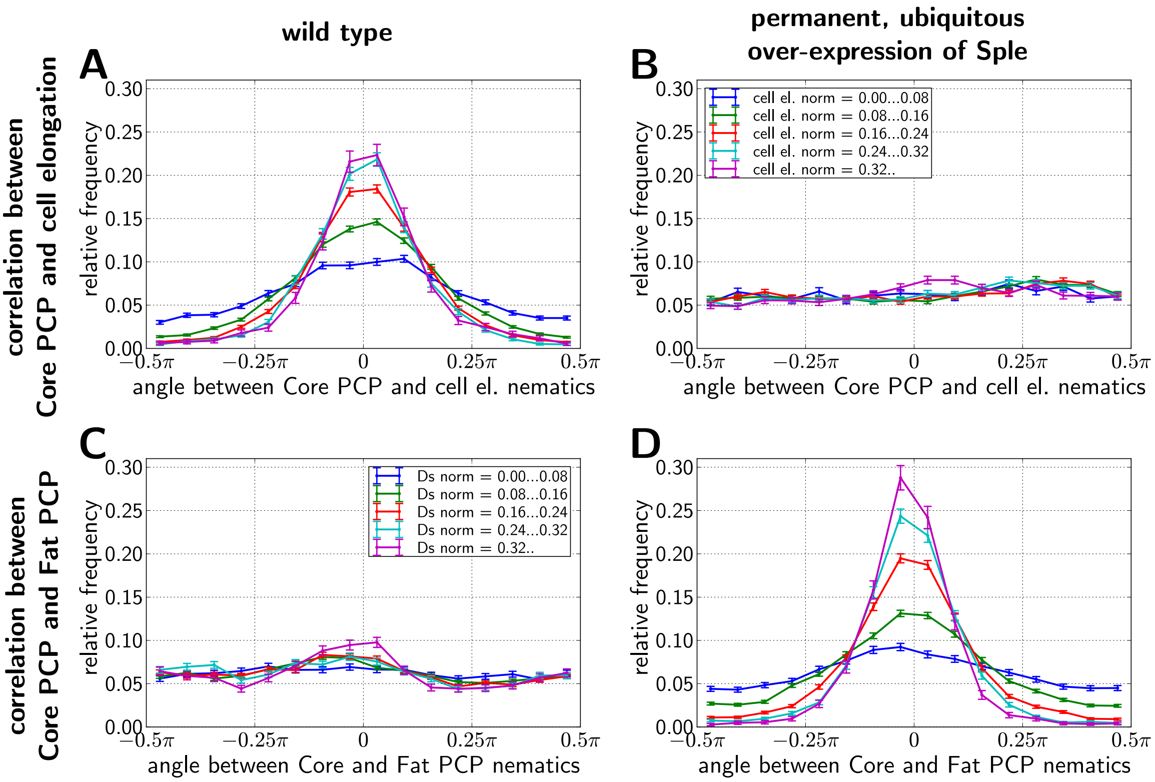

Figure 4.3: Histograms of angle differences between Core PCP, Fat PCP, and cell elongation nematics on the single cell level in wings at 32 hAPF. **(A,B)** Histograms of the angular differences between Core PCP, quantified by Fmi nematics, and cell elongation nematics. Different curves show different ranges of the norm of the cell elongation nematics (legend shown in panel B is also valid for panel A). **(C,D)** Histograms of the angular differences between Core PCP and Fat PCP, quantified by Fmi nematics and Ds nematics, respectively. Different curves show different ranges for the norm of the Ds nematics (legend shown in panel C is also valid for panel D). **(A,C)** Histograms for the data of three wild type wings. **(B,D)** Histograms for the data of three wings permanently and ubiquitously over-expressing Sple. Error bars in panels A-D indicate the standard deviation assuming a Poisson distribution for each bin.

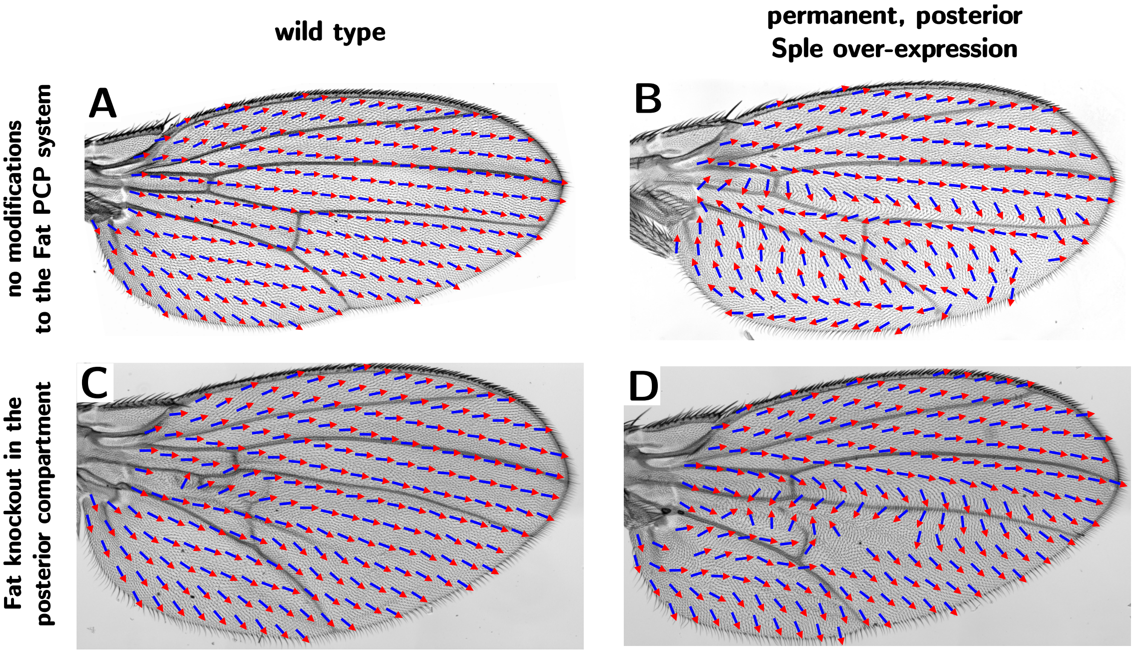
wild type
permanent, posterior Sple over-expression
no modifications to the Fat PCP system
Fat knockout in the posterior compartment
A
B
C
D

Figure 4.4: Over-expression of the Core PCP protein Sple made the fruit fly wing hair pattern dependent on perturbations of the Fat PCP system, whereas the wild type wing hair pattern remained mainly unchanged. Shown are the wing hair patterns for **(A)** wild type (condition 1), **(B)** permanently, posterior over-expression of Sple (condition 7), **(C)** flies with a permanently perturbed Fat PCP system by knockdown of Fat in the posterior compartment, and **(D)** both, permanent Sple over-expression and knockdown of Fat in the posterior compartment.

over-expressing Sple, there was a tendency of Core PCP to be aligned with Fat PCP and this alignment was more pronounced for a stronger intracellular anisotropy of Fat PCP proteins (Fig. 4.3D).

A possible reason for the data shown in Figs. 4.2 and 4.3 is that in wild type tissue, Core PCP is coupled to cell elongation more strongly than to Fat PCP; whereas in tissue over-expressing Sple, Core PCP is coupled more strongly to Fat PCP. To further test this hypothesis, we modified the Fat PCP system by inducing a knockdown of Fat in the posterior compartment (Fig. 4.4). This modification alone did not alter the wild type wing hair pattern much (compare Fig. 4.4A,C). However, in a genetic background of permanent Sple over-expression in the posterior compartment (condition 7), knockdown of Fat significantly affected the wing hair pattern (compare Fig. 4.4B,D). These observations suggest that indeed, Sple over-expression makes the Core PCP system more dependent on the Fat PCP system.

To investigate which sign a coupling between Core PCP and Fat PCP would have in tissue over-expressing Sple, we quantified the vector pattern of Fat PCP in a 32 hAPF wild type wing (Fig. 4.5). The observed pattern was similar to the opposite wing hair

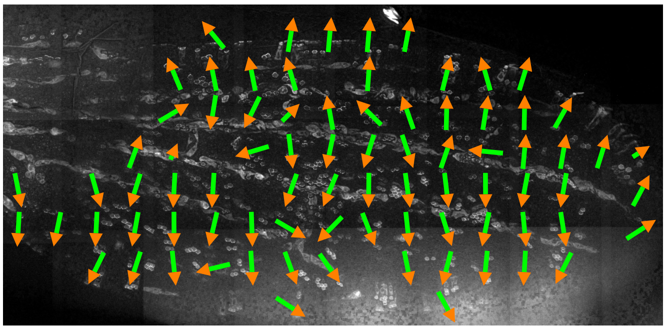

Figure 4.5: Fat PCP pattern in an in vivo wild type wing at 32 hAPF, quantified from a clonal Dachs staining. On the original image, also longitudinal and cross veins are visible because Dachs-containing cells moved inside of these veins. The method used for quantification is explained in Appendix E.2.2.

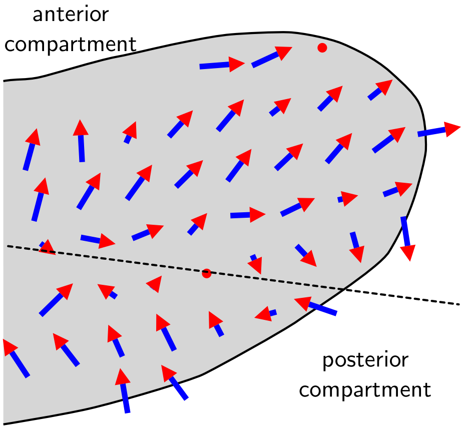

Figure 4.6: Quantified Core PCP pattern at 16 hAPF, in wings that permanently over-expressed Sple in the posterior compartment. The pattern shown was quantified from clones with Stbm staining. The polarity of clones from 5 wings were binned into boxes and averaged. The dashed line indicates the estimated position of the boundary between anterior and posterior compartments. Quantification of clone polarity and alignment of wings are explained in Appendix E.2.1.

pattern of a wing ubiquitously over-expressing Sple (Fig. 4.2B). These observations indicate that Core PCP (pointing towards Fz) and Fat PCP (pointing towards Ds) tend to be antiparallel in tissue over-expressing Sple.

In order to test whether Sple over-expression also influences the Core PCP pattern at earlier developmental times, we quantified the Core PCP pattern at 16 hAPF for the case of permanent, posterior Sple over-expression (Fig. 4.6). In the anterior compartment, Core PCP mainly pointed towards the wing margin. This is consistent with the known early Core PCP pattern in wild type wings (Fig. 1.9A) [54]. However, in the posterior compartment, Core PCP pointed away from the margin, which is the opposite direction as compared to the wild type Core PCP pattern at 16 hAPF. Thus, Sple over-expression significantly affects also the Core PCP patterns at the beginning of the time interval considered.

4.2 Effective hydrodynamic theory for polarity reorientation

In this section, we develop a hydrodynamic theory for Core PCP reorientation in the fruit fly wing. Our theory is motivated on the one hand by an earlier theory for Core PCP reorientation in the fruit fly wing [54, 58] and on the other hand by our experimental findings presented in the preceding section. Although the wing consists of material that is highly out of thermodynamic equilibrium, we describe it as if it was close to equilibrium on large length and time scales. In this sense, our hydrodynamic theory is an effective theory.

We describe Core PCP by a continuous vector field, which we denote by $\boldsymbol{p}$. Similar to earlier work [54, 58], $\boldsymbol{p}$ is coupled to a symmetric, traceless tensor field $\tilde{s}_{ij}$, which reflects an effective tissue shear. Here, in order to also account for possible effects of Sple over-expression on Core PCP, we extended this approach by a coupling to another continuous vector field $\boldsymbol{q}$, which represents Fat PCP. Focusing on the angle dynamics of the polarity field $\boldsymbol{p}$, we assume for simplicity that all three fields are normalized to one: $|\boldsymbol{p}| = |\tilde{s}| = |\boldsymbol{q}| = 1$.[2] In the following, we focus on the relations that are relevant for describing the angle dynamics of the vector field $\boldsymbol{p}$, assuming that the fields $\tilde{s}_{ij}$ and $\boldsymbol{q}$ are known.

As starting point, in Section 4.2.1, we present an expression for an effective free energy for the polarity field $\boldsymbol{p}$. Subsequently, in Section 4.2.2, we develop a generic equation for the angle dynamics of $\boldsymbol{p}$. Finally, in Section 4.2.3, we present analytical expressions for stationary solutions to our theory.

4.2.1 Effective free energy

We start with an expression for an effective free energy for the polarity field $\boldsymbol{p}$, which reads

$$F_{\mathrm{total}} = \int \left[\frac{K}{2}(\partial_i p_j)(\partial_i p_j) + \frac{M}{2} p_i \tilde{Q}_{ij} p_j - Z p_i q_i + \frac{\Lambda_{\|}}{2} p_i p_i \right] \mathrm{d}^2 x + F_{\mathrm{boundary}}. \tag{4.1}$$

Here, the symbol K denotes the elastic coefficient describing the tendency of the polarity field $\boldsymbol{p}$ to align locally. Put differently, the first term corresponds to the Frank free energy for bend and splay deformation, where both elastic moduli are equal to K [134, 149]. Since the free energy is minimal for a homogeneous polarity field, the elasticity K has to be positive.

The second term in Eq. (4.1) describes a coupling between the polarity field $\boldsymbol{p}$ and the cell elongation nematic $\tilde{Q}_{ij}$ (as defined in Chapter 2). The corresponding elastic coupling coefficient is denoted by M. For negative M, the polarity $\boldsymbol{p}$ tends to align parallel to the cell elongation $\tilde{Q}_{ij}$; whereas for positive M, polarity tends to align perpendicular to the cell elongation.

The third term in Eq. (4.1) describes a coupling between the polarity fields $\boldsymbol{p}$ and $\boldsymbol{q}$ with elastic coefficient Z. For negative Z, both polarity fields tend to align antiparallel; whereas for positive Z, both polarity fields tend to point in the same direction.

The forth term ensures the normalization of the vector field $\boldsymbol{p}$, where the coefficient $\Lambda_{\|}$ takes the role of a Lagrange multiplier. We discuss the contributions from the boundary denoted by F_{boundary} in Appendix G.2.

---

[2] The norm of symmetric, traceless tensors is defined in Appendix A.2.2.

4.2.2 Generic dynamics of the polarity field

We describe the time evolution of the polarity field $\boldsymbol{p}$ following a non-equilibrium approach used for polar gels and liquid crystals [63, 134]. In these theories, the dynamics of the polarity field includes a relaxation of the free energy F_{total} and a coupling to material shear. In addition, we explicitly allow for possible couplings to the T1 transitions nematic $\tilde{T}_{ij}$ and to the cell division nematic $\tilde{C}_{ij}$, which are defined in Chapter 2. Taken together, we propose the following polarity dynamics:

$$\frac{\mathrm{D}p_i}{\mathrm{D}t} = -\frac{1}{\gamma_1}\frac{\delta F_{\text{total}}}{\delta p_i} - \nu\tilde{v}_{ij}p_j - \nu_{\mathrm{T1}}\tilde{T}_{ij}p_j - \nu_{\mathrm{CD}}\tilde{C}_{ij}p_j. \tag{4.2}$$

Here, $\mathrm{D}p_i/\mathrm{D}t$ denotes the corotational derivative of the polarity field $\boldsymbol{p}$. It is defined by

$$\frac{\mathrm{D}p_i}{\mathrm{D}t} = \frac{\partial p_i}{\partial t} + \mathrm{v}_j(\partial_j p_i) - \omega\epsilon_{ij}p_j. \tag{4.3}$$

Here, $\mathbf{v}$ denotes the velocity field and $\omega\epsilon_{ij} = (\partial_j \mathrm{v}_i - \partial_i \mathrm{v}_j)/2$, which is consistent with our definitions in Section 2.2.

In Eq. (4.2), the coefficient γ_1 describes dissipative relaxation of the polarity field towards an effective equilibrium. The coefficients ν, ν_{T1}, and ν_{CD} describe reactive couplings to the shear rate $\tilde{v}_{ij}$, to the T1 transition nematic $\tilde{T}_{ij}$, and to the cell division nematic $\tilde{C}_{ij}$, respectively.

Effective nematic coupling

Inserting Eq. (4.1) into Eq. (4.2) yields the following bulk dynamics of the polarity field $\boldsymbol{p}$:

$$\frac{\mathrm{D}p_i}{\mathrm{D}t} = -k\tilde{s}_{ij}p_j + \frac{Z}{\gamma_1}q_i + \frac{1}{\gamma_1}\partial_j\Big(K\partial_j p_i\Big) - \frac{\Lambda_\parallel}{\gamma_1}p_i. \tag{4.4}$$

Here, we introduced the scalar k and the nematic $\tilde{s}_{ij}$ with norm one $|\tilde{s}| = 1$. They are defined such that:

$$k\tilde{s}_{ij} = \frac{M}{\gamma_1}\tilde{Q}_{ij} + \nu\tilde{v}_{ij} + \nu_{\mathrm{T1}}\tilde{T}_{ij} + \nu_{\mathrm{CD}}\tilde{C}_{ij}. \tag{4.5}$$

Thus, $k\tilde{s}_{ij}$ represents a coupling to an effective shear field, where the normalized nematic $\tilde{s}_{ij}$ represents the shear axis and k is a combination of coupling strength and shear rate. This effective shear field encompasses cell elongation, tissue shear, T1 transitions, and cell divisions. Such an effective shear field is motivated by our observation that in the fruit fly wing, all four nematic tensors on the right hand side of Eq. (4.5) are mostly parallel or perpendicular to each other (Section 2.3.2). Therefore, we could not clearly separate their individual contributions to polarity reorientation.

Simplified polarity angle dynamics

Since $\boldsymbol{p}$, $\tilde{s}_{ij}$, and $\boldsymbol{q}$ are normalized quantities, Eq. (4.4) can be rephrased in terms of their respective angles ψ, θ, and ϕ. For a given coordinate system, they are defined by:

$$\boldsymbol{p} = \begin{pmatrix} \cos\psi \\ \sin\psi \end{pmatrix}, \quad \boldsymbol{q} = \begin{pmatrix} \cos\phi \\ \sin\phi \end{pmatrix}, \quad \text{and} \quad \tilde{\boldsymbol{s}} = \begin{pmatrix} \cos(2\theta) & \sin(2\theta) \\ \sin(2\theta) & -\cos(2\theta) \end{pmatrix}. \tag{4.6}$$

Then, Eq. (4.4) can be transformed into the following polarity angle dynamics:

$$\frac{\partial\psi}{\partial t} = k \sin\big(2[\psi - \theta]\big) - \zeta \sin\big(\psi - \phi\big) + \kappa \partial_i \partial_i \psi, \tag{4.7}$$

Here, we call k the *nematic coupling coefficient* and $\zeta = Z/\gamma_1$ the *polar coupling coefficient*. The coefficient $\kappa = K/\gamma_1$ quantifies the tendency of the polarity field $\boldsymbol{p}$ to align locally.[3] Note that here, convection is neglected because the velocity field is mainly perpendicular to gradients in the polarity angle. We also neglect the corotational term, which is discussed in Appendix F.6.1. Furthermore, the elasticity K is assumed to be homogeneous. Corrections emerging from inhomogeneities in K are discussed in Appendix F.6.3.

Invariances

In order to simplify the later discussion of stationary solutions, we shortly discuss some invariances of the polarity angle dynamics, Eq. (4.7). By construction, the angle dynamics shows a continuous rotation-invariance. In addition, it shows three discrete invariances. These are invariances with respect to the following transformations:

$$\phi \mapsto \phi + \pi, \qquad \zeta \mapsto -\zeta; \tag{4.8}$$

$$\phi \mapsto \phi + \pi, \qquad \psi \mapsto \psi + \pi; \tag{4.9}$$

$$\theta \mapsto \theta + \pi/2, \qquad k \mapsto -k. \tag{4.10}$$

Here, each line corresponds to a separate invariance of Eq. (4.7). The first two invariances state that a sign flip of $\boldsymbol{q}$ corresponds to either a sign flip of ζ or a sign flip of $\boldsymbol{p}$. The third invariance states that a rotation of the effective shear axis by $\pi/2$ corresponds to a sign flip of k.

4.2.3 Stationary solutions

Here, we discuss stationary solutions of the polarity angle dynamics Eq. (4.7). In particular, we present analytical expressions for the homogeneous solutions. Furthermore, we analytically solve the one-dimensional case, which assumes homogeneity of ψ in

---

[3] In Appendix D, we derive values for κ by coarse-graining a cellular Core PCP model.

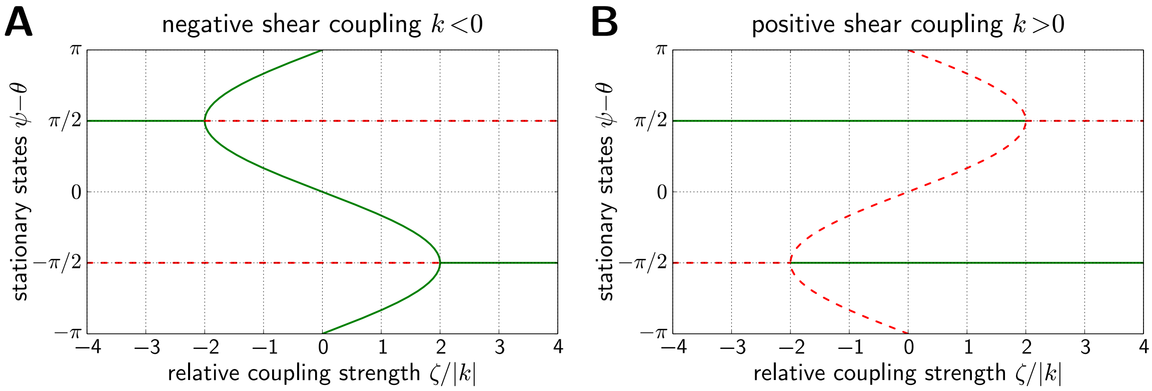

Figure 4.7: Homogeneous stationary solutions of the polarity dynamics Eq. (4.7) and their stability with respect to homogeneous perturbations. For each value of $\zeta/|k|$, the stationary angle ψ is shown with respect to the angle of the nematic coupling θ. Here, the angle of $\boldsymbol{q}$ is given by $\phi - \theta = -\pi/2$. The green solid lines represent linearly stable solutions and the red dashed lines represent linearly unstable solutions. **(A)** Negative nematic coupling coefficient $k < 0$. **(B)** Positive nematic coupling coefficient $k < 0$.

one direction. For both cases we assume time-independent and homogeneous angles ϕ and θ with particular relative orientations of $\phi - \theta = z\pi/2$, where z is an integer. In Section 4.3, we compare the stationary solutions discussed here with experimentally quantified wing hair patterns.

Homogeneous stationary solutions

We look for stationary solutions of the equation

$$\frac{\mathrm{d}\psi}{\mathrm{d}t} = k \sin\big(2[\psi - \theta]\big) - \zeta \sin\big(\psi - \phi\big), \tag{4.11}$$

where $\phi - \theta = z\pi/2$ for integer z. Here, we discuss the case $z = -1$. For other values of z, the stationary states can be constructed using the invariances in Eqs. (4.8)-(4.10) (see also Table F.1 on page 194).

For $z = -1$, i.e. for $\phi - \theta = -\pi/2$, the stationary solutions in terms of $\psi - \theta$ are depicted in Fig. 4.7 (see also Table F.1). Interestingly, for $|\zeta/k| \geq 2$, the polar coupling completely shadows the nematic coupling in the sense that the stationary states and their stability are the same as in the absence of a nematic coupling ($|\zeta/k| \to \infty$). Only for weak polar coupling $|\zeta/k| < 2$, the nematic coupling influences the stationary states and their stability.

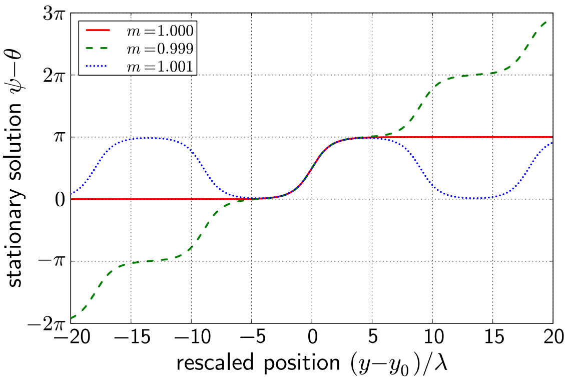

Figure 4.8: One-dimensional stationary solutions of the angle dynamics Eq. (4.7), where polar coupling is neglected ($\zeta = 0$) and the nematic coupling coefficient is negative $k < 0$. The general analytical expression of the stationary solutions are given by Eq. (4.13). Shown are the curves for $\theta = 0$, $n = 1$, and three different values for the parameter m.

Inhomogeneous one-dimensional stationary solutions

One-dimensional stationary solutions of Eq. (4.7) correspond to solutions of the ordinary differential equation

$$\frac{\partial^2 \psi}{\partial y^2} = -\frac{k}{\kappa} \sin\left(2[\psi - \theta]\right) + \frac{\zeta}{\kappa} \sin\left(\psi - \phi\right), \tag{4.12}$$

where homogeneity of ψ in x direction is assumed. The general solution consists of many cases and is systematically presented in Appendix F.1.1. Here, we merely discuss the solutions for the two special cases of nematic coupling only ($\zeta = 0$) and polar coupling only ($k = 0$).

Nematic coupling only For nematic coupling only, i.e. for $\zeta = 0$ and $k \neq 0$, all solutions to Eq. (4.12) can be expressed as

$$\psi(y) = \theta + \frac{n\pi}{2} + \mathrm{am}\left(\frac{y - y_0}{m\lambda}\middle| m\right). \tag{4.13}$$

Here, the integer n is even for $k > 0$ and odd for $k < 0$. The function am denotes the inverse of the incomplete elliptic integral of the first kind [160]. It depends on $(y-y_0)/m\lambda$ and on the so-called modulus m, where y_0 and m are integration constants. The stationary solution contains a characteristic length scale λ, which is defined by

$$\lambda = \left(\frac{\kappa}{2|k|}\right)^{1/2}. \tag{4.14}$$

It compares the relative tendency of the polarity field $\boldsymbol{p}$ to align locally to the strength of nematic coupling. We call λ the characteristic *nematic length scale*. For a strong nematic coupling k, the nematic length scale is small; while for a strong local polarity alignment κ, the length scale is big.

The shape of the general solution in Eq. (4.13) depends on the value of m. In

Fig. 4.8, the stationary solution for $k < 0$ is shown for three different values of m. For $|m| < 1$, the solution is in general quasi-periodic (green dashed line); for $|m| > 1$, the solution is in general periodic (blue dotted line); and for $|m| = 1$, the solution is in general monotonic and asymptotically approaches multiples of π (red solid line). For $|m| \neq 1$, the period is given by multiples of the first complete elliptic integral, which diverges for $|m| \to 1$ [160]. As illustrated by Fig. 4.8, stationary solutions may have plateaus, where $\psi - \theta$ takes values close to multiples of π (for $k < 0$); or multiples of π plus $\pi/2$ (for $k > 0$). Note that these angles correspond to the stable stationary states for the homogeneous case with $\zeta = 0$, respectively (Fig. 4.7).

Polar coupling only Similarly, for polar coupling only, i.e. for $k = 0$ and $\zeta \neq 0$, the general form of the stationary solution is given by

$$\psi(y) = \phi + n\pi + 2\mathrm{am}\left(\frac{y - y_0}{m\mu}\middle| m\right). \tag{4.15}$$

Here, the integer n is even for $\zeta < 0$ and odd for $\zeta > 0$. The scalars y_0 and m are integration constants, which may take any real value. Again, the stationary solution contains a characteristic length scale μ, which is defined by

$$\mu = \left(\frac{\kappa}{|\zeta|}\right)^{1/2}. \tag{4.16}$$

It compares the tendency of the polarity field $\boldsymbol{p}$ to align locally to the strength of polar coupling. We call μ the characteristic *polar length scale*. For a strong polar coupling ζ, the polar length scale is small; while for a strong local polarity alignment κ, it is big. Note that the stationary solution for polar coupling only, Eq. (4.15), shares main features with the stationary solution for the case of nematic coupling only, Eq. (4.13).

General solution The general solution presented in Appendix F.1.1 contains both length scales, λ and μ, as parameters. Also, it depends on the sign of the coefficients of nematic coupling k and polar coupling ζ. In Section 4.3, we compare the stationary solutions presented here to observed wing hair patterns in order to obtain the characteristic length scales λ and μ, and the signs of the coupling coefficients k and ζ.

4.3 Comparison of theory and experiment

Here, we compare the experimentally obtained wing hair patterns to solutions of our hydrodynamic theory for polarity reorientation. To this end, we first define a coordinate system for fruit fly wings, which is based on wing vein positions (Fig. 4.9A). Note that recent work shows that for a given genotype and a given temperature, the posi-

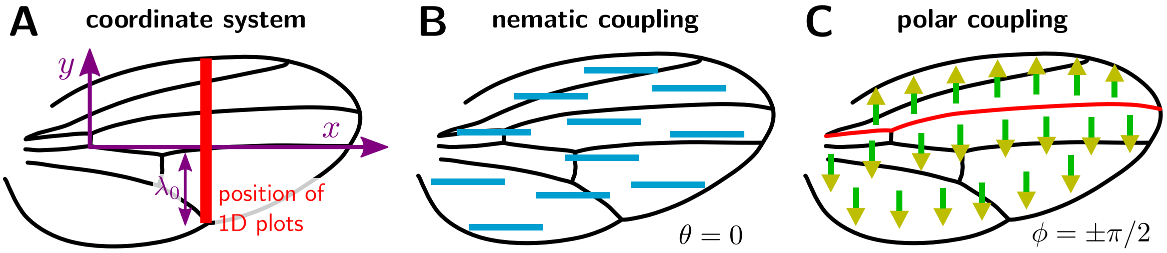

Figure 4.9: Wing coordinate system and assumed couplings of the polarity field ψ. **(A)** In each fruit fly wing, we define a coordinate system with respect to wing veins. The origin is located at the intersection of vein L4 with the ACV (compare Fig. 1.4). The x axis also passes the distal end of L4. The y axis is defined to be perpendicular to the x axis. We define the length unit λ_0 by the distance of the distal end of vein L5 from the x axis. Also indicated is a line (red solid line) along which we later plot the polarity angle ψ. The angles ψ, θ, and ϕ are zero if they point in positive x direction, and they increase in counter-clockwise direction. **(B)** The assumed angle field θ, which reorients ψ via a nematic coupling (compare Eq. (4.7)). **(C)** The assumed angle field ϕ, which reorients ψ via a polar coupling (compare Eq. (4.7)). The field ϕ flips at the vein L3 (red solid line).

tions of fruit fly wing veins vary on the order of a single cell diameter [21]. To account for variations in wing size, we also define a reference length λ_0 from vein positions.

In our hydrodynamic description for the reorientation of the polarity angle ψ, we define all angles with respect to the coordinate system in Fig. 4.9A. To extract key features, we assume that the angle of the effective nematic coupling θ is zero everywhere, which means that it is oriented along the proximo-distal axis (Fig. 4.9B). This is based on the experimentally quantified cell elongation pattern (Fig. 4.2E) and on our quantifications in Section 2.3.2. Also, we use a simplified angle field ϕ for the polar coupling, which is parallel to the y axis everywhere and flips at vein L3 (Fig. 4.9C). This pattern is based on the observed Fat PCP pattern at 32 hAPF (Fig. 4.5).

In our theoretical description, we assume that the values of the dynamic coefficients k, ζ, and κ depend on the genetic conditions, which may vary in space and time. In particular, we are interested in how Sple over-expression affects these dynamic coefficients. For wild type tissue, we denote these coefficients by k_{wt}, ζ_{wt}, and κ_{wt}; and for tissues over-expressing Sple, we denote them by k_{so}, ζ_{so}, and κ_{so}.

In order to obtain values for these coefficients, we first compared experimentally quantified wing hair patterns to one-dimensional stationary solutions of our theory (Section 4.3.1). Afterwards, in Section 4.3.2, we numerically solve the polarity angle dynamics in two dimensions and for a time that corresponds to the pupal stage between 16 hAPF and 32 hAPF. Then, we compare the final polarity patterns from our numerical solutions to the corresponding quantified wing hair patterns.

4.3.1 Fits of wing hair profiles to stationary solutions

As a first step for comparing our theory with experimental data, we fitted quantified wing hair angles to stationary solutions of the polarity angle dynamics. Because we noticed that the observed wing hair patterns varied mainly along the y axis (see Fig. 4.1), we plotted the wing hair angles along the line shown in red in Fig. 4.9A. Consistent with that, we fit these wing hair angle profiles to stationary solutions of our theory, where we assume homogeneity in x direction (see Section 4.2.3). The fits are shown in Fig. 4.10 and discussed in the following. Technical details on the fitting procedure are presented in Appendix F.2.

Characteristic length scales

Our fits allowed us to measure the characteristic nematic and polar length scales λ and μ, which appear as parameters in the stationary solutions. With respect to the observed wing hair patterns, these length scales represent characteristic distances over which the wing hair direction varies smoothly. In terms of our hydrodynamic theory, these length scales reflect quotients of the dynamic coefficients k, ζ, and κ (as stated by Eqs. (4.14) and (4.16)). Since the dynamic coefficients depend on the genetic conditions, the characteristic length scales do so as well. We denote these length scales in wild type-like tissue by λ_{wt} and μ_{wt}, and in tissue over-expressing Sple by λ_{so} and μ_{so}.

Note that we also studied genetic conditions with time-dependent Sple over-expression. In order to fit the wing hair profile of such genetic conditions, we chose those length scale parameters for the fit (either λ_{wt} and μ_{wt} or λ_{so} and μ_{so}) that reflected the spatial distribution of Sple over-expression at 32 hAPF. This corresponds to the time when the wing hairs emerge. Which set of coefficients and length scales was used in each compartment of a given genetic condition is listed in Table 4.2.

Wild type-like conditions

First, we discuss the wild type length scales λ_{wt} and μ_{wt} as well as the signs of the coefficients k_{wt} and ζ_{wt}. Observed wild type wing hair patterns were largely homogeneous (Fig. 4.1A) with a wing hair angle corresponding to $\psi \approx 0$. We compare this to homogeneous stationary states of our hydrodynamic theory. In the region posterior to vein L3, we have $\phi - \theta = -\pi/2$ (Fig. 4.9B,C). We find that in order for a homogeneous stationary state close to $\psi = 0$ to be stable with respect to homogeneous perturbations, the polar coupling has to be weak ($|\zeta_{\mathrm{wt}}/k_{\mathrm{wt}}| \ll 1$) and the nematic coupling coefficient k_{wt} has to be negative (Fig. 4.7).[4] This is consistent with our experimental observation that a perturbation of the Fat PCP system did not alter the wild type wing hair pattern much (Fig. 4.4A,C). Thus, we chose $k_{\mathrm{wt}} < 0$ and, for simplicity,

---

[4] A similar argument applies for the region anterior to vein L3.

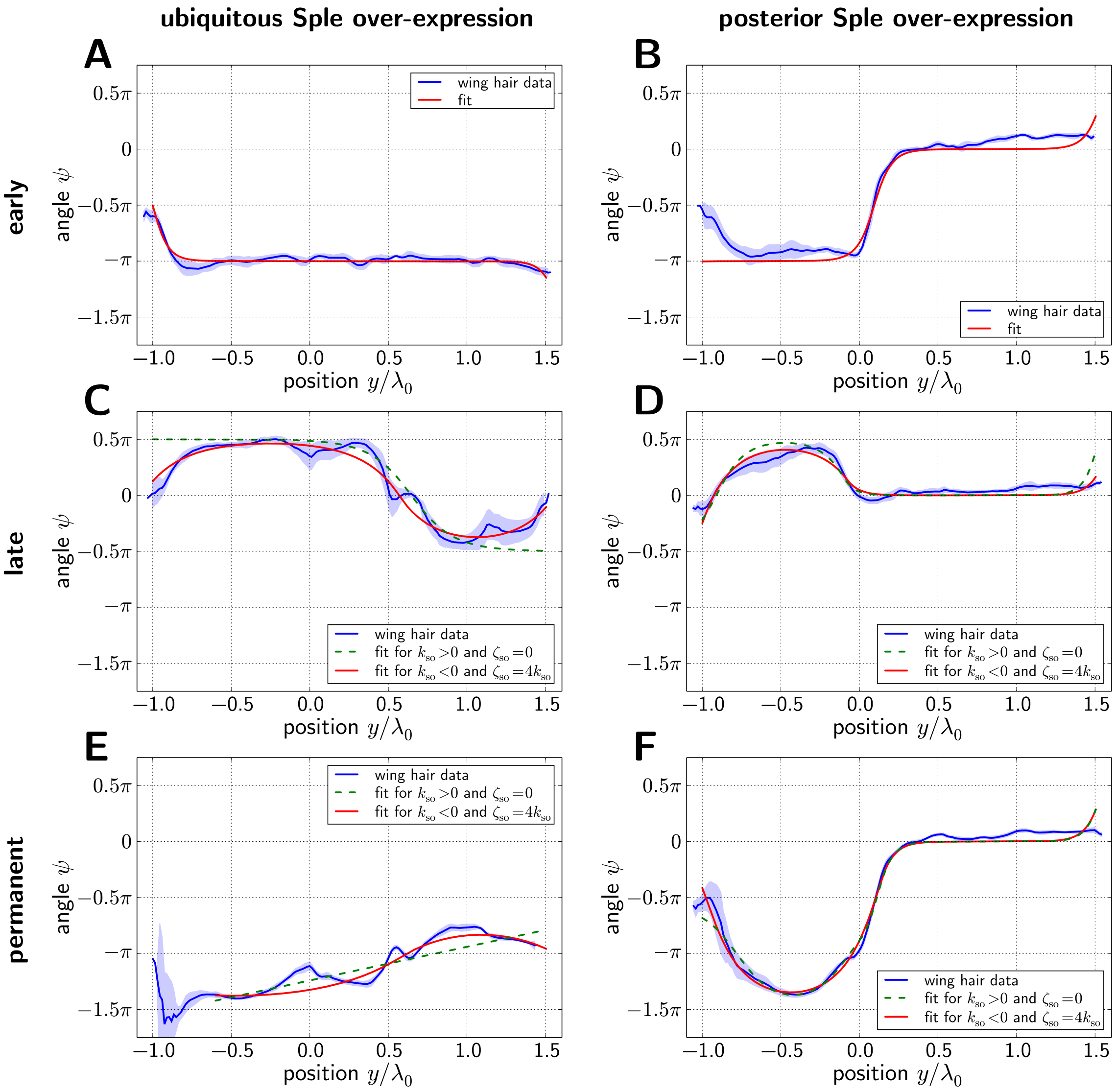

Figure 4.10: Wing hair angles (blue solid lines) plotted along the line shown in red in Fig. 4.9A; and fits (red solid lines and green dashed lines) to stationary solutions of the ψ dynamics Eq. (4.7). In panels C-F, two different fits are shown. One fit assumes nematic coupling only for Sple over-expression ($k_{\mathrm{so}} > 0$ and $\zeta_{\mathrm{so}} = 0$; green dashed lines) and the other fit assumes a dominating polar coupling for Sple over-expression ($k_{\mathrm{so}} < 0$ and $\zeta_{\mathrm{so}} = 4k_{\mathrm{so}}$; red solid lines). For each plot, the data of at least eight wings were taken into account. The blue hatched region indicates the standard deviation of quantified wing hair angles. The y coordinate is given in terms of λ_0, which is defined in Fig. 4.9A. Details on the wing hair angle plots and on the fitting are presented in Appendices E.1.2 and F.2, respectively.

Table 4.1: Characteristic length scales obtained from the fits shown in Fig. 4.10. Listed are all conditions of ubiquitous ("ubi.") and of posterior ("post.") Sple over-expression. The length scales are given for two cases depending on the Sple over-expression parameter values. For the case of nematic coupling only ($k_{\mathrm{so}} > 0$, $\zeta_{\mathrm{so}} = 0$; green dashed lines in Fig. 4.10) and for the case of dominating polar coupling ($k_{\mathrm{so}} > 0$, $\zeta_{\mathrm{so}} = 4k_{\mathrm{so}}$; red solid lines in Fig. 4.10). For early over-expression conditions, both fits are identical, since the stationary solutions do not depend on ζ_{so} and k_{so}. All length scales are given in terms of λ_0, which is defined in Fig. 4.9A.

Condition	**Fit**	**nematic coupling only** $k_{\mathrm{so}} > 0$, $\zeta_{\mathrm{so}} = 0$		**dominating polar coupling** $k_{\mathrm{so}} < 0$, $\zeta_{\mathrm{so}} = 4k_{\mathrm{so}}$	
		$\lambda_{\mathrm{wt}}/\lambda_0$	$\lambda_{\mathrm{so}}/\lambda_0$	$\lambda_{\mathrm{wt}}/\lambda_0$	$\mu_{\mathrm{so}}/\lambda_0$
early ubi. (2)	Fig. 4.10A	0.061	–	0.061	–
early post. (5)	Fig. 4.10B	0.071	–	0.071	–
late ubi. (3)	Fig. 4.10C	–	0.170	–	0.179
permanent ubi. (4)	Fig. 4.10E	–	177.4	–	0.388
late post. (6)	Fig. 4.10D	0.061	0.118	0.072	0.141
permanent post. (7)	Fig. 4.10F	0.065	0.152	0.070	0.158

$\zeta_{\mathrm{wt}} = 0$. Thus, we assume no polar coupling in wild type tissue, corresponding to $\mu_{\mathrm{wt}} \to \infty$.

In order to determine the nematic length scale under wild type conditions λ_{wt}, we fitted the wing hair angles for both early Sple over-expression conditions (conditions 2 and 5) to the stationary solution of the ψ dynamics (Fig. 4.10A,B; fit function in Eq. (4.13)). For both conditions, the wing hair patterns were largely well described by the fit functions. Also, we found similar values for the nematic length scale $\lambda_{\mathrm{wt}} \approx 0.07\,\lambda_0$ (Table 4.1).

Sple over-expression conditions

Now, we discuss how Sple over-expression changes the length scale parameters and the signs of k and ζ. We found that different values for the length scales λ_{so} and μ_{so} and different signs of ζ_{so} and k_{so} were consistent with the quantified wing hair data (for details, see Appendix F.2.3). Here, we focus on two example cases:

1. We found that all wing hair profiles could be fitted by considering nematic coupling only ($\zeta_{\mathrm{so}} = 0$), where the nematic coupling coefficient for Sple over-expression k_{so} was positive (Fig. 4.10C-F, green dashed lines). In this case, Sple over-expression would change the sign of the nematic coupling coefficient k. The parameter values for the nematic length scale λ_{so} that resulted from these fits are listed in Table 4.1.

2. All wing hair profiles could also be fitted assuming a dominating polar coupling for Sple over-expression with negative coupling coefficients $\zeta_{\mathrm{so}} < 0$ and $k_{\mathrm{so}} < 0$. For the fits shown in Fig. 4.10C-F (red solid lines), we set $\zeta_{\mathrm{so}} = 4k_{\mathrm{so}}$. With Eqs. (4.14) and (4.16) follows that $\lambda_{\mathrm{so}} = \sqrt{2}\mu_{\mathrm{so}}$, which we used as a restriction for these fits. The resulting parameter values for the polar length scale μ_{so} are listed in Table 4.1.

For each of these two cases, most wing hair patterns were largely well described by the fit curves and all length scales were mainly similar among different genetic conditions (Table 4.1).

The main exception to this was the case of permanent, ubiquitous over-expression (condition 4). In this case, we first had to restrict the fit to positions $y > -0.6\lambda_0$, because close to the distal end of vein L5, the condition of homogeneity in x direction was not fulfilled in the quantified wing hair patterns.[5] Moreover, the fit curves (Fig. 4.10E) captured main features of the quantified wing hair angles only badly, in particular around the position $y = 0$. These deviations could be due to a possible additional effect of wing veins on Core PCP reorientation (Appendix F.6.2). Because of all this, we ignore the length scales from the corresponding fits in the following.

Summary

To summarize, our comparison of wing hair patterns to stationary states of the polarity angle dynamics suggested that in wild type tissue, Core PCP is mainly reoriented by a nematic coupling with $k_{\mathrm{wt}} < 0$ and a characteristic length scale of $\lambda_{\mathrm{wt}}/\lambda_0 = 0.06\ldots0.07$. For tissue over-expressing Sple, several parameter values were consistent with our observations. One possibility is that, Sple over-expression induces a dominating nematic coupling with a positive coefficient ($k_{\mathrm{wt}} > 0$ and for instance $\zeta_{\mathrm{so}} = 0$). Then, our fits yielded a nematic length scale of $\lambda_{\mathrm{so}}/\lambda_0 = 0.12\ldots0.17$. Otherwise, if Sple over-expression does not change the sign of the nematic coupling, our fits suggest that polar coupling dominates with $\zeta_{\mathrm{so}} < 0$. Then, we found a polar length scale of $\mu_{\mathrm{so}}/\lambda_0 = 0.14\ldots0.18$ (for $\zeta_{\mathrm{so}} = 4k_{\mathrm{so}}$).

4.3.2 Numerical solution of the polarity reorientation dynamics

In this section, we compare quantified wing hair patterns to two-dimensional solutions of our hydrodynamic theory. To this end, we numerically solved the dynamic equation Eq. (4.7) for the polarity angle ψ on a domain that was defined by a wild type wing blade at 32 hAPF (for details, see Appendix F.3). We focused on a time interval that corresponds to the developmental times between 16 hAPF and 32 hAPF. Note that the end of this time interval corresponds to the start of Core PCP-controlled wing

---

[5] Close to the end of vein L5, the quantified wing hair direction fields showed a topological point defect for this genetic condition.

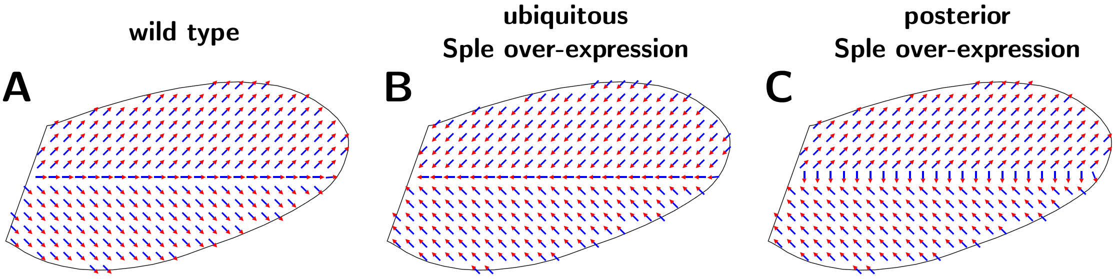

Figure 4.11: Initial conditions used for the numerical solution of Eq. (4.7) for three different genetic conditions. Shown are coarse-grained versions of the initial ψ field used. The precise functional form of all three patterns is given in Appendix F.3.1.

hair outgrowth. Therefore, we compare the final states of our numerical solutions to quantified wing hair patterns. However before that, we discuss initial conditions and determine coefficients that appear in the polarity angle dynamics. The boundary conditions are discussed separately (Appendix G, Eq. (G.10)).

Initial conditions

As initial angle field ψ for our numerical solutions, we used the patterns depicted in Fig. 4.11. They are based on quantified Core PCP patterns at 16 hAPF. Here, we shortly discuss these patterns (for details, see Appendix F.3.1).

The wild type Core PCP pattern at 16 hAPF points towards the wing margin everywhere (Fig. 1.9A) [54]. Therefore, we chose a simplified initial condition with $\psi_A^{\mathrm{IC}} = \pi/4$ in the anterior compartment and $\psi_P^{\mathrm{IC}} = -\pi/4$ in the posterior compartment (Fig. 4.11A). In between both compartments, the polarity angle bends over.

For permanent, posterior over-expression of Sple, we used the initial condition shown in Fig. 4.11C. This pattern is based on the observed Core PCP pattern at 16 hAPF (Fig. 4.6). In the anterior compartment, this pattern corresponded to the wild type Core PCP pattern. However, in the posterior compartment, Core PCP was mainly flipped as compared to the wild type pattern. Therefore, we chose $\psi_A^{\mathrm{IC}} = \pi/4$ and $\psi_P^{\mathrm{IC}} = -5\pi/4$ for this case. Consistent with that, for ubiquitous Sple over-expression, we also flipped the initial polarity in the anterior compartment to $\psi_A^{\mathrm{IC}} = -3\pi/4$ (Fig. 4.11B).

For all numerical solutions presented here, we used one of the patterns in Fig. 4.11 as initial state. More precisely, for a given genetic condition (1-7), we chose the initial state that reflects the corresponding space-dependent Sple over-expression at early times (Table 4.2).

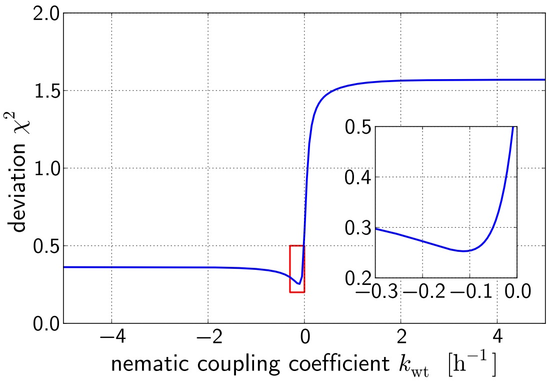

Figure 4.12: Deviation χ^2 between numerical solutions to Eq. (4.7) and quantified time-dependent Core PCP data in wild type wings. The deviation χ^2 is defined in Eq. (4.17) and is computed for 200 different values of k_{wt}. The inset shows a magnification of the red box. For the inset, the deviation χ^2 is computed for 200 different values of k_{wt}.

Determination of the nematic coupling coefficient in wild type tissue

In Section 4.3.1, we set $\zeta_{\mathrm{wt}} = 0$ and we determined the length scale λ_{wt}. Here, we show how we determined the nematic coupling coefficient k_{wt}. This is the missing coefficient necessary to describe polarity reorientation in wild type tissue.

In order to determine k_{wt}, we observed the reorientation of the Core PCP pattern in a developing wild type wing. Therefore, for the time interval between 16 hAPF and 32 hAPF, we quantified the nematic Core PCP pattern in the whole wing blade once per hour. The so-obtained Core PCP patterns were fitted to numerical solutions of Eq. (4.7). For the numerical solutions, we varied k_{wt} and assumed $\zeta_{\mathrm{wt}} = 0$ and $\lambda_{\mathrm{wt}} = 0.07\,\lambda_0$, where for a given value of k_{wt}, we computed κ_{wt} according to Eq. (4.14). The initial condition was given by the quantified nematic Core PCP pattern at 16 hAPF, where the vector direction of the polarity was fixed by hand. In order to quantify the deviation from the experimental data, we define

$$\chi^2 = \frac{1}{N_t N_i} \sum_{t,i} \Big[1 - \cos\big(2[\psi^i(t) - \psi^i_{\mathrm{exp}}(t)] \big) \Big], \tag{4.17}$$

where the sum runs over all $N_t = 16$ time points between 17 hAPF and 32 hAPF and all N_i of boxes used for the numerical solution. The angles $\psi^i(t)$ and $\psi^i_{\mathrm{exp}}(t)$ denote the polarity angles of the numerical solution and of the quantified nematic pattern, respectively, in box i and at time t. χ^2 varies between zero and two. For $\chi^2 = 0$, theoretical and experimental polarity are always parallel to each other; whereas for $\chi^2 = 2$ theoretical and experimental polarity are always perpendicular to each other. Varying k_{wt}, we found that χ^2 was minimal for approximately $k_{\mathrm{wt}} = -0.1\,\mathrm{h}^{-1}$ (Fig. 4.12).

In Appendices F.6.1 and F.6.1, we use this method to study the influence of additional assumptions on the polarity angle dynamics.

Table 4.2: Initial conditions and dynamic coefficients (either k_{wt}, ζ_{wt}, and κ_{wt}; or k_{so}, ζ_{so}, and κ_{so}) used for the numerical solution of Eq. (4.7). Listed are the wild type condition and all conditions of ubiquitous ("ubi.") and posterior ("post.") Sple over-expression. The possible initial conditions are "wild type" (Fig. 4.11A), "ubi. over-expression" (Fig. 4.11B), and "post. over-expression" (Fig. 4.11C). The dynamic parameters are listed separately for the region corresponding to the posterior compartment ($y < 0$) and for the region corresponding to the anterior compartment ($y > 0$).

Condition	**Initial condition**	**posterior region**	**anterior region**
wild type (1)	wild type	wild type	wild type
early ubi. (2)	ubi. over-expression	wild type	wild type
late ubi. (3)	wild type	over-expression	over-expression
permanent ubi. (4)	ubi. over-expression	over-expression	over-expression
early post. (5)	post. over-expression	wild type	wild type
late post. (6)	wild type	over-expression	wild type
permanent post. (7)	post. over-expression	over-expression	wild type

Comparison to quantified wing hair patterns

Here, we show comparisons of final states of our numerical solutions to the observed wing hair patterns. For the numerical solution corresponding a given genetic condition, we chose the coefficients k, ζ, and κ according to the space- and time-dependent pattern of Sple over-expression (Table 4.2).

Wild type-like conditions First, we discuss the genetic conditions that can be described by wild type coefficients only. These comprise the wild type case (condition 1) and the early over-expression cases (conditions 2 and 5). We used the parameter values $k_{\mathrm{wt}} = -0.1\,\mathrm{h}^{-1}$, $\zeta_{\mathrm{wt}} = 0$, and $\lambda_{\mathrm{wt}} = 0.07\,\lambda_0$, where κ_{wt} is computed using Eq. (4.14). The comparison of the numerical solutions with the observed wing hair patterns is shown in Fig. 4.13. We found that in all three cases, the numerical solutions largely matched the observed wing hair patterns.

However, we found minor deviations in both cases of early over-expression. In distal regions in the quantified wing hair patterns for the early, posterior over-expression case (Fig. 4.13G), polarity bended over larger length scales than it did in the corresponding numerical solution. This could be due to effective inhomogeneities in k or κ.

In the quantified wing hair patterns for the early, ubiquitous over-expression case (Fig. 4.13D), there was a topological defect distally, whereas in the corresponding numerical solution, this defect was effectively shifted onto the margin. Furthermore, proximally in these wings, polarity was not everywhere oriented along the proximo-distal axis. This could be due to an incomplete decay of Sple molecules in this region,

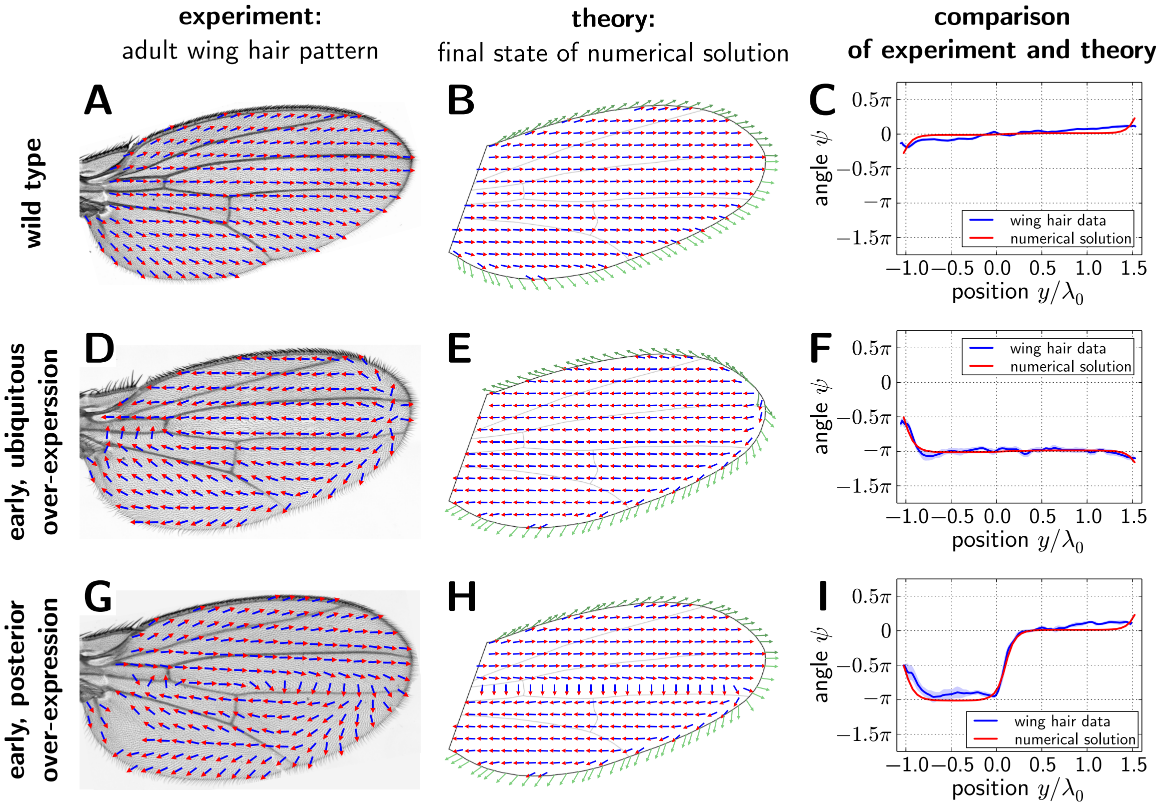

Figure 4.13: Comparison of **(A,D,G)** observed wing hair patterns to **(B,E,H)** final states of the numerical solution of Eq. (4.7). Shown are those conditions that could be completely described by wild type coefficients in our theory (see also Table 4.2). The parameter values used are listed in Table 4.3. **(C,F,I)** For a more quantitative comparison, we plot quantified wing hair angles (blue solid line) and final polarity angles ψ of our numerical solutions (red solid line) along the line shown in red in Fig. 4.9A. For the wing hair angles, we used the data of at least eight wings for each genetic condition. The blue hatched regions indicate the standard deviation of the wing hair angles as defined in Appendix E.1.2.

which would then still have an influence on Core PCP reorientation.

Moreover, in both cases of early over-expression (Fig. 4.13D,G), there was very proximally and posteriorly a region where wing hair polarity pointed distally and posteriorly and was thus different from the hair polarity observed more distally. We speculate that this could be due to some additional influence by hinge tissue, which is not taken into account in our theoretical description.

Sple over-expression conditions Now, we discuss the conditions where during the time interval considered, Sple over-expression occurs. Using numerical solutions, we found that many combinations for the values of k_{so} and ζ_{so} reproduced the observed wing hair patterns. However, we asked for the simplest scenario and considered two cases that were similar to those discussed for the fits of wing hair angles (see preceding section). The first case considers nematic coupling only ($\zeta_{\mathrm{so}} = 0$), where Sple over-expression flips the sign of the nematic coupling coefficient to $k_{\mathrm{so}} > 0$. In contrast to that, the second case assumes no influence of Sple over-expression on the nematic coupling coefficient, such that $k_{\mathrm{so}} = k_{\mathrm{wt}}$. Instead, Sple over-expression is assumed to induce a dominant polar coupling with $\zeta_{\mathrm{so}} < 0$.

First, we discuss the case of nematic coupling only ($\zeta_{\mathrm{so}} = 0$). Consistent with the length scales found from the fits (Table 4.1), we chose $\lambda_{\mathrm{so}} = 0.15\,\lambda_0$. Furthermore, we chose the particular value $k_{\mathrm{so}} = 0.1\,\mathrm{h}^{-1}$ and compared the results of the numerical solutions to the wing hair patterns (Fig. 4.14). We found that in particular in the cases of late over-expression (conditions 3 and 5; Fig. 4.14A-C,G-I), the numerical solutions clearly disagreed with the observed wing hair patterns. This was also true for other values of k_{so}. Therefore, a nematic coupling alone could not explain the experimental data.

For the case where Sple over-expression induces a dominant polar coupling without affecting the nematic coupling, many values of $\zeta_{\mathrm{so}} < 0$ largely reproduced the observed wing hair patterns. As an example, we choose $\zeta_{\mathrm{so}} = -0.4\,\mathrm{h}^{-1}$, here. From Eqs. (4.14) and (4.16) follows that $\lambda_{\mathrm{so}}/\mu_{\mathrm{so}} = \sqrt{2}$. For this ratio, the fits dicussed above yielded an average polar length scale of $\mu_{\mathrm{so}} = 0.16\,\lambda_0$. Table 4.3B lists the resulting parameter values and Fig. 4.15 compares the numerical solutions to the observed wing hair patterns. For all four genetic conditions, our theory could largely reproduce the observed wing hair patterns.

We found minor deviations for the case of permanent, ubiquitous over-expression, where very distally, the final state of the numerical solution pointed posteriorly while the wing hair directions were oriented anteriorly, there (Fig. 4.15D,E). This could be due to the initial condition, which could not be determined via quantification but by analogy to other quantified patterns (see above). Also, close to vein L4 ($y \approx 0$), the wing hair pattern pointed more proximally than the final state of the numerical solution did (Fig. 4.15F). This could be due to an additional effect of wing veins, which we did not take into account in our description (see also Appendix F.6.2).

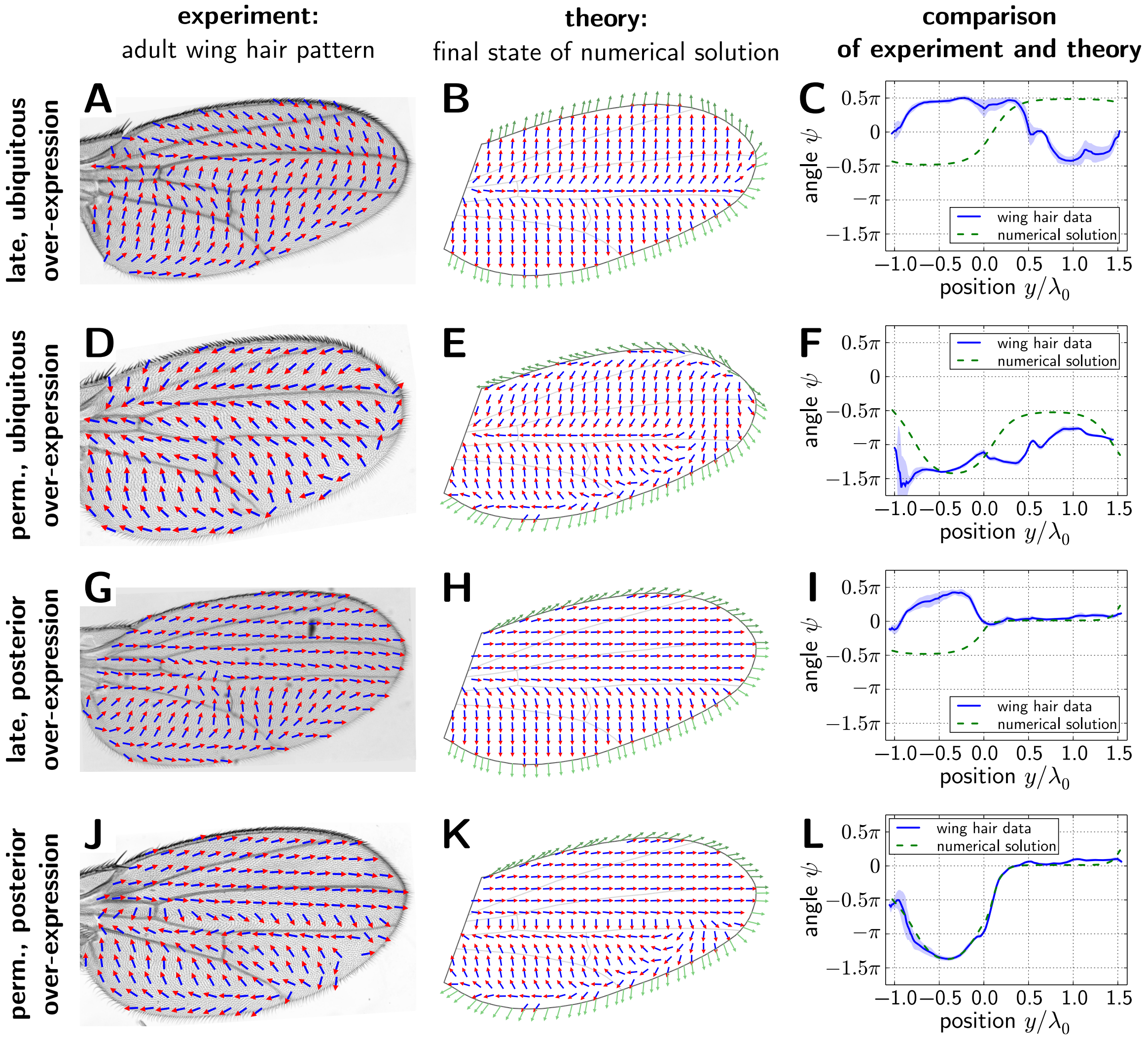

Figure 4.14: Comparison of **(A,D,G,J)** observed wing hair patterns to **(B,E,H,K)** final states of the numerical solution of Eq. (4.7) assuming a nematic coupling only for Sple over-expression ($\zeta_{\text{so}} = 0$). The parameter values used are listed in Table 4.3A. **(C,F,I,L)** For a more quantitative comparison, we plot quantified wing hair angles (blue solid line) and final polarity angles ψ of our numerical solution (green dashed line) along the line shown in red in Fig. 4.9A. For the wing hair angles, we used the data of at least eight wings for each genetic condition. The blue hatched regions indicate the standard deviation of the wing hair angles as defined in Appendix E.1.2.

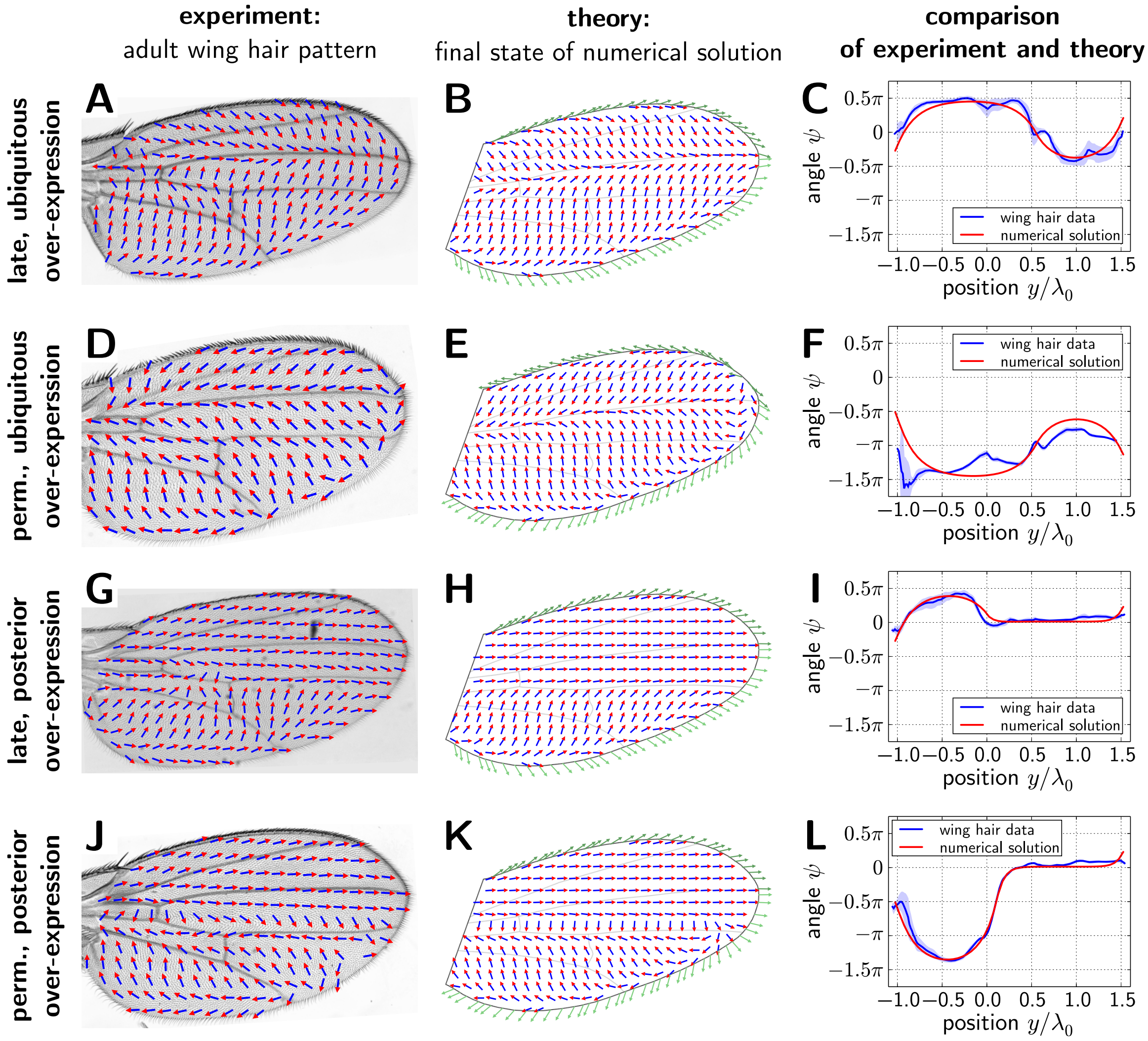

Figure 4.15: Comparison of **(A,D,G,J)** observed wing hair patterns to **(B,E,H,K)** final states of the numerical solution of Eq. (4.7) assuming a dominating polar coupling for Sple over-expression with $\zeta_{\mathrm{so}} < 0$. The parameter values used are listed in Table 4.3B. **(C,F,I,L)** For a more quantitative comparison, we plot quantified wing hair angles (blue solid line) and final polarity angles ψ of our numerical solution (red solid line) along the line shown in red in Fig. 4.9A. For the wing hair angles, we used the data of at least eight wings for each genetic condition. The blue hatched regions indicate the standard deviation of the wing hair angles as defined in Appendix E.1.2.

Table 4.3: Parameter values for the dynamic coefficients used for the numerical solution of Eq. (4.7). The length scales are given for the case of nematic coupling only (Fig. 4.14) and for the case of a dominating polar coupling in Sple over-expressing tissue (Fig. 4.15). For wild type and early over-expression conditions (Fig. 4.13), both cases are identical. All lengths are given in terms of λ_0, which is defined in Fig. 4.9A.

(A) nematic coupling only, Sple over-expression flips the sign of k					
k_{wt}	ζ_{wt}	κ_{wt}	k_{so}	ζ_{so}	κ_{so}
$-0.1\,\mathrm{h}^{-1}$	0	$0.98 \times 10^{-3}\,\lambda_0^2\,\mathrm{h}^{-1}$	$0.1\,\mathrm{h}^{-1}$	0	$4.5 \times 10^{-3}\,\lambda_0^2\,\mathrm{h}^{-1}$

(B) dominating polar coupling in Sple over-expressing tissue					
k_{wt}	ζ_{wt}	κ_{wt}	k_{so}	ζ_{so}	κ_{so}
$-0.1\,\mathrm{h}^{-1}$	0	$0.98 \times 10^{-3}\,\lambda_0^2\,\mathrm{h}^{-1}$	$-0.1\,\mathrm{h}^{-1}$	$-0.4\,\mathrm{h}^{-1}$	$10.24 \times 10^{-3}\,\lambda_0^2\,\mathrm{h}^{-1}$

Some topological defects in the observed wing hair patterns could not be captured by our numerical solutions. For late, posterior over-expression, there was a defect pair in the middle of the wing (Fig. 4.15G), whereas in the cases of permanent, posterior and permanent, ubiquitous over-expression (Fig. 4.15D,J), there were defects distally between veins L5 and L4. Such defects could be created by inhomogeneities in the polarity dynamics, which we do not assume here.

Note that for these numerical solutions, the value of κ_{so} was ten-fold increased as compared to the wild type value κ_{wt}. However, an increase of κ due to Sple over-expression is consistent with our observation of a significantly increased intensity of the Core PCP protein Strabismus at cell membranes in tissue over-expressing Sple [159]. Since Strabismus is a trans-membrane protein, this could indeed indicate an increased effective tendency of Core PCP to align locally.

4.4 Discussion

In this chapter, we developed an effective hydrodynamic theory that describes the reorientation of Core PCP in the developing fruit fly wing. Since the Core PCP system is known to control the direction of wing hair outgrowth, we tested our theory by comparison to observed wing hair patterns of adult flies. To this end, we newly developed an algorithm to quantify the pattern of local wing hair direction in fly wing images. We showed that our theory could not only reproduce the quantified wing hair patterns of wild type flies. Moreover, it was for the first time possible to theoretically reproduce the wing hair patterns of genetically modified flies.

We showed that in wild type tissue, Core PCP reorientation could be accounted for by a coupling to an effective shear field. This effective shear field encompasses possible couplings to the actual tissue shear, cell elongation, T1 transitions, and cell divisions.

Here, we used a simplified effective shear field that is homogeneously oriented along the long axis of the wing. We showed that a coupling strength of $k = -0.1\,\mathrm{h}^{-1}$ described best the observed reorientation of Core PCP in a wild type wing. Although we could not differentiate between the individual effects possibly contributing to the effective shear field, hints indicated that cell elongation could play a dominant role (Appendix F.6.1). We also compared our description to earlier work, where Core PCP was coupled to a measured shear field with a coupling coefficient of $\nu = -3$ (Appendix F.6.1) [54, 58].

In our hydrodynamic description, we described the tendency of Core PCP to align locally in wild type tissue by the parameter κ_{wt}. We obtained a value for this parameter by comparing wing hair patterns to our hydrodynamic theory. As an independent check, we obtained that the order of magnitude of κ_{wt} is consistent with the turnover time scale of sub-cellular Core PCP clusters, which was measured elsewhere (Appendix F.5) [36, 37, 54].

The genetic modification considered here was the over-expression of the Core PCP protein Sple, where we varied the location and time interval of over-expression. We discussed possible effects of Sple over-expression on the dynamics of Core PCP reorientation. We found that in contrast to wild type tissue, in tissue over-expressing Sple, a coupling to the effective shear field alone could not account for the observed wing hair patterns. However, all observations were consistent with the hypothesis that Sple over-expression enhances a coupling of Core PCP to the Fat PCP system. This hypothesis is also supported by the experimental finding that Sple over-expression made wing hair patterns more dependent on perturbations of the Fat PCP system.

In tissue over-expressing Sple, a coupling strength of Core PCP to Fat PCP of $\zeta_{\mathrm{so}} = -0.4\,\mathrm{h}^{-1}$ was consistent with all oberved wing hair patterns. As an independent check, in Appendix F.4, we obtain a value of $\zeta_{\mathrm{late}} = -0.2\,\mathrm{h}^{-1}$ in wild type tissue that lacks the Core PCP protein Pk. This is consistent with an assumed antagonistic relationship between the Core PCP proteins Pk and Sple [40, 159]. Put differently, over-expression of Sple couples Core PCP to Fat PCP in a similar manner as the lack of Pk does.

In order to allow for the numerical solution of our hydrodynamic theory, we formulated boundary conditions based on a physical theory (Appendix G). This physical theory describes a coupling of Core PCP at the wing margin to the directions of bristles growing out of the margin. Furthermore, it describes the preferred directions of the margin bristles by an effective potential. As a result, we did not only obtain boundary conditions for our hydrodynamic theory describing Core PCP. We also could largely reproduce observed directions of wing margin bristles (Appendix G.4).

Chapter 5

Conclusions and outlook

With this work, we contributed to the theoretical understanding of biological tissues. In particular, we focused on epithelial tissues, which can be represented as two-dimensional cellular networks. We applied our theoretical concepts to experiments on the developing wing of the fruit fly, *Drosophila melanogaster*.

Throughout this thesis, we focused on different aspects of the following general question: How do cells organize into two-dimensional tissues? In Chapter 2, we discuss how the deformation of a cellular network is reflected on the cellular level. In Chapter 3, we studied the rheological behavior of two-dimensional cellular networks using vertex model simulations. In Chapter 4, we developed a hydrodynamic description for polarity reorientation and applied it to the fruit fly wing. In the following, we describe the reults and the further implications of each part in more detail.

The large-scale deformation of a cellular network is reflected by cellular events

In Chapter 2, we developed a theoretical framework that decomposes large-scale deformations of cellular networks into cellular contributions. These cellular contributions comprise cell shape changes and topological transitions. We used rigorous geometric arguments to show that our decomposition is exact for smooth deformations.

We separately discussed isotropic and anisotropic parts of the deformation, corresponding to the trace and to the traceless, symmetric part of the displacement gradient, respectively. The isotropic part describes the relative area change of the cellular network. It is straight-forward to show that it can be decomposed into a relative change of the average cell area, the average division rate, and the negative average cell extrusion rate.

However, the major novelty of Chapter 2 is the exact decomposition of the anisotropic part of large-scale deformation, which corresponds to large-scale shear. Other decompositions of large-scale shear were proposed before, but they needed approximations [85, 150–153] or they were very coarse [128, 154, 161]. In Chapter 2, we showed that large-scale shear of a cellular network can be exactly decomposed into the change of cell shape anisotropy and into contributions by the different kinds of topological transitions. Moreover, our rigorous geometric arguments revealed that subtle correlation effects do additionally contribute to large-scale shear. These effects are created by inhomogeneous deformations of the network combined with an inhomogeneous distribution of cell elongation. Such correlation effects have been overseen by previous attempts to study deformations of cellular networks [85, 128, 150–154, 161].

As a key idea, our theoretical framework is based on a tiling of the cellular network into triangles. Such a triangulation allows for the appropriate description of inhomogeneous deformations within the cellular network, where each triangle is characterized by a single deformation tensor. In this sense, the triangles are the smallest unit of our discrete description. As a result of the triangulation, cell shape changes are associated to triangle shape changes, and topological transitions are associated with the disappearance and appearance of triangles.

We applied our theoretical framework to deformations observed in the fruit fly wing during the pupal stage. Our analysis quantitatively confirmed earlier observations, where two phases were identified [54]. During the first phase, cells in the wing elongated along the axis of the wing, and during the second phase, this elongation was partially relieved by oriented T1 transitions. However, in addition to the earlier work, our quantitative analysis revealed that during the first phase, T1 transitions were oriented perpendicular to the cell elongation. This inspires the discussion about the mechanical properties of the wing epithelium. In particular, the oriented T1 transitions during the first phase suggest the existence of active anisotropic stresses.

Clearly, the application of our theoretical framework is not only restricted to the fruit fly wing. It can as well be applied to any other piece of biological tissue – as long as it is approximately planar. During the recent years, dissection and microscopy techniques for biological tissues have been considerably improved. This allows experimentalists to image, segment, and track an increasing number of cells in vivo or in vitro [51, 54, 154, 161]. This goes along with a growing need to transform this huge amount of data into a true understanding of how the tissue behavior results from cellular processes. In this context, our theoretical framework answers the question of how tissue deformation results from cellular events. At the same time, it can be used as a basis for an understanding of tissue mechanics. Note that besides biological tissues, our ideas can also be applied to other two-dimensional cellular networks, for instance to two-dimensional foams.

Our theoretical framework represents a triangulation-based approach to describe the deformation of flat two-dimensional cellular networks. In principle, this approach could be generalized in different ways. First, one could imagine a three-dimensional generalization. This generalization would then be based on tetrahedrons instead of triangles. In three dimensions, tetrahedrons (three-simplices) are the natural unit to define a displacement gradient just like triangles (two-simplices) are in two dimensions. Then, shape measures would be defined for tetrahedrons with respect to a regular reference tetrahedron, and topological transitions would correspond to the disappearance and appearance of tetrahedrons.

Second, one could consider a generalization to curved two-dimensional cellular networks. The triangulation of such a curved network would correspond to a so-called piecewise-flat manifold. Such a generalization would bear an additional advantage: Given a network state with arbitrary topology, it becomes possible to define a reference state for the whole tissue – not only for single triangles. Such a reference state would be made up of equilateral triangles, but it had the same topology as the given state. In flat geometries, this is only possible if all cells are hexagonal. In contrast to that, allowing for curved triangulations, equilateral triangles can be put together arbitrarily. However, one major problem for such an approach is that it is unclear how to define tissue-wide averages of directional quantities like shear in a curved network. This relates to the problem of defining a global direction in a manifold with nonzero Gaussian curvature.

Large-scale rheological tissue properties depend on cellular fluctuations

In Chapter 3, we studied the large-scale rheological behavior of two-dimensional tissues. To this end, we used a vertex model, which represents cells as polygons. The vertex model describes the elastic properties of the cells with an effective work function. These elastic properties comprise cell area elasticity, cell perimeter elasticity, and a cell-cell interfacial tension, called line tension.

We studied how the large-scale rheological behavior of vertex model tissue depended on the amplitude of line tension fluctuations. To this end, we performed simple shear simulations and focused on a mean field description of the steady state. We found that first, the cellular shear modulus was largely independent on the shear rate and on the fluctuation amplitude. Thus, the shear stress was largely proportional to the cell elongation. Then, we analyzed cell elongation relaxation using the theoretical framework from Chapter 2. We found that vertex model tissue behaved like a plastic solid for low fluctuation amplitude and like a visco-elastic fluid for high fluctuation amplitude. We observed crossover behavior for intermediate fluctuation amplitudes.

To obtain these results, we extended the vertex model in three aspects. First, we introduced skewed boundary conditions into the vertex model, which are similar to so-called Lees-Edwards boundary conditions [156]. This allows for perpetual simple shear simulations. The advantage of such simulations is that they can be run long enough to ensure that the steady state is reached. Moreover, the duration of such simulatuions can be freely adjusted in order to provide enough statistics.

Second, we introduced cell-scale fluctuations into the vertex model. To this end, we added mutually independent Ornstein-Uhlenbeck noise sources to the line tensions of all cell-cell interfaces. Note that the original vertex model only describes elastic cell properties and no viscosities. Now, the introduced fluctuations add a characteristic time scale into the vertex model. Therefore, they allow for the finite viscosity that we observed in the simulations.

Third, in contrast to earlier vertex model studies [58, 81, 118, 121–123], we allowed for N-fold vertices with $N > 3$. This greatly simplified the treatment of T1 and T2 transitions. Furthermore, although three-fold vertices appear to be always preferred for homogeneous line tensions [58, 122], the fluctuations introduced a generally inhomogeneous distribution of line tensions. This resulted in N-fold vertices with $N > 3$ to be occasionally preferred over three-fold vertices.

Of note, we observed that in simple shear simulations without line tension fluctuations, the applied strain typically localized into shear bands. We introduced a statistical measure to quantify the persistence of shear bands. Using this measure, we showed that shear bands could be abolished by line tension fluctuations.

In addition to studying the passive rheological properties of epithelial tissues, the developed vertex model extensions could also be used to study active tissue properties. Developing animals provide many examples for autonomously shearing tissues [31, 128, 162]. To understand such actively shearing tissues, one may ask for the minimal requirements for persistent and autonomous shear of vertex model tissue. Preliminary results indicated that persistently and autonomously shearing vertex model tissue could be created by line tension fluctuations with anisotropic amplitude.[1] Alternatively, it could be created by isotropic line tension fluctuations combined with an anisotropic line tension offset. Future work could probe the behavior of such active anisotropic vertex model tissue using simple shear simulations. We would expect that for small shear rates, the tissue behaves like a linear active visco-elastic material [59, 61, 63].

A simple hydrodynamic description accounts for the reorientation of Core PCP in the fruit fly wing

In Chapter 4, motivated by the observed reorientation of Core PCP in the fruit fly wing, we developed a hydrodynamic description for the reorientation of a polarity field in a two-dimensional material. Our description is an extension of earlier work [54, 58], which considered a coupling of a polarity field to material shear, analogously to liquid crystal theory [134]. In addition to that, we introduced a coupling to a second polarity field, and we considered a local polarity alignment effect.

We systematically obtained analytical expressions for stationary states of our hydrodynamic description. To this end, we assumed homogeneity in one dimension and we focused on the cases where the effective nematic shear field and the second polarity field were either parallel or perpendicular to each other. The stationary solutions typically contain domains within which the polarity angle assumes characteristic values. These characteristic values depend on the ratio between nematic and polar coupling strengths. Furthermore, the domains are separated by boundary regions within which the polarity angle bends smoothly. The width of these boundaries is defined by the ratio of the local polarity alignment strength to the nematic and polar coupling strengths. In principle, these results may as well be useful to other fields of physics, for instance for describing polar liquid crystals being simultaneously subject to a shear field and a coupling to an external vector field [134, 163].

---

[1] These preliminary results are not presented in this thesis.

We applied our hydrodynamic description for polarity reorientation to the Core PCP field in the fruit fly wing, where the second polarity field corresponds to Fat PCP. Our description could not only account for the typical wild type wing hair pattern. Moreover, it also accounted for reproducible wing hair patterns of flies that were genetically perturbed following six different protocols. This is the first time that the wing hair pattern of a genetically altered fly could be reproduced by a quantitative theory.

In our description, we proposed a coupling of the polarity field to an effective shear field, which is oriented along the long axis of the fly wing. Note that in principle, our effective shear field summarizes possible couplings to several nematic fields like actual tissue shear, oriented T1 transitions, oriented cell divisions, and cell elongation.[2] In this work, we determined the coefficient describing the reorientation by the effective shear field in wild type tissue. To this end, we fitted our description to the quantified time-dependent Core PCP data of a developing wild type wing. However, we could not clarify the contributions of the individual nematic fields to the effective shear field. This is because all of the nematic fields listed above were largely aligned with each other in the fly wings studied. To disentangle the contributions by the individual nematic fields, future work could study Core PCP reorientation under perturbed mechanical conditions.

Our work has a number of biological implications. First, our work contributes to the discussion about how the polar order in the wild type wing hair pattern is created. In particular, we provide evidence demonstrating that a coupling to the effective shear field is sufficient to explain Core PCP reorientation in wild type tissue. This suggests that the polar order of wing hairs is created by the nematic order of the effective shear field.

Moreover, independently of our theoretical description, our experimental data directly suggest that the coupling to a nematic field dominates Core PCP reorientation in wild type tissue. In particular, in the wild type and the early Sple over-expression wing hair patterns, nearly all wing hairs point either distally or proximally. This is reminiscent of stationary states of a vector field being coupled to a nematic field. However, such a coupling to a nematic field contradicts “factor X” models, which assume that Core PCP order is created by the polar coupling to a protein gradient.

Second, our work contributes to the discussion about possible couplings between Core PCP and Fat PCP. In particular, our results suggest that Sple enhances a coupling of Core PCP to Fat PCP. This is consistent with the findings of a number of recent publications [39, 57, 140, 141]. Future work could verify this idea and determine the effective coupling strength of Core PCP to Fat PCP in tissue over-expressing Sple. To this end, one could quantify the time-dependent Core PCP pattern in Sple over-expression wings and compare to our theoretical description.

---

[2] Furthermore, preliminary theoretical results indicate that an effective shear coupling could also be of a purely geometrical origin, created by the change of cell elongation.

Third, from comparing our theoretical description to experimental data, we obtained a value for the coefficient describing local polarity alignment in wild type tissue. By coarse-graining of a cell-scale Core PCP model, we showed that this coefficient corresponds to a cellular PCP time scale of $\sim 1\,\mathrm{min}$. This is consistent with measured turnover time scales of Core PCP clusters [36, 37, 54].

Finally, in order to numerically solve our theoretical description for polarity reorientation, we proposed particular boundary conditions, which were motivated by observed polarity patterns in the fly wing. In particular, we chose boundary conditions where the polarity field was coupled to the local direction of bristles growing out of the wing margin. Furthermore, the preferred directions of wing margin bristles were described by an effective potential. As a result, our theory did not only reproduce observed wing hair patterns, but also the directions of wing margin bristles. This suggests that first, the direction of margin bristles is coupled to the Core PCP field at the wing margin; and second, this coupling and the preferred directions of wing margin bristles are largely independent of Sple over-expression.

To compare our theoretical results to biological polarity patterns, we developed an algorithm to quantify wing hair polarity patterns of fruit fly wings. The main idea is to compute a local nematic auto-correlation. In particular, the algorithm does not rely on any object recognition and is therefore very robust and runs very fast. Thus, the idea can be applied to any image processing problem where some local axis needs to be quantified reliably and fast. Moreover, with a slight modification, one could quantify a local vector direction instead of a local axis. This could for instance be achieved by a cross-correlation between two different color channels.

Appendices

Appendix A

Algebra of real 2×2 matrices

Here, we present fundamental algebraic relations for 2×2 matrices with real-valued entries. These relations are mainly applied in Chapter 2 and in Appendix B.

A.1 Sum decomposition into scaling rotations and nematics

A.1.1 Sum decomposition

Any 2×2 matrix S_{ij} with real elements can be uniquely decomposed into two parts:

$$S_{ij} = A_{ij} + \tilde{B}_{ij}. \tag{A.1}$$

The matrix A_{ij} comprises the trace and the antisymmetric part of S_{ij}, and the matrix $\tilde{B}_{ij}$ corresponds to the traceless, symmetric part of S_{ij}.

A.1.2 Scaling rotations

We call the matrix A_{ij} a *scaling rotation*, because it can be expressed as the product of a scalar c with a rotation:

$$A_{ij} = c\,\mathrm{R}_{ij}(\vartheta). \tag{A.2}$$

Here, the matrix $\mathrm{R}_{ij}(\vartheta)$ denotes a rotation by the angle ϑ:

$$\mathbf{R}(\vartheta) = \begin{pmatrix} \cos\vartheta & -\sin\vartheta \\ \sin\vartheta & \cos\vartheta \end{pmatrix}. \tag{A.3}$$

For given matrix A_{ij}, the scalar c is given by $c = (A_{xx}^2 + A_{yx}^2)^{1/2}$. Then, the angle ϑ is given by the two relations $\cos\vartheta = A_{xx}/c$ and $\sin\vartheta = A_{yx}/c$.

A.1.3 Determinant

Writing out everything in components, one can show that the determinant of the matrix S_{ij} reads:

$$\det(\boldsymbol{S}) = c^2 - |\tilde{B}|^2. \tag{A.4}$$

Here, $|\tilde{B}|$ is the norm of the traceless, symmetric matrix $\tilde{B}_{ij}$ as defined in Section A.2.2. In the next section, we discuss properties of traceless, symmetric matrices in detail.

A.2 Properties of nematics

In Eq. (A.1), the matrix $\tilde{B}_{ij}$ is a symmetric, traceless matrix. For a given coordinate system, it describes a symmetric, traceless tensor. In this work, we call symmetric, traceless tensors *nematic tensors* or just *nematics*. We denote them with a tilde above the tensor symbol: $\tilde{B}_{ij}$. Here, we focus on the two-dimensional case.

A.2.1 Components of a nematic

Given a Cartesian coordinate system with x and y axes. Then, a nematic $\tilde{B}_{ij}$ is described by the following matrix:

$$\tilde{\boldsymbol{B}} = \begin{pmatrix} \tilde{B}_{xx} & \tilde{B}_{xy} \\ \tilde{B}_{xy} & -\tilde{B}_{xx} \end{pmatrix}. \tag{A.5}$$

Thus, it possesses two independent scalar degrees of freedom, $\tilde{B}_{xx}$ and $\tilde{B}_{xy}$.

A.2.2 Norm and angle of a nematic

Similar to a vector, a nematic $\tilde{B}_{ij}$ can be characterized by a norm $|\tilde{B}|$ and an angle ϕ with

$$\tilde{\boldsymbol{B}} = |\tilde{B}| \begin{pmatrix} \cos(2\phi) & \sin(2\phi) \\ \sin(2\phi) & -\cos(2\phi) \end{pmatrix}. \tag{A.6}$$

For given components $\tilde{B}_{xx}$ and $\tilde{B}_{xy}$, the norm is defined by $|\tilde{B}| = (\tilde{B}_{xx}^2 + \tilde{B}_{xy}^2)^{1/2}$. Then, the angle ϕ is defined by $\cos(2\phi) = \tilde{B}_{xx}/|\tilde{B}|$ and $\sin(2\phi) = \tilde{B}_{xy}/|\tilde{B}|$.

In contrast to a vector, a nematic possesses a π rotational symmetry. Therefore, the angle ϕ characterizes an axis instead of a direction. Table A.1 summarizes how the orientation of this axis depends on the signs of the components $\tilde{B}_{xx}$ and $\tilde{B}_{xy}$.

Table A.1: Orientation of the axis of a nematic tensor $\tilde{B}_{ij}$ depending on the signs of the components $\tilde{B}_{xx}$ and $\tilde{B}_{xy}$.

$\tilde{B}_{xx}$	$\tilde{B}_{xy}$	**axis of the nematic tensor**
>0	$=0$	parallel to the x axis
<0	$=0$	parallel to the y axis
$=0$	>0	diagonal with an angle of $+\pi/4$ with respect to the x axis
$=0$	<0	diagonal with an angle of $-\pi/4$ with respect to the x axis

A.2.3 Orthonormal basis in the formal vector space of nematics

According to Section A.2.1, any nematic tensor $\tilde{B}_{ij}$ can be expressed as a linear combination of two particular nematics:

$$\tilde{\boldsymbol{B}} = \tilde{B}_{xx}\tilde{\boldsymbol{C}}_1 + \tilde{B}_{xy}\tilde{\boldsymbol{C}}_2. \tag{A.7}$$

Here, we defined:

$$\tilde{\boldsymbol{C}}_1 = \begin{pmatrix} 1 & 0 \\ 0 & -1 \end{pmatrix} \qquad \text{and} \qquad \tilde{\boldsymbol{C}}_2 = \begin{pmatrix} 0 & 1 \\ 1 & 0 \end{pmatrix}. \tag{A.8}$$

In that sense, the pair of the nematics $\tilde{\boldsymbol{C}}_1$ and $\tilde{\boldsymbol{C}}_2$ constitute a basis in the formal vector space of nematics. The coefficient $\tilde{B}_{xx}$ characterizes the component of $\tilde{B}_{ij}$ parallel or perpendicular to the x axis and $\tilde{B}_{xy}$ characterizes the component of $\tilde{B}_{ij}$ diagonal to the x axis, i.e. at an angle of $\pi/4$ or $-\pi/4$ with respect to the x axis (compare Table A.1).

Now, we generalize this idea. For a given nematic $\tilde{Q}_{ij}$ with $|\tilde{Q}| \neq 0$, we want to decompose any nematic $\tilde{B}_{ij}$ into a contribution parallel or perpendicular to $\tilde{Q}_{ij}$ and into a contribution diagonal to $\tilde{Q}_{ij}$. To this end, we first define the following two nematics:

$$\tilde{\boldsymbol{D}}_1 = \frac{1}{|\tilde{Q}|}\tilde{\boldsymbol{Q}} \qquad \text{and} \qquad \tilde{\boldsymbol{D}}_2 = \frac{1}{|\tilde{Q}|}\boldsymbol{\epsilon}\cdot\tilde{\boldsymbol{Q}}. \tag{A.9}$$

Here, the dot denotes the matrix product and the matrix ϵ_{ij} denotes the generator of rotations:

$$\boldsymbol{\epsilon} = \begin{pmatrix} 0 & -1 \\ 1 & 0 \end{pmatrix}. \tag{A.10}$$

Now, we show that the pair of nematics $\tilde{\boldsymbol{D}}_1$ and $\tilde{\boldsymbol{D}}_2$ constitutes an orthonormal basis in the formal vector space of nematics. To this end, we introduce the following scalar product between two nematics $\tilde{X}_{ij}$ and $\tilde{Y}_{ij}$:

$$\langle\tilde{\boldsymbol{X}}|\tilde{\boldsymbol{Y}}\rangle = \frac{1}{2}\tilde{X}_{ij}\tilde{Y}_{ij}. \tag{A.11}$$

Because $\langle \tilde{\boldsymbol{Q}} | \tilde{\boldsymbol{Q}} \rangle = |\tilde{Q}|^2$ and $\langle \tilde{\boldsymbol{Q}} | \boldsymbol{\epsilon} \cdot \tilde{\boldsymbol{Q}} \rangle = 0$, we obtain:

$$\langle \tilde{\boldsymbol{D}}_a | \tilde{\boldsymbol{D}}_b \rangle = \delta_{ab} \qquad (\text{for } a, b \in \{1, 2\}). \tag{A.12}$$

Here, δ_{ab} denotes the Kronecker symbol. Thus, the pair of nematics $\tilde{\boldsymbol{D}}_1$ and $\tilde{\boldsymbol{D}}_2$ constitutes indeed an orthonormal basis. It is complete, because the formal vector space of nematics is two-dimensional.

As a consequence, any nematic $\tilde{B}_{ij}$ can be expressed as a linear combination of $\tilde{\boldsymbol{D}}_1$ and $\tilde{\boldsymbol{D}}_2$:

$$\tilde{\boldsymbol{B}} = \langle \tilde{\boldsymbol{D}}_1 | \tilde{\boldsymbol{B}} \rangle \, \tilde{\boldsymbol{D}}_1 + \langle \tilde{\boldsymbol{D}}_2 | \tilde{\boldsymbol{B}} \rangle \, \tilde{\boldsymbol{D}}_2. \tag{A.13}$$

The coefficient $\langle \tilde{\boldsymbol{D}}_1 | \tilde{\boldsymbol{B}} \rangle$ characterizes the component of $\tilde{B}_{ij}$ parallel or perpendicular to $\tilde{Q}_{ij}$. Furthermore, because the tensor $\epsilon_{ik}\tilde{Q}_{kj}$ corresponds to the nematic $\tilde{Q}_{ij}$ rotated by $\pi/4$ (Section A.3.2), the coefficient $\langle \tilde{\boldsymbol{D}}_2 | \tilde{\boldsymbol{B}} \rangle$ characterizes the component of $\tilde{B}_{ij}$ diagonal to $\tilde{Q}_{ij}$. Eq. (A.7) corresponds to the special case where the nematic $\tilde{Q}_{ij}$ is parallel to the x axis.

A.2.4 Infinitesimal changes of norm and angle

Infinitesimal changes in norm and angle of a nematic $\tilde{B}_{ij}$ induce changes in the nematic itself. From Eq. (A.6) follows:

$$\delta \tilde{B}_{ij} = \delta |\tilde{B}| \frac{\tilde{B}_{ij}}{|\tilde{B}|} + 2\delta\phi \epsilon_{ik} \tilde{B}_{kj}. \tag{A.14}$$

Here, $\delta \tilde{B}_{ij}$ denotes the infinitesimal change of the nematic $\tilde{B}_{ij}$ and the scalars $\delta|\tilde{B}|$ and $\delta\phi$ denote the infinitesimal changes of its norm and angle, respectively. Eq. (A.14) expresses $\delta \tilde{B}_{ij}$ in terms of the basis constructed from $\tilde{B}_{ij}$. With:

$$\tilde{\boldsymbol{D}}_1 = \frac{1}{|\tilde{B}|} \tilde{\boldsymbol{B}} \qquad \text{and} \qquad \tilde{\boldsymbol{D}}_2 = \frac{1}{|\tilde{B}|} \boldsymbol{\epsilon} \cdot \tilde{\boldsymbol{B}}, \tag{A.15}$$

we obtain:

$$\delta \tilde{B}_{ij} = \delta |\tilde{B}| \, \tilde{\boldsymbol{D}}_1 + 2\delta\phi |\tilde{B}| \, \tilde{\boldsymbol{D}}_2. \tag{A.16}$$

Thus, the change of $\tilde{B}_{ij}$ decomposes into two components. One component is parallel or perpendicular to $\tilde{B}_{ij}$ and characterizes the change of its norm. The other component is diagonal to $\tilde{B}_{ij}$ and characterizes the change of its angle.

A.3 Products between scaling rotations and nematics

Here, we present relations for products between scaling rotations and nematics. These relations were derived using Eqs. (A.3) and (A.6) and writing out the matrix components explicitly.

A.3.1 Two scaling rotations

The matrix product of two scaling rotations $c_1\mathrm{R}_{ij}(\vartheta_1)$ and $c_2\mathrm{R}_{ij}(\vartheta_2)$ is:

$$c_1\mathbf{R}(\vartheta_1)\cdot c_2\mathbf{R}(\vartheta_2) = c_1c_2\,\mathbf{R}(\vartheta_1+\vartheta_2). \tag{A.17}$$

Thus, it is again a scaling rotation with scalar c_1c_2 and angle $\vartheta_1+\vartheta_2$.

A.3.2 A scaling rotation and a nematic

The matrix product of a scaling rotation $c\mathrm{R}_{ij}(\vartheta)$ and a nematic $\tilde{B}_{ij}$ with norm $|\tilde{B}|$ and angle ϕ reads:

$$c\mathbf{R}(\vartheta)\cdot\tilde{\boldsymbol{B}} = c|\tilde{B}|\begin{pmatrix}\cos(2\phi+\vartheta) & \sin(2\phi+\vartheta)\\ \sin(2\phi+\vartheta) & -\cos(2\phi+\vartheta)\end{pmatrix}. \tag{A.18}$$

Thus, the product of scaling rotation and a nematic is again a nematic. Furthermore, the application of the scaling rotation $c\mathrm{R}_{ij}(\vartheta)$ on the nematic $\tilde{B}_{ij}$ scales the norm of $\tilde{B}_{ij}$ by the scalar c and rotates the axis of $\tilde{B}_{ij}$ by the angle $\vartheta/2$.

We ask what happens if the order of the factors in the product is reversed. We obtain:

$$\tilde{\boldsymbol{B}}\cdot c\mathbf{R}(\vartheta) = c\mathbf{R}(-\vartheta)\cdot\tilde{\boldsymbol{B}}. \tag{A.19}$$

Here, we used that $\tilde{\boldsymbol{B}}\cdot c\mathbf{R}(\vartheta) = (c\mathbf{R}^{\mathrm{T}}(\vartheta)\cdot\tilde{\boldsymbol{B}}^{\mathrm{T}})^{\mathrm{T}}$, where the superscript T denotes the matrix transpose. Also, we used that $\mathbf{R}^{\mathrm{T}}(\vartheta) = \mathbf{R}(-\vartheta)$ and that the transpose of a nematic is the nematic itself. Hence, when reversing the order of a scaling rotation and a nematic, the rotation angle flips its sign.

As a consequence, the nematic $\tilde{B}_{ij}$ rotated by an angle ϑ can be expressed as

$$\mathbf{R}(2\vartheta)\cdot\tilde{\boldsymbol{B}} = \mathbf{R}(\vartheta)\cdot\tilde{\boldsymbol{B}}\cdot\mathbf{R}(-\vartheta). \tag{A.20}$$

In particular, the matrix ϵ_{ij} corresponds to a rotation by the angle $\pi/2$: $\epsilon_{ij} = \mathrm{R}_{ij}(\pi/2)$. Thus, $\epsilon_{ik}\tilde{B}_{kj}$ corresponds to the nematic $\tilde{B}_{ij}$ rotated by $\pi/4$.

A.3.3 Two nematics

The matrix product of two nematics $\tilde{\boldsymbol{B}}_1$ and $\tilde{\boldsymbol{B}}_2$ with norms $|\tilde{B}_1|$ and $|\tilde{B}_2|$ and angles ϕ_1 and ϕ_2 reads:

$$\tilde{\boldsymbol{B}}_1\cdot\tilde{\boldsymbol{B}}_2 = |\tilde{B}_1||\tilde{B}_2|\,\mathbf{R}\big(2[\phi_1-\phi_2]\big). \tag{A.21}$$

Thus, it is a scaling rotation. The scaling factor is the product of the norms $|\tilde{B}_1||\tilde{B}_2|$ and the rotation angle is twice the difference between the nematic angles $2[\phi_1-\phi_2]$.

A.4 Exponentials of real 2×2 matrices

A.4.1 Definition

We define the exponential of a matrix G_{ij} by the Taylor series of the exponential function:

$$\exp\left(\boldsymbol{G}\right) = \sum_{n=0}^{\infty} \frac{1}{n!} \boldsymbol{G}^n. \tag{A.22}$$

This series converges for any matrix $\boldsymbol{G}$. In the following, we separately discuss the exponentials of antisymmetric, of symmetric, and of symmetric, traceless matrices. Before that, we shortly discuss a few general properties of matrix exponentials.

A.4.2 General properties

Determinant of matrix exponentials

In the following sections, we will make use of the well-known equation:

$$\det\big[\exp\left(\boldsymbol{G}\right)\big] = \exp\left(G_{kk}\right). \tag{A.23}$$

It relates the determinant of $\exp\left(\boldsymbol{G}\right)$ to the trace of G_{ij}.

Exponential of a rotated matrix

Here, we ask for the exponential of the matrix G_{ij} rotated by the angle ϑ:

$$\boldsymbol{G'} = \mathbf{R}(\vartheta) \cdot \boldsymbol{G} \cdot \mathbf{R}(-\vartheta). \tag{A.24}$$

From Eq. (A.22) follows:

$$\exp\left(\boldsymbol{G'}\right) = \mathbf{R}(\vartheta) \cdot \exp\left(\boldsymbol{G}\right) \cdot \mathbf{R}(-\vartheta). \tag{A.25}$$

Thus, the exponential of a rotated matrix corresponds to the rotated matrix exponential.

Product of matrix exponentials

Beware that in general, for two matrices $\boldsymbol{G}_1$ and $\boldsymbol{G}_2$:

$$\exp\left(\boldsymbol{G_1}\right) \cdot \exp\left(\boldsymbol{G_2}\right) \neq \exp\left(\boldsymbol{G_1} + \boldsymbol{G_2}\right). \tag{A.26}$$

However, equality holds if $\boldsymbol{G}_1$ and $\boldsymbol{G}_2$ commute: $\boldsymbol{G}_1 \cdot \boldsymbol{G}_2 = \boldsymbol{G}_2 \cdot \boldsymbol{G}_1$.

A.4.3 Exponentials of antisymmetric matrices

Any real antisymmetric 2 × 2 matrix can be written as $\theta\epsilon_{ij}$, where θ is a scalar. Its exponential can be interpreted as a rotation by θ:

$$\exp\left(\theta\boldsymbol{\epsilon}\right) = \mathbf{R}(\theta). \tag{A.27}$$

This can be derived from the definition of $\mathrm{R}_{ij}(\theta)$ (Eq. (A.3)), from Eq. (A.22), and from the Taylor series of the sine and cosine functions.

A.4.4 Exponentials of symmetric matrices

The exponential of any symmetric 2 × 2 matrix Q_{ij} can be decomposed into:

$$\exp\left(\boldsymbol{Q}\right) = \exp\left(Q_{kk}/2\right)\,\exp(\tilde{\boldsymbol{Q}}). \tag{A.28}$$

Here, $\tilde{Q}_{ij}$ denotes the traceless part of Q_{ij}: $\tilde{Q}_{ij} = Q_{ij} - Q_{kk}\delta_{ij}/2$. Eq. (A.28) follows because the tensors $Q_{kk}\delta_{ij}/2$ and $\tilde{Q}_{ij}$ commute. Furthermore, we used that $\exp\left(Q_{kk}\boldsymbol{I}/2\right) = \exp\left(Q_{kk}/2\right)\boldsymbol{I}$, where $\boldsymbol{I}$ denotes the identity matrix with $I_{ij} = \delta_{ij}$.

Hence, the exponential of Q_{ij} can be interpreted as a scaling by $\exp\left(Q_{kk}/2\right)$ followed by the transformation $\exp(\tilde{\boldsymbol{Q}})$. As explained in the next subsection, $\exp(\tilde{\boldsymbol{Q}})$ can be interpreted as a pure shear deformation. Note that the scaling by $\exp\left(Q_{kk}/2\right)$ changes the area by a factor of $\exp\left(Q_{kk}\right)$ whereas $\exp(\tilde{\boldsymbol{Q}})$ leaves the area unchanged. This is consistent with Eq. (A.23).

A.4.5 Exponentials of nematics

Interpretation

Here, we discuss the effect of the exponential $\exp(\tilde{\boldsymbol{Q}})$ of a nematic $\tilde{Q}_{ij}$. To this end, we first note that:

$$\tilde{\boldsymbol{Q}} = \mathbf{R}(\Phi)\cdot\begin{pmatrix}|\tilde{Q}| & 0\\ 0 & -|\tilde{Q}|\end{pmatrix}\cdot\mathbf{R}(-\Phi). \tag{A.29}$$

Here, the scalars $|\tilde{Q}|$ and Φ denote norm and angle of the nematic $\tilde{Q}_{ij}$, respectively. Eq. (A.29) follows from Eqs. (A.18) and (A.20). Then, we use Eqs. (A.22) and (A.25), to obtain

$$\exp(\tilde{\boldsymbol{Q}}) = \mathbf{R}(\Phi)\cdot\begin{pmatrix}\exp(|\tilde{Q}|) & 0\\ 0 & \exp(-|\tilde{Q}|)\end{pmatrix}\cdot\mathbf{R}(-\Phi) \tag{A.30}$$

Thus, the effect of $\exp(\tilde{\boldsymbol{Q}})$ can be interpreted as follows. Along an axis with angle Φ, there is a stretching by the factor $\exp(|\tilde{Q}|)$ and perpendicular to it, there is a shortening by the factor $\exp(-|\tilde{Q}|)$. This corresponds to a pure shear deformation.

For instance, the transformation $\exp(\tilde{\boldsymbol{Q}})$ applied to a circle yields an ellipse with aspect ratio $\exp(2|\tilde{Q}|)$ where the orientation of the long axis is given by the angle Φ.

Sum representation

Similar to Section A.1.1, we decompose $\exp(\tilde{\boldsymbol{Q}})$ into a trace part and a traceless, symmetric part. To this end, we first note that $\tilde{Q}_{ij}\tilde{Q}_{jk} = |\tilde{Q}|^2\delta_{ik}$ and as a consequence,

$$\tilde{\boldsymbol{Q}}^n = \begin{cases} |\tilde{Q}|^n \boldsymbol{I} & \text{for even } n \text{ and} \\ |\tilde{Q}|^{n-1}\tilde{\boldsymbol{Q}} & \text{for odd } n. \end{cases} \tag{A.31}$$

Here, $\boldsymbol{I}$ denotes the identity matrix with $I_{ij} = \delta_{ij}$. Then, from Eq. (A.22) follows:

$$\exp(\tilde{\boldsymbol{Q}}) = \cosh(|\tilde{Q}|)\boldsymbol{I} + \frac{\sinh(|\tilde{Q}|)}{|\tilde{Q}|}\tilde{\boldsymbol{Q}} \tag{A.32}$$

for $|\tilde{Q}| \neq 0$ and $\exp(\tilde{\boldsymbol{Q}}) = \boldsymbol{I}$ for $|\tilde{Q}| = 0$.

A.5 Product decomposition of real 2×2 matrices

Here, we show that for any real 2×2 matrix S_{ij}, there exists a unique symmetric matrix Q_{ij} and an angle Θ such that:

$$\boldsymbol{S} = \exp(\boldsymbol{Q}) \cdot \mathbf{R}(\Theta). \tag{A.33}$$

To this end, we prove existence and uniqueness of such a decomposition separately.

A.5.1 Existence of the decomposition

Here, for a given matrix S_{ij}, we first provide values for the symmetric matrix Q_{ij} and the angle Θ. Then, we show that Eq. (A.33) is indeed fulfilled for these values.

Values for Q_{ij} and Θ

In order to provide the symmetric matrix Q_{ij}, we separately define its trace Q_{kk} and its traceless, symmetric part $\tilde{Q}_{ij}$. The trace Q_{kk} is defined by:

$$Q_{kk} = \ln\big[\det(\boldsymbol{S})\big]. \tag{A.34}$$

In order to provide the values for $\tilde{Q}_{ij}$ and Θ, we split S_{ij} into a scaling rotation A_{ij} and a nematic $\tilde{B}_{ij}$ (as in Section A.1.1):

$$S_{ij} = A_{ij} + \tilde{B}_{ij}. \tag{A.35}$$

The angle Θ is defined to be the angle of the scaling rotation A_{ij}:

$$A_{ij} = c\mathrm{R}_{ij}(\Theta). \tag{A.36}$$

Finally, the nematic $\tilde{Q}_{ij}$ is defined by the following expression:

$$\tilde{Q}_{ij} = \frac{\operatorname{arcsinh}\left[|\tilde{B}| \exp\left(-Q_{kk}/2\right)\right]}{|\tilde{B}|} \tilde{B}_{ik}\mathrm{R}_{kj}(-\Theta). \tag{A.37}$$

Proof that Eq. (A.33) holds

Now, we show that Eq. (A.33) holds with the above definitions for Q_{ij} and Θ. To this end, we first compute $\exp(\tilde{\boldsymbol{Q}})$ using Eq. (A.32):

$$\exp(\tilde{\boldsymbol{Q}}) = \cosh(|\tilde{Q}|)\boldsymbol{I} + \frac{\sinh(|\tilde{Q}|)}{|\tilde{Q}|}\tilde{\boldsymbol{Q}}. \tag{A.38}$$

Therefore, we need the values for the hyperbolic sine and cosine of $|\tilde{Q}|$. Using Eq. (A.37), the hyperbolic sine of $|\tilde{Q}|$ turns out to be

$$\sinh(|\tilde{Q}|) = |\tilde{B}| \exp(-Q_{kk}/2). \tag{A.39}$$

Then, the hyperbolic cosine of $|\tilde{Q}|$ can be computed using the relation

$$1 = \cosh^2(|\tilde{Q}|) - \sinh^2(|\tilde{Q}|) \tag{A.40}$$

and Eqs. (A.4) and (A.34). We obtain

$$\cosh(|\tilde{Q}|) = c \exp(-Q_{kk}/2). \tag{A.41}$$

Insertion of hyperbolic sine and cosine into Eq. (A.38) yields:

$$\exp(\tilde{\boldsymbol{Q}}) = c \exp(-Q_{kk}/2)\, \boldsymbol{I} + \exp(-Q_{kk}/2)\, \tilde{\boldsymbol{B}} \cdot \mathbf{R}(-\Theta). \tag{A.42}$$

Here, we also used Eq. (A.37). The following relation follows

$$\exp(Q_{kk}/2)\, \exp(\tilde{\boldsymbol{Q}}) \cdot \mathbf{R}(\Theta) = \boldsymbol{A} + \tilde{\boldsymbol{B}}. \tag{A.43}$$

Finally, Eq. (A.33) follows using Eqs. (A.28) and (A.35).

A.5.2 Uniqueness of the decomposition

Here, we show that the decomposition in Eq. (A.33) is unique. Put differently, we show that from

$$\exp(\boldsymbol{Q}) \cdot \mathbf{R}(\Theta) = \exp(\boldsymbol{Q'}) \cdot \mathbf{R}(\Theta') \tag{A.44}$$

with scalars Θ, Θ' and with symmetric matrices Q_{ij}, Q'_{ij} follows that $\Theta = \Theta'$ and $Q_{ij} = Q'_{ij}$. The symmetric matrices Q_{ij} and Q'_{ij} divide into traces Q_{kk} and Q'_{kk} and symmetric, traceless parts $\tilde{Q}_{ij}$ and $\tilde{Q}'_{ij}$, respectively.

First, we take the determinant on both sides of Eq. (A.44) and obtain:

$$Q_{kk} = Q'_{kk}. \tag{A.45}$$

Then, Eq. (A.44) becomes

$$\begin{aligned} &\cosh(|\tilde{Q}|)\, \mathbf{R}(\Theta) + \frac{\sinh(|\tilde{Q}|)}{|\tilde{Q}|}\, \tilde{\boldsymbol{Q}} \cdot \mathbf{R}(\Theta) \\ =&\cosh(|\tilde{Q}'|)\, \mathbf{R}(\Theta') + \frac{\sinh(|\tilde{Q}'|)}{|\tilde{Q}'|}\, \tilde{\boldsymbol{Q}}' \cdot \mathbf{R}(\Theta'), \end{aligned} \tag{A.46}$$

where we used Eq. (A.32).

Only the scaling rotation part on each side of Eq. (A.46) reads

$$\cosh(|\tilde{Q}|)\, \mathbf{R}(\Theta) = \cosh(|\tilde{Q}'|)\, \mathbf{R}(\Theta'). \tag{A.47}$$

Separating scaling and rotations on both sides, we obtain

$$|\tilde{Q}| = |\tilde{Q}'| \tag{A.48}$$

$$\Theta = \Theta'. \tag{A.49}$$

Finally, from the traceless, symmetric part of Eq. (A.46), we obtain

$$\tilde{Q}_{ij} = \tilde{Q}'_{ij}. \tag{A.50}$$

Thus, for a given matrix S_{ij}, the symmetric matrix Q_{ij} and the angle Θ are uniquely defined from Eq. (A.33).

Appendix B

Deformation of triangle networks

B.1 Equivalence of two definitions for the displacement gradient

Consider the deformation of a group G of triangles from an initial state to a final state without topological transitions. Here, we show the equivalence of two different definitions of the displacement gradient U_{ij}^G of group G. More precisely, we show that the triangle-based definition of the displacement gradient in Eq. (2.35)

$$U_{ij}^G = \left\langle U_{ij}^m \right\rangle \tag{B.1}$$

is equivalent to the definition in Eq. (2.36), which is only based on the margin deformation of group G. To this end, we transform the right hand side of Eq. (B.1) into an expression that only depends on cell center positions on the margin of group G.

First, we introduce a continuous displacement field $\boldsymbol{u}(\boldsymbol{r})$, which is defined on the whole area of group G. It is based on the initial and final positions of the cell centers, denoted by $\boldsymbol{R}^\alpha$ and $\boldsymbol{R'}^\alpha$, respectively. The displacement of cell centers $\boldsymbol{R}^\alpha$ is given by

$$\boldsymbol{u}(\boldsymbol{R}^\alpha) = \boldsymbol{R'}^\alpha - \boldsymbol{R}^\alpha. \tag{B.2}$$

Then, within each triangle of G, the displacement field $\boldsymbol{u}(\boldsymbol{r})$ is linearly interpolated using Eqs. (2.14), (2.15), and (2.16). Consequently, the discrete displacement gradient U_{ij}^m of any triangle m of G is given by the derivative (compare Eq. (2.17)):

$$U_{ij}^m = \left(\frac{\partial u_j}{\partial r_i}\right)_m . \tag{B.3}$$

Here, the derivative on the right hand side is constant within the triangle m. It can thus be evaluated anywhere within triangle m.

Now, we can express U_{ij}^G in terms of $\boldsymbol{u}(\boldsymbol{r})$. Insertion of Eq. (B.3) into Eq. (B.1) yields:

$$U_{ij}^G = \frac{1}{A^G} \sum_{m \in G} A^m \left(\frac{\partial u_j}{\partial r_i}\right)_m . \tag{B.4}$$

Here, the sum runs over all triangles m of group G. The areas A^G and A^m denote the initial areas of group G and triangle m, respectively. The sum in Eq. (B.4) can be transformed into the following integral over the initial area of the group:

$$U_{ij}^G = \frac{1}{A^G} \int_{A^G} \frac{\partial u_j}{\partial r_i} \, \mathrm{d}^2 r. \tag{B.5}$$

Using Stoke's theorem, the area integral can be expressed as a closed line integral over the initial margin of the group:[1]

$$U_{ij}^G = \frac{1}{A^G} \oint n_i u_j \, \mathrm{d}\ell. \tag{B.7}$$

Here, the vector $\boldsymbol{n}$ denotes the local unit normal vector of the margin pointing outside of the group.[2]

Finally, in order to explicitly express U_{ij}^G in terms of individual cell center positions, we separately integrate over each triangle side being part of the margin of G:

$$U_{ij}^G = \frac{1}{A^G} \sum_{\alpha=1}^{n} \int_0^{|\boldsymbol{R}^{\alpha+1} - \boldsymbol{R}^\alpha|} n_i u_j \, \mathrm{d}\ell. \tag{B.8}$$

Here, the sum runs over all cell centers $\boldsymbol{R}^\alpha$ on the margin of G in counter-clockwise order. The scalar $|\boldsymbol{R}^{\alpha+1} - \boldsymbol{R}^\alpha|$ denotes the norm of the vector $\boldsymbol{R}^{\alpha+1} - \boldsymbol{R}^\alpha$ and corresponds to the length of the triangle side connecting the centers of cells α and $\alpha + 1$. The integral in Eq. (B.8) can be expressed in terms of cell center positions:

$$\int_0^{|\boldsymbol{R}^{\alpha+1} - \boldsymbol{R}^\alpha|} n_i u_j \, \mathrm{d}\ell = \frac{1}{2} \epsilon_{ik} \Big(R_k^\alpha - R_k^{\alpha+1} \Big) \Big(\big[R_j'^\alpha + R_j'^{\alpha+1} \big] - \big[R_j^\alpha + R_j^{\alpha+1} \big] \Big). \tag{B.9}$$

Here, we used the relation $n_i |\boldsymbol{R}^{\alpha+1} - \boldsymbol{R}^\alpha| = -\epsilon_{ik}(R_k^{\alpha+1} - R_k^\alpha)$. Also, $\boldsymbol{u}(\boldsymbol{r})$ in the cell centers $\boldsymbol{R}^\alpha$ and $\boldsymbol{R}^{\alpha+1}$ is given by Eq. (B.2). Between the cell centers, $\boldsymbol{u}(\boldsymbol{r})$ is obtained

---

[1] To more clearly see the equivalence between Eqs. (B.5) and (B.7), consider Gauss' theorem, which is a special case of Stoke's theorem:

$$\int_{A^G} \frac{\partial f_k}{\partial r_k} \, \mathrm{d}^2 r = \oint n_k f_k \, \mathrm{d}\ell. \tag{B.6}$$

Here, $\boldsymbol{f}(\boldsymbol{r})$ is a vector field. For fixed $i, j \in \{x, y\}$, the equivalence between Eqs. (B.5) and (B.7) follows with $f_k = \delta_{ik} u_j$.

[2] Between two cell centers $\boldsymbol{R}^\alpha$, the normal vector $\boldsymbol{n}$ is properly defined, because the triangulation margin is a straight line, there. However in general, the direction of $\boldsymbol{n}$ changes discontinuously in cell centers $\boldsymbol{R}^\alpha$. Correspondingly, $\boldsymbol{n}$ is not properly defined in cell centers. After all, this is not a problem, because the cell centers themselves have zero weight in the integral in Eq. (B.7).

by linear interpolation. Finally, from Eqs. (B.8) and (B.9), we obtain Eq. (2.36):

$$U_{ij}^G = \frac{\epsilon_{ik}}{2A^G} \sum_{\alpha=1}^{n} \Big(R_k^\alpha - R_k^{\alpha+1} \Big) \Big(\big[R'^{\alpha}_j + R'^{\alpha+1}_j \big] - \big[R_j^\alpha + R_j^{\alpha+1} \big] \Big). \tag{B.10}$$

B.2 Triangle transformation parameters in terms of triangle state change

B.2.1 Finite transformations

Like in Section 2.1.3, we consider a triangle that is deformed from an initial state to a final state. The initial state is characterized by the tensor S_{ij} and the final state is characterized by the tensor S'_{ij}. The transformation is characterized by the tensor M_{ij}. Here, we relate the transformation parameters ΔN_{ij} and $\Delta\Psi$ to changes of the state parameters Q_{ij} and Θ.

In the main text, we show that Eq. (2.22) holds, which relates the transformation tensor to the state tensors:

$$\boldsymbol{S'} = \boldsymbol{M} \cdot \boldsymbol{S}. \tag{B.11}$$

Inserting the parametrizations of transformation and state tensors (Eqs. (2.7) and (2.19)), we obtain:

$$\exp(\boldsymbol{Q'}) \cdot \mathbf{R}(\Theta') = \exp(\boldsymbol{\Delta N}) \cdot \mathbf{R}(\Delta\Psi) \cdot \exp(\boldsymbol{Q}) \cdot \mathbf{R}(\Theta). \tag{B.12}$$

Now, we multiply both sides from right by $\mathbf{R}(-\Theta) \cdot \exp(-\boldsymbol{Q})$:

$$\exp(\boldsymbol{\Delta N}) \cdot \mathbf{R}(\Delta\Psi) = \exp(\boldsymbol{Q'}) \cdot \mathbf{R}(\Delta\Theta) \cdot \exp(-\boldsymbol{Q}). \tag{B.13}$$

Here, we defined $\Delta\Theta = \Theta' - \Theta$ and swapped both sides of the equation. By taking the determinant on both sides, we can separate the isotropic part from the anisotropic part:

$$\Delta N_{kk} = \Delta Q_{kk} \tag{B.14}$$

$$\exp\big(\boldsymbol{\Delta \tilde{N}}\big) \cdot \mathbf{R}(\Delta\Psi) = \exp\big(\boldsymbol{\tilde{Q}'}\big) \cdot \mathbf{R}(\Delta\Theta) \cdot \exp\big(-\boldsymbol{\tilde{Q}}\big). \tag{B.15}$$

Here, we defined $\Delta Q_{kk} = Q'_{kk} - Q_{kk}$ and we used Eqs. (A.23) and (A.28). From the isotropic part, Eq. (B.14), follows Eq. (2.23) in the main text using Eq. (2.11). Furthermore, the anisotropic part, Eq. (B.15), corresponds to Eq. (2.24) in the main text.

In order to obtain separate equations for $\Delta\tilde{N}_{ij}$ and $\Delta\Psi$, we express the three exponentials in Eq. (B.15) using Eq. (A.32):

$$\begin{aligned}&\left[\cosh(|\Delta\tilde{N}|)\boldsymbol{I} + \frac{\sinh(|\Delta\tilde{N}|)}{|\Delta\tilde{N}|}\boldsymbol{\Delta\tilde{N}}\right]\cdot\mathbf{R}(\Delta\Psi)\\ &\qquad = \left[\cosh(|\tilde{Q}'|)\boldsymbol{I} + \frac{\sinh(|\tilde{Q}'|)}{|\tilde{Q}'|}\boldsymbol{\tilde{Q}'}\right]\cdot\mathbf{R}(\Delta\Theta)\cdot\left[\cosh(|\tilde{Q}|)\boldsymbol{I} - \frac{\sinh(|\tilde{Q}|)}{|\tilde{Q}|}\boldsymbol{\tilde{Q}}\right].\end{aligned}\tag{B.16}$$

Expansion of the products on both sides yields

$$\begin{aligned}&\cosh(|\Delta\tilde{N}|)\,\mathbf{R}(\Delta\Psi) + \frac{\sinh(|\Delta\tilde{N}|)}{|\Delta\tilde{N}|}\boldsymbol{\Delta\tilde{N}}\cdot\mathbf{R}(\Delta\Psi)\\ &\qquad = \cosh(|\tilde{Q}'|)\cosh(|\tilde{Q}|)\,\mathbf{R}(\Delta\Theta) - \frac{\sinh(|\tilde{Q}'|)}{|\tilde{Q}'|}\frac{\sinh(|\tilde{Q}|)}{|\tilde{Q}|}\boldsymbol{\tilde{Q}'}\cdot\mathbf{R}(\Delta\Theta)\cdot\boldsymbol{\tilde{Q}}\\ &\qquad\quad + \cosh(|\tilde{Q}|)\frac{\sinh(|\tilde{Q}'|)}{|\tilde{Q}'|}\boldsymbol{\tilde{Q}'}\cdot\mathbf{R}(\Delta\Theta) - \cosh(|\tilde{Q}'|)\frac{\sinh(|\tilde{Q}|)}{|\tilde{Q}|}\,\mathbf{R}(\Delta\Theta)\cdot\boldsymbol{\tilde{Q}}.\end{aligned}\tag{B.17}$$

Now, we separate scaling rotation part and nematic part on both sides of Eq. (B.17) (Section A.1). For the scaling rotation part, we obtain:

$$\begin{aligned}&\cosh(|\Delta\tilde{N}|)\,\mathbf{R}(\Delta\Psi)\\ &\qquad = \cosh(|\tilde{Q}'|)\cosh(|\tilde{Q}|)\,\mathbf{R}(\Delta\Theta) - \frac{\sinh(|\tilde{Q}'|)}{|\tilde{Q}'|}\frac{\sinh(|\tilde{Q}|)}{|\tilde{Q}|}\boldsymbol{\tilde{Q}'}\cdot\mathbf{R}(\Delta\Theta)\cdot\boldsymbol{\tilde{Q}}.\end{aligned}\tag{B.18}$$

Using Eqs. (A.19) and (A.21), we obtain for the matrix product: $\boldsymbol{\tilde{Q}'}\cdot\mathbf{R}(\Delta\Theta)\cdot\boldsymbol{\tilde{Q}} = |\tilde{Q}'||\tilde{Q}|\,\mathbf{R}(2\Delta\Phi - \Delta\Theta)$. Here, $\Delta\Phi = \Phi' - \Phi$ and Φ, Φ' are the respective angles of the nematics $\boldsymbol{\tilde{Q}}$, $\boldsymbol{\tilde{Q}'}$. Then, we obtain from Eq. (B.18):

$$\begin{aligned}&\cosh(|\Delta\tilde{N}|)\,\mathbf{R}(\Delta\Psi)\\ &\qquad = \cosh(|\tilde{Q}'|)\cosh(|\tilde{Q}|)\,\mathbf{R}(\Delta\Theta) - \sinh(|\tilde{Q}'|)\sinh(|\tilde{Q}|)\,\mathbf{R}\big(2\Delta\Phi - \Delta\Theta\big).\end{aligned}\tag{B.19}$$

Now, we explicitly write down the xx and the yx components of Eq. (B.19):

$$\begin{aligned}\cosh(|\Delta\tilde{N}|)\cos(\Delta\Psi) &= \cosh\big(|\tilde{Q}'| + |\tilde{Q}|\big)\sin(\Delta\Phi)\sin(\Delta\Phi - \Delta\Theta)\\ &\quad + \cosh\big(|\tilde{Q}'| - |\tilde{Q}|\big)\cos(\Delta\Phi)\cos(\Delta\Phi - \Delta\Theta)\\ \cosh(|\Delta\tilde{N}|)\sin(\Delta\Psi) &= -\cosh\big(|\tilde{Q}'| + |\tilde{Q}|\big)\cos(\Delta\Phi)\sin(\Delta\Phi - \Delta\Theta)\\ &\quad + \cosh\big(|\tilde{Q}'| - |\tilde{Q}|\big)\sin(\Delta\Phi)\cos(\Delta\Phi - \Delta\Theta).\end{aligned}\tag{B.20}$$

Here, we used addition theorems for the trigonometric and the hyperbolic functions. The rotation angle $\Delta\Psi$ results from Eq. (B.20) for known $\cosh(|\Delta\tilde{N}|)$. The latter can be obtained by squaring and adding both equations (B.20):

$$\begin{aligned}\cosh\left(|\Delta\tilde{N}|\right) = \Big[&\cosh^2\big(|\tilde{Q}'|+|\tilde{Q}|\big)\sin^2\left(\Delta\Phi-\Delta\Theta\right)\\ &+\cosh^2\big(|\tilde{Q}'|-|\tilde{Q}|\big)\cos^2\left(\Delta\Phi-\Delta\Theta\right)\Big]^{1/2}.\end{aligned} \tag{B.21}$$

Finally, in order to obtain the shear nematic $\Delta\tilde{N}_{ij}$, we consider the symmetric, traceless part of Eq. (B.17), which reads:

$$\begin{aligned}&\frac{\sinh\left(|\Delta\tilde{N}|\right)}{|\Delta\tilde{N}|}\boldsymbol{\Delta\tilde{N}}\cdot\mathbf{R}(\Delta\Psi)\\ &\qquad=\cosh\left(|\tilde{Q}|\right)\frac{\sinh\left(|\tilde{Q}'|\right)}{|\tilde{Q}'|}\boldsymbol{\tilde{Q}'}\cdot\mathbf{R}(\Delta\Theta)-\cosh\left(|\tilde{Q}'|\right)\frac{\sinh\left(|\tilde{Q}|\right)}{|\tilde{Q}|}\mathbf{R}(\Delta\Theta)\cdot\boldsymbol{\tilde{Q}}.\end{aligned} \tag{B.22}$$

Multiplication by the transpose of Eq. (B.19) on both sides and simplification yields:

$$\begin{aligned}&\frac{\sinh\left(|\Delta\tilde{N}|\right)\cosh\left(|\Delta\tilde{N}|\right)}{|\Delta\tilde{N}|}\boldsymbol{\Delta\tilde{N}}\\ &\quad=\frac{1}{2}\sinh\Big[2\big(|\tilde{Q}'|-|\tilde{Q}|\big)\Big]\frac{\boldsymbol{\tilde{Q}'}}{|\tilde{Q}'|}\\ &\qquad+\frac{1}{2}\sinh\left(2|\tilde{Q}|\right)\frac{\boldsymbol{\tilde{Q}'}}{|\tilde{Q}'|}\cdot\Bigg(\sinh^2\left(|\tilde{Q}'|\right)\Big[\boldsymbol{I}-\mathbf{R}\big(-2[\Delta\Phi-\Delta\Theta]\big)\Big]\\ &\qquad\qquad+\cosh^2\left(|\tilde{Q}'|\right)\Big[\boldsymbol{I}-\mathbf{R}\big(2[\Delta\Phi-\Delta\Theta]\big)\Big]\Bigg).\end{aligned} \tag{B.23}$$

Here, we used addition theorems for the hyperbolic functions and Eqs. (A.18) and (A.19). With

$$\mathrm{R}_{ij}\big(2[\Delta\Phi-\Delta\Theta]\big)=\cos\big(2[\Delta\Phi-\Delta\Theta]\big)I_{ij}+\sin\big(2[\Delta\Phi-\Delta\Theta]\big)\epsilon_{ij}, \tag{B.24}$$

we finally obtain:

$$\begin{aligned}\frac{\sinh\left(|\Delta\tilde{N}|\right)\cosh\left(|\Delta\tilde{N}|\right)}{|\Delta\tilde{N}|}\boldsymbol{\Delta\tilde{N}}=&\frac{1}{2}\sinh\Big[2\big(|\tilde{Q}'|-|\tilde{Q}|\big)\Big]\frac{\boldsymbol{\tilde{Q}'}}{|\tilde{Q}'|}\\ &+\sinh\big(2|\tilde{Q}|\big)\cosh\big(2|\tilde{Q}'|\big)\sin^2\big(\Delta\Phi-\Delta\Theta\big)\frac{\boldsymbol{\tilde{Q}'}}{|\tilde{Q}'|}\\ &+\frac{1}{2}\sinh\big(2|\tilde{Q}|\big)\sin\big(2[\Delta\Phi-\Delta\Theta]\big)\frac{\boldsymbol{\epsilon}\cdot\boldsymbol{\tilde{Q}'}}{|\tilde{Q}'|}.\end{aligned} \tag{B.25}$$

Now, the shear nematic $\Delta\tilde{N}_{ij}$ can be obtained in two steps. First, the norm $|\Delta\tilde{N}|$ is computed from Eq. (B.21). Then, the norm $|\Delta\tilde{N}|$ is inserted into Eq. (B.25) in order to obtain the nematic $\Delta\tilde{N}_{ij}$.

B.2.2 Infinitesimal transformations

Here, we approximate Eqs. (B.20) and (B.25) to first order in the changes of the triangle properties $\Delta\tilde{Q}_{ij}$ and $\Delta\Theta$. To this end, we first introduce the following infinitesimal quantities: $\delta\tilde{N}_{ij} = \Delta\tilde{N}_{ij}$, $\delta\Psi = \Delta\Psi$, $\delta\tilde{Q}_{ij} = \Delta\tilde{Q}_{ij}$, $\delta|\tilde{Q}| = |\tilde{Q}'| - |\tilde{Q}|$, $\delta\Phi = \Delta\Phi$, and $\delta\Theta = \Delta\Theta$.

Now, from Eq. (B.25) follows to first order:

$$\boldsymbol{\delta\tilde{N}} = \delta|\tilde{Q}|\frac{\tilde{\boldsymbol{Q}}}{|\tilde{Q}|} + (\delta\Phi - \delta\Theta)\sinh\big(2|\tilde{Q}|\big)\frac{\boldsymbol{\epsilon}\cdot\tilde{\boldsymbol{Q}}}{|\tilde{Q}|}. \tag{B.26}$$

From Eq. (B.20), we obtain to first order:

$$\delta\Psi = \delta\Phi - (\delta\Phi - \delta\Theta)\cosh(2|\tilde{Q}|). \tag{B.27}$$

In order to show that Eqs. (B.26) and (B.27) correspond indeed to Eqs. (2.27) and (2.28) in the main text, we first note that $\delta\tilde{U}_{ij} = \delta\tilde{N}_{ij}$. Then, we transform Eq. (B.26) into:

$$\delta\tilde{U}_{ij} = \delta\tilde{Q}_{ij} - 2\delta\Phi\epsilon_{ik}\tilde{Q}_{kj} + (\delta\Phi - \delta\Theta)\frac{\sinh\big(2|\tilde{Q}|\big)}{|\tilde{Q}|}\epsilon_{ik}\tilde{Q}_{kj}. \tag{B.28}$$

Here, we applied Eq. (A.14). Now, we use Eq. (B.27), from which follows $\delta\Phi - \delta\Theta = (\delta\Phi - \delta\Psi)/\cosh(2|\tilde{Q}|)$. Insertion into Eq. (B.28) yields:

$$\delta\tilde{U}_{ij} = \delta\tilde{Q}_{ij} + \delta\tilde{J}_{ij}, \tag{B.29}$$

where we defined

$$\delta\tilde{J}_{ij} = -2\Big[c\delta\Psi + (1-c)\delta\Phi\Big]\epsilon_{ik}\tilde{Q}_{kj}. \tag{B.30}$$

Here, we also defined $c = \tanh\big(2|\tilde{Q}|\big)/2|\tilde{Q}|$.

Finally, in order to obtain Eq. (2.28), we transform Eq. (B.27) into:

$$\delta\Psi = \delta\Theta - (\delta\Phi - \delta\Theta)\Big[\cosh(2|\tilde{Q}|) - 1\Big]. \tag{B.31}$$

In order to transform this equation further, we first multiply Eq. (B.26) from right with $\boldsymbol{\epsilon}\cdot\tilde{\boldsymbol{Q}}$ and then take the trace. Using $\delta\tilde{U}_{ij} = \delta\tilde{N}_{ij}$, we obtain:

$$\delta\tilde{U}_{ij}\epsilon_{jk}\tilde{Q}_{ki} = 2(\delta\Phi - \delta\Theta)|\tilde{Q}|\sinh\big(2|\tilde{Q}|\big). \tag{B.32}$$

Now, we use this equation to substitute the term $\delta\Phi - \delta\Theta$ in Eq. (B.31). Then, we finally obtain:

$$\delta\Psi = \delta\Theta - \delta\Xi, \tag{B.33}$$

where we defined

$$\delta\Xi = \delta\tilde{U}_{ij}\epsilon_{jk}\tilde{Q}_{ki}\frac{\cosh(2|\tilde{Q}|) - 1}{2|\tilde{Q}|\sinh(2|\tilde{Q}|)}. \tag{B.34}$$

B.2.3 Shear-induced rotation of a single triangle

Here, we discuss Eq. (B.33) in detail. According to this equation, triangle rotation $\delta\Psi$ corresponds to the change in the triangle orientation angle Θ with an additional shear-induced contribution to triangle rotation $\delta\Xi$.

In this section, we illusterate the meaning of the shear-induced contribution to object rotation $\delta\Xi$ (Fig. B.1). We first consider a reference object, which is the Minerva head depicted in Fig. B.1A(i). Analogously to Section 2.1.2, we parametrize an arbitrarily rotated and deformed state of this head by the orientation angle Θ and by the shape tensor Q_{ij} (Fig. B.1A). The orientation angle Θ represents the direction in which the Minerva head looks in Fig. B.1A(ii). The symmetric, traceless part of the shape tensor Q_{ij} is the elongation nematic $\tilde{Q}_{ij}$, which is represented by the ellipse surrounding the Minerva head in Fig. B.1A(iii). The norm of the elongation nematic $|\tilde{Q}|$ determines the aspect ratio of the ellipse, which is $\exp(2|\tilde{Q}|)$ (Section A.4.5). The angle Φ of the elongation nematic $\tilde{Q}_{ij}$ determines the orientation of the long axis of the ellipse.

Now, we consider a particular sequence of infinitesimal pure shear deformations applied to the Minerva head (Fig. B.1B). For pure shear deformations, the components of the discrete displacement gradient read:

$$\delta U_{kk} = 0 \tag{B.35}$$

$$\delta\tilde{U}_{ij} \neq 0 \tag{B.36}$$

$$\delta\Psi = 0. \tag{B.37}$$

Surprisingly, although the rotational part of the displacement gradient is zero $\delta\Psi = 0$, the orientation of the Minerva head changes: $\delta\Theta \neq 0$ (see Fig. B.1B). According to Eq. (2.28), this orientation change is entirely shear-induced: $\delta\Theta = \delta\Xi$.

Let us discuss this effect in more detail. We apply the following shear to the triangle (blue double bars in Fig. B.1B):

$$\delta\tilde{U}_{ij} = |\delta\tilde{U}|\frac{\epsilon_{ik}\tilde{Q}_{kj}}{|\tilde{Q}|}. \tag{B.38}$$

Here, $|\delta\tilde{U}|$ denotes the norm of $\delta\tilde{U}_{ij}$. Thus, the shear axis is always tilted by an angle of $\pi/4$ with respect to the elongation axis (Section A.3.2).

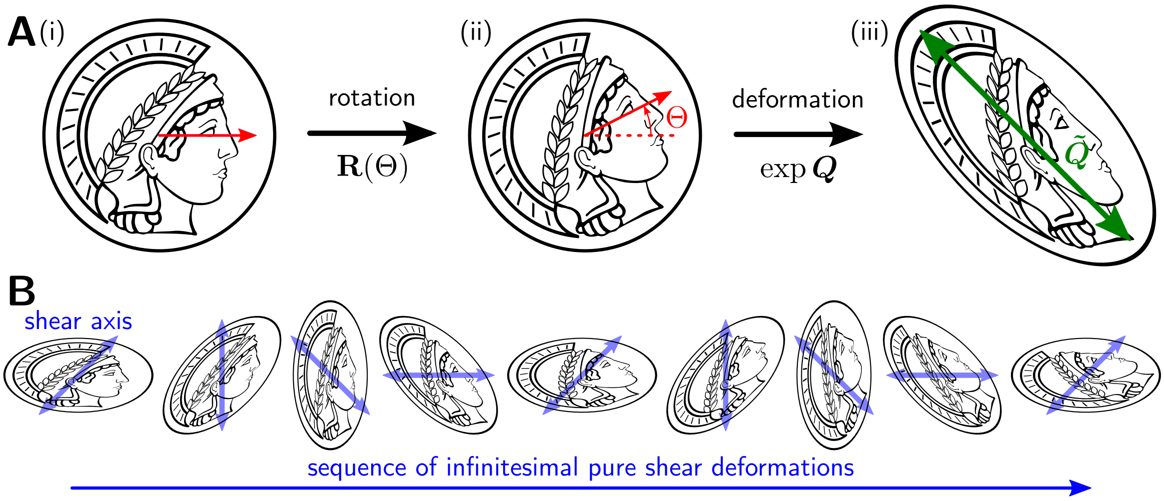

Figure B.1: Illustration for the shear-induced contribution $\delta\Xi$ to the rotation of an object. **(A)** We define a deformed state of the Minerva head (i) by two parameters, the orientation angle Θ and the symmetric shape tensor Q_{ij} (compare Fig. 2.4B). The orientation angle Θ corresponds to the direction in which the Minerva head looks (red arrow in (ii)). For the shape tensor Q_{ij}, we focus on its symmetric, traceless part, which is the elongation nematic $\tilde{Q}_{ij}$. The elongation nematic describes the shape of the ellipse surrounding the Minerva head (iii). **(B)** The elongated Minerva head is subject to subsequent pure shear deformations. Here, we show snapshots from such a sequence of infinitesimal deformations. The deformations are defined such that the shear axis (blue double arrows) is always tilted by an angle of $\pi/4$ with respect to the axis of elongation. As a consequence, the norm of the elongation $|\tilde{Q}|$ stays constant, but the axis of elongation Φ rotates (compare Fig. 2.8B). The deformations do not contain a rotational component: $\delta\Psi = 0$. However surprisingly, comparing the first, the middle, and the last snapshot illustrates that Θ increases. Here, we chose $|\tilde{Q}| = (\ln 2)/2$. With Eq. (B.41) follows that $\delta\Theta = \delta\Xi = 0.2\,\delta\Phi$.

The shear $\delta\tilde{U}_{ij}$ can be separated into components proportional and diagonal to $\tilde{Q}_{ij}$. Multiplying Eq. (2.27) with $\tilde{Q}_{jl}$ and taking the trace, we obtain:

$$\delta|\tilde{Q}| = 0. \tag{B.39}$$

Furthermore, multiplying Eq. (2.27) with $\epsilon_{jk}\tilde{Q}_{kl}$ and taking the trace, we obtain:

$$\delta\Phi = \frac{|\delta\tilde{U}|}{2c|\tilde{Q}|}. \tag{B.40}$$

Thus, the applied shear deformations keep the aspect ratio $\exp(2|\tilde{Q}|)$ of the ellipse constant, but rotate its long axis $\delta\Phi \neq 0$ (compare Fig. 2.8B and Fig. B.1B).

Now, we discuss the shear-induced contribution to rotation $\delta\Xi$. We obtain from Eq. (2.30):

$$\delta\Xi = \delta\Phi \left[1 - \frac{1}{\cosh\left(2|\tilde{Q}|\right)}\right]. \tag{B.41}$$

Here, we also used Eq. (B.40) and the relation $\delta\tilde{U}_{ij}\epsilon_{jk}\tilde{Q}_{ki} = 2|\delta\tilde{U}||\tilde{Q}|$, which follows from Eq. (B.38). Thus, for the discussed example, there is a constant ratio between the rotation of the Minerva head $\delta\Theta = \delta\Xi$ and the rotation of the long axis of the ellipse $\delta\Phi$.

B.3 Components of the displacement gradient for groups of triangles

B.3.1 Shear of a group of triangles in the absence of topological transitions

Here, we derive Eq. (2.40) in the main text, which describes the shear $\delta\tilde{U}^G_{ij}$ of a group G of triangles during an infinitesimal transformation. To this end, we coarse grain the shear on the single-triangle level $\delta\tilde{U}^m_{ij}$. From Eq. (2.35) follows:

$$\delta\tilde{U}^G_{ij} = \langle\delta\tilde{U}^m_{ij}\rangle_{\mathrm{i}}. \tag{B.42}$$

Here, the “i” at the averaging brackets indicates that for the area-weighted average, we use the respective areas in the initial state. We insert the single triangle shear from Eq. (2.27) into the above equation and obtain:

$$\delta\tilde{U}^G_{ij} = \left\langle\delta\tilde{Q}^m_{ij} + \delta\tilde{J}^m_{ij}\right\rangle_{\mathrm{i}}. \tag{B.43}$$

Now, we express $\langle\delta\tilde{Q}^m_{ij}\rangle_{\mathrm{i}}$ in terms of the change of $\tilde{Q}^G_{ij}$. To this end, we first rewrite $\langle\delta\tilde{Q}^m_{ij}\rangle_{\mathrm{i}}$ into:

$$\langle\delta\tilde{Q}^m_{ij}\rangle_{\mathrm{i}} = \langle\tilde{Q}'^m_{ij}\rangle_{\mathrm{i}} - \langle\tilde{Q}^m_{ij}\rangle_{\mathrm{i}}. \tag{B.44}$$

Here, $\tilde{Q}^m_{ij}$ and $\tilde{Q}'^m_{ij}$ denote the elongation of triangle m in the initial and final states, respectively. The change of $\tilde{Q}^G_{ij}$ can be written as:

$$\delta\tilde{Q}^G_{ij} = \langle\tilde{Q}'^m_{ij}\rangle_{\mathrm{f}} - \langle\tilde{Q}^m_{ij}\rangle_{\mathrm{i}}. \tag{B.45}$$

Here, the “f” at the averaging bracket indicates that for the area-weighted average, we use the respective areas in the final state. Thus, from Eqs. (B.44) and (B.45), we obtain:

$$\langle\delta\tilde{Q}^m_{ij}\rangle_{\mathrm{i}} = \delta\tilde{Q}^G_{ij} + \langle\tilde{Q}'^m_{ij}\rangle_{\mathrm{i}} - \langle\tilde{Q}'^m_{ij}\rangle_{\mathrm{f}}. \tag{B.46}$$

Now, we simplify $\langle \tilde{Q}'^{m}_{ij} \rangle_{\mathrm{i}} - \langle \tilde{Q}'^{m}_{ij} \rangle_{\mathrm{f}}$. By definition of the averaging bracket, it reads:

$$\langle \tilde{Q}'^{m}_{ij} \rangle_{\mathrm{i}} - \langle \tilde{Q}'^{m}_{ij} \rangle_{\mathrm{f}} = \frac{1}{A^G} \sum_{m \in G} A^m \tilde{Q}^m_{ij} - \frac{1}{A'^G} \sum_{m \in G} A'^m \tilde{Q}'^m_{ij}. \tag{B.47}$$

Here, the scalars A^m and A^G denote the respective areas in the initial state. The scalars A'^m and A'^G denote the areas in the final state. Because of Eq. (2.23), the following relation holds to linear order:

$$A'^m = (1 + \delta U^m_{kk}) A^m. \tag{B.48}$$

Using $\delta U^G_{kk} = \langle \delta U^m_{kk} \rangle_{\mathrm{i}}$, it follows that

$$A'^G = (1 + \delta U^G_{kk}) A^G. \tag{B.49}$$

Insertion of Eqs. (B.48) and (B.49) into Eq. (B.47) yields to linear order:

$$\langle \tilde{Q}'^{m}_{ij} \rangle_{\mathrm{i}} - \langle \tilde{Q}'^{m}_{ij} \rangle_{\mathrm{f}} = \delta U^G_{kk} \frac{1}{A^G} \sum_{m \in G} A^m \tilde{Q}'^m_{ij} - \frac{1}{A^G} \sum_{m \in G} A^m \delta U^m_{kk} \tilde{Q}'^m_{ij}. \tag{B.50}$$

To linear order, $\tilde{Q}'^m_{ij}$ can be replaced by $\tilde{Q}^m_{ij}$ on the right hand side:

$$\langle \tilde{Q}'^{m}_{ij} \rangle_{\mathrm{i}} - \langle \tilde{Q}'^{m}_{ij} \rangle_{\mathrm{f}} = \delta U^G_{kk} \tilde{Q}^G_{ij} - \left\langle \delta U^m_{kk} \tilde{Q}^m_{ij} \right\rangle_{\mathrm{i}}. \tag{B.51}$$

Substituting this equation together with Eq. (B.46) into Eq. (B.43), we obtain:

$$\delta \tilde{U}^G_{ij} = \delta \tilde{Q}^G_{ij} + \delta U^G_{kk} \tilde{Q}^G_{ij} - \left\langle \delta U^m_{kk} \tilde{Q}^m_{ij} \right\rangle_{\mathrm{i}} + \langle \delta \tilde{J}^m_{ij} \rangle_{\mathrm{i}}. \tag{B.52}$$

Now, we introduce the correlation term

$$\delta \tilde{D}^G_{ij} = -\Big(\left\langle \delta U^m_{kk} \tilde{Q}^m_{ij} \right\rangle_{\mathrm{i}} - \delta U^G_{kk} \tilde{Q}^G_{ij} \Big) + \Big(\left\langle \delta \tilde{J}^m_{ij} \right\rangle_{\mathrm{i}} - \delta \tilde{J}^G_{ij} \Big), \tag{B.53}$$

where $\delta \tilde{J}^G_{ij}$ is defined by Eq. (2.41). Inserted into Eq. (B.52), we finally obtain:

$$\delta \tilde{U}^G_{ij} = \delta \tilde{Q}^G_{ij} + \delta \tilde{J}^G_{ij} + \delta \tilde{D}^G_{ij}. \tag{B.54}$$

B.3.2 Rotation of a group of triangles

For the sake of completeness, we discuss in this section the rotational part of an infinitesimal transformation of a group G of triangles from an initial state to a final state. To this end, we first discuss transformations in the absence of topological transitions. Then, we discuss possibilities to take topological transitions into account. Finally, we summarize and discuss the large-scale vorticity of a cellular network.

Absence of topological transitions

Here, we discuss the rotational part $\delta\Psi^G$ of the displacement gradient U_{ij}^G of the group G. To this end, we proceed similar as in the previous section (Section B.3.1).

We define $\delta\Psi^G$ to be the antisymmetric part of U_{ij}^G analogously to Eq. (2.25). Then, from Eq. (2.35) follows:

$$\delta\Psi^G = \big\langle \delta\Psi^m \big\rangle_{\mathrm{i}}. \tag{B.55}$$

As in the previous section, the "i" at the averaging brackets indicates usage of the areas in the initial state. Inserting the relation for the single triangle rotation $\delta\Psi^m$, Eq. (2.28), yields:

$$\delta\Psi^G = \big\langle \delta\Theta^m - \delta\Xi^m \big\rangle_{\mathrm{i}}. \tag{B.56}$$

Analogously to the previous section, we obtain for $\langle\delta\Theta^m\rangle_{\mathrm{i}}$:

$$\langle\delta\Theta^m\rangle_{\mathrm{i}} = \delta\Theta^G + \delta U_{kk}^G\Theta^G - \big\langle \delta U_{kk}^m\Theta^m \big\rangle_{\mathrm{i}}. \tag{B.57}$$

Here, $\delta\Theta^G$ denotes the change of the absolute orientation angle Θ^G of the whole group. For the initial state, we defined Θ^G by: $\Theta^G = \langle\Theta^m\rangle_{\mathrm{i}}$.

Hence, we can rewrite Eq. (B.56) into:

$$\delta\Psi^G = \delta\Theta^G - \delta\Xi^G - \delta\Gamma^G. \tag{B.58}$$

Here, we defined:

$$\delta\Xi^G = \delta\tilde{U}_{ij}^G\epsilon_{jk}\tilde{Q}_{ki}^G\frac{\cosh(2|\tilde{Q}^G|) - 1}{2|\tilde{Q}^G|\sinh(2|\tilde{Q}^G|)}. \tag{B.59}$$

This is a mean field version of the shear-induced rotation term. Furthermore, we defined

$$\delta\Gamma^G = \Big(\big\langle \delta U_{kk}^m\Theta^m \big\rangle_{\mathrm{i}} - \delta U_{kk}^G\Theta^G\Big) + \Big(\big\langle \delta\Xi^m \big\rangle_{\mathrm{i}} - \delta\Xi^G\Big). \tag{B.60}$$

This is a correlation term. It is nonzero for inhomogeneous isotropic expansion and for inhomogeneous shear.

Topological transitions

Here, we propose a possibility to treat the rotational part during topological transitions. To this end, we make use of a continuous gauge freedom in the definition of Θ^m for a single triangle m. Then, we clarify that there exists always a particular gauge where the effect of any topological transition on average triangle rotation is zero.

First, we discuss the continuous gauge freedom in the definition of Θ^m. The orientation angle Θ^m of a given triangle m depends on the state of the equilateral reference triangle. More precisely, when rotating the reference triangle by an angle $\Delta\vartheta^m$, the orientation angle Θ^m of triangle m changes by:

$$\Theta^m \mapsto \Theta^m - \Delta\vartheta^m. \tag{B.61}$$

This follows directly from the way Θ^m is defined (Eq. (2.7) and Fig. 2.4B). Thus, there is a continuous gauge freedom, which is manifest in the choice of the angle $\Delta\vartheta^m$. Moreover, the gauge freedom is in principle local, because one has the freedom to choose for each individual triangle m of the triangulation a distinct reference triangle with a distinct $\Delta\vartheta^m$. However, for a given triangle m, the orientation of the reference triangle $\Delta\vartheta^m$ has to be constant in time. Then, the change of the angle Θ^m between initial and final states is a gauge invariant. Furthermore, triangle area, elongation and all triangle transformation properties including the rotation angle $\Delta\Psi^m$ are gauge invariants. Hence, relations derived so far that connect triangle state properties and triangle transformation properties are gauge invariant as well.

Now, we show that there is always a gauge where there is no effect of topological transitions on the average triangle rotation. Put differently, for a cellular network that is being constantly deformed, we define the $\Delta\vartheta^m$ for each triangle m such that the change in the average orientation angle Θ during each topological transition is zero. To this end, we first pick an arbitrary gauge for all triangles that are present in the initial state. Then, we subsequently define appropriate gauges for the triangles that are created during each occurring topological transition.

As an example, we discuss the case of a single T1 transition. Like in Section 2.1.5 on page 35, we consider the quadrilateral $\square$ that is made up of the two disappearing triangles m, n before the transition. The same quadrilateral is made up the two appearing triangles p, q after the transition. We define the orientation of the reference triangle $\Delta\vartheta$ for each the two appearing triangles p, q such that during the transition:

$$\Delta\Theta^{\boxtimes} = 0. \tag{B.62}$$

Here, we defined $\Delta\Theta^{\boxtimes} = \Theta^{\boxslash} - \Theta^{\boxbslash}$ with $\Theta^{\boxslash} = (A^p\Theta^p + A^q\Theta^q)/A^{\square}$ and $\Theta^{\boxbslash} = (A^m\Theta^m + A^n\Theta^n)/A^{\square}$. In order to fulfill Eq. (B.62), one could for instance define the angle $\Delta\vartheta^p$ for the triangle p such that

$$\Theta^p = \Theta^{\boxbslash}. \tag{B.63}$$

If one similarly defines $\Delta\vartheta^q$ for the triangle q such that $\Theta^q = \Theta^{\boxbslash}$, then Eq. (B.62) holds.

Similarly, one could define gauges for the triangles appearing during a cell division or during a T2 transition such that the average Θ does not change. This is always possible, because during each topological transition, at least one triangle appears and with it, one scalar degree of gauge freedom ($\Delta\vartheta$). This degree of freedom can always be fixed such that the change in average Θ is zero.

Large-scale vorticity

With a particular gauge as defined in the previous subsection, Eq. (B.58) remains true even in the presence of topological transitions. Here, we discuss the rotation rate instead of the absolute rotation. To this end, we introduce an infinitesimal time interval δt during which an infinitesimal transformation occurs. As in Section 2.2, we consider the whole triangulation as group G. Correspondingly, we omit the superscript G at all quantities.

We define the vorticity for the whole triangulation by:

$$\omega = \frac{\delta \Psi}{\delta t}. \tag{B.64}$$

Then, from Eq. (B.58) follows:

$$\omega = \frac{\mathrm{d}\Theta}{\mathrm{d}t} - \Xi - \Gamma. \tag{B.65}$$

Here, $\mathrm{d}/\mathrm{d}t$ denope the time derivative and the angle Θ denotes the average triangle orientation angle $\Theta = \langle \Theta^m \rangle$. We also defined

$$\Xi = \tilde{v}_{ij} \epsilon_{jk} \tilde{Q}_{ki} \frac{\cosh(2|\tilde{Q}|) - 1}{2|\tilde{Q}| \sinh(2|\tilde{Q}|)} \tag{B.66}$$

$$\Gamma = \Big(\langle v_{kk}^m \Theta^m \rangle - v_{kk} \Theta \Big) + \left(\frac{\langle \delta \Xi^m \rangle}{\delta t} - \Xi \right). \tag{B.67}$$

Here, the nematics $\tilde{v}_{ij}$ and $\tilde{Q}_{ij}$ denote average shear and triangle elongation as defined in Section 2.2. Furthermore, v_{kk}^m denotes the isotropic expansion rate for a single triangle m and v_{kk} denotes the average for the whole triangulation.

Hence, according to Eq. (B.65), large-scale vorticity corresponds to the change of the average triangle orientation angle. Furthermore, there may be a shear-induced rotation effect Ξ (Fig. B.1) and correlations contributing to large-scale vorticity Γ.

B.4 Integrated shear depends on the deformation protocol

Here, we show that the integrated network shear is path-dependent – also in the absence of topological transitions. More precisely, for a finite transformation of a cellular network from an initial state B to a final state C, the integrated shear depends not only on the states B and C, but also on the states passed in between.

We express this claim in the form of an equation. To this end, we consider a trajectory γ through the space of network states with initial state B and final state C.

More precisely, we define γ to be a continuously differentiable function mapping the closed interval $[0,1]$ to the space of network states with $\gamma(0)=B$ and $\gamma(1)=C$. Here, we do not consider topological transitions. Thus, a network state can be described by the set of all vertex positions $\boldsymbol{P}^m$.

Path independence of network shear means that there is a tensor-valued function $\tilde{H}_{ij}(B,C)$ that corresponds to the integrated network shear and that depends only on the states B and C:

$$\int_\gamma \delta\tilde{U}_{ij} = \tilde{H}_{ij}(B,C). \tag{B.68}$$

In particular, $\tilde{H}_{ij}(B,C)$ should be independent on the trajectory γ chosen between B and C. The integral on the left hand side of Eq. (B.68) is defined as follows. Consider a network state $\gamma(s)$ on the trajectory γ for some parameter value $s\in[0,1]$. The network shear for the infinitesimal transformation from the network state $\gamma(s)$ to the network state $\gamma(s+\mathrm{d}s)$ is defined by Eq. (2.36). We denote this network shear by $\mathrm{d}\tilde{U}_{ij}$. Then, the left hand side of Eq. (B.68) is defined by

$$\int_\gamma \delta\tilde{U}_{ij} = \int_0^1 \frac{\mathrm{d}\tilde{U}_{ij}}{\mathrm{d}s}\,\mathrm{d}s. \tag{B.69}$$

In this sense, the integral on the left hand side of Eq. (B.68) is a line integral through the space of network states.

Before proving the path dependence of integrated shear, we discuss two aspects of it. First, the path dependence of integrated shear has the following direct consequence. Consider a network transformation along a cyclic trajectory γ, where the initial and final network states are the same. Then, in general, the following equation holds:

$$\oint_\gamma \delta\tilde{U}_{ij} \neq 0. \tag{B.70}$$

Thus, although after a transformation of the network along the path γ, the final state of the network is the same as the initial state, the integrated shear is in general nonzero.

Second, note that in contrast to the integrated shear, the integral of the isotropic expansion δU_{kk} is path-independent:

$$\int_\gamma \delta U_{kk} = \ln\left(\frac{A^G(C)}{A^G(B)}\right). \tag{B.71}$$

Here, the integral on the left hand side is defined analogously to Eq. (B.69). The scalar $A^G(B)$ denotes the area of the triangulation in any state B. Eq. (B.71) can be obtained by integration of Eq. (2.38).

In Section B.4.1, we demonstrate that already for a single triangle, network shear is path-dependent. In Section B.4.2 we generalize the claim and show that there is no

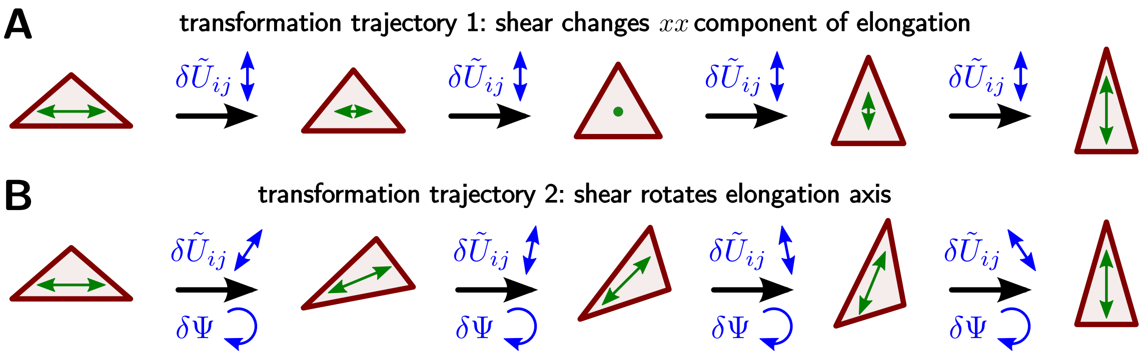
A
transformation trajectory 1: shear changes xx component of elongation
$\delta\tilde{U}_{ij}$
$\delta\tilde{U}_{ij}$
$\delta\tilde{U}_{ij}$
$\delta\tilde{U}_{ij}$
B
transformation trajectory 2: shear rotates elongation axis
$\delta\tilde{U}_{ij}$
$\delta\Psi$
$\delta\tilde{U}_{ij}$
$\delta\Psi$
$\delta\tilde{U}_{ij}$
$\delta\Psi$
$\delta\tilde{U}_{ij}$
$\delta\Psi$
y
x

Figure B.2: Illustration of two different finite transformations of a triangle with the same initial and final states. **(A)** The triangle elongation norm is continuously changed by shear along the y axis, which is perpendicular and parallel to the elongation axis (Figs. 2.6B and 2.8A). **(B)** The elongation axis is continuously rotated, because the shear axis is always at an angle of $\pi/4$ with respect to the elongation axis (Fig. 2.8B). For this transformation, there is a rotational component $\delta\Psi$ in the displacement gradient. It compensates for shear-induced rotation (Fig. B.1) such that $\delta\Theta = 0$.

integrating factor that would allow for a path-independent integration of shear – even if we combine it with possible rotations or area changes.

B.4.1 Single triangle

Here, we show that the integrated shear for a single triangle is path-dependent. To this end, we consider two different transformation trajectories that share the same initial and final states (Fig. B.2). In the initial state, the triangle is elongated along the x axis with the norm $\tilde{Q}_0$ and in the final state, it is elongated along the y axis with the same norm $\tilde{Q}_0$.

Now, we show that the integrated shear along both trajectories differ. First, we compute the integrated shear along the trajectory γ_A shown in Fig. B.2A. The triangle state at any point of the trajectory γ_A can be parametrized by $\tilde{Q}_{xx}$. The other component of the elongation nematic is always $\tilde{Q}_{xy} = 0$. Furthermore, the triangle area A is constant during the whole time and the orientation angle Θ is zero always. Then, the integrated shear is given by:

$$\int_{\gamma_A} \delta\tilde{U}_{ij} = \int_{\gamma_A} \delta\tilde{Q}_{ij}. \tag{B.72}$$

Here, we used Eq. (2.27). Integration yields:

$$\int_{\gamma_A} \delta\tilde{U}_{xx} = -2\tilde{Q}_0 \qquad \text{and} \qquad \int_{\gamma_A} \delta\tilde{U}_{xy} = 0. \tag{B.73}$$

Now, we compute the integrated shear along the trajectory γ_B shown in Fig. B.2B. The triangle state at any point of the trajectory γ_B can be parametrized by the angle Φ of the elongation nematic $\tilde{Q}_{ij}$. Then, the elongation nematic at any time is given by

$$\tilde{\boldsymbol{Q}} = \tilde{Q}_0 \begin{pmatrix} \cos(2\Phi) & \sin(2\Phi) \\ \sin(2\Phi) & -\cos(2\Phi) \end{pmatrix}. \tag{B.74}$$

Like above, the triangle area A is constant during the whole time and the orientation angle Θ is zero always. Then, the integrated shear is given by:

$$\int_{\gamma_B} \delta\tilde{U}_{ij} = \frac{\sinh(2\tilde{Q}_0)}{\tilde{Q}_0}\epsilon_{ik}\int_0^{\pi/2} \tilde{Q}_{kj}\mathrm{d}\Phi. \tag{B.75}$$

Here, we used Eq. (B.26) and $\delta\tilde{U}_{ij} = \delta\tilde{N}_{ij}$ with $\delta\Theta = 0$. In components, this equation reads:

$$\int_{\gamma_B} \boldsymbol{\delta\tilde{U}} = \sinh(2\tilde{Q}_0)\int_0^{\pi/2} \begin{pmatrix} -\sin(2\Phi) & \cos(2\Phi) \\ \cos(2\Phi) & \sin(2\Phi) \end{pmatrix} \mathrm{d}\Phi. \tag{B.76}$$

Thus, we find:

$$\int_{\gamma_B} \delta\tilde{U}_{xx} = -\sinh(2\tilde{Q}_0) \qquad \text{and} \qquad \int_{\gamma_B} \delta\tilde{U}_{xy} = 0. \tag{B.77}$$

This is different from the integrated shear along γ_A (Eq. (B.73)). In words, there is more shear needed to rotate the elongation nematic (trajectory B) than to change one component of the elongation nematic (trajectory A). Hence, the integrated shear is path-dependent already for a single triangle.

B.4.2 General proof

Here, we generalize the claim that there is no solution to Eq. (B.68). More precisely, we show that there is no integrating factor that would allow for a path-independent integration of shear. In addition, we also take rotation and isotropic expansion into account.

We first rephrase the question in mathematical terms. Be γ a trajectory through the space of network states with initial state B and final state C. Then, we ask if there is a tensor-valued function F_{ij} and a scalar-valued function G such that:

$$\int_\gamma F_{ij}\, \delta U_{ij} = G(C) - G(B). \tag{B.78}$$

Here, the integral on the left hand side is defined analogously to Eq. (B.69). The function F_{ij} should only depend on the current state of the network. Similarly, for any network state B, the function $G(B)$ should only depend on B. Clearly, there is always the trivial solution $F_{ij} = 0$ and $G = 0$. Here, we look for non-trivial solutions.[3]

To further clarify the meaning of Eq. (B.78), we split F_{ij} into its components:

$$F_{ij} = \frac{A_\triangle}{2}\left(f^{\mathrm{Tr}}\delta_{ij} + \tilde{f}_{ij} - \epsilon_{ij} f^{\mathrm{A}}\right). \tag{B.80}$$

Here, $A_\triangle$ denotes the area of the triangulation. The scalars f^{Tr} and f^{A} correspond to trace and antisymmetric part of F_{ij}, respectively. The nematic $\tilde{f}_{ij}$ corresponds to the symmetric, traceless part of F_{ij}. The factor $A_\triangle/2$ was introduced to simplify transformations that follow later.[4] Because F_{ij} should only depend on the network state, also f^{Tr}, f^{A}, and $\tilde{f}_{ij}$ should only depend on the network state. Insertion of Eq. (B.80) into Eq. (B.78) yields:

$$\int_\gamma A_\triangle \left[\frac{1}{2} f^{\mathrm{Tr}} \delta U_{kk} + \frac{1}{2}\tilde{f}_{ij}\delta\tilde{U}_{ij} + f^{\mathrm{A}}\delta\Psi\right] = G(C) - G(B). \tag{B.81}$$

Thus, we ask, whether there is a linear combination of integrated shear, integrated rotation, and integrated isotropic expansion that corresponds to the change in a state property. In particular, we ask whether there is a solution with nonzero shear coefficient $\tilde{f}_{ij}$.

---

[3] The fact that Eq. (B.78) is indeed a generalization of Eq. (B.68) can be seen as follows. First, the existence of solutions F_{ij}, G to Eq. (B.78) is equivalent to the existence of solutions F'_{ijkl}, G'_{kl} to

$$\int_\gamma F'_{ijkl}\, \delta U_{ij} = G'_{kl}(C) - G'_{kl}(B). \tag{B.79}$$

Here, F'_{ijkl} and G'_{kl} should also only depend on the current state of the network. The equivalence can be seen as follows. If there is a solution F_{ij}, G to Eq. (B.78), then $F'_{ijkl} = F_{ij}$ and $G'_{kl} = G$ for any $k, l \in \{x, y\}$ is a non-trivial solution to Eq. (B.79). Conversely, is there is a non-trivial solution F'_{ijkl}, G'_{kl} to Eq. (B.79), there are $k, l \in \{x, y\}$ such that second rank tensor F'_{ijkl} (for fixed k, l) is nonzero. Then, $F_{ij} = F'_{ijkl}$ and $G = G'_{kl}$ is a non-trivial solution to Eq. (B.78). Now, Eq. (B.68) is a special case of Eq. (B.79), where we choose $F'_{ijkl} = (\delta_{ik}\delta_{jl} + \delta_{jk}\delta_{il} - \delta_{ij}\delta_{kl})/2$ and G'_{kl} is chosen as follows. If Eq. (B.68) holds, one can always express $\tilde{H}_{ij}(B, C)$ as the difference of a state-dependent function $\tilde{K}$: $\tilde{H}_{ij}(B, C) = \tilde{K}_{ij}(C) - \tilde{K}_{ij}(B)$. We set $G'_{kl} = \tilde{K}_{kl}$.

[4] The factor $A_\triangle/2$ does not change our argument. In principle, one could also include it into f^{Tr}, f^{A}, and $\tilde{f}_{ij}$.

Proof of path-dependence of integrated shear

Here, we show that a solution to Eq. (B.81) does not exist with nonzero shear coefficient $\tilde{f}_{ij}$. To this end, we discuss the following counter example. Consider a triangulation consisting of three unconnected triangles, which we denote by 1, 2, and 3.[5] All three triangles have nonzero elongation norm: $|\tilde{Q}^m| \neq 0$ with $m \in \{1, 2, 3\}$. Here, we consider an infinitesimal deformation of these triangles without topological transitions.

We demonstrate that from Eq. (B.81) follows that the nematic $\tilde{f}_{ij}$ has to be zero. To this end, we first consider the infinitesimal version of Eq. (B.81):

$$A_\triangle \left[\frac{1}{2} f^{\mathrm{Tr}} \delta U_{kk} + \frac{1}{2} \tilde{f}_{ij} \delta \tilde{U}_{ij} + f^{\mathrm{A}} \delta \Psi \right] = \delta G. \tag{B.82}$$

Here, δG denotes an infinitesimal change of the state property G. We insert the components of δU_{ij}, which read:

$$\delta U_{kk} = \frac{1}{A_\triangle} \sum_{m=1}^{3} \delta A^m \tag{B.83}$$

$$\delta \tilde{U}_{ij} = \frac{1}{A_\triangle} \sum_{m=1}^{3} A^m \left(\delta |\tilde{Q}^m| \frac{\tilde{Q}^m_{ij}}{|\tilde{Q}^m|} + (\delta \Phi^m - \delta \Theta^m) \sinh\left(2|\tilde{Q}^m|\right) \frac{\epsilon_{ik} \tilde{Q}^m_{kj}}{|\tilde{Q}^m|} \right) \tag{B.84}$$

$$\delta \Psi = \frac{1}{A_\triangle} \sum_{m=1}^{3} A^m \Big(\delta \Theta^m \cosh\left(2|\tilde{Q}^m|\right) - \delta \Phi^m \Big[\cosh\left(2|\tilde{Q}^m|\right) - 1 \Big] \Big). \tag{B.85}$$

Here, we used Eqs. (2.26), (B.26) with $\delta \tilde{U}_{ij} = \delta \tilde{N}_{ij}$, (B.27), and (2.35). Insertion into Eq. (B.82) yields:

$$\begin{aligned} \delta G = \sum_{m=1}^{3} \Bigg[& \frac{1}{2} f^{\mathrm{Tr}} \delta A^m \\ & + A^m |\tilde{f}| \cos\left(2[\Phi_f - \Phi^m]\right) \delta |\tilde{Q}^m| \\ & + A^m |\tilde{f}| \sin\left(2[\Phi_f - \Phi^m]\right) (\delta \Phi^m - \delta \Theta^m) \sinh\left(2|\tilde{Q}^m|\right) \\ & + A^m f^{\mathrm{A}} \Big(\delta \Theta^m \cosh\left(2|\tilde{Q}^m|\right) - \delta \Phi^m \Big[\cosh\left(2|\tilde{Q}^m|\right) - 1 \Big] \Big) \Bigg]. \end{aligned} \tag{B.86}$$

Here, $|\tilde{f}|$ and Φ_f denote norm and angle of the nematic $\tilde{f}_{ij}$, respectively. We also used Eqs. (A.19) and (A.21) to derive Eq. (B.86).

---

[5] It is also possible to construct counter examples with more than three triangles. The important points here are, that there have to be at least three triangles and that they are unconnected. However, in principle the three triangles can also be connected by other triangles as discussed below.

We look for solutions of Eq. (B.86). Because G is a state quantity and because the state quantities A^m, $|\tilde{Q}^m|$, Φ^m, and Θ^m of all three triangles can be changed independently of each other, we can read the following partial derivatives off Eq. (B.86):

$$\frac{\partial G}{\partial A^m} = \frac{1}{2} f^{\mathrm{Tr}} \tag{B.87}$$

$$\frac{\partial G}{\partial |\tilde{Q}^m|} = A^m |\tilde{f}| \cos\left(2[\Phi_f - \Phi^m]\right) \tag{B.88}$$

$$\frac{\partial G}{\partial \Phi^m} = A^m |\tilde{f}| \sin\left(2[\Phi_f - \Phi^m]\right) \sinh\left(2|\tilde{Q}^m|\right) - A^m f^{\mathrm{A}} \left[\cosh\left(2|\tilde{Q}^m|\right) - 1\right] \tag{B.89}$$

$$\frac{\partial G}{\partial \Theta^m} = -A^m |\tilde{f}| \sin\left(2[\Phi_f - \Phi^m]\right) \sinh\left(2|\tilde{Q}^m|\right) + A^m f^{\mathrm{A}} \cosh\left(2|\tilde{Q}^m|\right) \tag{B.90}$$

for $m \in \{1,2,3\}$. Thus, these are in total 12 scalar equations.

Now, we show that $f^A = 0$ using the following Maxwell relations for $m, n \in \{1,2,3\}$:

$$\left(\frac{\partial}{\partial \Phi^m} + \frac{\partial}{\partial \Theta^m}\right) \frac{\partial G}{\partial A^n} = \frac{\partial}{\partial A^n} \left(\frac{\partial G}{\partial \Phi^m} + \frac{\partial G}{\partial \Theta^m}\right). \tag{B.91}$$

Separately evaluating left hand side and right hand side, we obtain:

$$\frac{1}{2} \left(\frac{\partial f^{\mathrm{Tr}}}{\partial \Phi^m} + \frac{\partial f^{\mathrm{Tr}}}{\partial \Theta^m}\right) = f^{\mathrm{A}} \delta_{mn} + A^m \frac{\partial f^{\mathrm{A}}}{\partial A^n}. \tag{B.92}$$

Now, we exploit the fact that the left hand side is independent on n. Insertion of $m = 3, n = 1$ and $m = 3, n = 2$ into Eq. (B.92) yields:

$$\frac{\partial f^{\mathrm{A}}}{\partial A^1} = \frac{\partial f^{\mathrm{A}}}{\partial A^2}. \tag{B.93}$$

Insertion of $m = 1, n = 1$ and $m = 1, n = 2$ into Eq. (B.92) yields:

$$f^{\mathrm{A}} + A^1 \frac{\partial f^{\mathrm{A}}}{\partial A^1} = A^1 \frac{\partial f^{\mathrm{A}}}{\partial A^2}. \tag{B.94}$$

With Eq. (B.93) finally follows $f^{\mathrm{A}} = 0$.

Finally, we show that $|\tilde{f}| = 0$ using the following Maxwell relations for $m, n \in \{1,2,3\}$:

$$\begin{aligned} &\left(\cos\left(2[\Phi_f - \Phi^m]\right) \frac{\partial}{\partial |\tilde{Q}^m|} + \frac{\sin\left(2[\Phi_f - \Phi^m]\right)}{\sinh\left(2|\tilde{Q}^m|\right)} \frac{\partial}{\partial \Phi^m}\right) \frac{\partial G}{\partial A^n} \\ &\quad = \frac{\partial}{\partial A^n} \left(\cos\left(2[\Phi_f - \Phi^m]\right) \frac{\partial G}{\partial |\tilde{Q}^m|} + \frac{\sin\left(2[\Phi_f - \Phi^m]\right)}{\sinh\left(2|\tilde{Q}^m|\right)} \frac{\partial G}{\partial \Phi^m}\right). \end{aligned} \tag{B.95}$$

Separately evaluating left hand side and right hand side, we obtain:

$$\frac{1}{2}\left(\cos\left(2[\Phi_f - \Phi^m]\right)\frac{\partial f^{\mathrm{Tr}}}{\partial|\tilde{Q}^m|} + \frac{\sin\left(2[\Phi_f - \Phi^m]\right)}{\sinh\left(2|\tilde{Q}^m|\right)}\frac{\partial f^{\mathrm{Tr}}}{\partial\Phi^m}\right) = |\tilde{f}|\delta_{mn} + A^m\frac{\partial|\tilde{f}|}{\partial A^n}. \tag{B.96}$$

For the right hand side, we used $f^A = 0$. Now, we exploit the fact that the left hand side is independent on n. Insertion of $m = 3, n = 1$ and $m = 3, n = 2$ into Eq. (B.96) yields:

$$\frac{\partial|\tilde{f}|}{\partial A^1} = \frac{\partial|\tilde{f}|}{\partial A^2}. \tag{B.97}$$

Insertion of $m = 1, n = 1$ and $m = 1, n = 2$ into Eq. (B.96) yields:

$$|\tilde{f}| + A^1\frac{\partial|\tilde{f}|}{\partial A^1} = A^1\frac{\partial|\tilde{f}|}{\partial A^2}. \tag{B.98}$$

With Eq. (B.97) finally follows $|\tilde{f}| = 0$. Hence, there is no solution to Eq. (B.81) with nonzero shear coefficient $\tilde{f}_{ij}$. In other words, integrated large-scale shear depends not only on the initial and final states, but on the trajectory of states passed – even if one adds a state-dependent factor and possible contributions by rotation and isotropic expansion.

General solution of Eq. (B.81)

From Eq. (B.87) follows that G and f^{Tr} depend only on $A_\triangle$. Then, Eq. (B.82) becomes:

$$f^{\mathrm{Tr}}(A_\triangle) = 2\frac{\mathrm{d}G(A_\triangle)}{\mathrm{d}A_\triangle}. \tag{B.99}$$

Here, we used Eq. (2.38). Thus, there is a solution of Eq. (B.81) for any differentiable function $G(A_\triangle)$. For instance, for $G(A_\triangle) = \ln(A_\triangle)$ we obtain Eq. (B.71).

Modification of the proof connecting the three triangles

The three unconnected triangles discussed above can be connected such that the proof still applies. Therefore, the triangulation consists of the three triangles already discussed, but additionally includes connecting triangles of vanishing area $A^m \to 0$. Their contribution to the large-scale deformation δU_{ij} is vanishing and hence, the above argument still applies.

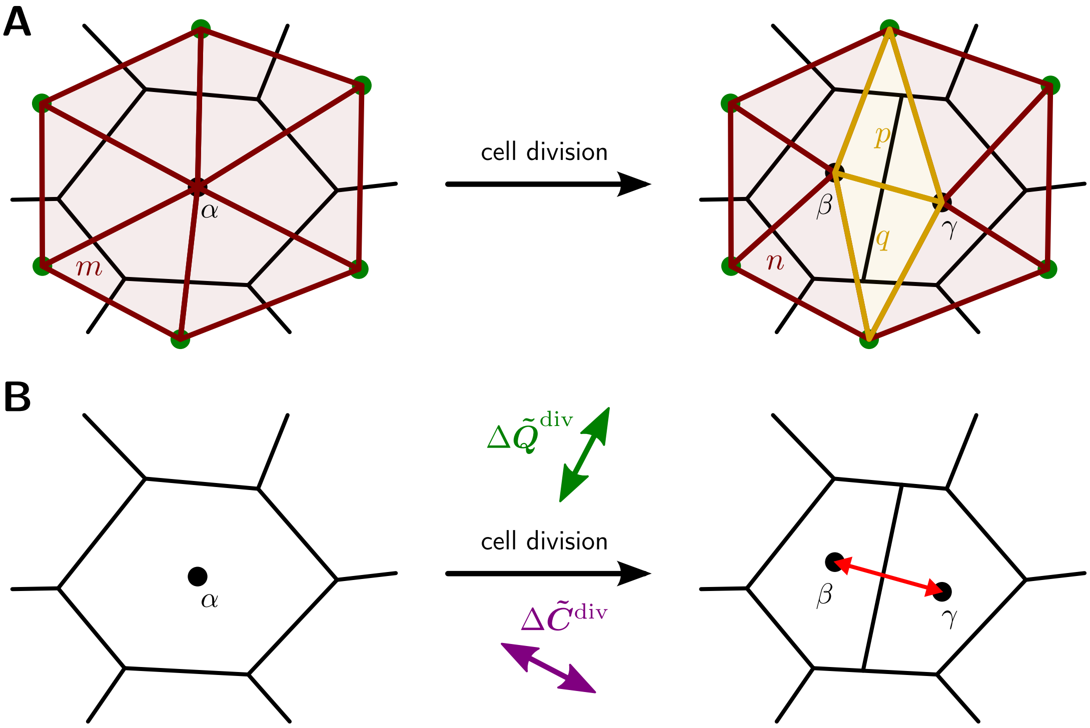

Figure B.3: Division of the N-sided cell α with $N = 6$. **(A)** Triangulation change due to the division. The shapes of the N triangles initially touching cell α change discontinuously. Also, two triangles, p and q, are newly created (yellow). **(B)** Typically, the axis of the nematic $\Delta\tilde{C}_{ij}$ (magenta double arrow) is approximately parallel to the division axis (red double arrow), which is defined by the line connecting the centers of the two daughter cells β and γ.

B.5 Shear contributions by single topological transitions

B.5.1 Cell divisions

Here, we discuss the contribution by a single cell division to local shear. To this end, we proceed in a similar way as for the T1 transitions in Section 2.1.5.

First, we note that during a single cell division, two additional triangles (p and q) appear (yellow triangles in Fig. B.3A). Also, the shape of all triangles that belonged to the mother cell α changes discontinuously upon division (red triangles). This is because one corner of each of these triangles is displaced from the center of cell α to the center of one of the daughters β or γ. Thus, in order to describe the effect of the cell division on local shear, we consider the group of all triangles that belonged to the mother cell α before the division (red triangles). For a N-sided cell α, these are N triangles. After the division, the group consists of the same triangles as before; but now, it also includes the two newly created triangles p and q. Thus, after the division, the group encompasses the two daughter cells β and γ.

Now, we discuss the contribution of the cell division to pure shear. Since the margin of the group does not move during the cell division, we obtain for the shear of the group:

$$\delta\tilde{U}_{ij}^{\text{div}} = 0. \tag{B.100}$$

However, like during the T1 transition, the average triangle elongation changes discontinuously. Before and after the division, the average elongation reads:

$$\tilde{Q}_{ij}^{\alpha} = \frac{1}{A^{\text{div}}}\sum_{m=1}^{N} A^m \tilde{Q}_{ij}^m \qquad \text{(before cell division)} \tag{B.101}$$

$$\tilde{Q}_{ij}^{\beta,\gamma} = \frac{1}{A^{\text{div}}}\left[A^p\tilde{Q}_{ij}^p + A^q\tilde{Q}_{ij}^q + \sum_{n=1}^{N} A^n\tilde{Q}_{ij}^n\right] \qquad \text{(after cell division)}, \tag{B.102}$$

respectively. Here, A^{div} denotes the total area of the group. We use different indices m and n for the N red triangles before and after the division to indicate that the elongation for each of these triangles changes discontinuously. For this reason and because of the two newly appearing triangles, the change of average triangle elongation is in general finite:

$$\Delta\tilde{Q}_{ij}^{\text{div}} = \tilde{Q}_{ij}^{\beta,\gamma} - \tilde{Q}_{ij}^{\alpha}. \tag{B.103}$$

Like for the T1 transitions, we introduce a contribution to shear by the cell division $\Delta\tilde{C}_{ij}^{\text{div}} = -\Delta\tilde{Q}_{ij}^{\text{div}}$. In analogy to Eq. (2.48), we obtain

$$\delta\tilde{U}_{ij}^{\text{div}} = \Delta\tilde{Q}_{ij}^{\text{div}} + \delta\tilde{J}_{ij}^{\text{div}} + \delta\tilde{D}_{ij}^{\text{div}} + \Delta\tilde{C}_{ij}^{\text{div}}. \tag{B.104}$$

We define the contributions $\delta\tilde{J}_{ij}^{\text{div}}$ and $\delta\tilde{D}_{ij}^{\text{div}}$ to be zero during the cell division.

The axis of the shear contribution by the cell division $\Delta\tilde{C}_{ij}^{\text{div}}$ is mostly close to the division axis connecting the two daughter cell centers (magenta and red double arrows in Fig. B.3B). This is because the triangles become typically squeezed perpendicular to division axis during the cell division such that $\Delta\tilde{Q}_{ij}^{\text{div}}$ is approximately perpendicular to the division axis (green double arrow).

B.5.2 T2 transitions

Here, we discuss the contribution by a single T2 transition to local shear. To this end we proceed in a similar way as for T1 transitions and cell divisions.

First, we discuss the triangulation changes induced by the T2 transition. Because we only allow for threefold vertices, we consider T2 transitions only for three-sided cells. Thus, during the T2 transition of a cell α, three triangles (m, n, and p) disappear and a single triangle (q) appears (Fig. B.4). Thus, we focus on the triangle-shaped

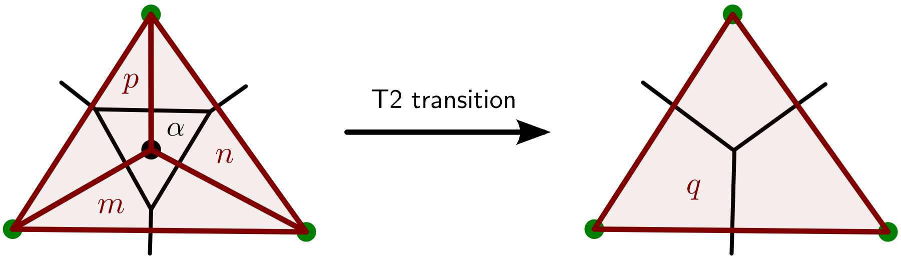

Figure B.4: T2 transition on the three-sided cell α. During the T2 transition, three triangles (m, n, and p) disappear and are replaced by a single triangle q.

group G that consists of the triangles m, n, and p before the T2 transition. After the T2 transition, it consists only of the triangle q.

The pure shear of G during the T2 transition reads

$$\delta \tilde{U}_{ij}^{\mathrm{T2}} = 0, \tag{B.105}$$

because the margin of G does not move. However, the average triangle elongation changes discontinuously:

$$\Delta \tilde{Q}_{ij}^{\mathrm{T2}} = \tilde{Q}_{ij}^{q} - \tilde{Q}_{ij}^{\alpha}. \tag{B.106}$$

Here, we defined the average elongation before and after the T2 transition by:

$$\tilde{Q}_{ij}^{\alpha} = \frac{1}{A^{\mathrm{T2}}}\left[A^m \tilde{Q}_{ij}^m + A^n \tilde{Q}_{ij}^n + A^p \tilde{Q}_{ij}^p\right] \qquad \text{(before T2 transition)} \tag{B.107}$$

$$\tilde{Q}_{ij}^{q} = \tilde{Q}_{ij}^{q} \qquad \text{(after T2 transition).} \tag{B.108}$$

Here, A^{T2} denotes the total area of the group. Similarly to above, we introduce a contribution to shear by the T2 transition $\Delta \tilde{E}_{ij}^{\mathrm{T2}} = -\Delta \tilde{Q}_{ij}^{\mathrm{T2}}$ and write analogously to Eq. (2.48):

$$\delta \tilde{U}_{ij}^{\mathrm{T2}} = \Delta \tilde{Q}_{ij}^{\mathrm{T2}} + \delta \tilde{J}_{ij}^{\mathrm{T2}} + \delta \tilde{D}_{ij}^{\mathrm{T2}} + \Delta \tilde{E}_{ij}^{\mathrm{T2}}. \tag{B.109}$$

We define the contributions $\delta \tilde{J}_{ij}^{\mathrm{T2}}$ and $\delta \tilde{D}_{ij}^{\mathrm{T2}}$ to be zero during the T2 transition.

B.6 Topological transitions at the network margin

Here, we discuss topological transitions at the network margin and how they affect the triangulation. We clarify how the sequence of cell centers along the triangulation margin changes due to the topological transitions. Also, we show that topological transitions at the network margin instantaneously change the part of the cellular network that is covered by triangles.

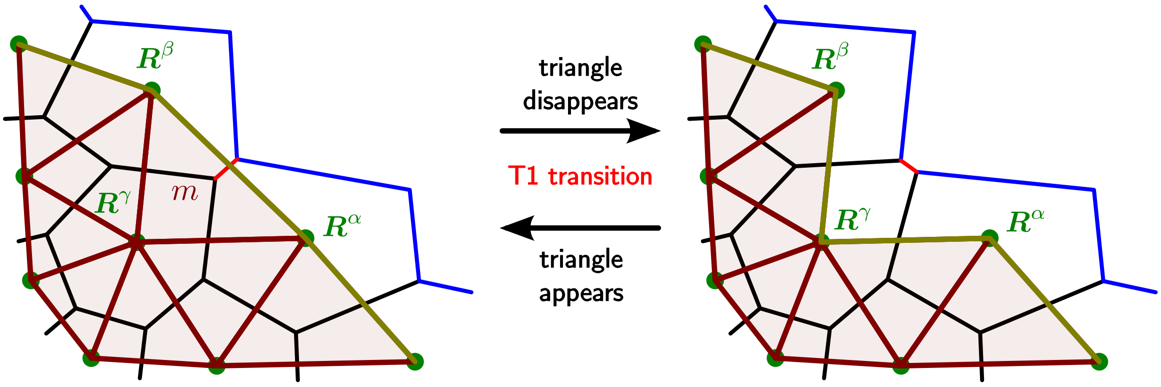

Figure B.5: Illustration of the effect of a T1 transition at the margin of the cellular network. Black solid lines show cell-cell interfaces. Blue solid lines show the margin of the cellular network. Red triangles indicate the triangulation and the yellow solid line indicates the margin of the triangulation. A T1 transition could occur from left to right or from right to left (bright red solid lines). From left to right: the T1 transition leads to removal of the triangle m. Also, the sequence of cell centers along the triangulation margin is changed from $\ldots, \boldsymbol{R}^\alpha, \boldsymbol{R}^\beta, \ldots$ to $\ldots, \boldsymbol{R}^\alpha, \boldsymbol{R}^\gamma, \boldsymbol{R}^\beta, \ldots$. From right to left: the triangle m is gained and the sequence of cell centers along the triangulation margin is changed.

B.6.1 T1 transitions

Fig. B.5 illustrates the effects of a single T1 transition at the network margin. If the T1 transition leads to the creation of a new margin bond, a triangle (m) disappears (from left to right in Fig. B.5). Therefore, the total area covered by triangles decreases. On the other hand, if the T1 transition removes a margin bond of the cellular network, a triangle is created (from right to left). Correspondingly, the total area covered by triangles increases.

Also, during T1 transitions at the margin, the sequence of cell centers along the triangulation margin changes. If a network margin bond is created, a further cell center is added to the triangulation margin (from left to right in Fig. B.5). Conversely, if a bond is removed from the network margin due to the T1 transition, a cell center is removed from the triangulation margin (from right to left).

B.6.2 Cell divisions

Fig. B.6 illustrates the possible effects of a single cell division at the network margin. There are two cases: Both daughter cells touch the network margin or only one daughter cell touches the network margin. First, if both daughter cells touch the network margin, one triangle is created by the cell division (Fig. B.6A). Also, in the sequence of cell centers along the triangulation margin, the mother cell center $\boldsymbol{R}^\alpha$ is replaced by

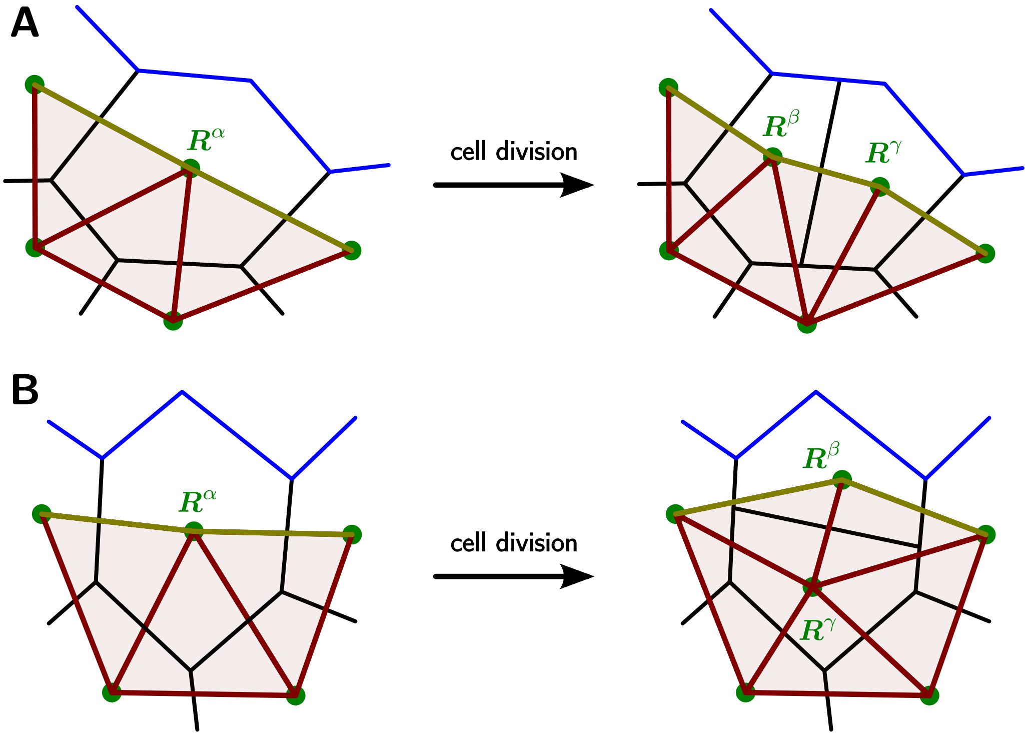

Figure B.6: Illustration of the effect of cell divisions at the margin of the cellular network. Black solid lines show cell-cell interfaces. Blue solid lines show the margin of the cellular network. Red triangles indicate the triangulation and the yellow solid line indicates the margin of the triangulation. There are two possible cases: **(A)** Both daughter cells touch the margin of the cellular network. Then, the sequence of cell centers along the triangulation margin changes from $\ldots, \boldsymbol{R}^{\alpha}, \ldots$ to $\ldots, \boldsymbol{R}^{\beta}, \boldsymbol{R}^{\gamma}, \ldots$. **(B)** Only one daughter cell touches the margin of the cellular network. Then, the sequence of cell centers along the triangulation margin changes from $\ldots, \boldsymbol{R}^{\alpha}, \ldots$ to $\ldots, \boldsymbol{R}^{\beta}, \ldots$.

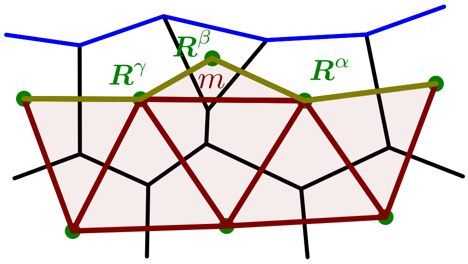

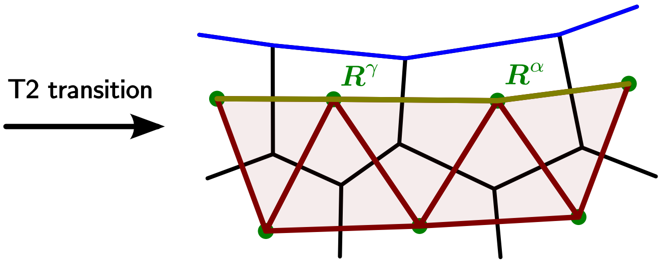

Figure B.7: Illustration of the effect of a T2 transition at the margin of the cellular network. Black solid lines show cell-cell interfaces. Blue solid lines show the margin of the cellular network. Red triangles indicate the triangulation and the yellow solid line indicates the margin of the triangulation. The triangle m disappears and the sequence of cell centers along the triangulation margin changes from $\dots, \boldsymbol{R}^\alpha, \boldsymbol{R}^\beta, \boldsymbol{R}^\gamma, \dots$ to $\dots, \boldsymbol{R}^\alpha, \boldsymbol{R}^\gamma, \dots$.

both daughter cell centers $\boldsymbol{R}^\beta, \boldsymbol{R}^\gamma$. Thus, the total area covered by triangles changes in general, too.

Second, if only one daughter cell β touches the network margin, two triangles are created by the division (Fig. B.6B). In the sequence of cell centers along the triangulation margin, the mother cell center $\boldsymbol{R}^\alpha$ is replaced by the daughter cell center $\boldsymbol{R}^\beta$. Because $\boldsymbol{R}^\beta$ is in general at a different position than $\boldsymbol{R}^\alpha$, the total area covered by triangles changes.

B.6.3 T2 transitions

Fig. B.7 illustrates the effects of a single T2 transition at the network margin. During a T2 transition, one triangle (m) is removed from the triangulation. Correspondingly, the total area covered by triangles decreases. In the sequence of cell centers along the triangulation margin, the center of the disappearing cell is removed.

B.7 Alternative triangulation

In this section, we shortly discuss an alternative method to tile the cellular network into triangles. We first define this alternative triangulation method. Then, we show that with this triangulation method, the shear created by T1 transitions is zero. Finally, we list advantages and disadvantages as compared to the triangulation method presented in the main text (Section 2.1.1).

The alternative triangulation method is defined as follows (Fig. B.8A). Each abutting pair of a bond b (blue solid line) and a cell α (green dot marks center) gives rise to a triangle (red dashed lines), which we label by $\langle\alpha, b\rangle$. The endpoints of the bond b are two vertices, which we label by m and n. Then, the corners of the triangle $\langle\alpha, b\rangle$

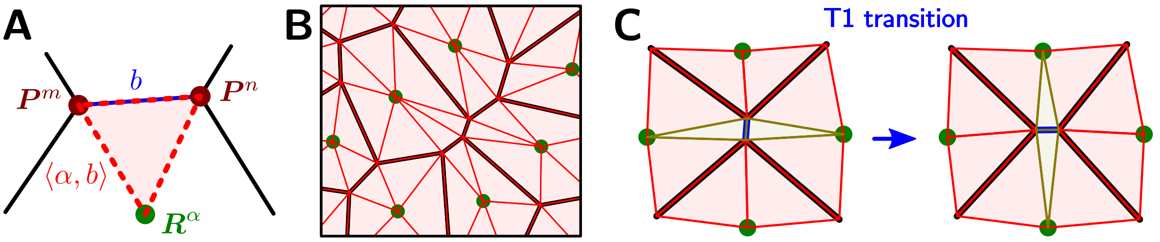

Figure B.8: Illustration of an alternative triangulation method. The cellular network is shown by solid black lines and cell centers are marked by green dots. **(A)** Each abutting pair of a bond b (blue solid line) and a cell α gives rise to a triangle $\langle\alpha,b\rangle$. The corners of the triangle $\langle\alpha,b\rangle$ are defined by the cell center $\boldsymbol{R}^\alpha$ (green dot) and the vertex positions $\boldsymbol{P}^m$ and $\boldsymbol{P}^n$ (dark red dots). **(B)** Triangulation of the network shown in Fig. 2.2A,C. Here, triangles are shown by solid red lines. **(C)** During the T1 transition on the blue bond, two triangles disappear (yellow solid lines) and two other triangles appear (also yellow solid lines). Upon appearance and disappearance, these triangles have area zero. Triangles that stay during the T1 transition are marked by red solid lines.

are defined by the center $\boldsymbol{R}^\alpha$ of cell α and the vertex positions $\boldsymbol{P}^m$ and $\boldsymbol{P}^n$. This rule uniquely defines a tiling of the entire cellular network into triangles (Fig. B.8B).

Now, we discuss the contribution of a single T1 transition to tissue shear (Fig. B.8C). In Section 2.1.5, we explained how a finite change of average triangle elongation during a topological transition can be considered as the shear caused by the topological transition. So, how does the average triangle elongation change during the T1 transition, here? During the T1 transition, there are no geometrical changes, i.e. the red triangles do not change their shape. Furthermore, two triangles disappear (yellow solid lines in Fig. B.8C) and two other triangles appear (also yellow solid lines). Upon appearance and disappearance, these triangles have area zero. As a consequence, the average triangle elongation does not change during the T1 transition, where we count in all triangles shown in Fig. B.8C. Hence, the shear by T1 transitions is always zero for the triangulation method discussed here.

Finally, we compare the triangulation method discussed here to the method presented in the main text (Section 2.1.1). For the method discussed here, each N-sided cell is split exactly into N triangles, whereas for the method discussed in the main text, a single triangle overlaps in general with several cells. Therefore, cellular quantities like cellular shear can be more accurately defined with the alternative triangulation. A further advantage of the alternative method discussed here is that the triangulation covers the entire cellular network including the margin part, which is not true for the method presented in the main part. However, the method presented in the main part is easier to apply to experimental data (Section B.8). The reason for this is that the alternative method discussed here uses vertex positions, which are hard to define for the artificial intermediate states introduced in Section B.8.1.

B.8 Application to experimental data

Here, we show how we extracted the average divergence v_{kk} and the average shear rate $\tilde{v}_{ij}$ of the flow field from experimental movies (shown as blue solid lines in Figs. 2.14, 2.16, 2.18, and 2.19). Also, we explain how we computed the average elongation $\tilde{Q}_{ij}$ and the individual components of the average shear rate $\tilde{v}_{ij}$ (curves shown in Figs. 2.16, 2.17, 2.19, and 2.20). To this end, we first segmented the movies as described in Section 2.3.1. As a result, we obtained snapshots of the cellular network at discrete time points t_i, which were separated by intervals of $\sim 5\,\text{min}$. Then, we computed the before-mentioned large-scale quantities for each time interval $t_i \dots t_{i+1}$ separately.

B.8.1 Introduction of artificial intermediate network states

In order to compute the components v_{kk} and $\tilde{v}_{ij}$ of the flow field, we constructed artificial intermediate network states between the observed states at the times t_i and t_{i+1} (Fig. B.9). These artificial states also allowed us to separate shear contributions by geometrical changes from shear contributions by topological transitions.

We constructed the artificial states as follows. First, we constructed the artificial state D out of the observed state E at time t_{i+1} (Fig. B.9D,E). Therefore, the state D is a copy of state E where all cell divisions are reverted that occur during the time interval $t_i \dots t_{i+1}$. To this end, any pair of daughter cells is fused to a mother cell. Then, the position of the mother cell center is defined as the midpoint between the former daughter cell centers.

Then, we constructed the artificial state B out of the observed state A at time t_i (Fig. B.9A,B). In the first place, the state B is a copy of state A. However, we removed all cells that were not present in the artificial state D anymore. These are the cells that undergo a T2 transition during the time interval considered.

Finally, we constructed the artificial network state C out of the artificial state B (Fig. B.9B,C). To this end, we moved all cell centers of state B to their respective positions in state D. Thus, the topology in state C is the same as in state B, but the cell centers are at the same positions as in state D.

Note that for the artificial states that we constructed here, not the whole network information is defined. Rather, each artificial state defines the information about the identities and positions of all cell centers. Also, it carries the neighborship information between cells. This is sufficient to triangulate the network state as described in the main text (Section 2.1.1). However, vertex positions are not defined in the artificial states.

B.8.2 Computation of the large-scale quantities

In order to compute the velocity gradient v_{ij}, we first compute the displacement gradient U_{ij} from the displacement of the triangulation margin between the network states

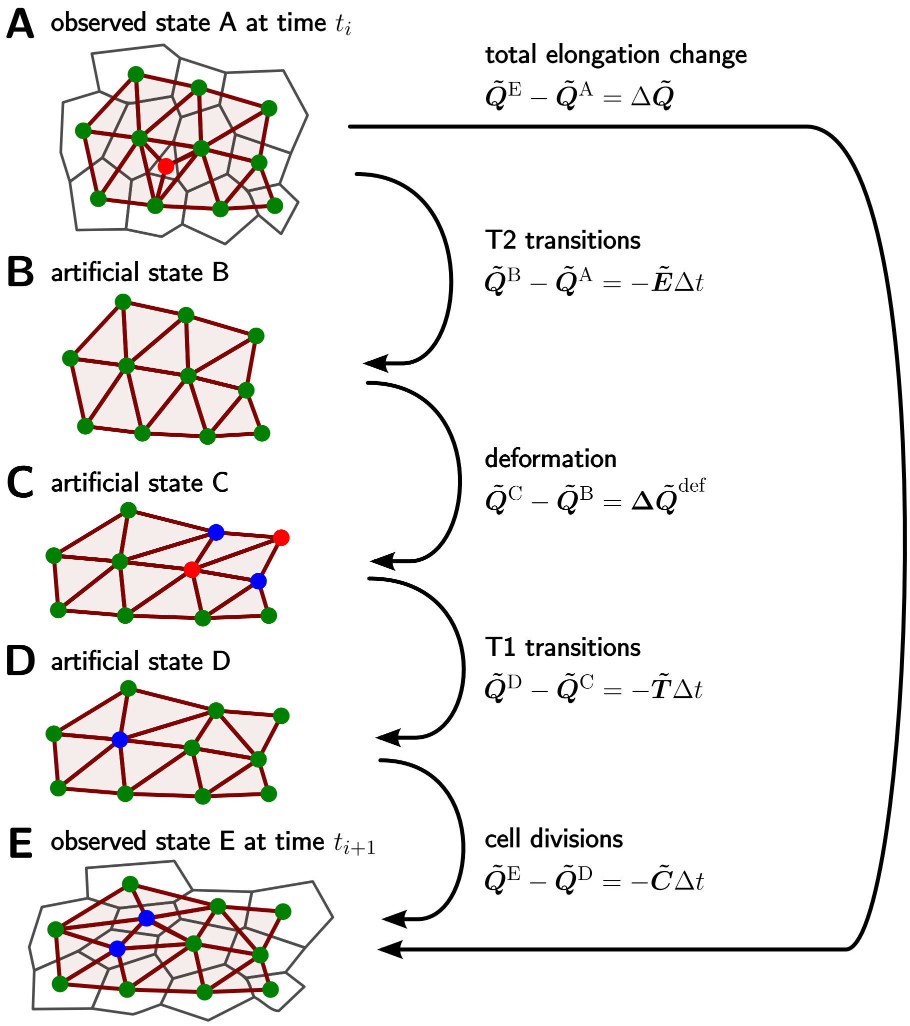
A observed state A at time t_i
B artificial state B
C artificial state C
D artificial state D
E observed state E at time t_{i+1}
total elongation change
$\tilde{\boldsymbol{Q}}^{\mathrm{E}} - \tilde{\boldsymbol{Q}}^{\mathrm{A}} = \Delta\tilde{\boldsymbol{Q}}$
T2 transitions
$\tilde{\boldsymbol{Q}}^{\mathrm{B}} - \tilde{\boldsymbol{Q}}^{\mathrm{A}} = -\tilde{\boldsymbol{E}}\Delta t$
deformation
$\tilde{\boldsymbol{Q}}^{\mathrm{C}} - \tilde{\boldsymbol{Q}}^{\mathrm{B}} = \Delta\tilde{\boldsymbol{Q}}^{\mathrm{def}}$
T1 transitions
$\tilde{\boldsymbol{Q}}^{\mathrm{D}} - \tilde{\boldsymbol{Q}}^{\mathrm{C}} = -\tilde{\boldsymbol{T}}\Delta t$
cell divisions
$\tilde{\boldsymbol{Q}}^{\mathrm{E}} - \tilde{\boldsymbol{Q}}^{\mathrm{D}} = -\tilde{\boldsymbol{C}}\Delta t$

Figure B.9: Illustration of artificial intermediate network states introduced for a given time interval $t_i \dots t_{i+1}$. Panels A and E illustrate observed network states at times t_i and t_{i+1}. In order to separate shear contributions by geometrical changes from shear contributions by topological transitions, we construct artificial intermediate network states (panels B-D). In all panels, cell centers are indicated by green dots and triangles are indicated by red solid lines. Additionally, in panels A and E, bonds are indicated by gray solid lines. The artificial network states are constructed such that between the states A and B, all T2 transitions occur. A cell undergoing a T2 transition is indicated by the red dot in panel A. Between states B and C, all displacements of cell centers occur. Between states C and D, all T1 transitions occur. Here, one T1 transition is shown: the two cells losing contact are marked by red dots and the two cells gaining contact are marked by blue dots in panel C. Between states D and E, all cell divisions occur. Here, we show one cell division: mother and daughter cells are marked by blue dots in panels D and E.

B and C using Eq. (2.36). Then, we compute the velocity gradient v_{ij} as follows:

$$v_{ij} = \frac{U_{ij}}{\Delta t}. \tag{B.110}$$

Here, $\Delta t = t_{i+1} - t_i$ denotes the duration of the time interval. The components v_{kk}, $\tilde{v}_{ij}$, and ω of the velocity gradient are defined as in Eq. (2.51) (v_{kk} and $\tilde{v}_{ij}$ are plotted as blue solid lines in Figs. 2.14, 2.16, 2.18, and 2.19).

We define the average elongation in any of the network states $X \in \{A, B, C, D, E\}$ analogously to Eq. (2.39):

$$\tilde{Q}^X_{ij} = \left\langle \tilde{Q}_{ij}(X) \right\rangle_X. \tag{B.111}$$

Here, the average $\langle \cdot \rangle_X$ of any triangle quantity q^m is defined by

$$\langle q^m \rangle_X = \frac{1}{A_\triangle(X)} \sum_m A^m(X) q^m. \tag{B.112}$$

The symbols $A_\triangle(X)$, $A^m(X)$, and $\tilde{Q}_{ij}(X)$ denote the value of the respective quantity in the state X. In Figs. 2.17 and 2.20, the average elongation $\tilde{Q}^X_{ij}$ was computed for the observed network states ($X = A, E$).

According to Eq. (2.53), the shear rate $\tilde{v}_{ij}$ decomposes as follows:

$$\tilde{v}_{ij} = \frac{\mathrm{D}\tilde{Q}_{ij}}{\mathrm{D}t} + \tilde{T}_{ij} + \tilde{C}_{ij} + \tilde{E}_{ij} + \tilde{D}_{ij}. \tag{B.113}$$

Now, we show how for a given time interval $t_i \dots t_{i+1}$, we computed the individual terms on the right hand side for the experimental movies. The corotational derivative of the average elongation is computed via:

$$\frac{\mathrm{D}\tilde{Q}_{ij}}{\mathrm{D}t} = \frac{\tilde{Q}^E_{ij} - \tilde{Q}^A_{ij}}{\Delta t} + \tilde{J}_{ij}. \tag{B.114}$$

Here, we compute $\tilde{J}_{ij}$ as follows:

$$\tilde{J}_{ij} = -2 \left[c\omega + (1-c) \frac{\Delta\Phi}{\Delta t} \right] \epsilon_{ik} \tilde{Q}^{\mathrm{avg}}_{kj}. \tag{B.115}$$

We defined $\tilde{Q}^{\mathrm{avg}}_{ij} = (\tilde{Q}^A_{ij} + \tilde{Q}^E_{ij})/2$ and $c = \tanh(2|\tilde{Q}^{\mathrm{avg}}|)/2|\tilde{Q}^{\mathrm{avg}}|$. Furthermore, $\Delta\Phi = \Phi^E - \Phi^A$, where Φ^A and Φ^E denote the respective angles of the nematics $\tilde{Q}^A_{ij}$ and $\tilde{Q}^E_{ij}$. The corotational derivative of the average elongation $\mathrm{D}\tilde{Q}_{ij}/\mathrm{D}t$ is plotted as green solid lines in Figs. 2.16 and 2.19.

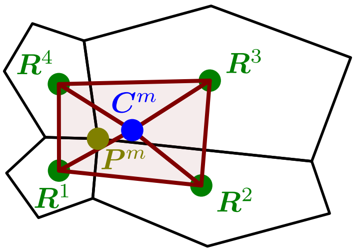

Figure B.10: Illustration of the triangulation method for the case of N-fold vertices with $N > 3$. Here, we show the fourfold vertex m at position $\boldsymbol{P}^m$ (yellow dot). It touches four cells with centers $\boldsymbol{R}^1, \ldots, \boldsymbol{R}^4$ (green dots). We defined the following tiling into triangles around vertex m. Four triangles were created (red solid lines). For each triangle, two corners were defined by two subsequent cell centers. The third corner was defined by the average position $\boldsymbol{C}^m$ of all four cell centers (blue dot).

We computed the shear contributions by topological transitions as follows:

$$\tilde{T}_{ij} = \frac{1}{\Delta t}\Big(\tilde{Q}^C_{ij} - \tilde{Q}^D_{ij}\Big) \tag{B.116}$$

$$\tilde{C}_{ij} = \frac{1}{\Delta t}\Big(\tilde{Q}^D_{ij} - \tilde{Q}^E_{ij}\Big) \tag{B.117}$$

$$\tilde{E}_{ij} = \frac{1}{\Delta t}\Big(\tilde{Q}^A_{ij} - \tilde{Q}^B_{ij}\Big). \tag{B.118}$$

They correspond to the red, cyan, and yellow solid lines in Figs. 2.16 and 2.19, respectively.

In the computation of the correlation contribution $\tilde{D}_{ij}$ we had to take into account that the time intervals are finite, here. Therefore, we included higher order terms:

$$\begin{aligned}\tilde{D}_{ij} = &-\frac{1}{\Delta t}\Big\langle \Big(U^m_{kk} + (U^m_{kk})^2/4 + (\Delta\Psi^m)^2 - |\tilde{U}^m|^2\Big)\tilde{Q}^m_{ij}(C)\Big\rangle_B \\ &+ \frac{1}{\Delta t}\Big\langle U^m_{kk} + (U^m_{kk})^2/4 + (\Delta\Psi^m)^2 - |\tilde{U}^m|^2\Big\rangle_B \Big\langle \tilde{Q}^m_{ij}(C)\Big\rangle_B \\ &+ \frac{1}{\Delta t}\Bigg\langle \left(1 + \frac{U^m_{kk}}{2}\right)\left(-2\Delta\Theta^m + 2\big(\Delta\Phi^m - \Delta\Theta^m\big)\left[\frac{\sinh\big(2|\tilde{\tilde{Q}}^m|\big)}{2|\tilde{\tilde{Q}}^m|} - 1\right]\right)\epsilon_{ik}\tilde{\tilde{Q}}^m_{kj} \\ &\qquad + \frac{U^m_{kk}}{2}\Big[\tilde{Q}^m_{ij}(C) - \tilde{Q}^m_{ij}(B)\Big]\Bigg\rangle_B \\ &- \tilde{J}_{ij}.\end{aligned} \tag{B.119}$$

Here, the displacement gradient U^m_{ij} for an individual triangle is defined between states B and C by Eqs. (2.14) and (2.18). Its components U^m_{kk}, $\tilde{U}^m_{ij}$, and $\Delta\Psi^m$ are defined analogously to Eq. (2.37). Also, we defined $\Delta\Theta^m = \Theta^m(C) - \Theta^m(B)$, $\Delta\Phi^m = \Phi^m(C) - \Phi^m(B)$, and $\tilde{\tilde{Q}}^m_{ij} = [\tilde{Q}^m_{ij}(B) + \tilde{Q}^m_{ij}(C)]/2$. The correlation contribution $\tilde{D}_{ij}$ is plotted as magenta solid lines in Figs. 2.16 and 2.19.

B.8.3 Triangulation for vertices with more than three bonds

In the main text (Section 2.1.1), we described a method to tile the cellular network into triangles. There, we restricted to the case where only threefold vertices appear. However, in the experimental data, we observed N-fold vertices with $N > 3$. Here, we explain how we created triangles for these vertices.

A N-fold vertex m touches N cells with centers $\boldsymbol{R}^\alpha$ with $\alpha = 1, \ldots, N$ (Fig. B.10). In order to create the triangles for a vertex with $N > 3$, we computed the average position $\boldsymbol{C}^m$ of the cell centers:

$$\boldsymbol{C}^m = \frac{1}{N} \sum_{\alpha=1}^{n} \boldsymbol{R}^\alpha. \tag{B.120}$$

Then, we created N triangles as follows. For each triangle, two of the corners were defined by two subsequent cell centers $\boldsymbol{R}^\alpha$ and $\boldsymbol{R}^{\alpha+1}$ with $\alpha = 1, \ldots, N-1$ (or $\boldsymbol{R}^N$ and $\boldsymbol{R}^1$). The third corner of each triangle was defined by the position $\boldsymbol{C}^m$. For $N = 3$, we created a single triangle as described in the main text.

Appendix C

Simple shear simulations using the vertex model

C.1 Implementation of the vertex model

C.1.1 Boundary conditions

Here, we explain how periodic boundary conditions and skewed periodic boundary conditions were implemented in the vertex model. To this end, we first discuss the internal representation of network states. Then, we explain and define the concept of periodicity vectors. Finally, both will help us to rigorously define the boundary conditions.

Representation of a network state

The entire information about a given network state can be subdivided into a topological and a geometrical part. Here, we discuss the geometrical part in detail. In the simulations presented in this work, the only geometrical information stored were the vertex positions $\boldsymbol{P}^m$ and the quantities L_x, L_y, and γ characterizing the boundary conditions. The scalars L_x and L_y denote the width and the height of the simulation box and we call the scalar γ the *simple shear variable*. All vertex positions fulfill:

$$0 \leq P_x^m < L_x \tag{C.1}$$

$$0 \leq P_y^m < L_y. \tag{C.2}$$

All other geometrical quantities used – like for instance bond lengths l^b, cell areas A^α, and cell perimeters L^α – were computed from the vertex positions together with the boundary conditions. To this end, bond vectors had to be computed first. All other geometrical quantities were then computed from bond vectors only. Thus, the only place where the boundary conditions come into play is the computation of bond vectors out of the vertex positions.

Periodicity of directed bonds

Now, we introduce the concept of periodicity for directed bonds. Here, a *directed bond* is a structure like a bond that additionally possesses the directional information about its starting point and its endpoint.

To illustrate the necessity of the periodicity concept for periodic boundary conditions, consider two given vertices m and n. For periodic boundary conditions, the vertex m can be connected to the vertex n by infinitely many different directed bonds b (Fig. C.1). Clearly, there is always the possibility to connect the vertex m directly to the vertex n without crossing the margin of the simulation box (Fig. C.1A). However, the directed bond b could also cross for instance once the upper margin of the simulation box before reaching vertex n (Fig. C.1B). It could also cross the right margin once (Fig. C.1C). Furthermore, it could cross the upper margin once and the right margin once or it could cross the upper margin twice (Fig. C.1D and E, respectively).

Hence, when computing bond vectors from vertex positions in our simulations, we also needed to select which one of these directed bonds is actually meant. To this end, we define a two-dimensional *periodicity vector*

$$\boldsymbol{q}^b = (q_x^b, q_y^b) \tag{C.3}$$

for each directed bond b. Here, q_x^b and q_y^b are integers. In general, for a directed bond b starting in m and ending in n, the periodicity vector $\boldsymbol{q}^b$ is defined as follows. When going from m to n, for each crossing of the right margin of the simulation box, q_x^b is increased by one. For each crossing of the left margin, q_x^b is decreased by one. Similarly, for each crossing of the upper (lower) margin, q_y^b is increased (decreased) by one. In each panel of Fig. C.1, the respective periodicity vector $\boldsymbol{q}^b$ is indicated.

Periodic boundary conditions without skew

Here, we show how for periodic boundary conditions, we computed the bond vector $\boldsymbol{l}^b$ of any directed bond b. If the directed bond b starts at vertex m, ends in vertex n, and has the periodicity vector $\boldsymbol{q}^b$, we write:

$$\boldsymbol{l}^b = \boldsymbol{P}^n - \boldsymbol{P}^m + \boldsymbol{B}(\boldsymbol{q}^b). \tag{C.4}$$

Here, the vector $\boldsymbol{B}(\boldsymbol{q}^b)$ characterizes the behavior of the periodic simulation box. More precisely, it corresponds to the way the integer periodicity vector $\boldsymbol{q}^b$ influences the bond vector $\boldsymbol{l}^b$. For periodic boundary conditions without skew, it is given by:

$$\boldsymbol{B}(\boldsymbol{q}^b) = \begin{pmatrix} q_x^b L_x \\ q_y^b L_y \end{pmatrix}. \tag{C.5}$$

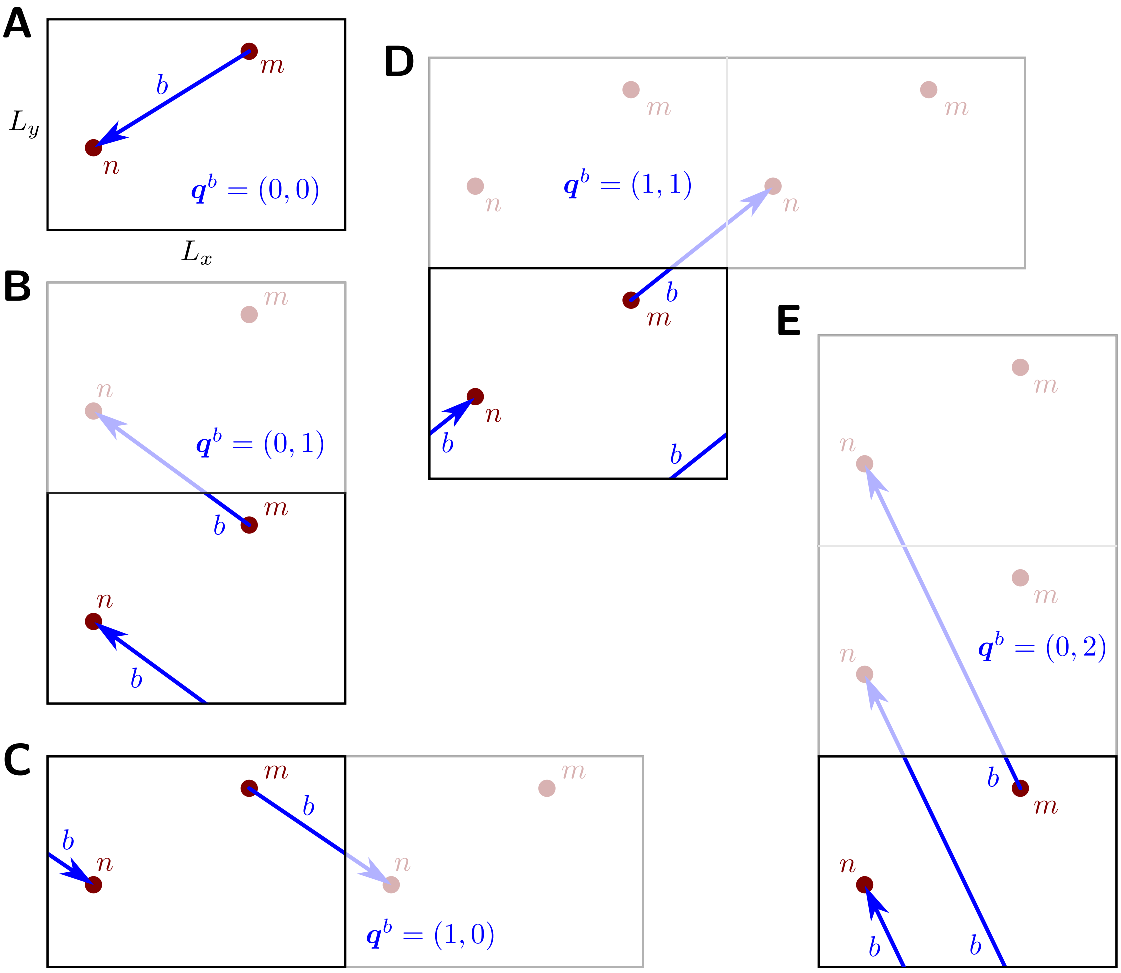
A
B
C
D
E
m
n
b
L_y
L_x
$\boldsymbol{q}^b = (0,0)$
$\boldsymbol{q}^b = (0,1)$
$\boldsymbol{q}^b = (1,0)$
$\boldsymbol{q}^b = (1,1)$
$\boldsymbol{q}^b = (0,2)$

Figure C.1: Illustrations of directed bonds b (blue arrows) starting in vertex m and ending in vertex n (red dots). For periodic boundary conditions, there are infinitely many possibilities to connect vertex m to vertex n. Here, we show a few examples. Each panel shows a different directed bond b corresponding to a different periodicity vector $\boldsymbol{q}^b$. **(A)** The periodicity vector is $\boldsymbol{q}^b = (0,0)$. Correspondingly, the directed bond b does not cross any margin of the simulation box. **(B)** The periodicity vector is $\boldsymbol{q}^b = (0,1)$ and correspondingly, b crosses the upper margin once. **(C)** The periodicity vector is $\boldsymbol{q}^b = (1,0)$ and b crosses the right margin once. **(D)** The periodicity vector is $\boldsymbol{q}^b = (1,1)$ and b crosses the upper margin and the right margin once, respectively. **(E)** The periodicity vector is $\boldsymbol{q}^b = (0,2)$ and b crosses the upper margin twice.

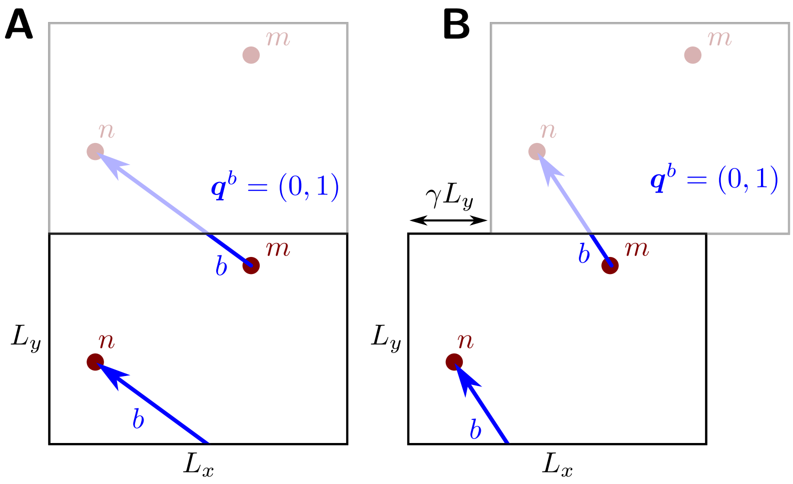

Figure C.2: Influence of the skew γL_y on the bond vector of the directed bond b (blue arrow). The periodicity of b is $\boldsymbol{q}^b = (0, 1)$. **(A)** Without skew. **(B)** With skew.

Because this is the only place where the boundary conditions come into play, Eq. (C.5) can formally be considered as the definition of the periodic boundary conditions without skew.

Skewed periodic boundary conditions

For skewed periodic boundary conditions, we additionally allow for a nonzero skew γL_y. Fig. C.2 illustrates how the skew affects the bond vector of a directed bond b with periodicity vector $\boldsymbol{q}^b = (0, 1)$: The skew γL_y is added to the x component of the bond vector. In contrast to that, for zero periodicity, the bond vector should not be affected by the skew because it does not cross the upper or lower margin of the simulation box (Fig. C.1A). In general, for an arbitrary periodicity vector, the vector $\boldsymbol{B}(\boldsymbol{q}^b)$ is given by:

$$\boldsymbol{B}(\boldsymbol{q}^b) = \begin{pmatrix} q_x^b L_x + q_y^b \gamma L_y \\ q_y^b L_y \end{pmatrix}. \tag{C.6}$$

Thus, for each crossing of the upper (lower) margin of the simulation box, the skew γL_y is added to (subtracted from) the x component of the bond vector $\boldsymbol{l}^b$. Eq. (C.6) can formally be considered as the definition of the skewed periodic boundary conditions.

C.1.2 Numerical minimization of the work function

In Section 3.1.1, we explained that force-balanced states of the vertex model are described as minima of a work function W. Here, we explain how such minima were numerically computed. To this end, we first show how the value of W was computed in a given network state. Then, we present how the multidimensional minimization of W was carried out.

As explained in Section C.1.1, the geometrical information of a network state was stored in terms of the vertex positions $\boldsymbol{P}^m$. For a given network state, the value of W

was computed as follows from the vertex positions $\boldsymbol{P}^m$. First, all bond vectors $\boldsymbol{l}^b$ were computed out of the vertex positions $\boldsymbol{P}^m$ using the boundary conditions as described in Section 3.1.1. Then, cell areas A^α, cell perimeters L^α, and bond lengths l^b were computed using only the bond vectors $\boldsymbol{l}^b$. Finally, the value of the work function W was computed using A^α, L^α, and l^b. Similarly, the gradient of W with respect to the position $\boldsymbol{P}^m$ of a given vertex m could be computed using only bond vectors.

A given network state was relaxed to a minimum of W using the conjugate gradient method [58, 155]. The conjugate gradient method uses successive *line minimizations*, each of which minimizes W along a line through the state space. The directions of these lines depend on the local gradient of W with respect to the vertex positions. In the simulations presented in this work, the state space corresponded to the space of network states. It consisted of all vertex positions $\boldsymbol{P}^m$ and, depending on the boundary conditions, of the quantities L_x, L_y, and γ. Moreover, after each line minimization, our algorithm checked for possible topological transitions according to Section C.1.3.

C.1.3 T1 and T2 transitions

Here, we explain how T1 and T2 transitions were realized in our simulations. During each minimization of the work function W, our algorithm checked for possible T1 and T2 transitions after each line minimization. During such a check, all bonds were tested for a T1 transition to occur and all cells were tested for a T2 transition to occur. The rules for these tests are explained in the following.

Note that in all vertex model simulations presented here, we allowed for N-fold vertices with $N \geq 3$. This is different from earlier vertex model implementations [58, 82, 121, 123], where only $N = 3$ was allowed. Allowing $N \geq 3$ greatly simplifies the treatment of T1 and T2 transitions.

T1 transitions

Because we allowed for N-fold vertices with $N \geq 3$, each *proper T1 transition* can be split into two *half T1 transitions*. During one proper T1 transition, a bond first shrinks to a single vertex (first half T1 transition). Then, the vertex expands again into a new bond (second half T1 transition).

Now, we define criteria for each type of half T1 transition separately. This is because half T1 transitions of both types may occur independently of each other. First, we discuss the shrinkage of a bond. A bond b was shrunk by a half T1 transition whenever its length l^b was smaller than a cutoff length parameter Θ_{T1}:

$$l^b < \Theta_{\mathrm{T1}}. \tag{C.7}$$

In all simulations, we set $\Theta_{\mathrm{T1}} = 10^{-6}$ in dimensionless units. Upon shrinkage of a bond b, both vertices of bond b were fused into a single vertex.

Second, to test whether a bond b should be expanded, we proceeded as follows. We tested every possibility to split a given vertex m into two vertices n and p. Then, we tested if the dimensionless force $\boldsymbol{F}^{n,p}$ that would drive n and p apart could overcome the effective line tension Λ^b_{eff} by a newly created bond b between n and p:

$$|F^{n,p}| > \Lambda^b_{\text{eff}}. \tag{C.8}$$

Here, $|F^{n,p}|$ denotes the norm of the force $\boldsymbol{F}^{n,p}$ and Λ^b_{eff} is given by

$$\Lambda^b_{\text{eff}} = \Lambda_0 + \Gamma(L^\alpha + L^\beta). \tag{C.9}$$

The cells α and β are the cells that would become neighbors through expansion of bond b. Hence, the norm $|F^{n,p}|$ was compared to the effective line tension Λ^b_{eff}, which includes the baseline line tension Λ_0 and the contributions of the perimeter contractility of the cells α and β. Line tension fluctuations were not included.

If the criterion Eq. (C.8) was fulfilled for a vertex m, we picked the possibility of splitting m into two vertices n, p for which the difference $|F^{n,p}| - \Lambda^b_{\text{eff}}$ was maximal. Then, we created the bond b connecting n and p. The positions of the new vertices were chosen as follows. The position of n was the same as that of m before. However, the position of vertex p was chosen such that the bond vector $\boldsymbol{l}^b$ of b was given by

$$\boldsymbol{l}^b = \frac{\boldsymbol{F}^{n,p}}{|F^{n,p}|} c_{\text{T1}} \Theta_{\text{T1}}. \tag{C.10}$$

Here, c_{T1} is a scalar parameter. In all simulations, we set $c_{\text{T1}} = 10$. Clearly, c_{T1} must be larger or equal to one, because otherwise, a bond would be shrunk again immediately after it was expanded. In Eq. (C.10) the force $\boldsymbol{F}^{n,p}$ is used to define the direction of the new bond.

Occasionally, we observed oscillations of vertex splitting and bond shrinkage. In order to prevent this, we introduced a maximum number n_{T1} of T1 splittings that could occur during a single minimization on a single vertex m. We set this number to $n_{\text{T1}} = 10$. When it was reached for a vertex m, this vertex could not be split anymore during the ongoing minimization.

T2 transitions

Allowing for N-fold vertices with $N \geq 3$ greatly simplified the implementations of T2 transitions. Before, for a T2 transition on a n-sided cell α, the number sides of α had to be reduced to three by subsequent T1 transitions [58]. Then, α could be shrunk to a three-fold vertex. In contrast to that, in this work, such a cell α was immediately shrunk to a n-fold vertex.

A cell α was shrunk to a vertex whenever its area became smaller than the cutoff

Table C.1: Parameter values used for the growth simulations presented in Sections 3.1.3 and C.2. The varied parameters are marked by ellipses "...". All parameter values are given in dimensionless units (Section 3.1.2, page 53).

Parameter	**Value**
mechanics	
perimeter elasticity Γ	0.04
baseline line tension Λ_0	0.12
line tension fluctuation amplitude Λ_F	$0.02 \ldots 0.10$
topological transitions	
T1 bond shrinkage cutoff Θ_{T1}	10^{-6}
bond length factor for T1 vertex splitting c_{T1}	10
maximum number of T1 splittings of a vertex per minimization n_{T1}	10
T2 cell area cutoff Θ_{T2}	10^{-3}
time scales	
average cell cycle length τ_{div}	$1 \ldots 100$
numerical time step Δt	0.01

area parameter Θ_{T2}:

$$A^{\alpha} < \Theta_{\mathrm{T2}}. \tag{C.11}$$

In all simulations, we set $\Theta_{\mathrm{T2}} = 10^{-3}$ in dimensionless units.

C.2 Growth simulation details

Here, we present the technical details for the growth simulations presented in Section 3.1.3. Starting from a relaxed pattern of 6×6 hexagonal cells, we simulated time steps of length $\Delta t = 0.01$ for a total simulation time of τ_{div}, which varied between $\tau_{\mathrm{div}} = 1$ and $\tau_{\mathrm{div}} = 100$ in dimensionless units. Table C.1 summarizes all parameter values used.

Each time step consisted in the following parts. First, we checked if a cell should divide. In a given time step, a given cell divided with a probability of $\Delta t/\tau_{\mathrm{div}}$ – independent of earlier divisions and independent of divisions of other cells. Cell division was implemented as in ref. [58] without doubling of the preferred cell area and with isotropic orientation of the division furrow. Afterwards, we updated the line tension noise η^b for each bond b of the network (Section 3.1.2). Finally, the network was relaxed to a new minimum of the work function (Section C.1.2). For the minimization, the width and height of the simulation box L_x and L_y were kept free, but the simple shear variable was fixed to zero: $\gamma = 0$. Put differently, for the minimization of W, not only the vertex positions $\boldsymbol{P}^m$ were varied, but also L_x and L_y.

Table C.2: Parameter values used for the simple shear simulations presented in Sections 3.2 and C.3.1. The varied parameters are marked by ellipses "...". All parameter values are given in dimensionless units (Section 3.1.2, page 53).

Parameter	**Value**
mechanics	
perimeter elasticity Γ	0.04
baseline line tension Λ_0	0.12
line tension fluctuation amplitude Λ_F	$0.02 \ldots 0.10$
topological transitions	
T1 bond shrinkage cutoff Θ_{T1}	10^{-6}
bond length factor for T1 vertex splitting c_{T1}	10
maximum number of T1 splittings of a vertex per minimization n_{T1}	10
T2 cell area cutoff Θ_{T2}	10^{-3}
time scales	
simple shear rate $\dot{\gamma}$	$0 \ldots 1$
numerical time step Δt	0.01

C.3 Simple shear simulations

C.3.1 Simulation details

Here, we present the technical details for the simple shear simulations discussed in Section 3.2. Starting from a relaxed pattern of 10×10 hexagonal cells, we simulated time steps of length $\Delta t = 0.01$. The total simulation time T depended on the line tension fluctuation amplitude Λ_F. For $\Lambda_F \leq 0.04$, we set $T = 1000$ and for $\Lambda_F > 0.04$, we set $T = 100$. Table C.2 summarizes all parameter values used.

Each time step consisted in the following parts. First, we updated the line tension noise η^b for each bond b of the network (Section 3.1.2). Then, the simple shear variable γ was increased by $\dot{\gamma}\Delta t$, where the simple shear rate $\dot{\gamma}$ is a simulation parameter, here. Finally, the network was relaxed to a new minimum of the work function (Appendix C.1.2). During the minimization, the simple shear variable γ and the simulation box dimensions L_x and L_y were kept constant. Thus, for the minimization of W, only the vertex positions $\boldsymbol{P}^m$ were varied.

In order to ensure a constant number of cells, we proceeded as follows. Upon each T2 transition, we forced the division of a randomly chosen cell. Cell division was implemented as in ref. [58] without doubling of the preferred cell area and with isotropic orientation of the division furrow.

C.3.2 Fluctuations inhibit shear banding

Here, we develop a method to quantitatively test for the appearance of shear bands in our simple shear simulations. Using this method, we find that even for high shear rates ($\dot{\gamma} = 1$), shear bands could be prevented by line tension fluctuations with an amplitude of at least $\Lambda_F \geq 0.02$.

Quantitative characterization of shear bands

We first develop a quantitative method to detect the appearance of shear bands. The appearance of shear bands corresponds to inhomogeneities in the shear field. In particular, a shear band is a region where most of the shear is localized. In simple shear simulations without fluctuations, we observe the formation of a single shear band that persisted until the end of the simulation. But also for small fluctuation amplitude, we observed shear bands. However occasionally, they disappeared and another shear band appeared in a different position. Here, we quantify the average persistence of shear bands.

In order to quantify the persistence of shear bands, we focus on T1 transitions and on the positions where they occur. When a shear band is formed, most T1 transitions would occur within this shear band. In contrast to that, when the shear is distributed throughout the whole simulation box, also the T1 transitions occur uniformly distributed within the whole simulation box. Thus, in order to quantify the persistence of shear bands, we measure spatio-temporal correlations in the occurrence of T1 transitions. In particular, we choose to look for correlations in the occurrence of T1 vertex splittings.[1]

Now, we define spatio-temporal correlations in the occurrence of T1 vertex splittings. For the sake of clarity, we first present the definition in a continuous description. Afterwards, we present the discrete definition used to analyze the simulations.

We start with a locally averaged rate density of T1 splittings that varies in space and time $\rho(\boldsymbol{r}, t)$. Then, the total rate of T1 splittings $r(t)$ is given by the integral:

$$r(t) = \int \rho(\boldsymbol{r}, t)\, \mathrm{d}^2 r. \tag{C.12}$$

Here, we integrate over the whole simulation box.

Typically, the shear bands we observed were roughly parallel to the x axis. Therefore, all T1 transitions occurring in a shear band have similar y coordinates. Therefore, in order to quantify the persistence of a shear band, we first define a complex number $p(t)$ that relates to the average y position of all T1 splittings at a time t:

$$p(t) = \int \rho(\boldsymbol{r}, t) \exp\left(\frac{2\pi \mathrm{i} r_y}{L_y}\right) \mathrm{d}^2 r. \tag{C.13}$$

---

[1] Of course, one could alternatively look for correlations in T1 bond shrinkages or both.

Here, we integrate over the whole simulation box, the scalar r_y is the y component of the integration variable $\boldsymbol{r}$, and i is the imaginary unit. In this equation, the y position r_y of a single T1 vertex splitting is taken into account by the complex number $\exp(2\pi \mathrm{i} r_y/L_y)$, which has norm one. We choose this representation because of periodicity in y direction. For the average y position of T1 splittings $\bar{y}$, we would then have $p = \exp(2\pi \mathrm{i}\bar{y}/L_y)$. From a different perspective, one could say that $p(t)$ corresponds to the first Fourier mode of $\rho(\boldsymbol{r}, t)$ with respect to the y axis.

In order to measure the average persistence of shear bands, we look at the persistence of the average y position of the T1 splittings. Therefore, we quantify the auto-correlation of $p(t)$:

$$c(\tau) = \frac{\big\langle p(t)p^*(t+\tau)\big\rangle}{\big\langle r(t)r(t+\tau)\big\rangle}. \tag{C.14}$$

Here, the asterisk "$*$" indicates complex conjugation. We normalized $c(\tau)$ by the auto-correlation of $r(t)$ such that the norm of $c(\tau)$ is never larger than one. In addition, this normalization removed contributions in $c(\tau)$ that are only due to fluctuations in the T1 splitting rate $r(t)$. Note that here, we are merely interested in the persistence of the average y position of the T1 splittings.

The auto-correlation $c(\tau)$ has the following meaning. A positive real part of $c(\tau)$ corresponds to cases where at times separated by the time lag τ, the average y positions of T1 splittings are similar. A negative real part of $c(\tau)$ corresponds to cases where the average y positions of T1 splittings are shifted by $L_y/2$ with respect to each other. A nonzero imaginary part of $c(\tau)$ corresponds to cases where the average y positions of T1 splittings are shifted by $L_y/4$ with respect to each other. If distributions of T1 splittings separated by the time lag τ are uncorrelated, the correlation $c(\tau)$ is zero. Hence, a finite life time of shear bands will be visible in a decay of the real part of $c(\tau)$ from positive values towards zero.

Before presenting how the auto-correlation $c(\tau)$ depends on the fluctuation amplitude Λ_F, we define a discrete version of $c(\tau)$ that we used to analyze the simulations. In the simulations, the T1 splittings were discrete events and the time intervals were finite. We denote the total number of T1 splittings occurring during a given time interval $t_j \dots t_{j+1}$ by R_j. Then, the continuous T1 splitting rate r corresponds to $R_j/(t_{j+1} - t_j)$. Furthermore, the continuous quantity p corresponds to $P_j/(t_{j+1} - t_j)$, where we defined:

$$P_j = \sum_{k=1}^{R_j} \exp\left(\frac{2\pi \mathrm{i} y_k}{L_y}\right). \tag{C.15}$$

Here, the sum runs over all T1 splittings occurring during the time interval and y_k denotes the y position of the kth T1 splitting. Then, for $\tau = m\Delta t$ with integer m, the

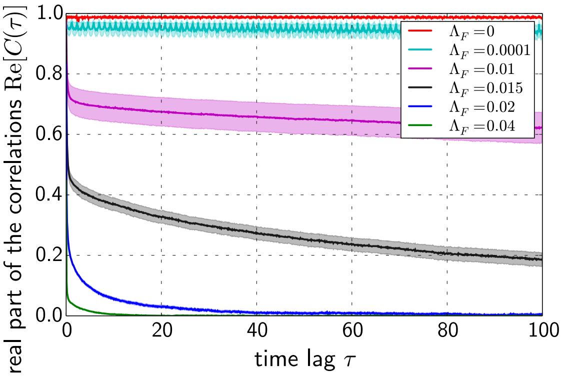

Figure C.3: The real part of the auto-correlation $C(\tau)$ as defined by Eq. (C.16) for different values of the line tension fluctuation amplitude Λ_F and for the simple shear rate $\dot{\gamma} = 1$. All other parameter values used are the same as in Table C.2. The solid lines indicate the respective averages computed from 100 separate simulation runs. The hatched regions represent the corresponding standard errors of the mean.

auto-correlation $c(\tau)$ corresponds to $C(\tau)$, which is defined as follows:

$$C(\tau) = \frac{1}{Z_m} \sum_{j=0}^{N-m-1} P_j P^*_{j+m}. \tag{C.16}$$

Here, we defined

$$Z_m = \sum_{j=0}^{N-m-1} R_j R_{j+m}. \tag{C.17}$$

The integer N denotes the total number of time intervals in the simulation. Note that we tested a number of alternative quantities to characterize the average life time of shear bands. The auto-correlation $c(\tau)$ (with its discrete version $C(\tau)$) turned out to be the most reliable one.

Fluctuation-dependent persistence of shear bands

Now, we show how the persistence of shear bands depended on the line tension fluctuation amplitude Λ_F. To this end, we ran simple shear simulations starting from a 10×10 pattern of hexagonal cells. The total duration of these simulation was $T = 1000$ and we used time steps of length $\Delta t = 0.01$.[2] We set the shear rate to $\dot{\gamma} = 1$ and varied the value of the line tension fluctuation amplitude Λ_F between 0 and 0.04. For each value of Λ_F, we performed 100 independent simulation runs.[3] All other parameter values are the same as in Section C.3.1, Table C.2. Also, as explained in Section C.3.1, the total number of cells was kept constant by forcing a random cell division upon occurrence of a T2 transition.

---

[2] Note that in order to save disk space, the quantities R_j and P_j defined above were summed over 10 intervals with length Δt: $t_{j+1} - t_j = 10\Delta t$. Thus, the line tension noise η^b was updated and the network was relaxed at times separated by Δt. However, the quantities R_j and P_j were written to disk only after every tenth of these intervals.

[3] However, for $\Lambda_F = 0$, we only performed a single simulation run, because without line tension noise, the simulations are deterministic – at least in the absence T2 transitions.

In Fig. C.3, we plot the auto-correlation $C(\tau)$ for different values of the line tension fluctuation amplitude Λ_F. The imaginary part of $C(\tau)$ was never significantly different from zero. Therefore, we only discuss the real part, here. Without line tension fluctuations ($\Lambda_F = 0$, red solid line), the real part of $C(\tau)$ was close to one for all τ. This is consistent with the observation of a shear band that persisted until the end of the simulation. For very small fluctuation amplitude ($\Lambda_F = 0.0001$, cyan solid line), the situation was similar. For slightly larger fluctuation amplitude ($\Lambda_F = 0.01$, magenta solid line, and $\Lambda_F = 0.015$, black solid line), the real part of $C(\tau)$ decreased with τ, but there was still a significant correlation even for $\tau = 100$. However for $\Lambda_F \geq 0.02$ (blue and green solid lines), the correlation reached zero within the error bounds before $\tau = 100$. Hence, there were no persistent shear bands for $\Lambda_F \geq 0.02$.

C.3.3 Average flow field

Here, we derive the average velocity gradient v_{ij} for periodic boundary conditions. We use the definition from Chapter 2, which reads (Eq. (2.50)):

$$v_{ij} = \frac{1}{\delta t A^G} \oint n_i \delta u_j \,\mathrm{d}\ell. \tag{C.18}$$

Here, the scalar δt represents an infinitesimal time interval and A^G denotes the area of the triangulation. The integral runs around the margin of the triangulation. The vector $\boldsymbol{n}$ denotes the unit normal vector of the triangulation margin pointing outside. The vector $\boldsymbol{\delta u}$ denotes the local displacement of the margin during the time interval δt.

As a first simplification step, we transform Eq. (C.18) into

$$v_{ij} = -\frac{\epsilon_{ik}}{\delta t A^G} \oint \delta u_j \,\mathrm{d}\ell_k. \tag{C.19}$$

Here, the integration goes in counter-clockwise direction around the triangulation margin. The differential $\mathrm{d}\ell_k$ is a vector with norm $\mathrm{d}\ell$ that points in counter-clockwise direction along the margin. Then, we have $n_i \mathrm{d}\ell = -\epsilon_{ik}\mathrm{d}\ell_k$, which we used to derive Eq. (C.19) from Eq. (C.18).

In order to compute Eq. (C.19), we first have to define the triangulation margin. For periodic boundary conditions (with or without skew), the triangulation margin is not uniquely defined. However, one possible definition can be obtained as follows. To define a first piece of the triangulation margin, one picks a cell center $\boldsymbol{R}^\alpha$ and connects it to its copy $\boldsymbol{R}^\alpha + \boldsymbol{B}(1,0)$ (green dots and red line in Fig. C.4).[4] We denote the curve that defines this connection by $c(1,0)$. It should go only along triangle sides,

---

[4] For skewed periodic boundary conditions, the vector $\boldsymbol{B}(\boldsymbol{q})$ is defined by Eq. (C.6) given the periodicity vector $\boldsymbol{q}$.

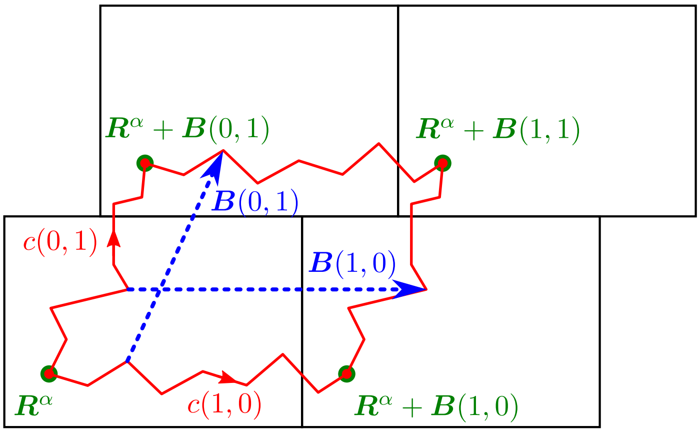
$\boldsymbol{R}^\alpha + \boldsymbol{B}(0,1)$
$\boldsymbol{R}^\alpha + \boldsymbol{B}(1,1)$
$\boldsymbol{B}(0,1)$
$c(0,1)$
$\boldsymbol{B}(1,0)$
$\boldsymbol{R}^\alpha$
$c(1,0)$
$\boldsymbol{R}^\alpha + \boldsymbol{B}(1,0)$

Figure C.4: Construction of a triangulation margin (red solid lines) for periodic boundary conditions. A triangulation margin can be constructed starting from the center $\boldsymbol{R}^\alpha$ of an arbitrary cell α (green dot). The triangulation margin is created by connecting $\boldsymbol{R}^\alpha$ to its copies $\boldsymbol{R}^\alpha + \boldsymbol{B}(1,0)$ and $\boldsymbol{R}^\alpha + \boldsymbol{B}(0,1)$ (red solid lines). The corresponding curves are denoted by $c(1,0)$ and $c(0,1)$, respectively. Then, in order to obtain a closed contour, $c(1,0)$ is shifted by $\boldsymbol{B}(0,1)$ and $c(0,1)$ is shifted by $\boldsymbol{B}(1,0)$ (blue arrows).

i.e. $c(1,0)$ should be made up of line segments connecting neighboring cell centers. Similarly, a second piece of the margin can be obtained by connecting $\boldsymbol{R}^\alpha$ to its copy $\boldsymbol{R}^\alpha + \boldsymbol{B}(0,1)$. The corresponding curve is denoted by $c(0,1)$. Finally, in order to obtain a closed contour, one adds a copy of $c(1,0)$ that is shifted by $\boldsymbol{B}(0,1)$ and a copy of $c(0,1)$ that is shifted by $\boldsymbol{B}(1,0)$ (blue arrows). All four paths together yield the triangulation margin. The triangulation area is $A^G = L_x L_y$, because it can be puzzled together from the simulation box rectangle.

For the given definition of the triangulation margin, we obtain from Eq. (C.19):

$$\begin{aligned} v_{ij} = -\frac{\epsilon_{ik}}{\delta t L_x L_y} \Bigg(\int_{c(1,0)} \Big[\delta u_j(\boldsymbol{r}) - \delta u_j\big(\boldsymbol{r} + \boldsymbol{B}(0,1)\big)\Big] \, \mathrm{d}\ell_k \\ - \int_{c(0,1)} \Big[\delta u_j(\boldsymbol{r}) - \delta u_j\big(\boldsymbol{r} + \boldsymbol{B}(1,0)\big)\Big] \, \mathrm{d}\ell_k \Bigg). \end{aligned} \tag{C.20}$$

Here, both line integrals go along the positions $\boldsymbol{r}$ of the curves $c(1,0)$ and $c(0,1)$, respectively. Now, for a given periodicity vector $\boldsymbol{q}$, we denote the change of the vector $\boldsymbol{B}(\boldsymbol{q})$ during the time interval δt by the vector $\boldsymbol{\delta B}(\boldsymbol{q})$. Then, we have for the displacement difference:

$$\boldsymbol{\delta u}\big(\boldsymbol{r} + \boldsymbol{B}(\boldsymbol{q})\big) - \boldsymbol{\delta u}(\boldsymbol{r}) = \boldsymbol{\delta B}(\boldsymbol{q}). \tag{C.21}$$

Therefore, we obtain from Eq. (C.20):

$$v_{ij} = \frac{\epsilon_{ik}}{L_x L_y}\Big(\dot{B}_j(0,1)B_k(1,0) - \dot{B}_j(1,0)B_k(0,1)\Big). \tag{C.22}$$

Here, we defined $\dot{B}_j(\boldsymbol{q}) = \delta B_j(\boldsymbol{q})/\delta t$.

For skewed periodic boundary conditions, we insert $\boldsymbol{B}(\boldsymbol{q})$ as defined by Eq. (C.6) and obtain for the velocity gradient $\boldsymbol{v}$:

$$\boldsymbol{v} = \begin{pmatrix} \dot{L}_x/L_x & 0 \\ \dot{\gamma} + \gamma(\dot{L}_y/L_y - \dot{L}_x/L_x) & \dot{L}_y/L_y \end{pmatrix}. \tag{C.23}$$

With Eq. (2.51) the components of v_{ij} read:

$$v_{kk} = \frac{\dot{L}_x}{L_x} + \frac{\dot{L}_y}{L_y} \tag{C.24}$$

$$\tilde{v}_{xx} = \frac{1}{2}\left(\frac{\dot{L}_x}{L_x} - \frac{\dot{L}_y}{L_y}\right) \tag{C.25}$$

$$\tilde{v}_{xy} = \frac{\dot{\gamma}}{2} - \gamma\tilde{v}_{xx} \tag{C.26}$$

$$\omega = -\tilde{v}_{xy}. \tag{C.27}$$

For our simple shear simulations, we set L_x and L_y constant and we prescribed $\dot{\gamma}$. Then,

$$v_{kk} = 0 \tag{C.28}$$

$$\tilde{v}_{xx} = 0 \tag{C.29}$$

$$\tilde{v}_{xy} = \dot{\gamma}/2 \tag{C.30}$$

$$\omega = -\dot{\gamma}/2. \tag{C.31}$$

C.3.4 Steady state axis of the elongation nematic

Here, we theoretically discuss simple shear simulations where the elongation relaxation nematic $\tilde{F}_{ij}$ is parallel to the elongation nematic $\tilde{Q}_{ij}$. In particular, we derive a relation between the steady state angle Ψ and the steady state norm $|\tilde{Q}|$ of the elongation $\tilde{Q}_{ij}$. For $\tilde{F}_{ij}$ parallel to $\tilde{Q}_{ij}$, Eq. (3.5) reads:

$$\frac{\mathrm{d}\tilde{Q}_{ij}}{\mathrm{d}t} = \tilde{v}_{ij} + \omega\frac{1}{|\tilde{Q}|}\tanh\big(2|\tilde{Q}|\big)\epsilon_{ik}\tilde{Q}_{kj} - \frac{\tilde{Q}_{ij}}{|\tilde{Q}|}|\tilde{F}|\big(|\tilde{Q}|\big). \tag{C.32}$$

Here, we used the definition of the corotational derivative, Eq. (2.54).

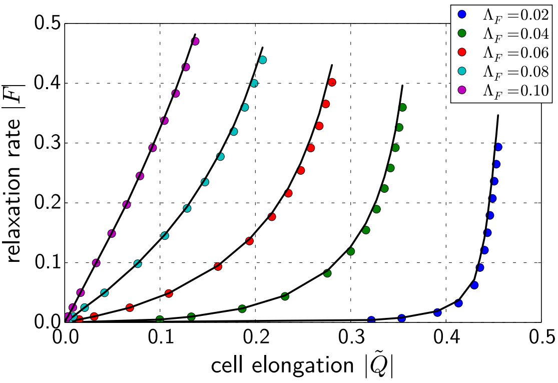

Figure C.5: Relaxation rate of elongation $|\tilde{F}|$ depending on the elongation norm $|\tilde{Q}|$. Comparison of steady state simulation results (colored dots) to theory, Eq. (C.35) (black solid lines). Note that Eq. (C.35) was derived for the case where the nematics $\tilde{F}_{ij}$ and $\tilde{Q}_{ij}$ are parallel.

Now, we decompose Eq. (C.32) into the part proportional to $\tilde{Q}_{ij}$ and into the part proportional to $\epsilon_{ik}\tilde{Q}_{kj}$ (Section A.2.3). We obtain for the steady state:

$$\frac{\dot{\gamma}}{2}\sin(2\Phi) = |\tilde{F}|\big(|\tilde{Q}|\big) \tag{C.33}$$

$$\cos(2\Phi) = \tanh\big(2|\tilde{Q}|\big). \tag{C.34}$$

Here, we used the values for $\tilde{v}_{ij}$ and ω derived in Section C.3.3 for fixed L_x, L_y and for constant $\dot{\gamma}$. Also, we used our result from Section A.3.3.

Interestingly, from Eqs. (C.33) and (C.34) follows a relationship between $\dot{\gamma}$ and the steady state values of $|\tilde{Q}|$ and $|\tilde{F}|(|\tilde{Q}|)$:

$$\frac{\dot{\gamma}}{2\cosh\big(2|\tilde{Q}|\big)} = |\tilde{F}|\big(|\tilde{Q}|\big). \tag{C.35}$$

Note that such a relationship only exists for simple shear simulations.

We compare Eq. (C.35) to observed steady state values of $|\tilde{F}|$ and $|\tilde{Q}|$ for different simple shear rates $\dot{\gamma}$ and different line tension fluctuation amplitudes Λ_F (Fig. C.5). We find that the theory described the simulation results well. Deviations between simulation results and theory occurred because $\tilde{F}_{ij}$ and $\tilde{Q}_{ij}$ were not exactly parallel to each other (Fig. 3.8A).

C.4 Quantification of observables

C.4.1 Definition of stress

Here, we define the stress tensor σ_{ij} characterizing the mean field stress that is exerted by the simulation box on the vertex model tissue. We define σ_{ij} such that for a virtual deformation, we have the following virtual change of the work function δW:

$$\delta W = L_x L_y \sigma_{ij} \delta U_{ij}. \tag{C.36}$$

Here, δU_{ij} denotes the displacement gradient characterizing the virtual deformation of the whole vertex model tissue.[5]

For skewed periodic boundary conditions, we insert δU_{ij} for given virtual changes δL_x, δL_y, and $\delta\gamma$ of the boundary conditions. Using Eq. (C.23), we have:

$$\delta W = \sigma_{xx} L_y \delta L_x + \sigma_{yy} L_x \delta L_y + \sigma_{yx}\Big(L_x L_y \delta\gamma + \gamma L_x \delta L_y - \gamma L_y \delta L_x\Big). \tag{C.38}$$

This corresponds to the following partial derivatives:

$$\frac{\partial W(L_x, L_y, \gamma)}{\partial L_x} = \sigma_{xx} L_y - \sigma_{yx}\gamma L_y \tag{C.39}$$

$$\frac{\partial W(L_x, L_y, \gamma)}{\partial L_y} = \sigma_{yy} L_x + \sigma_{yx}\gamma L_x \tag{C.40}$$

$$\frac{\partial W(L_x, L_y, \gamma)}{\partial \gamma} = \sigma_{yx} L_x L_y. \tag{C.41}$$

In order to simplify this, we perform a coordinate transformation. We substitute γ in the work function $W(L_x, L_y, \gamma)$ by a newly defined skew variable $s = \gamma L_y / L_x$. This leads to the following set of equations:

$$\sigma_{xx} = \frac{1}{L_y}\,\frac{\partial W(L_x, L_y, s)}{\partial L_x} \tag{C.42}$$

$$\sigma_{yy} = \frac{1}{L_x}\,\frac{\partial W(L_x, L_y, s)}{\partial L_y} \tag{C.43}$$

$$\sigma_{yx} = \frac{1}{L_x^2}\,\frac{\partial W(L_x, L_y, s)}{\partial s}. \tag{C.44}$$

We used these equations to compute three of the components of σ_{ij}. We defined the fourth component by:

$$\sigma_{xy} = \sigma_{yx}. \tag{C.45}$$

This corresponds to the absence of chiral terms in the work function. The shear stress

---

[5] To see that Eq. (C.36) is a sensible mean field definition of σ_{ij}, we expand it using the definition of δU_{ij}, Eq. (2.36), and Appendix B.1. We obtain:

$$\delta W = \oint f_j \delta u_j \,\mathrm{d}\ell. \tag{C.37}$$

Here, the integral goes along the triangulation margin defined in Section C.3.3. The vector $f_j = \sigma_{ij} n_i$ corresponds to the line density of the force that the simulation box exerts onto the vertex model tissue in a given point of the triangulation margin.

nematic $\tilde{\sigma}_{ij}$ is defined to be the symmetric, traceless part of σ_{ij}:

$$\tilde{\sigma}_{ij} = \frac{1}{2}\Big(\sigma_{ij} + \sigma_{ji} - \sigma_{kk}\delta_{ij}\Big). \tag{C.46}$$

C.4.2 Shear components

Here, we explain how the quantities appearing in Eq. (3.5) were computed in the simple shear simulations. First, we discuss the case without topological transitions. Afterwards, we explain how topological transitions were incorporated.

Without topological transition

Without topological transitions and for a given time interval $t \ldots (t{+}\Delta t)$, we computed the quantities $\tilde{v}_{ij}$, $\mathrm{D}\tilde{Q}_{ij}/\mathrm{D}t$, and $\tilde{D}_{ij}$ as follows. In general, the deformation from the initial state at time t to the final state at time $t+\Delta t$ is finite. Thus, in order to reduce deviations due to higher order terms, we constructed $N = 99$ intermediate states by linear interpolation of the vertex positions $\boldsymbol{P}^m$ and of the simple shear variable γ. These intermediate states divided the whole deformation between the states at times t and $t + \Delta t$ into $N + 1$ successive smaller deformations. Then, the displacement gradient of the network related to the whole deformation U_{ij} was computed by the sum of the displacement gradients related to the smaller deformations:

$$U_{ij} = \sum_{s=0}^{N} \langle U_{ij}^m \rangle. \tag{C.47}$$

Here, the sum runs over all $N + 1$ smaller deformations s. For $s = 0$, the initial state of the smaller deformation is the state at time t and the final state is the first intermediate state. For $1 \leq s \leq N - 1$, the initial state is the sth intermediate state and the final state is the $(s + 1)$th intermediate state. For $s = N$, the initial state is the Nth intermediate state and the final state is the state at time $t + \Delta t$. The tensor U_{ij}^m is the discrete displacement gradient of the triangle m for the current smaller deformation s. It is defined by Eq. (2.18). The averaging bracket is also related to the current smaller deformation s. It is defined by Eq. (2.34) with the area weights taken from the initial state of the current smaller deformation. Note that the network was triangulated as in Section B.8.3.

Now, the shear rate $\tilde{v}_{ij}$ was computed via:

$$\tilde{v}_{ij} = \frac{\tilde{U}_{ij}}{\Delta t}. \tag{C.48}$$

Here, $\tilde{U}_{ij}$ denotes the symmetric, traceless part of U_{ij}.

The corotational elongation derivative was computed as follows:

$$\frac{\mathrm{D}\tilde{Q}_{ij}}{\mathrm{D}t} = \frac{\Delta\tilde{Q}_{ij}}{\Delta t} + \tilde{J}_{ij}. \tag{C.49}$$

Here, $\Delta\tilde{Q}_{ij} = \tilde{Q}_{ij}(t+\Delta t) - \tilde{Q}_{ij}(t)$ denotes the change of the average elongation $\tilde{Q}_{ij}$ during the time interval Δt. In a given state, the average elongation $\tilde{Q}_{ij}$ is given by Eq. (2.39). The nematic $\tilde{J}_{ij}$ denotes the corotational contribution to shear. It is defined by:

$$\tilde{J}_{ij} = -2\left[c\frac{\Delta\Psi}{\Delta t} + (1-c)\frac{\Delta\Phi}{\Delta t}\right]\epsilon_{ik}\tilde{\tilde{Q}}_{kj}. \tag{C.50}$$

Here, we defined $c = \tanh(2|\tilde{\tilde{Q}}|)/(2|\tilde{\tilde{Q}}|)$, where $\tilde{\tilde{Q}} = [\tilde{Q}_{ij}(t) + \tilde{Q}_{ij}(t+\Delta t)]/2$ and $|\tilde{\tilde{Q}}|$ is the norm of $\tilde{\tilde{Q}}_{ij}$. The angle $\Delta\Psi$ is defined to be the antisymmetric part of U_{ij} (as in Eq. (2.37)). Also, we defined $\Delta\Phi = \Phi(t+\Delta t) - \Phi(t)$, where Φ denotes the angle of $\tilde{\tilde{Q}}_{ij}$. Expressions in parentheses indicate the state in which the respective quantity is evaluated.

The correlations contributing to shear were computed as follows:

$$\tilde{D}_{ij} = -\frac{1}{\Delta t}\left(\tilde{K}^G_{ij} - \tilde{\tilde{Q}}_{ij}U_{kk}\right) + \frac{1}{\Delta t}\tilde{K}^R_{ij} - \tilde{J}_{ij}. \tag{C.51}$$

Here, the scalar U_{kk} denotes the trace of U_{ij}. The nematics $\tilde{K}^G_{ij}$ and $\tilde{K}^R_{ij}$ represent correlations that are defined as follows:

$$\tilde{K}^G_{ij} = \sum_{s=0}^{N}\left\langle \tilde{\tilde{Q}}^m_{ij} U^m_{kk} \right\rangle \tag{C.52}$$

$$\tilde{K}^R_{ij} = \sum_{s=0}^{N}\left\langle \left[-2\Delta\Psi^m + (\Delta\Theta^m - \Delta\Psi^m)\frac{\sinh(2|\tilde{\tilde{Q}}^m|) - 2|\tilde{\tilde{Q}}^m|\cosh(2|\tilde{\tilde{Q}}^m|)}{|\tilde{\tilde{Q}}^m|\left[\cosh(2|\tilde{\tilde{Q}}^m|) - 1\right]}\right]\epsilon_{ij}\tilde{\tilde{Q}}^m_{kj}\right\rangle. \tag{C.53}$$

In both equations the sums run over all small deformations and the averaging brackets are defined like in Eq. (C.47). For a given triangle m, the nematic $\tilde{\tilde{Q}}^m_{ij}$ denotes the average of the elongations in the initial and the final states of the current small deformation s. Note that $\tilde{\tilde{Q}}^m_{ij}$ is different from $\tilde{\tilde{Q}}_{ij}$ defined below Eq. (C.50), which relates to the whole deformation during the time interval Δt. The angle $\Delta\Psi^m$ is the antisymmetric part of U^m_{ij} and relates to the current small deformation s. The angle $\Delta\Theta^m$ denotes the change of the orientation angle Θ^m during the current small deformation. The scalar $|\tilde{\tilde{Q}}^m|$ denotes the norm of the nematic $\tilde{\tilde{Q}}^m_{ij}$.

Incorporation of topological transitions

Now, we explain how topological transitions were incorporated. At the beginning of each time interval Δt, the topological contributions to shear, $\tilde{T}_{ij}$, $\tilde{C}_{ij}$, and $\tilde{E}_{ij}$, were set to zero.

Now, we consider the effect of a single topological transition occurring during a minimization of the work function. Upon occurrence of a single topological transition, the average cell elongation $\tilde{Q}_{ij}$ changes instantaneously by $\Delta\tilde{Q}_{ij}$. Thus, to take the effect of this topological transition on shear into account, we added $-\Delta\tilde{Q}_{ij}/\Delta t$ to the corresponding nematic $\tilde{T}_{ij}$, $\tilde{C}_{ij}$, or $\tilde{E}_{ij}$.

In addition, because during a topological transition, the triangulation changes, we could not evaluate Eqs. (C.47), (C.52), and (C.53) for a deformation during which topological transitions occurred. Therefore, we evaluated U_{ij}, $\tilde{K}^G_{ij}$, and $\tilde{K}^R_{ij}$ separately in between topological transitions. In the end, the individual contributions were added up, respectively. More precisely, consider a number n of topological transitions occurring during the time interval Δt. We denote the initial state of the network at time t by A and the final state at time $t + \Delta t$ by D. The network state before the kth topological transition is denoted by B_k and the state after the kth topological transition is denoted by C_k. Thus, the order in which these network states occur is:

$$A \xrightarrow{\text{deformation}} B_1 \xrightarrow{\text{top. transition}} C_1 \xrightarrow{\text{deformation}} B_2 \xrightarrow{\text{top. transition}} C_2 \dots C_n \xrightarrow{\text{deformation}} D. \tag{C.54}$$

Then, for instance the deformation gradient U_{ij} related to the whole deformation from A to D is defined as follows:

$$U_{ij} = U_{ij}(A, B_1) + U_{ij}(C_1, B_2) + \dots + U_{ij}(C_n, D). \tag{C.55}$$

Here, the tensor $U_{ij}(X, Y)$ for any two network states X and Y without any topological transition in between is defined as in Eq. (C.47). In particular, the deformation from X to Y is therefore divided into $N + 1$ smaller deformations by introducing $N = 99$ intermediate states. The definition in Eq. (C.55) is sensible, because during any topological transition, no deformation occurs.

In the presence of topological transitions, the definitions of the nematics $\tilde{K}^G_{ij}$ and $\tilde{K}^R_{ij}$ are modified analogously to Eq. (C.55). These modifications affect the nematic $\tilde{D}_{ij}$, which depends on $\tilde{K}^G_{ij}$ and $\tilde{K}^R_{ij}$. In contrast to that, the computation of $\mathrm{D}\tilde{Q}_{ij}/\mathrm{D}t$ and $\tilde{J}_{ij}$ is not altered by topological transitions.

Note that in order to save disk space, all quantities, $\tilde{v}_{ij}$, $\mathrm{D}\tilde{Q}_{ij}/\mathrm{D}t$, $\tilde{T}_{ij}$, $\tilde{C}_{ij}$, $\tilde{E}_{ij}$, and $\tilde{D}_{ij}$, are averaged over 10 successive time intervals of length Δt before being written to the data file.

C.4.3 Quantification of uncertainties

Here, we explain how the uncertainties in Figs. 3.6 and 3.8 were computed.

Fig. 3.6A,B: For each time point, the nematic tensors $\tilde{Q}_{ij}$ and $\tilde{\sigma}_{ij}$ were averaged over 100 simulation runs. Then, the uncertainties of the xx and xy components of both tensors correspond to the respective standard errors of the mean. For the nematic $\tilde{Q}_{ij}$, we denote them by $\Delta\tilde{Q}_{xx}$ and $\Delta\tilde{Q}_{xy}$. Then, the uncertainties of the angles and the norms were computed according to standard rules for the propagation of uncertainty for independent variables. For the nematic $\tilde{Q}_{ij}$, we defined:

$$\Delta|\tilde{Q}| = 2\Big[(\tilde{Q}_{xx}\Delta\tilde{Q}_{xx})^2 + (\tilde{Q}_{xy}\Delta\tilde{Q}_{xy})^2\Big]^{1/2} \tag{C.56}$$

$$\Delta\Phi = \frac{1}{2|\tilde{Q}|}\Big[(\tilde{Q}_{xy}\Delta\tilde{Q}_{xx})^2 + (\tilde{Q}_{xx}\Delta\tilde{Q}_{xy})^2\Big]^{1/2}. \tag{C.57}$$

Here, $\Delta|\tilde{Q}|$ and $\Delta\Phi$ denote the time-dependent uncertainties in norm and angle of $\tilde{Q}_{ij}$, respectively.

Fig. 3.6C,D, Fig. 3.8A,B: The uncertainties represented by the error bars are obtained as follows. For a given parameter pair (Λ_F, $\dot{\gamma}$) and a given simulation run, the steady state values of $\tilde{Q}_{ij}$, $\tilde{\sigma}_{ij}$, and $\tilde{F}_{ij}$ were determined by averaging the tensor components for all time points $t \geq t_0$. Here, the time t_0 is a cutoff time (see main text). Then, for a given parameter pair (Λ_F, $\dot{\gamma}$), the steady state values of $\tilde{Q}_{ij}$, $\tilde{\sigma}_{ij}$, and $\tilde{F}_{ij}$ were averaged over all 100 individual simulation runs. The uncertainties of the tensor components were defined by the respective standard errors of the mean. Finally, the uncertainties of the steady state norms and angles were computed as in Eqs. (C.56) and (C.57), respectively.

Appendix D

Coarse-graining of a cellular Core PCP model

Here, we coarse grain the cellular Core PCP model introduced in refs. [54, 121]. To this end, we consider a regular hexagonal packing for simplicity. We discuss the time evolution of a small perturbation of the homogeneous polar ground state in the hydrodynamic limit. We show that the obtained relaxation corresponds to the generic decay of the bend and splay modes of the Frank free energy [134, 149].

This chapter is organized as follows. In Section D.1, we first present the cellular Core PCP model. Then, in Section D.2, we introduce the hexagonal grid and we transform the Core PCP model to Fourier space for convenience. Then, in Section D.3 we show that the ground state of the homogeneous system shows a continuous degeneracy. In Section D.4, we discuss the relaxation of a small perturbation of the ground state in the hydrodynamic limit. Finally, in Section D.5, we compare to generic relaxation dynamics of a polarity field. As result, we obtain phenomenological coefficients describing the relaxation of bend and splay modes in the cellular Core PCP model.

D.1 Core PCP vertex model

Here, we describe the Core PCP model introduced in refs. [54, 121]. It is based on the vertex model presented in Section 3.1.1.

The PCP protein distribution within the network is described by scalar variables $\sigma_b(\boldsymbol{R}^\alpha)$ on each side of each bond b.[1] In particular, if the bond b is shared by the cells α and β, we denote the respective PCP protein amounts by the variables $\sigma_b(\boldsymbol{R}^\alpha)$ and $\sigma_b(\boldsymbol{R}^\beta)$. The variable $\sigma_b(\boldsymbol{R}^\alpha)$ is a real number. It takes negative values whenever there is more Stbm and associated proteins than Fz and associated proteins. Conversely, it takes positive values whenever there is more Fz and associated proteins than Stbm and associated proteins.

Allowed configurations of the protein amounts $\sigma_b(\boldsymbol{R}^\alpha)$ within a given cell α are defined by the following conditions:

---

[1] Here, we choose for convenience the notation $\sigma_b(\boldsymbol{R}^\alpha)$ instead of "σ_b^α", which is used in refs. [54, 121].

$$\sum_b \sigma_b(\boldsymbol{R}^\alpha) = 0 \qquad \text{(Condition I)} \tag{D.1}$$

$$\sum_b \sigma_b^2(\boldsymbol{R}^\alpha) = 1 \qquad \text{(Condition II).} \tag{D.2}$$

Here, both sums run over all bonds b of cell α. Condition I requires that the total amount of Stbm and associated proteins equals the total amount of Fz and associated proteins. Condition II is needed in order to bound the total amount of PCP proteins within the cell.

Interactions between Core PCP proteins are described by an effective energy. It is given by

$$E = \sum_b \sigma_b(\boldsymbol{R}^\alpha)\sigma_b(\boldsymbol{R}^\beta) - J\sum_{\langle b,c\rangle} \sigma_b(\boldsymbol{R}^\alpha)\sigma_c(\boldsymbol{R}^\alpha). \tag{D.3}$$

Here, the first sum runs over all bonds b of the network, and α and β are the cells that touch b. The second sum runs over all unsorted pairs of neighboring bonds b and c, where cell α touches both bonds. The first term describes inter-cellular interactions across bonds. Unequal signs of $\sigma_b(\boldsymbol{R}^\alpha)$ across bonds are energetically favored. The second term describes intracellular interactions. The dimensionless coefficient $J > 0$ characterizes the intracellular interaction strength as compared to the inter-cellular interaction strength. Equal signs of $\sigma_b(\boldsymbol{R}^\alpha)$ in neighboring bonds of a given cell are energetically favored. Note that as compared to refs. [54, 121], we define a dimensionless energy in order to reduce the number of free parameters.

Based on the effective energy E, the model defines a time evolution of the variables $\sigma_b(\boldsymbol{R}^\alpha)$. To this end, Conditions I and II are imposed by introducing Lagrange multipliers $\lambda_{\mathrm{I}}^\alpha$ and $\lambda_{\mathrm{II}}^\alpha$ into the energy:

$$\bar{E} = E + \sum_\alpha \left(\lambda_{\mathrm{I}}^\alpha \sum_b \sigma_b(\boldsymbol{R}^\alpha)\right) - \sum_\alpha \left(\lambda_{\mathrm{II}}^\alpha \left[1 - \sum_b \sigma_b^2(\boldsymbol{R}^\alpha)\right]\right). \tag{D.4}$$

Then, the time evolution of the variables $\sigma_b(\boldsymbol{R}^\alpha)$ is defined by

$$\frac{\mathrm{d}\sigma_b(\boldsymbol{R}^\alpha)}{\mathrm{d}t} = -r\frac{\partial \bar{E}}{\partial[\sigma_b(\boldsymbol{R}^\alpha)]}. \tag{D.5}$$

Here, the rate r is a parameter representing an inter-cellular relaxation time scale.[2] Consistent with that, the rate Jr represents an intracellular relaxation time scale.

---

[2] Note that here, we reduced the number of free parameters as compared to refs. [54, 121]. In particular, we set $r = \gamma J_1$ and $J = J_2/J_1$, where γ, J_1, and J_2 were parameters defined in refs. [54].

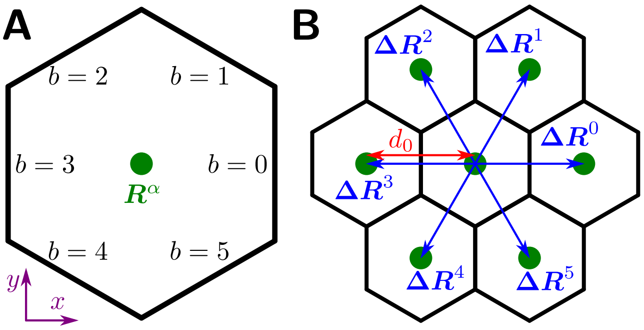
A
$b=2$
$b=1$
$b=3$
$b=0$
$\boldsymbol{R}^\alpha$
$b=4$
$b=5$
y
x
B
$\boldsymbol{\Delta R}^2$
$\boldsymbol{\Delta R}^1$
d_0
$\boldsymbol{\Delta R}^0$
$\boldsymbol{\Delta R}^3$
$\boldsymbol{\Delta R}^4$
$\boldsymbol{\Delta R}^5$

Figure D.1: Conventions used for a regular hexagonal grid of cells. **(A)** Definition of the bond indices b for a given cell α. It increases in counter-clockwise order. **(B)** Definition of the vector $\boldsymbol{\Delta R}^b$. The vector $\boldsymbol{\Delta R}^b$ denotes the distance vector of the center of a given cell α to the center of the cell that touches α via bond b.

Table D.1: Components of the vectors $\boldsymbol{\Delta R}_b$ for all possible values of the bond index b.

b	0	1	2	3	4	5
ΔR_x^b	d_0	$d_0/2$	$-d_0/2$	$-d_0$	$-d_0/2$	$d_0/2$
ΔR_y^b	0	$d_0\sqrt{3}/2$	$d_0\sqrt{3}/2$	0	$-d_0\sqrt{3}/2$	$-d_0\sqrt{3}/2$

D.2 Fourier transformation on a hexagonal grid

D.2.1 Hexagonal grid

For simplicity, we consider a $n_x \times n_y$ pattern of regular, hexagonal cells, where one side of the hexagons is oriented parallel to the y axis (Fig. D.1). The distance between two abutting cell centers is denoted by d_0, and we prescribe periodic boundary conditions.

Around a given cell α, the bond index b can take the values $b = 0, \ldots, 5$ (Fig. D.1A). The bond index b is zero for the bond being located in positive x direction as seen from the center of cell α, and it increases in counter-clockwise order. Correspondingly, we slightly change the notation for $\sigma_b(\boldsymbol{R}^\alpha)$. The bond index b in $\sigma_b(\boldsymbol{R}^\alpha)$ does not denote a global bond index anymore. From here on, it denotes the local bond index $b = 0, \ldots, 5$ relating to cell α.

In addition, we introduce the vectors $\boldsymbol{\Delta R}^b$ for $b = 0, \ldots, 5$ (Fig. D.1B). For given b, the vector $\boldsymbol{\Delta R}^b$ denotes the distance vector of the center of a given cell α to the center of the cell that touches α via bond b. The vector components of $\boldsymbol{\Delta R}^b$ are listed in Table D.1.

In order to facilitate the later Fourier transformation, we rewrite the energy E using the vectors $\boldsymbol{\Delta R}^b$. We obtain from Eq. (D.3):

$$E = \frac{1}{2}\sum_{\alpha,b} \sigma_b(\boldsymbol{R}^\alpha)\sigma_{b+3}(\boldsymbol{R}^\alpha + \boldsymbol{\Delta R}^b) - J\sum_{\alpha,b}\sigma_b(\boldsymbol{R}^\alpha)\sigma_{b+1}(\boldsymbol{R}^\alpha). \tag{D.6}$$

Here, both sums run over all cells α of the grid and over all bond indices $b = 0, \ldots, 5$. Moreover, here and in the following, bond indices b, $b+1$, and $b+3$ are always meant

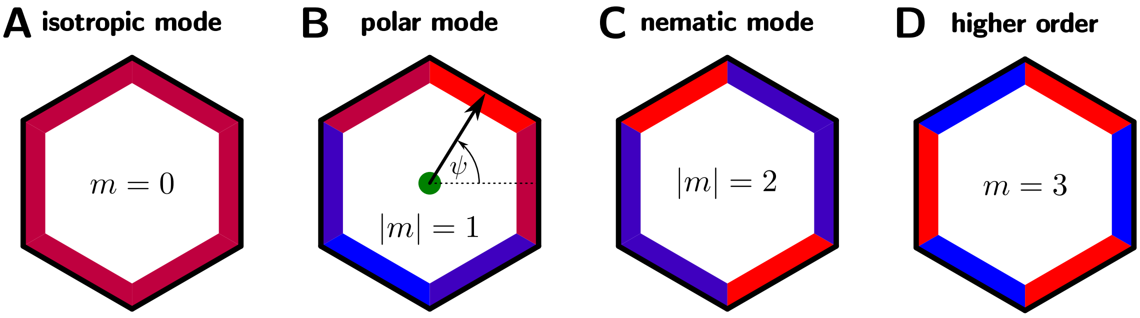

Figure D.2: Illustration of the angular Fourier modes η_m for a single cell depending on the mode index $m = -2, \ldots, 3$. The colored fields indicate the respective values of σ_b. Red indicates a positive value and blue indicates a negative value. **(A)** The mode with $m = 0$ corresponds to an isotropic protein distribution. **(B)** The modes with $|m| = 1$ correspond to a polar protein distribution. Also indicated is the polarity angle ψ. **(C)** The modes with $|m| = 2$ correspond to a nematic protein distribution. **(D)** The mode with $m = 3$ corresponds to a higher order anisotropy.

modulo six. The factor $1/2$ in front of the first term is necessary, because now, the first sum accounts for each bond twice.

D.2.2 Discrete Fourier transformation with respect to angle and position

Single hexagonal cell

We first discuss the angular Fourier transformation of the protein distribution $\sigma_b(\boldsymbol{R}^\alpha)$ within a single hexagonal cell α. We define a complex angular Fourier mode η_m by:

$$\eta_m = 6^{-1/2} \sum_{b=0}^{5} \sigma_b \exp\left(-\frac{2\pi \mathrm{i} m b}{6}\right). \tag{D.7}$$

Here, the integer m enumerates the Fourier modes. It can take the values $m = -2, \ldots, 3$. The symbol "i" denotes the imaginary unit and we dismissed the argument of σ_b.

Eq. (D.7) defines six different Fourier modes η_m, where the meaning of η_m depends on $m = -2, \ldots, 3$ (Fig. D.2). The mode with $m = 0$ characterizes the average amount of PCP proteins within the cell (Fig. D.2A). It is an isotropic measure. The modes with $|m| = 1$ characterize a polar distribution of PCP proteins within the cell (Fig. D.2B). The corresponding polarity angle ψ of cell α is defined by

$$\psi = -\arg(\eta_1). \tag{D.8}$$

Here, “arg” denotes the angle argument of a complex number. The modes with $|m| = 2$ characterize a nematic distribution of PCP proteins within the cell (Fig. D.2C). Finally, the corresponding nematic angle is $-\arg(\eta_2)/2$. The mode with $m = 3$ corresponds to a higher order anisotropy (Fig. D.2D).

Hexagonal grid

Now, we extend this angular Fourier transformation by a spatial Fourier transformation. As a result, we have a Fourier transformation in space and in the angle simultaneously. For our hexagonal grid, we define:

$$\eta_m(\boldsymbol{k}) = (6n_x n_y)^{-1/2} \sum_{\alpha,b} \sigma_b(\boldsymbol{R}^\alpha) \exp\left(-\frac{2\pi \mathrm{i} m b}{6} - \mathrm{i}\boldsymbol{k}\cdot\boldsymbol{R}^\alpha\right). \tag{D.9}$$

Here, the vector $\boldsymbol{k}$ denotes a wave vector, and the sum runs over all cells α of the grid and all bond indices $b = 0, \ldots, 5$. For later reference, we note that as a consequence of Eq. (D.9):

$$\eta_m(\boldsymbol{k}) = \eta^*_{-m}(-\boldsymbol{k}). \tag{D.10}$$

Here, we only allow for discrete values of $\boldsymbol{k}$. The x component of $\boldsymbol{k}$ varies in steps of $2\pi/(d_0 n_x)$ and the y component varies in steps of $4\pi/(d_0 n_y \sqrt{3})$. In particular, we allow for $\boldsymbol{k} = 0$. Moreover, $0 \le k_x < 2\pi/d_0$ and $0 \le k_y < 4\pi/(d_0\sqrt{3})$. Then, it can be shown that the inverse Fourier transformation reads:

$$\sigma_b(\boldsymbol{R}^\alpha) = (6n_x n_y)^{-1/2} \sum_{\boldsymbol{k},m} \eta_m(\boldsymbol{k}) \exp\left(\frac{2\pi \mathrm{i} m b}{6} + \mathrm{i}\boldsymbol{k}\cdot\boldsymbol{R}^\alpha\right). \tag{D.11}$$

Here, the sum runs over all allowed wave vectors $\boldsymbol{k}$ and over the mode index values $m = -2, \ldots, 3$.

D.2.3 Core PCP model in Fourier space

Now, we can rewrite the Core PCP model in Fourier space. First, we rephrase the conditions Eqs. (D.1) and (D.2). For Condition I, we obtain with Eq. (D.11):

$$\eta_0(\boldsymbol{k}) = 0 \qquad \text{(Condition I)} \tag{D.12}$$

for all allowed wave vectors $\boldsymbol{k}$. Thus, the isotropic modes with $m = 0$ can be ignored. This rephrases the requirement that the total amount of both kinds of proteins is equal within each cell. Similarly, Condition II can be rewritten by inserting Eq. (D.11) into Eq. (D.2):

$$\frac{1}{n_x n_y} \sum_{\boldsymbol{k},m} \eta_m(\boldsymbol{k}) \eta^*_m(\boldsymbol{k}+\boldsymbol{k}') = \delta_{\boldsymbol{k}'} \qquad \text{(Condition II)}. \tag{D.13}$$

Table D.2: Functional dependence of $G_{\Delta m}(\boldsymbol{k})$ on $\boldsymbol{k}$ for each possible value of Δm. Here, we list the exact dependence as they follow from Eq. (D.15) and Table D.1. For convenience, we note the expressions for $3G_{\Delta m}(\boldsymbol{k})$.

Δm	**exact value of** $3G_{\Delta m}(\boldsymbol{k})$
0	$\cos(d_0 k_x) + \cos\left(\frac{d_0 k_x}{2} + \frac{d_0 k_y \sqrt{3}}{2}\right) + \cos\left(\frac{d_0 k_x}{2} - \frac{d_0 k_y \sqrt{3}}{2}\right)$
1	$-\mathrm{i}\sin(d_0 k_x) - \mathrm{i}\mathrm{e}^{\mathrm{i}\pi/3}\sin\left(\frac{d_0 k_x}{2} + \frac{d_0 k_y \sqrt{3}}{2}\right) - \mathrm{i}\mathrm{e}^{-\mathrm{i}\pi/3}\sin\left(\frac{d_0 k_x}{2} - \frac{d_0 k_y \sqrt{3}}{2}\right)$
2	$\cos(d_0 k_x) - \mathrm{e}^{-\mathrm{i}\pi/3}\cos\left(\frac{d_0 k_x}{2} + \frac{d_0 k_y \sqrt{3}}{2}\right) - \mathrm{e}^{\mathrm{i}\pi/3}\cos\left(\frac{d_0 k_x}{2} - \frac{d_0 k_y \sqrt{3}}{2}\right)$
3	$-\mathrm{i}\sin(d_0 k_x) + \mathrm{i}\sin\left(\frac{d_0 k_x}{2} + \frac{d_0 k_y \sqrt{3}}{2}\right) + \mathrm{i}\sin\left(\frac{d_0 k_x}{2} - \frac{d_0 k_y \sqrt{3}}{2}\right)$
4	$\cos(d_0 k_x) - \mathrm{e}^{\mathrm{i}\pi/3}\cos\left(\frac{d_0 k_x}{2} + \frac{d_0 k_y \sqrt{3}}{2}\right) - \mathrm{e}^{-\mathrm{i}\pi/3}\cos\left(\frac{d_0 k_x}{2} - \frac{d_0 k_y \sqrt{3}}{2}\right)$
5	$-\mathrm{i}\sin(d_0 k_x) - \mathrm{i}\mathrm{e}^{-\mathrm{i}\pi/3}\sin\left(\frac{d_0 k_x}{2} + \frac{d_0 k_y \sqrt{3}}{2}\right) - \mathrm{i}\mathrm{e}^{\mathrm{i}\pi/3}\sin\left(\frac{d_0 k_x}{2} - \frac{d_0 k_y \sqrt{3}}{2}\right)$

Here, $\delta_{\boldsymbol{k}'}$ represents the Kronecker Delta. It is one for $\boldsymbol{k}' = 0$ and zero otherwise. The sum runs over all allowed wave vectors $\boldsymbol{k}$ and over the values $m = -2, \ldots, 3$ for the mode index.

Now, we discuss the energy E in Fourier space. Inserting Eq. (D.11) into Eq. (D.6), we obtain after some transformations:

$$E = \sum_{\boldsymbol{k},m} \eta_m^*(\boldsymbol{k}) \left[-J\cos\left(\frac{m\pi}{3}\right)\eta_m(\boldsymbol{k}) + \frac{(-1)^m}{2}\sum_{\Delta m} G_{\Delta m}(\boldsymbol{k})\eta_{m+\Delta m}(\boldsymbol{k}) \right]. \tag{D.14}$$

Here, the outer sum runs over all allowed wave vectors $\boldsymbol{k}$ and over the values $m = -2, \ldots, 3$ for the mode index. The inner sum runs over $\Delta m = 0, \ldots, 5$. The symbol $\eta_m^*(\boldsymbol{k})$ denotes the complex conjugate of $\eta_m(\boldsymbol{k})$. The index $m + \Delta m$ is meant modulo six. The symbol $G_{\Delta m}(\boldsymbol{k})$ is defined by

$$G_{\Delta m}(\boldsymbol{k}) = \frac{1}{6}\sum_b \exp\left(\frac{2\pi\mathrm{i}\Delta m b}{6} + \mathrm{i}\boldsymbol{k}\cdot\boldsymbol{\Delta R}^b\right). \tag{D.15}$$

Here, the sum runs over all bond indices $b = 0, \ldots, 5$. The symbol $G_{\Delta m}(\boldsymbol{k})$ represents the information about cell neighborships contained in $\boldsymbol{\Delta R}^b$ in Fourier space. It can be computed explicitly from the vectors $\boldsymbol{\Delta R}^b$. The functional dependence of $G_{\Delta m}(\boldsymbol{k})$ on Δm and $\boldsymbol{k}$ is shown in Table D.2. Note that for $\boldsymbol{k} = 0$,

$$G_{\Delta m}(0) = \delta_{\Delta m}. \tag{D.16}$$

Thus, $G_{\Delta m}(0)$ is one for $\Delta m = 0$ and zero otherwise.

Now, we discuss the Fourier transformation of the dynamics. To this end, we first introduce new Lagrange multipliers $\nu_{\mathrm{I}}(\boldsymbol{k})$ and $\nu_{\mathrm{II}}(\boldsymbol{k})$, which correspond to $\lambda_{\mathrm{I}}^{\alpha}$ and $\lambda_{\mathrm{II}}^{\alpha}$

in Fourier space, respectively. The conditions are imposed as follows:

$$\bar{E} = E + \sum_{\boldsymbol{k}} \nu_{\mathrm{I}}(\boldsymbol{k})\eta_0^*(\boldsymbol{k}) - \sum_{\boldsymbol{k}'} \nu_{\mathrm{II}}(\boldsymbol{k}') \left(\delta_{\boldsymbol{k}'} - \frac{1}{n_x n_y} \sum_{\boldsymbol{k},m} \eta_m^*(\boldsymbol{k})\eta_m(\boldsymbol{k}+\boldsymbol{k}') \right). \tag{D.17}$$

Here and in the following, $\boldsymbol{k}$ and $\boldsymbol{k}'$ run over all allowed wave vectors and $m = -2, \ldots, 3$. Eq. (D.17) can be derived from Eq. (D.4).

Now, the Fourier transformation of the time evolutions, Eq. (D.5), reads:[3]

$$\frac{\mathrm{d}\eta_m(\boldsymbol{k})}{\mathrm{d}t} = -2r \frac{\partial \bar{E}}{\partial[\eta_m^*(\boldsymbol{k})]}. \tag{D.19}$$

Insertion of $\bar{E}$ yields:

$$\begin{aligned} \frac{\mathrm{d}\eta_m(\boldsymbol{k})}{r\mathrm{d}t} = 2J\cos\left(\frac{m\pi}{3}\right)\eta_m(\boldsymbol{k}) - (-1)^m \sum_{\Delta m} G_{\Delta m}(\boldsymbol{k})\eta_{m+\Delta m}(\boldsymbol{k}) \\ - 2\delta_m \nu_{\mathrm{I}}(\boldsymbol{k}) - \frac{2}{n_x n_y}\sum_{\boldsymbol{k}'} \nu_{\mathrm{II}}(\boldsymbol{k}')\eta_m(\boldsymbol{k}+\boldsymbol{k}'). \end{aligned} \tag{D.20}$$

Here, the value of Lagrange multiplier $\nu_{\mathrm{I}}(\boldsymbol{k})$ is always set such that $\mathrm{d}\eta_0(\boldsymbol{k})/\mathrm{d}t = 0$ for all $\boldsymbol{k}$. Then, Condition I can stay fulfilled: $\eta_0(\boldsymbol{k}) = 0$.

The value of the Lagrange multiplier $\nu_{\mathrm{II}}(\boldsymbol{k})$ follows from the time derivative of Eq. (D.13). After some transformations, we obtain:

$$\nu_{\mathrm{II}}(\boldsymbol{k}') = \sum_{\boldsymbol{k},m} \eta_m^*(\boldsymbol{k}+\boldsymbol{k}') \left[J\cos\left(\frac{m\pi}{3}\right)\eta_m(\boldsymbol{k}) - \frac{(-1)^m}{2} \sum_{\Delta m} G_{\Delta m}(\boldsymbol{k})\eta_{m+\Delta m}(\boldsymbol{k}) \right]. \tag{D.21}$$

Note that in particular, $\nu_{\mathrm{II}}(0) = -E$.

Now, we have rewritten the entire Core PCP model in Fourier space. As a consequence of the time evolution, Eq. (D.20), we find for instance that the modes for different indices m are only coupled via the inter-cellular interactions and via Condition II. Moreover, the modes for different $\boldsymbol{k}$ are only coupled via Condition II.

---

[3] Here, with $z = x+iy$, we define the derivative of a function $f(z, z^*)$ depending on z and its complex conjugate z^* by:

$$\frac{\partial f(z,z^*)}{\partial z^*} = \frac{\partial f(x,y)}{\partial x}\frac{\partial x(z,z^*)}{\partial z^*} + \frac{\partial f(x,y)}{\partial y}\frac{\partial y(z,z^*)}{\partial z^*} = \frac{1}{2}\frac{\partial f(x,y)}{\partial x} + \frac{\mathrm{i}}{2}\frac{\partial f(x,y)}{\partial y}. \tag{D.18}$$

As a consequence, in Eq. (D.19), a factor of 2 appears as compared to Eq. (D.5). After all, this is because in Fourier space, E depends on the $\eta_m(\boldsymbol{k})$ and on their respective conjugates $\eta_m^*(\boldsymbol{k})$, which are in total twice as many variables as in the original model, where E depends only on the $\sigma_b(\boldsymbol{R}^\alpha)$. Note however, that in Fourier space, the variables are not independent of each other because of Eq. (D.10).

D.3 Continuous degeneracy of the homogeneous ground state

In this section, we discuss homogeneous states. Then, we have

$$\eta_m(\boldsymbol{k}) = 0 \qquad \text{for } \boldsymbol{k} \neq 0. \tag{D.22}$$

Furthermore, according to Condition I, $\eta_0(0) = 0$. Thus, the only remaining Fourier modes to discuss are $\eta_m(0)$ for $m = -2, -1, 1, 2, 3$.

Here, we discuss the ground state energies. The possible states are restricted by Condition II, which reads:

$$\sum_m |\eta_m(0)|^2 = n_x n_y \qquad \text{(Condition II)}. \tag{D.23}$$

Here, $|\eta_m(0)|$ denotes the complex norm of $\eta_m(0)$. The energy reads:

$$E = \sum_m \left[-J \cos\left(\frac{m\pi}{3}\right) + \frac{(-1)^m}{2} \right] |\eta_m(0)|^2. \tag{D.24}$$

We find that under the constraint of Condition II, E attains a global minimum for states where only the polar mode exists. Thus, because of Eq. (D.10), from which follows that $\eta_1(0) = \eta^*_{-1}(0)$, we have for the ground state:

$$|\eta_m(0)|^2 = \frac{n_x n_y}{2} \qquad \text{for } m = -1, 1 \text{ and} \tag{D.25}$$

$$|\eta_m(0)|^2 = 0 \qquad \text{for } m = -2, 2, 3. \tag{D.26}$$

The corresponding ground state energy reads:

$$E_0 = -\frac{n_x n_y}{2}(J + 1). \tag{D.27}$$

Note that this energy is independent of the complex argument of $\eta_1(0)$.[4] Thus, for the homogeneous case, the ground state of the Core PCP model is continuously degenerated with respect to the polarity angle ψ_0.[5]

---

[4] Note that the same is true for the energy of any homogeneous state, Eq. (D.24).

[5] Note that we find a continuous ground state degeneracy for a more general class of PCP models. In particular, such a general class may contain an arbitrary number of conditions as long as all conditions and the energy only contain terms that are linear and quadratic in the σ, and as long as the conditions or the energy do not introduce external anisotropies. Moreover, for the ground state degeneracy to appear, the σ do not even have to be scalars. They may also be objects containing several scalars (for instance one for each PCP protein).

D.4 Relaxation of hydrodynamic modes

Now, we discuss small long wavelength perturbations from a homogeneous polar ground state. The angle of the ground state be ψ_0, the wave vector of the perturbation be $\boldsymbol{q}$, and the amplitude of the perturbation be $\delta\psi$. Thus, we start from the following initial polarity angle field $\psi(\boldsymbol{r})$:

$$\psi(\boldsymbol{r}) = \psi_0 + \delta\psi \cos(\boldsymbol{q}\cdot\boldsymbol{r} + \varphi). \tag{D.28}$$

Here, the angle φ denotes a constant phase.

The polarity angle field $\psi(\boldsymbol{r})$ defines the following initial PCP protein distribution:

$$\sigma_b(\boldsymbol{R}^\alpha) = 3^{-1/2}\cos\left(\frac{2\pi b}{6} - \psi(\boldsymbol{R}^\alpha)\right). \tag{D.29}$$

This distribution clearly fulfills Condition I and the prefactor was chosen such that Condition II is fulfilled, too.

In the following, we examine the long term relaxation of this PCP field to first order in $\delta\psi$ and in the hydrodynamic limit, i.e. to second order in $d_0 q$. Here, q denotes the vector norm of $\boldsymbol{q}$. We choose the second order in $d_0 q$, because this is the lowest order that appears in a generic non-equilibrium theory for the relaxation of the Frank free energy (see below).

To examine the long-term relaxation of the PCP field, we first transform the initial condition into Fourier space. Up to first order in $\delta\psi$, we have:

$$\eta_1(0) = \left(\frac{n_x n_y}{2}\right)^{1/2} \mathrm{e}^{-\mathrm{i}\psi_0} \tag{D.30}$$

$$\eta_1(\boldsymbol{q}) = -\mathrm{i}\frac{\delta\psi}{2}\left(\frac{n_x n_y}{2}\right)^{1/2} \mathrm{e}^{-\mathrm{i}\psi_0 - \mathrm{i}\varphi} \tag{D.31}$$

$$\eta_1(-\boldsymbol{q}) = -\mathrm{i}\frac{\delta\psi}{2}\left(\frac{n_x n_y}{2}\right)^{1/2} \mathrm{e}^{-\mathrm{i}\psi_0 + \mathrm{i}\varphi}. \tag{D.32}$$

The corresponding modes $\eta_{-1}(\boldsymbol{k})$ for $\boldsymbol{k} \in \{-\boldsymbol{q}, 0, \boldsymbol{q}\}$ can be obtained using Eq. (D.10), which states that $\eta_m(\boldsymbol{k}) = \eta^*_{-m}(-\boldsymbol{k})$. All other modes $\eta_m(\boldsymbol{k})$ are zero to first order in $\delta\psi$.

Now, given this initial state, we systematically examine which of the modes $\eta_m(\boldsymbol{k})$ are non-zero to first order in $\delta\psi$ during time evolution. To this end, we also have to discuss the Lagrange multipliers $\nu_{\mathrm{II}}(\boldsymbol{k})$.

1. Initially, for $m \in \{-1, 1\}$, the modes $\eta_m(0)$ are of order 1, and the modes $\eta_m(\boldsymbol{k})$ with $\boldsymbol{k} \in \{-\boldsymbol{q}, \boldsymbol{q}\}$ are of first order in $\delta\psi$. The other modes $\eta_m(\boldsymbol{k})$ are of second or higher order in $\delta\psi$.

2. From Eq. (D.21) follows that initially, the Lagrange multiplier $\nu_{\mathrm{II}}(0)$ is of order

Table D.3: Values of $G_{\Delta m}(\boldsymbol{k})$ in the hydrodynamic limit, i.e. to second order in $d_0 k$. Here, k and ϕ_k denote the norm and the angle of the vector $\boldsymbol{k}$, respectively.

Δm	0	1	2	3	4	5
$G_{\Delta m}(\boldsymbol{k})$	$1-\frac{1}{4}d_0^2k^2$	$-\frac{\mathrm{i}}{2}\mathrm{e}^{\mathrm{i}\phi_k}d_0k$	$-\frac{1}{8}\mathrm{e}^{2\mathrm{i}\phi_k}d_0^2k^2$	0	$-\frac{1}{8}\mathrm{e}^{-2\mathrm{i}\phi_k}d_0^2k^2$	$-\frac{\mathrm{i}}{2}\mathrm{e}^{-\mathrm{i}\phi_k}d_0k$

1, and the Lagrange multipliers $\nu_{\mathrm{II}}(\boldsymbol{k})$ with $\boldsymbol{k} \in \{-\boldsymbol{q}, \boldsymbol{q}\}$ are of first order in $\delta\psi$. The other Lagrange multipliers $\nu_{\mathrm{II}}(\boldsymbol{k})$ are of second or higher order in $\delta\psi$.

3. During time evolution, the modes $\eta_m(\boldsymbol{k})$ and the Lagrange multipliers $\nu_{\mathrm{II}}(\boldsymbol{k})$ with $\boldsymbol{k} \notin \{-\boldsymbol{q}, 0, \boldsymbol{q}\}$ remain of second or higher order in $\delta\psi$. This is because they start out to be of second or higher order in $\delta\psi$. Then, for each subsequent infinitesimal time interval, the Lagrange multipliers $\nu_{\mathrm{II}}(\boldsymbol{k})$, Eq. (D.21), and the time derivatives of the modes $\eta_m(\boldsymbol{k})$, Eq. (D.20), are of second or higher order in $\delta\psi$.

4. Now, we discuss the time evolution of the modes $\eta_m(\boldsymbol{k})$ and the Lagrange multipliers $\nu_{\mathrm{II}}(\boldsymbol{k})$ for $\boldsymbol{k} \in \{-\boldsymbol{q}, 0, \boldsymbol{q}\}$. For $\boldsymbol{k} = 0$ and $m \in \{-1, 1\}$, the modes $\eta_m(0)$ and the Langrange multiplier $\nu_{\mathrm{II}}(\boldsymbol{0})$ remain of order 1. For $\boldsymbol{k} = 0$ and $m \notin \{-1, 1\}$, the modes $\eta_m(0)$ remain of second or higher order in $\delta\psi$. Otherwise, for $\boldsymbol{k} \in \{-\boldsymbol{q}, \boldsymbol{q}\}$ and $m \neq 0$ the modes $\eta_m(\boldsymbol{k})$ and the Langrange multipliers $\nu_{\mathrm{II}}(\boldsymbol{k})$ are never of order 1. They are typically of first order in $\delta\psi$. All of this follows from the initial conditions and from applying Eqs. (D.20) and (D.21) to subsequent time intervals.

   That for $|m| = 1$, the modes $\eta_m(0)$ remain of order 1 follows from Condition II, Eq. (D.13), and $\eta_1(0) = \eta_{-1}^*(0)$. Furthermore, from the dynamics, Eq. (D.20), follows that $\eta_1(0)$ remains constant to first order in $\delta\psi$.

Thus, in order to determine the relaxation time scale of the perturbation, we only need to examine the dynamics of the ten modes $\eta_m(\boldsymbol{k})$ for $\boldsymbol{k} \in \{-\boldsymbol{q}, \boldsymbol{q}\}$ and $m \neq 0$. However, from Eq. (D.10) follows that $\eta_m(-\boldsymbol{q}) = \eta_{-m}^*(\boldsymbol{q})$. Thus, it remains to discuss the dynamics of the five independent modes $\eta_m(\boldsymbol{q})$ with $m \in \{1, -1, 2, -2, 3\}$.

Now, we explicitly note the dynamics of these five modes, which follows from Eqs. (D.20) and (D.21). To this end, we use expressions for $G_{\Delta m}(\boldsymbol{k})$ that are computed to second order in $d_0 k$ (Table D.3). After a number of transformations, we obtain to second order in $d_0 q$:

$$\begin{aligned}\frac{\mathrm{d}\eta_1(\boldsymbol{q})}{r\mathrm{d}t} = &-\left[J+1+\frac{1}{8}\left(1-\frac{1}{2}\mathrm{e}^{-2\mathrm{i}(\psi_0-\phi_q)}\right)d_0^2q^2\right]\eta_1(\boldsymbol{q})\\ &-\mathrm{e}^{-2\mathrm{i}\psi_0}\left[J+1-\frac{1}{8}\left(1-\frac{1}{2}\mathrm{e}^{2\mathrm{i}(\psi_0-\phi_q)}\right)d_0^2q^2\right]\eta_{-1}(\boldsymbol{q})\\ &-\frac{\mathrm{i}}{4}\mathrm{e}^{\mathrm{i}\phi_q}d_0q\,\eta_2(\boldsymbol{q})+\frac{\mathrm{i}}{4}\mathrm{e}^{-\mathrm{i}\phi_q-2\mathrm{i}\psi_0}d_0q\,\eta_{-2}(\boldsymbol{q})\end{aligned}$$

$$+\frac{d_0^2q^2}{16}\left[\mathrm{e}^{-2\mathrm{i}(\psi_0+\phi_q)}-\mathrm{e}^{2\mathrm{i}\phi_q}\right]\eta_3(\boldsymbol{q}) \tag{D.33}$$

$$\begin{aligned}\frac{\mathrm{d}\eta_{-1}(\boldsymbol{q})}{r\mathrm{d}t} &= -\mathrm{e}^{2\mathrm{i}\psi_0}\left[J+1-\frac{1}{8}\left(1-\frac{1}{2}\mathrm{e}^{-2\mathrm{i}(\psi_0-\phi_q)}\right)d_0^2q^2\right]\eta_1(\boldsymbol{q})\\ &\quad -\left[J+1+\frac{1}{8}\left(1-\frac{1}{2}\mathrm{e}^{2\mathrm{i}(\psi_0-\phi_q)}\right)d_0^2q^2\right]\eta_{-1}(\boldsymbol{q})\\ &\quad +\frac{\mathrm{i}}{4}\mathrm{e}^{\mathrm{i}\phi_q+2\mathrm{i}\psi_0}d_0q\,\eta_2(\boldsymbol{q})-\frac{\mathrm{i}}{4}\mathrm{e}^{-\mathrm{i}\phi_q}d_0q\,\eta_{-2}(\boldsymbol{q})\\ &\quad +\frac{d_0^2q^2}{16}\left[\mathrm{e}^{2\mathrm{i}(\psi_0+\phi_q)}-\mathrm{e}^{-2\mathrm{i}\phi_q}\right]\eta_3(\boldsymbol{q})\end{aligned} \tag{D.34}$$

$$\begin{aligned}\frac{\mathrm{d}\eta_2(\boldsymbol{q})}{r\mathrm{d}t} &= \frac{\mathrm{i}}{2}\mathrm{e}^{-\mathrm{i}\phi_q}d_0q\,\eta_1(\boldsymbol{q})-2\left[J+1-\frac{1}{8}d_0^2q^2\right]\eta_2(\boldsymbol{q})+\frac{1}{8}\mathrm{e}^{2\mathrm{i}\phi_q}d_0^2q^2\,\eta_{-2}(\boldsymbol{q})\\ &\quad +\frac{\mathrm{i}}{2}\mathrm{e}^{i\phi_q}d_0q\,\eta_3(\boldsymbol{q})\end{aligned} \tag{D.35}$$

$$\begin{aligned}\frac{\mathrm{d}\eta_{-2}(\boldsymbol{q})}{r\mathrm{d}t} &= \frac{\mathrm{i}}{2}\mathrm{e}^{\mathrm{i}\phi_q}d_0q\,\eta_{-1}(\boldsymbol{q})+\frac{1}{8}\mathrm{e}^{-2\mathrm{i}\phi_q}d_0^2q^2\,\eta_2(\boldsymbol{q})-2\left[J+1-\frac{1}{8}d_0^2q^2\right]\eta_{-2}(\boldsymbol{q})\\ &\quad +\frac{\mathrm{i}}{2}\mathrm{e}^{-i\phi_q}d_0q\,\eta_3(\boldsymbol{q})\end{aligned} \tag{D.36}$$

$$\begin{aligned}\frac{\mathrm{d}\eta_3(\boldsymbol{q})}{r\mathrm{d}t} &= \frac{1}{8}\mathrm{e}^{-2\mathrm{i}\phi_q}d_0^2q^2\,\eta_1(\boldsymbol{q})+\frac{1}{8}\mathrm{e}^{2\mathrm{i}\phi_q}d_0^2q^2\,\eta_{-1}(\boldsymbol{q})+\frac{\mathrm{i}}{2}\mathrm{e}^{-\mathrm{i}\phi_q}d_0q\,\eta_2(\boldsymbol{q})+\frac{\mathrm{i}}{2}\mathrm{e}^{\mathrm{i}\phi_q}d_0q\,\eta_{-2}(\boldsymbol{q})\\ &\quad -2\left[J+1-\frac{1}{8}d_0^2q^2\right]\eta_3(\boldsymbol{q}).\end{aligned} \tag{D.37}$$

Here, q and ϕ_q denote norm and angle of the vector $\boldsymbol{q}$, respectively. They are defined by:

$$\boldsymbol{q}=q\begin{pmatrix}\cos\phi_q\\ \sin\phi_q\end{pmatrix}. \tag{D.38}$$

Now, we show that when discussing the relaxation of the modes $\eta_m(\boldsymbol{q})$ with $|m|=1$ to second order in d_0q, we can dismiss $\eta_3(\boldsymbol{q})$. First, we realize that the modes $\eta_m(\boldsymbol{q})$ with $|m|=2$ are of first order in d_0q, and the mode $\eta_3(\boldsymbol{q})$ is of second order in d_0q. Furthermore, the mode $\eta_3(\boldsymbol{q})$ feeds back into the dynamics of the other modes via factors that are of at least first order in d_0q. Thus, $\eta_3(\boldsymbol{q})$ only creates terms of at least third order in d_0q in the dynamics of the polar modes. Therefore, we can dismiss $\eta_3(\boldsymbol{q})$ when discussing the polar dynamics to second order in d_0q.

Using similar arguments, the dynamics of the remaining modes can be simplified to:

$$\frac{\mathrm{d}}{\mathrm{d}t}\begin{pmatrix}\eta_1(\boldsymbol{q})\\ \eta_{-1}(\boldsymbol{q})\\ \eta_2(\boldsymbol{q})\\ \eta_{-2}(\boldsymbol{q})\end{pmatrix}=-\boldsymbol{M}\begin{pmatrix}\eta_1(\boldsymbol{q})\\ \eta_{-1}(\boldsymbol{q})\\ \eta_2(\boldsymbol{q})\\ \eta_{-2}(\boldsymbol{q})\end{pmatrix}. \tag{D.39}$$

Here, the matrix $\boldsymbol{M}$ is defined by

$$\boldsymbol{M} = r \begin{pmatrix} a & b & c & d \\ b^* & a^* & -d^* & -c^* \\ 2c^* & 0 & e & 0 \\ 0 & -2c & 0 & e \end{pmatrix} \tag{D.40}$$

with

$$a = J + 1 + \frac{1}{8}\left(1 - \frac{1}{2}\mathrm{e}^{-2\mathrm{i}(\psi_0 - \phi_q)}\right) d_0^2 q^2 \tag{D.41}$$

$$b = \mathrm{e}^{-2\mathrm{i}\psi_0}\left[J + 1 - \frac{1}{8}\left(1 - \frac{1}{2}\mathrm{e}^{2\mathrm{i}(\psi_0 - \phi_q)}\right) d_0^2 q^2\right] \tag{D.42}$$

$$c = \frac{\mathrm{i}}{4}\mathrm{e}^{\mathrm{i}\phi_q} d_0 q \tag{D.43}$$

$$d = -\frac{\mathrm{i}}{4}\mathrm{e}^{-\mathrm{i}\phi_q - 2\mathrm{i}\psi_0} d_0 q \tag{D.44}$$

$$e = 2(J + 1). \tag{D.45}$$

The eigenvalues of $\boldsymbol{M}$ read to second order in $d_0 q$:

$$k_1 = k_2 = 2r(J + 1) \tag{D.46}$$

$$k_3 = 2r(J + 1) + \frac{r d_0^2 q^2}{8(J + 1)} \tag{D.47}$$

$$k_4 = \frac{r d_0^2 q^2}{8}\left(2 - \frac{1}{J + 1} - \cos\left(2[\psi_0 - \phi_q]\right)\right). \tag{D.48}$$

Here, the first two eigenvalues, k_1 and k_2, correspond to the two-dimensional eigenspace where $\eta_1(\boldsymbol{q})$ and $\eta_{-1}(\boldsymbol{q})$ are zero and $\eta_2(\boldsymbol{q})$ and $\eta_{-2}(\boldsymbol{q})$ take arbitrary non-zero values. Here we are interested in the relaxation of $\eta_1(\boldsymbol{q})$ and $\eta_{-1}(\boldsymbol{q})$, which is described by k_3 and k_4. The rate k_3 describes a fast relaxation, whereas the rate k_4 converges to zero for $d_0 q \to 0$. Thus, k_4 corresponds to the hydrodynamic relaxation mode. Note that this relaxation time scale depends on the angle difference between the angle of unperturbed polar ground state ψ_0 and the angle of the wave vector of the perturbation ϕ_q. Also note that the relaxation characterized by the eigenvalue k_4 involves both, polar and nematic modes.

D.5 Comparison to a generic first order polarity dynamics

Here, we compare the relaxation rate k_4 of the cellular Core PCP model in the hydrodynamic limit with the generic relaxation of a polarity field. To this end, we first formulate the generic theory.

D.5.1 Generic first order polarity dynamics

Here, we describe the generic relaxation of an inhomogeneous polarity field $\boldsymbol{p}$, which is normalized to one: $p_i p_i = 1$. We describe the energetic cost of deformations in the polarity field $\boldsymbol{p}$ by the Frank free energy in two dimensions [134, 149]:

$$F_d = \frac{1}{2} \int \Big[K_1(\partial_x p_x + \partial_y p_y)^2 + K_3(\partial_x p_y - \partial_y p_x)^2 + \Lambda_\| p_i p_i \Big] \, \mathrm{d}^2 r. \tag{D.49}$$

Here, K_1 and K_3 denote the elasticities associated with splay and bend deformations, respectively. The coefficient $\Lambda_\|$ is a Lagrange multiplier, which ensures the normalization of $\boldsymbol{p}$.

Then, in a hydrodynamic theory for systems close to equilibrium, the first order polarity dynamics in the absence of material flows is given by [59, 66]:

$$\frac{\partial p_i}{\partial t} = \frac{1}{\gamma_1} h_i. \tag{D.50}$$

Here, γ_1 is a phenomenological coefficient and h_i is the conjugated force for the flux $\partial p_i / \partial t$. It is given by the functional derivative $h_i = -\delta F_d / \delta p_i$. Insertion of F_d yields:

$$\frac{\partial p_i}{\partial t} = (\kappa_1 - \kappa_3) \partial_i \partial_j p_j + \kappa_3 \partial_j \partial_j p_i - \frac{\Lambda_\|}{\gamma_1} p_i. \tag{D.51}$$

Here, we defined the coefficients $\kappa_1 = K_1/\gamma_1$ and $\kappa_3 = K_3/\gamma_1$, characterizing the decay of splay and bend modes, respectively.

Now, we rephrase the polarity dynamics in terms of the polarity angle θ, which we define by:

$$\boldsymbol{p} = \begin{pmatrix} \cos\theta \\ \sin\theta \end{pmatrix}. \tag{D.52}$$

Then, the polarity angle dynamics reads:

$$\frac{\partial \theta}{\partial t} = (\kappa_1 - \kappa_3) \Big[- p_{\perp i} p_j (\partial_i \theta)(\partial_j \theta) + p_{\perp i} p_{\perp j} (\partial_i \partial_j \theta) \Big] + \kappa_3 \partial_i \partial_i \theta. \tag{D.53}$$

Here, we defined the following unit vector perpendicular to $\boldsymbol{p}$:

$$\boldsymbol{p}_\perp = \begin{pmatrix} -\sin\theta \\ \cos\theta \end{pmatrix}. \tag{D.54}$$

Now, we consider a small perturbation $\delta\theta$ with respect to the homogeneous ground state polarity angle ψ_0:

$$\theta(\boldsymbol{r}) = \psi_0 + \delta\theta(\boldsymbol{r}). \tag{D.55}$$

Then, the dynamics of $\delta\theta$ reads to linear order:

$$\frac{\partial\delta\theta}{\partial t} = (\kappa_1 - \kappa_3) p_{\perp i} p_{\perp j} \partial_i \partial_j \delta\theta + \kappa_3 \partial_i \partial_i \delta\theta. \tag{D.56}$$

Now, we define the Fourier transformation of $\delta\theta$ by

$$\delta\vartheta(\boldsymbol{q}) = \int \delta\theta(\boldsymbol{r}) \mathrm{e}^{-\mathrm{i}\boldsymbol{q}\cdot\boldsymbol{r}} \, \mathrm{d}^2 r. \tag{D.57}$$

Then, the relaxation dynamics in Fourier space reads:

$$\frac{\partial\delta\vartheta}{\partial t} = -(\kappa_1 - \kappa_3) p_{\perp i} p_{\perp j} q_i q_j \delta\vartheta - \kappa_3 q_i q_i \delta\vartheta. \tag{D.58}$$

This can be transformed into:

$$\frac{\partial\delta\vartheta}{\partial t} = -k_{\mathrm{gen}} \delta\vartheta, \tag{D.59}$$

where the rate k_{gen} is given by:

$$k_{\mathrm{gen}} = q^2 \left(\frac{\kappa_1 + \kappa_3}{2} - \frac{\kappa_1 - \kappa_3}{2} \cos\left(2[\psi_0 - \phi_q]\right) \right). \tag{D.60}$$

Here, q and ϕ_q denote angle and norm of $\boldsymbol{q}$, respectively, according to:

$$\boldsymbol{q} = q \begin{pmatrix} \cos\phi_q \\ \sin\phi_q \end{pmatrix}. \tag{D.61}$$

The rate k_{gen} represents the relaxation rate of a small perturbation in this generic theory.

D.5.2 Effective relaxation rates of bend and splay modes in the cellular Core PCP model

Now, we can directly compare the relaxation rate k_{gen} obtained from the generic theory to the hydrodynamic relaxarion rate k_4 in Eq. (D.48). We find that they show the same dependence on the angle difference $\psi_0 - \phi_q$. Thus, we can directly determine the effective relaxation rates of bend and splay modes for the cellular Core PCP model:

$$\kappa_1 = \frac{r d_0^2}{8}\left(3 - \frac{1}{J+1}\right) \qquad \text{(splay)} \qquad \text{(D.62)}$$

$$\kappa_3 = \frac{r d_0^2}{8}\left(1 - \frac{1}{J+1}\right) \qquad \text{(bend).} \qquad \text{(D.63)}$$

We verified these results using vertex model simulations (data not shown).

The interesting result here is the dependence on the dimensionless parameter of the cellular model J, which characterizes the ratio between intracellular and inter-cellular coupling strength. For given inter-cellular relaxation rate ($r = \text{const.}$), but vanishing intracellular coupling ($J \to 0$), bend modes do not relax ($\kappa_3 \to 0$), but splay modes do ($\kappa_1 \neq 0$). Conversely, for given intracellular relaxation rate ($Jr = \text{const}$), but vanishing inter-cellular coupling ($r \to 0$), neither bend nor splay modes relax ($\kappa_1 \to 0$ and $\kappa_3 \to 0$). The factors $r d_0^2$ in these results were expected, since the cell center distance d_0 was the only length parameter in the Core PCP model, and the rate r was the only time scale.

Appendix E

Quantification of polarity patterns in the fruit fly wing

Here, we present methods that we used to quantify polarity patterns in adult and pupal fruit fly wings. In Sections E.1 and E.2, we develop algorithms to quantify wing hair polarity and polarity of clonal PCP protein stainings, respectively. Here, *clonal staining* refers to a staining applied only within a random subset of cells in a tissue. In Section E.3, we rephrase known methods to quantify single cell PCP nematics and cell elongation nematics. Finally, in Section E.4, we present details on experimental procedures.

E.1 Hair polarity in the adult fly wing

In Section E.1.1, we describe an algorithm to quantify the local wing hair direction in digital images. Afterwards, in Sections E.1.2 and E.1.3, we describe how we create one-dimensional profiles of wing hair angles and wing margin bristles, respectively.

E.1.1 Quantification of the wing hair direction pattern

The basic idea for the quantification of wing hair direction is the following. In a grayscale light microscopic image of an adult fruit fly wing, hairs are visible as small black lines (Fig. E.1A,C). In all wing hair images that we examined, the direction of wing hairs showed at least local order. Because of this, wing images are effectively hatched by the hairs, where the local axis of the hatching is defined by the local wing hair direction. This is well illustrated by Fig. E.1A. Therefore, in order to quantify the vector direction of wing hairs, we proceeded in two steps. First, we determined the local axis of the wing hairs from a nematic image property characterizing the local hatching axis. Second, knowing the axis of the wing hairs, we fixed their vector direction.

This quantification algorithm has similarly been published in refs. [55, 159].

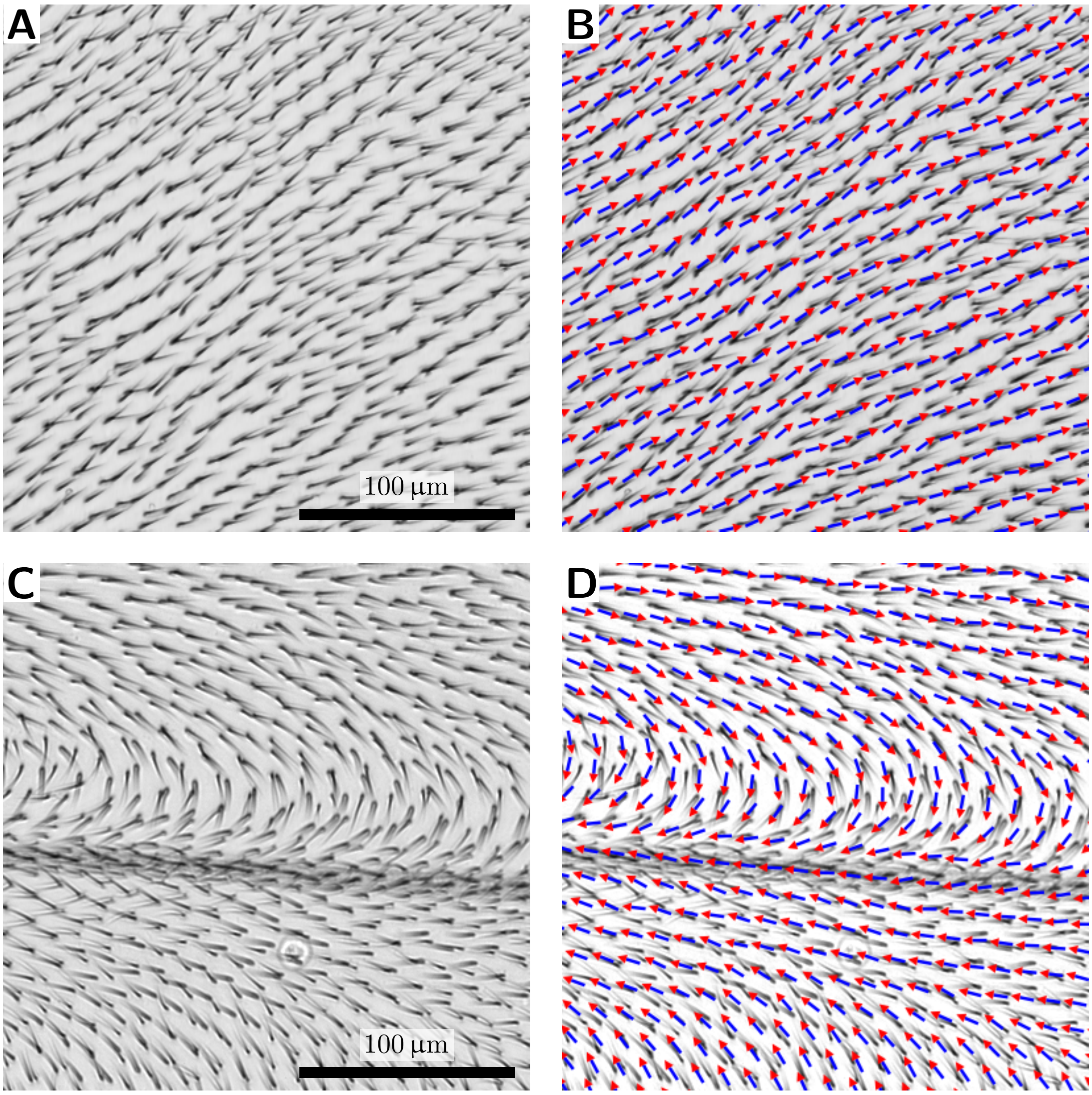

Figure E.1: Quantification of wing hair direction. **(A,B)** Magnified parts of adult fly wings, which carry wing hairs on their dorsal and ventral surfaces. **(C,D)** Quantified local directions of the wing hairs. **(A,C)** Magnified part from a wild type wing. **(B,D)** Magnified part from a wing permanently over-expressing Sple in the posterior compartment. Parameters used: $\lambda = 2\,\text{pixels} \approx 1.2\,\mu\text{m}$; $c = 5$.

Local wing hair axis

In order to access the local axis of the hatching, we locally define a nematic tensor auto-correlation. Be $I(\boldsymbol{r})$ the intensity distribution of the image depending on the pixel position $\boldsymbol{r}$. Then, we define the nematic tensor $\tilde{n}_{ij}(\boldsymbol{r})$ for each position $\boldsymbol{r}$ of the image:

$$\tilde{n}_{ij}(\boldsymbol{r}) = I(\boldsymbol{r}) \int_{\mathcal{C}(c\lambda)} I(\boldsymbol{r} + \boldsymbol{\Delta r}) \tilde{g}_{ij}(\boldsymbol{\Delta r}, \lambda) \, \mathrm{d}^2 \Delta r. \tag{E.1}$$

Here, the nematic $\tilde{g}_{ij}(\boldsymbol{\Delta r}, \lambda)$ is the kernel of the auto-correlation and λ is a parameter. For a given coordinate system, it is defined by the matrix

$$\tilde{\boldsymbol{g}}(\boldsymbol{\Delta r}, \lambda) = \mathrm{e}^{-\Delta r^2/\lambda^2} \begin{pmatrix} \cos(2\phi_{\boldsymbol{\Delta r}}) & \sin(2\phi_{\boldsymbol{\Delta r}}) \\ \sin(2\phi_{\boldsymbol{\Delta r}}) & -\cos(2\phi_{\boldsymbol{\Delta r}}) \end{pmatrix}. \tag{E.2}$$

The nematic $\tilde{g}_{ij}(\boldsymbol{\Delta r}, \lambda)$ has the same axis as $\boldsymbol{\Delta r}$, where $\phi_{\boldsymbol{\Delta r}}$ is the angle of $\boldsymbol{\Delta r}$. The norm of $\tilde{g}_{ij}(\boldsymbol{\Delta r}, \lambda)$ introduces the distance-dependent weighting $\mathrm{e}^{-\Delta r^2/\lambda^2}$, which decays on a characteristic length, given by the parameter λ. The integration in Eq. (E.1) runs over the area of a circle centered at the origin with radius $c\lambda$, where c is a cutoff parameter.

To obtain the local axis of wing hairs, we first computed the nematic tensor $\tilde{n}_{ij}(\boldsymbol{r})$ for each pixel, where the integral in Eq. (E.1) is substituted by a sum over pixels. Then, we divided the whole image into boxes with a side length of 20 pixels. We interpret the orientation of the average nematic within each box as the local wing hair axis.

We studied the sensibility of the quantified local hair axis with respect to the parameters λ and c. Note that the distance-dependent weighting in $\tilde{g}_{ij}(\boldsymbol{\Delta r}, \lambda)$ effectively acts as a low pass filter for the image information. Thus, the length scale λ should be chosen to be on the order of the width of the wing hairs. Fig. E.2 illustrates that the quantified local hair axis pattern is within the relevant parameter regime largely insensitive to both parameters. However, for large values of λ, the quantified local hair axis may become significantly biased by wing veins (see Fig. E.2E). For the wing hair pattern quantifications shown in Chapter 4, we chose $\lambda = 2$ pixels and $c = 5$.

Fixing the local wing hair vector direction

Having the image divided into boxes and knowing the local hair axis for each of these boxes, we need to fix the local vector directions. For each box i with axis angle ϕ_i, there are exactly two candidates for the vector direction angle ψ_i:

$$\psi_i = \phi_i \qquad \text{and} \qquad \psi_i = \phi_i + \pi. \tag{E.3}$$

The idea is to employ a semi-automated algorithm. All boxes have a *generation* property. The user defines the vector direction ψ_i for a subset of boxes: these are

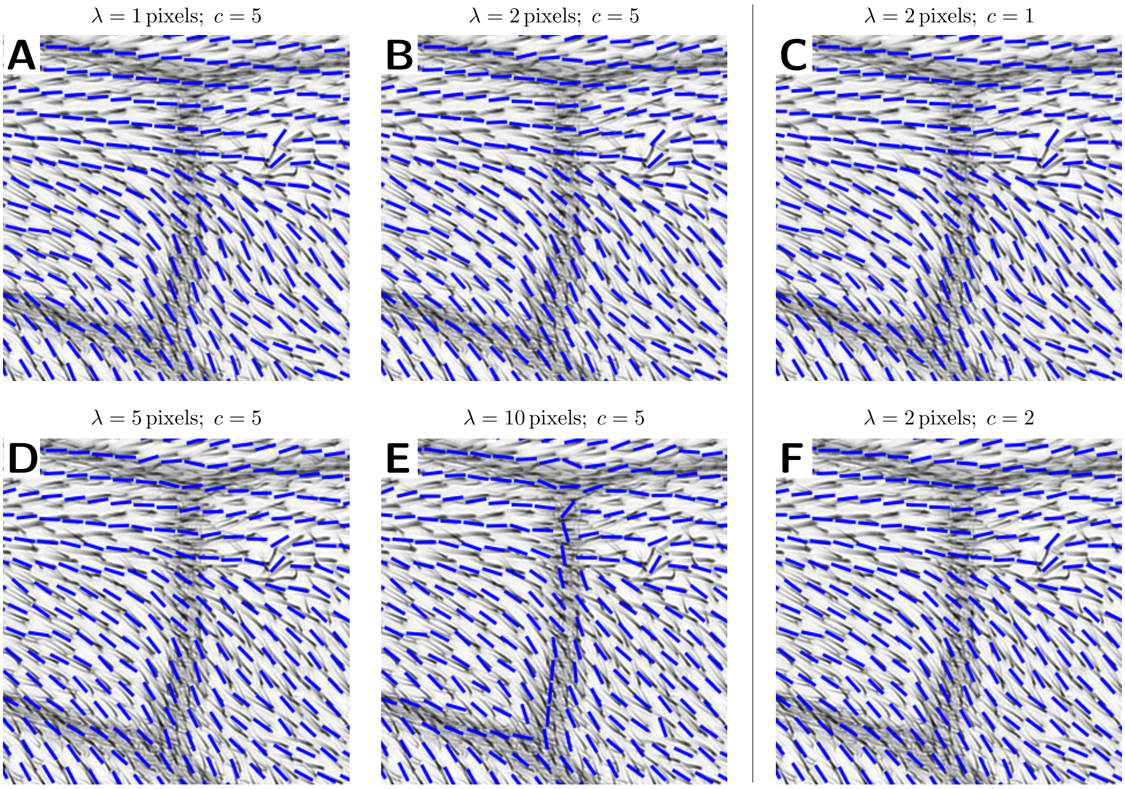
$\lambda = 1\,\mathrm{pixels};\ c = 5$
A
$\lambda = 2\,\mathrm{pixels};\ c = 5$
B
$\lambda = 2\,\mathrm{pixels};\ c = 1$
C
$\lambda = 5\,\mathrm{pixels};\ c = 5$
D
$\lambda = 10\,\mathrm{pixels};\ c = 5$
E
$\lambda = 2\,\mathrm{pixels};\ c = 2$
F

Figure E.2: A magnified region of an adult wing permanently over-expressing Sple in the posterior compartment and the local axis of wing hairs, which was quantified using different values for the parameters λ and c. The quantified wing hair axis (blue bars) depends only weakly on the length scale parameter λ and on the cutoff parameter c.

boxes of generation zero. Starting from these boxes, the algorithm iteratively fixes the vector direction of subsequent generations:

1. For each box i adjacent to at least a single box of an older generation, the average vector direction ψ_{avg} of all adjacent boxes that are of an older generation is computed:
$$p \begin{pmatrix} \cos \psi_{\text{avg}} \\ \sin \psi_{\text{avg}} \end{pmatrix} = \left\langle \begin{pmatrix} \cos \psi_j \\ \sin \psi_j \end{pmatrix} \right\rangle_j , \tag{E.4}$$
where the average runs over all adjacent boxes j of older generation and p is a scalar factor that may vary from box to box.

2. The vector direction of box i is set to that angle out of $\{\phi_i, \phi_i + \pi\}$ which is closer to ψ_{avg} and box i becomes a member of the current generation.

Steps 1 and 2 are repeated until all boxes have their vector direction fixed.

In a more elaborated version of the algorithm, several passes are required for fixing the vector direction of all boxes. In a first pass, step 2 is only executed for a box i, if ψ_{avg} deviates not more from ϕ_i than a cutoff angle $\Theta = 0.25\pi$. In a second pass, the vector directions of the remaining boxes are fixed. The motivation for this is that whenever the angle difference between neighboring boxes is high, the probability to pick the wrong vector direction is higher, too.

Figs. E.1B,D and E.3 show examples of quantified wing hair vector direction. In light microscopic wing hair images, the hairs from both layers, dorsal and ventral, are visible. That is why, wing hairs often appear to be organized into pairs (Fig. E.1A,C). Whenever the wing hair directions on both layers differ by more than ca.$\pi/2$, we masked the respective area of the wing (as in Fig. E.3B). However mostly, the hairs from both layers differ by less than ca. $\pi/4$.

E.1.2 Profiles of wing hair direction angles

In order to plot average wing hair angles along a line across the wing blade (as in Figs. 4.10, 4.13, 4.14, and 4.15), we proceeded as follows. First, we quantified the wing hair polarity patterns using the algorithm presented in Section E.1.1 and mapped to our reference coordinate system including a rescaling by the factor λ_0 (Fig. 4.9A). Then, we plotted the wing hair angles along the red line shown in Fig. 4.9A, which is parallel to the y axis.

Furthermore, we realized that in adult wings, the width ratio of anterior to posterior compartment is smaller than in wings at 32 hAPF. In order to compare observed wing hair patterns to results of our theory, we therefore inhomogeneously rescale the y coordinate of the wing hair data along the profile line as follows. First, we map adult vein and margin positions to their respective positions at 32 hAPF, where we take the same wild type wing as reference that already served as model for the wing blade

wild type

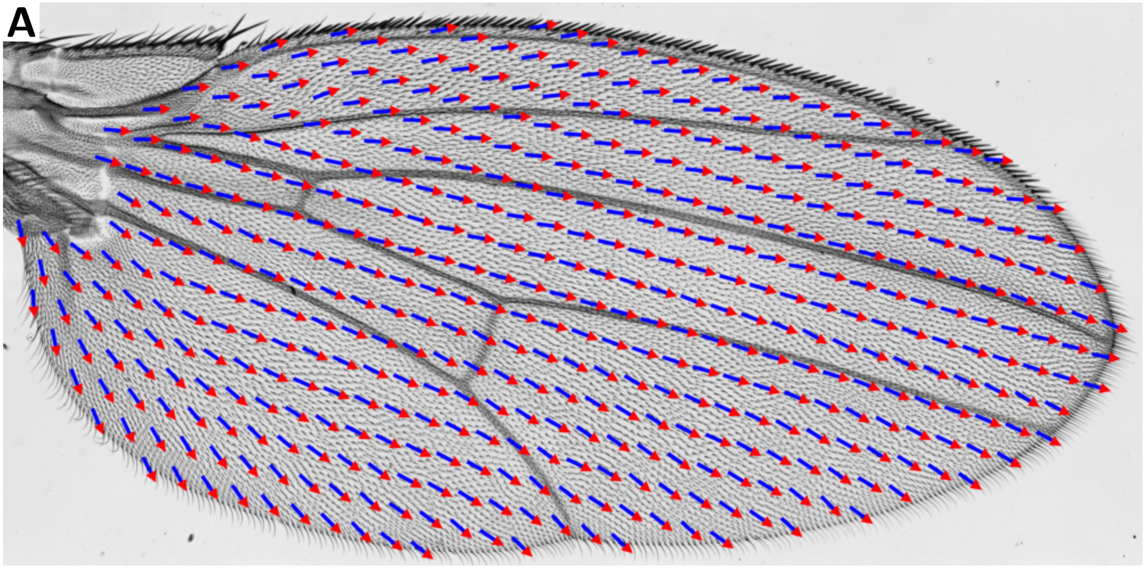

permanent Sple over-expression in the posterior compartment

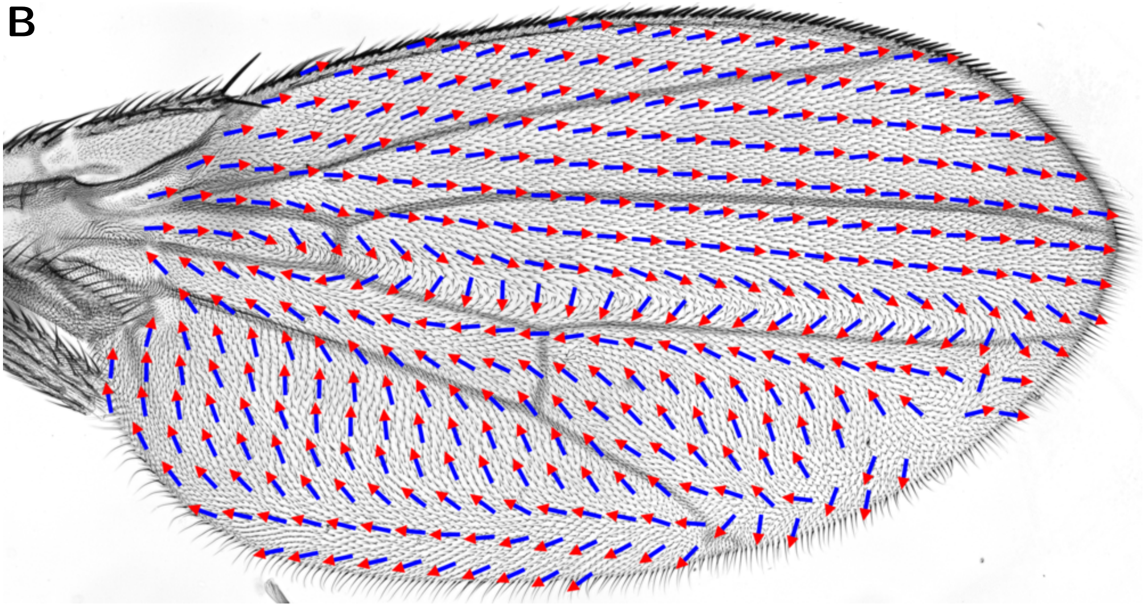

Figure E.3: Quantified wing hair direction patterns **(A)** in a wild type wing and **(B)** in a wing permanently over-expressing Sple in the posterior compartment. Polarity was averaged inside of coarser boxes containing 5×5 of the original boxes. Parameters used: $\lambda = 2\,\mathrm{pixels}$; $c = 5$.

outline for the numerical solutions. Then, we map all y positions in between veins (or between a vein and the margin) by linear interpolation.

After these transformations, the normalized hair polarity vectors of the different wings were averaged at each position y in order to obtain an average polarity vector $\boldsymbol{p}$. In the profile plots, we show the angle of the average polarity vector $\boldsymbol{p}$. The circular standard deviation σ_ψ of the angle is defined as follows [164, 165]

$$\sigma_\psi = \left(-2 \log |\boldsymbol{p}|\right)^{1/2}, \tag{E.5}$$

where $|\boldsymbol{p}|$ denotes the norm of the average polarity vector $\boldsymbol{p}$.

E.1.3 Profiles of bristle direction angles

In order to plot bristle angles along the wing margin, we first parametrize positions on the wing margin by the coordinate s (Fig. G.1A), where differences of s between two points on the margin are proportional to the corresponding margin arc length. The coordinate s takes the value of $s = 0$ at the posterior indentation between hinge and blade and the value of $s = 1$ at the anterior indentation. For discrete positions s, we quantified wing hair angles ψ_w at a distance w from the margin and bristle angles ψ_b using the wing hair algorithm presented in Section E.1.1. Margin angles ψ_m were quantified using a local linear fit and are defined to point in clockwise direction around the wing margin. All angles are defined to increase in counter-clockwise direction. The angle of zero is defined along the x axis of the coordinate system defined in Fig. 4.9A.

Throughout Chapter 4, we plot profiles of the bristle angle relative to the margin angle $\psi_b - \psi_m$ over s (for example in Fig. G.1B,C). In order to compare the profiles of different wings, the coordinate s was rescaled such that all vein positions match. To this end, we proceeded similarly as in Section E.1.2. First, the vein end positions s of wing veins were mapped onto the vein end positions of a reference wild type wing. Afterwards, the positions between two vein positions were interpolated linearly.

E.2 Quantification of polarity from images with a clonal staining

Here, we develop two different methods to quantify cell polarity from images where only random patches of cells are stained for a PCP protein. These patches are called *clones*. The first method, presented in Section E.2.1, uses segmented data. It is therefore more robust, but on the other hand, segmentation requires time-consuming hand-correction. In contrast to that, the second method, presented in Section E.2.1, is in general less robust but runs fully automatically in less than a minute on an image of approx. 10 megapixels. These quantification algorithms have been published in refs. [55, 159].

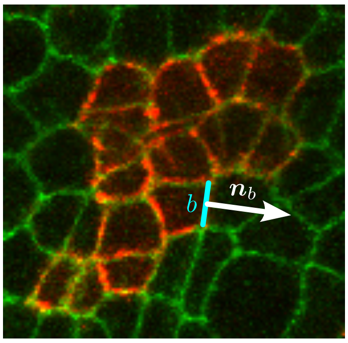

Figure E.4: Staining of Cadherin (green channel) and clonal staining for Strabismus (red channel) in a wing at 16 hAPF that permanently over-expressed Sple in the posterior compartment. The region shown belongs to the anterior compartment. Also indicated is the normal vector $\boldsymbol{n}_b$ to one cell boundary b between clone and non-clonal cells.

E.2.1 From segmented image data

Idea

For this method, we need image data with stainings for a membrane marker and a clonal staining for a PCP protein (Fig. E.4). First, we segment the cell outlines using the membrane marker staining as in ref. [54]. Then, from the clonal PCP protein staining, we define the polarity vector $\boldsymbol{p}^{\text{clone}}$ of a given clone as follows

$$\boldsymbol{p}^{\text{clone,seg.}} = \frac{\sum_b I_b \boldsymbol{n}_b}{\sum_b I_b}, \tag{E.6}$$

where the sum runs over all cell boundaries b between clonal and non-clonal cells. The vector $\boldsymbol{n}_b$ denotes the normal unit vector to this cell boundary pointing outside of the clone (Fig. E.4) and the scalar I_b is defined by the sum of the fluorescence intensities of the stained PCP protein along cell boundary b.

Application to a polarity pattern at 16 hAPF

We applied this idea to the quantification of the Core PCP pattern of 16 hAPF wings that permanently over-express Sple in the posterior compartment (result shown in Fig. 4.6). Therefore, we used a Cadherin staining for the segmentation and a clonal Strabismus staining to define the polarity (compare Fig. E.4). Since we chose a Strabismus staining, we additionally flipped the polarity vector $\boldsymbol{p}_{\text{clone}}$ in order to fulfill our convention for the sign of Core PCP (Section 1.4.1).

We quantified the polarity of all clones in five different wings using Eq. (E.6). Then, we aligned these wings as follows. Because we could not observe the landmarks used for the coordinate system shown in Fig. 4.9A, we had to choose a different coordinate system. In the Cadherin staining, we clearly identified three small precursor structures of sensory organs on vein L3 and one on the anterior cross vein. Therefore, we defined the vein L3 as x axis based on a linear fit through the three precursor structures on it. The origin was defined such that the y axis passes through the precursor structure on the anterior cross vein. Finally, all wings were scaled such that all distal wing margins

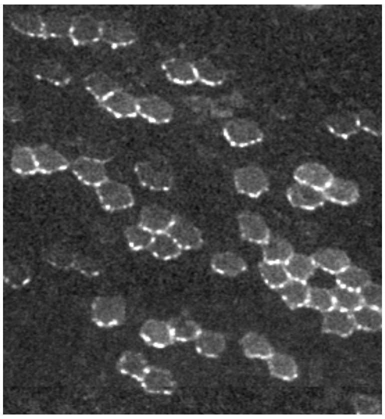

Figure E.5: Clonal staining of the Fat PCP protein Dachs in a wild type fruit fly wing at 32 hAPF.

intersected the x axis in the same point.

Using this coordinate system, we averaged the five clone polarity patterns as follows. We first divided the coordinate system into boxes. Finally, to obtain the polarity arrows shown in Fig. 4.6, we divided the sum of all clone polarity vectors within each box by the sum of their norms.

E.2.2 From unsegmented image data

Here, we develop a method to determine clone polarity merely from a grayscale image representing local fluorescence intensities of a clonal staining of a PCP protein. The main idea is to exploit the observation that typically, the fluorescence intensity within a clonal cell was slightly higher than outside of the clone (Fig. E.5). Therefore, we define the following polarity vector $\boldsymbol{p}^{\text{coarse}}(\boldsymbol{r})$ at each pixel position $\boldsymbol{r}$ of the image:

$$\boldsymbol{p}^{\text{coarse}}(\boldsymbol{r}) = \sum_{\boldsymbol{\Delta r}} \frac{\boldsymbol{\Delta r}}{|\boldsymbol{\Delta r}|} \exp\left(-\frac{|\boldsymbol{\Delta r}|^2}{\lambda_p^2}\right), \tag{E.7}$$

where the sum runs over those pixel positions $\boldsymbol{r} + \boldsymbol{\Delta r}$ that correspond to the 40% darkest pixel intensities within a cutoff radius of $|\boldsymbol{\Delta r}| \leq c\lambda_p$ around $\boldsymbol{r}$. We chose the length scale parameter $\lambda_p = 10$ pixels and the cutoff parameter $c = 2$.

When $\boldsymbol{r}$ is a position at the interface between a clonal and non-clonal area, $\boldsymbol{p}^{\text{coarse}}(\boldsymbol{r})$ would typically point away from the clone. In order to obtain a sensible measure for the clone polarity, $\boldsymbol{p}^{\text{coarse}}(\boldsymbol{r})$ should be weighted such that only the brightest pixels on the clone outline into account. To achieve such a weighting, we first subtract the locally averaged pixel intensity from the pixel intensity at $\boldsymbol{r}$:

$$\Delta I(\boldsymbol{r}) = I(\boldsymbol{r}) - \frac{1}{N_c} \sum_{\boldsymbol{\Delta r}} I(\boldsymbol{r} + \boldsymbol{\Delta r}), \tag{E.8}$$

where the sum runs over all N_c pixels within the cutoff radius $|\boldsymbol{\Delta r}| \leq c\lambda_p$. For positive

$\Delta I(\boldsymbol{r})$, the local pixel polarity $\boldsymbol{p}^{\text{coarse}}(\boldsymbol{r})$ is weighted by $\sqrt{\Delta I(\boldsymbol{r})}$; whereas for negative $\Delta I(\boldsymbol{r})$, it is not taken into account.

Furthermore, we refine the pixel polarity $\boldsymbol{p}^{\text{coarse}}(\boldsymbol{r})$ using a local nematic property similar to that defined for the wing hair axis quantification. For each pixel position $\boldsymbol{r}$, we define the nematic tensor

$$\tilde{w}_{ij}(\boldsymbol{r}) = \sum_{\boldsymbol{\Delta r} \leq c\lambda_n} I(\boldsymbol{r} + \boldsymbol{\Delta r})\tilde{g}_{ij}(\boldsymbol{\Delta r}, \lambda_n), \tag{E.9}$$

where the sum runs over all pixels in a circle with radius $c\lambda_n$ around $\boldsymbol{r}$. The length scale parameter is $\lambda_n = 10$ pixels and the cutoff parameter is $c = 2$ as above. The kernel $\tilde{g}_{ij}(\boldsymbol{\Delta r}, \lambda_n)$ is defined as in Section E.1.1.

On a cell boundary with the stained PCP protein on it, the axis of $\tilde{w}_{ij}(\boldsymbol{r})$ reflects the axis of the cell boundary. Thus, in order to obtain a refined polarity vector $\boldsymbol{p}^{\text{refined}}(\boldsymbol{r})$, we project $\boldsymbol{p}^{\text{coarse}}(\boldsymbol{r})$ onto an axis perpendicular to the axis of $\tilde{w}_{ij}(\boldsymbol{r})$:

$$p_i^{\text{refined}}(\boldsymbol{r}) = p_i^{\text{coarse}}(\boldsymbol{r}) - \frac{1}{|\tilde{w}(\boldsymbol{r})|}\tilde{w}_{ij}(\boldsymbol{r})p_j^{\text{coarse}}(\boldsymbol{r}), \tag{E.10}$$

where Einstein notation is used with Latin letters denoting dimension indices and the norm $|\tilde{w}(\boldsymbol{r})|$ is defined as in Section A.2.2.

Finally, we define the polarity of a clone by

$$\boldsymbol{p}^{\text{clone,unseg.}} = \sum_{\boldsymbol{r}} \Big[I(\boldsymbol{r})|\tilde{w}(\boldsymbol{r})|\Big]^{1/2} \boldsymbol{p}^{\text{refined}}(\boldsymbol{r}), \tag{E.11}$$

where the sum runs over all pixel positions $\boldsymbol{r}$ that belongs to a region encompassing the clone. However, only those pixels are counted in for which $I(\boldsymbol{r})$ is positive. The purpose of the squared root in the prefactor creates a quantity that is linear in the local pixel intensity. Applying this definition to real data, we found in general a good agreement with the clone polarity defined by Eq. (E.6) in the previous section, which involves segmentation.

Note that we compared different variants the clone polarity definition $\boldsymbol{P}^{\text{clone}}$. Therefore, we varied the prefactor in Eq. (E.11) and tried to omit the refining by the tensor $\tilde{w}_{ij}$. However, by visual inspection of the respective results and by comparison to results of Eq. (E.6), the definition presented here performed best.

E.3 Quantification of PCP and cell elongation nematics

We used known methods to quantify the nematics of PCP and cell elongation [54, 55, 58]. For both, the segmented cellular network is needed.

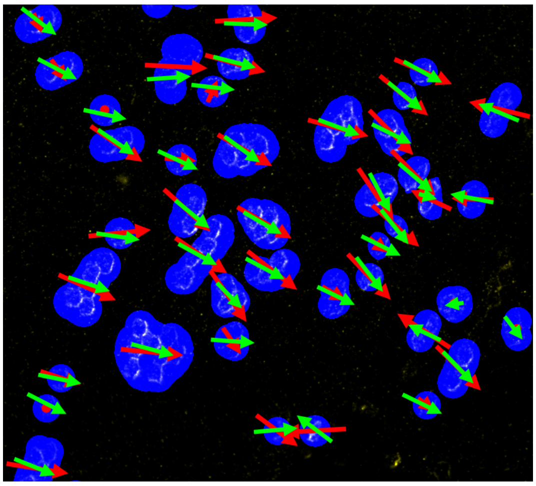

Figure E.6: Comparison of the two methods to determine the polarity of clones stained for PCP proteins. The green arrows represent the polarity determined via segmentation by Eq. (E.6); whereas the red arrows represent the polarity determined without segmentation by Eq. (E.11), were the sum in Eq. (E.11) included all pixels indicated in blue, respectively. Both methods were applied to clones with a Frizzled staining in a Prickle mutant wing at 32 hAPF.

E.3.1 Cell elongation nematics

Knowing the outline of a cell α, cell elongation is characterized by a nematic tensor $\tilde{Q}^\alpha_{ij}$ defined by

$$\tilde{\boldsymbol{Q}}^\alpha = \begin{pmatrix} Q^\alpha_1 & Q^\alpha_2 \\ Q^\alpha_2 & -Q^\alpha_1 \end{pmatrix}, \tag{E.12}$$

with

$$\begin{aligned} Q^\alpha_1 &= \frac{1}{A^\alpha}\int_{A^\alpha} \cos(2\phi)\,\mathrm{d}^2 r \\ Q^\alpha_2 &= \frac{1}{A^\alpha}\int_{A^\alpha} \sin(2\phi)\,\mathrm{d}^2 r, \end{aligned} \tag{E.13}$$

where the integrals goes over the area of cell α, which amounts to A^α. The angle ϕ denotes the angle of a point $\boldsymbol{r}$ within cell α with respect to the cell center $\boldsymbol{c}^\alpha$, which is defined by

$$\boldsymbol{c}^\alpha = \frac{1}{A^\alpha}\int_{A^\alpha} \boldsymbol{r}\,\mathrm{d}^2 r. \tag{E.14}$$

Thus, the nematic tensor $\tilde{Q}^\alpha_{ij}$ corresponds to the second Fourier mode of the cell shape anisotropy.

E.3.2 PCP nematics

Starting from a grayscale image representing the fluorescence intensity of a staining for a PCP protein, the polarity of cell α is characterized by a nematic tensor $\tilde{P}^\alpha_{ij}$ defined by

$$\tilde{\boldsymbol{P}}^\alpha = \begin{pmatrix} P^\alpha_1 & P^\alpha_2 \\ P^\alpha_2 & -P^\alpha_1 \end{pmatrix}, \tag{E.15}$$

with

$$\begin{aligned} P_1^\alpha &= \frac{1}{N_p} \int_0^{2\pi} \sigma^\alpha(\phi) \cos(2\phi)\, \mathrm{d}\phi \\ P_2^\alpha &= \frac{1}{N_p} \int_0^{2\pi} \sigma^\alpha(\phi) \sin(2\phi)\, \mathrm{d}\phi, \end{aligned} \tag{E.16}$$

where $N_p = \int_0^{2\pi} \sigma^\alpha(\phi)\, \mathrm{d}\phi$ and the function $\sigma^\alpha(\phi)$ denotes the fluorescence intensity on the cell outline at an angle ϕ as seen from the cell center $\boldsymbol{c}^\alpha$ defined in Eq. (E.14). In words, the nematic $\tilde{P}_{ij}^\alpha$ corresponds to the second Fourier mode of the angular distribution of the fluorescence intensity around cell α, normalized by the zeroth mode.

When the whole tissue is stained for a PCP protein, a vector direction can not be determined, because with our microscopy techniques, we could not determine on which side of the membrane a given protein resides [58]. Therefore, we determined a nematic $\tilde{P}_{ij}^\alpha$, which possesses an axis instead of a direction.

E.4 Experimental procedures

Here, we present all the genotypes of the flies used for the experiments presented in Chapter 4. For more details, see ref. [159]. The experimental protocols used to obtain all shown wing hair patterns are listed in Table E.1. In order to create flies that over-express the Core PCP protein Sple in a defined region and during a defined time period, we used the so-called TARGET system [166]. It makes use of so-called driver genes (for example *tub-Gal4*, *en(105)-Gal4*, or *wg-Gal4*), by which one can control the tissue region where the over-expression shall occur. Time-controlled over-expression is achieved by a protein called Gal80$^{\mathrm{TS}}$. Whenever this protein is present, over-expression is suppressed for low temperatures (18°C) and enabled for high temperatures (29°C). The Fat knockdown in the posterior compartment (wing hair patterns shown in Fig. 4.4) was achieved using the RNA interference method.

In order to directly study cell polarity during development of the flies, we used fusions of PCP proteins to fluorescent markers. All genotypes are listed in Table E.2. To access the developing wing, we either dissected it or we cut the pupal case and put the living pupa under the microscope. While with the first method, we could only make a single snapshot per wing, the second method allowed us to record many snapshots of a single wing.

Note that since we varied the temperature in some of our experiments and because the speed of development is temperature-dependent, we did not compare developmental times for different wings directly in Chapter 4. Instead, in our physical description, we considered a "reference" development which corresponds to a temperature of 25°C. Thus, all Core PCP reorientation rates estimated in Section 4.3 correspond to the development at 25°C. In order to obtain the actual rates, one has to consider the change of developmental speed, which may amount to up to a factor of two [19].

Table E.1: Conditions of space- and time-dependent Sple over-expression for which the wing hair pattern was studied. Shown is the genotype and the temperature protocol applied for all conditions listed in Section 4.1.1, where the number in parenthesis indicates the condition number defined in that section. Also shown are the cases of Fat knockdown in the posterior compartment (used in Fig. 4.4) and of Sple over-expression at the wing margin (used in Section G.1). In the last column, all figures are listed where the wing hair data or margin bristle data for the respective condition are shown.

Condition name	Genotype	Temperature protocol	Figures
wild type (1)	wild type	$25^\circ\mathrm{C}$ always	4.1A; 4.2A; 4.4A; 4.13A,C; G.1B,C; G.3; G.4A
posterior Fat knockdown	$w^{-}\ UAS\text{-}Dcr2;\ \frac{en(105)\text{-}Gal4}{UAS\text{-}fat\ RNAi}$	$25^\circ\mathrm{C}$ always	4.4C
ubiquitous Sple over-expression			
early (2)	$w^{-};\ \frac{tub\text{-}Gal80^{TS}}{+};\ \frac{tub\text{-}Gal4}{UAS\text{-}pk^{sple}}$	$29^\circ\mathrm{C} \xrightarrow{12\,\mathrm{hAPF}} 18^\circ\mathrm{C}$	4.1B; 4.10A; 4.13D,F; G.1B; G.3; G.4B
late (3)		$18^\circ\mathrm{C} \xrightarrow{30\,\mathrm{hAPF}} 29^\circ\mathrm{C}$	4.1D; 4.10C; 4.14A,C; 4.15A,C; G.1B; G.3; G.4D
permanent (4)	$w^{-};\ ;\ \frac{tub\text{-}Gal4}{UAS\text{-}pk^{sple}}$	$25^\circ\mathrm{C}$ always	4.1F; 4.2B; 4.10E; 4.14D,F; 4.15D,F; G.1B,C; G.3; G.4F
posterior Sple over-expression			
early (5)	$w^{-};\ \frac{en(105)\text{-}Gal4}{+};\ \frac{tub\text{-}Gal80^{TS}}{UAS\text{-}pk^{sple}}$	$29^\circ\mathrm{C} \xrightarrow{12\,\mathrm{hAPF}} 18^\circ\mathrm{C}$	4.1C; 4.10B; 4.13G,I; G.3; G.4C
late (6)		$18^\circ\mathrm{C} \xrightarrow{30\,\mathrm{hAPF}} 29^\circ\mathrm{C}$	4.1E; 4.10D; 4.14G,I; 4.15G,I; G.3; G.4E
permanent (7)		$29^\circ\mathrm{C}$ always	4.1G; 4.4B; 4.10F; 4.14J,L; 4.15J,L; G.3; G.4G
posterior Fat knockdown	$w^{-}\ UAS\text{-}Dcr2;\ \frac{en(105)\text{-}Gal4}{UAS\text{-}fat\ RNAi};\ \frac{UAS\text{-}pk^{sple}}{+}$	$25^\circ\mathrm{C}$ always	4.4D
Sple over-expression at the wing margin			
permanent	$w^{-};\ \frac{wg\text{-}Gal4}{+};\ \frac{UAS\text{-}pk^{sple}}{+}$	$25^\circ\mathrm{C}$ always	G.1C

Table E.2: Genotypes for the direct study of cell polarity during development. All experiments listed here were performed at $25^{\circ}\mathrm{C}$. The abbreviations “ubi.” and “post.” denote ubiquitous Sple over-expression and Sple over-expression in the posterior compartment, respectively.

Condition name	**Genotype**	**Antibody staining**	**Prep.**	**Figs.**
wild type (1)	$y^{-}\ w^{-}\ hs\text{-}Flp;\ ;\ ubi\text{-}stbm::EYFP^{VK33}$	–	*in vivo*	4.2C,E, 4.12
	$w^{-};\ Ds::EGFP\text{-}loxP\text{-}w^{+}\text{-}loxP$ $FRT40A$	–	*in vivo*	4.2G
	–	rabbit-anti-Fmi, mouse-anti-Ds2829	dissected	4.3A,C
	$w^{-}\ hs\text{-}Flp;\ ;$ $\frac{act5c\text{-}FRT\text{-}stop\text{-}FRT\text{-}EGFP::dachs}{+}$	–	*in vivo*	4.5
permanent ubi. (4)	$y^{-}\ w^{-}\ hs\text{-}Flp;\ ;\ \frac{tub\text{-}Gal4}{UAS\text{-}sple}$	rabbit-anti-Fmi, mouse-anti-Ds2829	dissected	4.3A,C; 4.2D,F,H
permanent post. (7)	$y^{-}\ w^{-}\ hs\text{-}Flp;\ \frac{en(105)\text{-}Gal4}{+};$ $\frac{UAS\text{-}sple}{act5c\text{-}FRT\text{-}stop\text{-}FRT\text{-}stbm::EYFP}$	–	dissected	4.6

Appendix F

Theory for polarity reorientation in the fruit fly wing

In this chapter, we present supplemental discussions of our theory for polarity reorientation. In Section F.1, we analytically solve for stationary solutions of the polarity angle dynamics. In Section F.2, we present technical details four fitting quantified wing hair angles to these stationary solutions. In Section F.3, we present technical details on the numerical solution of the polarity dynamics. In Section F.5 we compute an effective Core PCP protein turnover rate based on coefficients determined in Chapter 4 and on the coarse-graining of Core PCP dynamics presented in Appendix D. Finally, in Section F.6, we discuss the effect of additional terms in the polarity reorientation dynamics.

F.1 Derivation of stationary solutions

We analytically derive stationary solutions of the polarity angle dynamics Eq. (4.7), which we restate here:

$$\frac{\partial \psi}{\partial t} = k \sin\big(2[\psi - \theta]\big) - \zeta \sin\big(\psi - \phi\big) + \kappa \partial_i \partial_i \psi, \tag{F.1}$$

where we assume stationary and homogeneous angles ϕ and θ with particular relative orientations of $\phi - \theta = z\pi/2$, where z is an integer. Homogeneous stationary solutions and their linear stability with respect to homogeneous perturbations can be calculated using standard methods. They are listed in Table F.1.

F.1.1 Inhomogeneous stationary solutions

Here, we analytically compute stationary solutions of Eq. (F.1) without boundary conditions and assuming homogeneity in x direction. Therefore, we first rewrite the condition of stationarity of Eq. (F.1) into

$$2\frac{\mathrm{d}^2 \bar{\psi}}{\mathrm{d}y^2} = \frac{1}{\lambda^2} \sin\big(2\bar{\psi}\big) + \frac{2}{\mu^2} \sin\big(\bar{\psi} - \bar{\phi}\big), \tag{F.2}$$

Table F.1: Homogeneous stationary solutions of Eq. (F.1) and the condition of their linear stability with respect to homogeneous perturbations.

Case: $\phi - \theta = -\pi/2$			
Solution	$\psi_1 = \theta + \pi/2$	$\psi_2 = \theta - \pi/2$	$\sin(\psi_{3/4} - \theta) = \zeta/2k$
Stability for $k > 0$	$\zeta/\lvert k\rvert < 2$	$\zeta/\lvert k\rvert > -2$	never
Stability for $k < 0$	$\zeta/\lvert k\rvert < -2$	$\zeta/\lvert k\rvert > 2$	always

Case: $\phi - \theta = 0$			
Solution	$\psi_1 = \theta$	$\psi_2 = \theta + \pi$	$\cos(\psi_{3/4} - \theta) = \zeta/2k$
Stability for $k > 0$	$\zeta/\lvert k\rvert > 2$	$\zeta/\lvert k\rvert < -2$	always
Stability for $k < 0$	$\zeta/\lvert k\rvert > -2$	$\zeta/\lvert k\rvert < 2$	never

Case: $\phi - \theta = \pi/2$			
Solution	$\psi_1 = \theta + \pi/2$	$\psi_2 = \theta - \pi/2$	$\sin(\psi_{3/4} - \theta) = -\zeta/2k$
Stability for $k > 0$	$\zeta/\lvert k\rvert > -2$	$\zeta/\lvert k\rvert < 2$	never
Stability for $k < 0$	$\zeta/\lvert k\rvert > 2$	$\zeta/\lvert k\rvert < -2$	always

Case: $\phi - \theta = \pi$			
Solution	$\psi_1 = \theta$	$\psi_2 = \theta + \pi$	$\cos(\psi_{3/4} - \theta) = -\zeta/2k$
Stability for $k > 0$	$\zeta/\lvert k\rvert < -2$	$\zeta/\lvert k\rvert > 2$	always
Stability for $k < 0$	$\zeta/\lvert k\rvert < 2$	$\zeta/\lvert k\rvert > -2$	never

where we define

$$\lambda = \left(\frac{\kappa}{2|k|}\right)^{1/2} \tag{F.3}$$

$$\mu = \left(\frac{\kappa}{|\zeta|}\right)^{1/2} \tag{F.4}$$

$$\bar{\theta} = \begin{cases} \theta & \text{for } k < 0 \\ \theta - \pi/2 & \text{for } k > 0 \end{cases} \tag{F.5}$$

$$\bar{\psi} = \begin{cases} \psi - \bar{\theta} - \pi & \text{for } \zeta < 0 \\ \psi - \bar{\theta} & \text{for } \zeta > 0 \end{cases} \tag{F.6}$$

$$\bar{\phi} = \phi - \bar{\theta}. \tag{F.7}$$

We call the length scales λ and μ the nematic and polar length scale, respectively.

Analogy to classical mechanics

In order to analytically solve Eq. (F.2), we consider it as a problem of classical mechanics, where y is the time coordinate and $\bar{\psi}$ is the spatial coordinate. Then, Eq. (F.2) corresponds to the Newtonian equation of one-dimensional motion of a point particle of mass 2 in a potential $V(\bar{\psi})$:

$$2\frac{\mathrm{d}^2\bar{\psi}}{\mathrm{d}y^2} = -\frac{\partial V(\bar{\psi})}{\partial\bar{\psi}}, \tag{F.8}$$

where the potential is given by

$$V(\bar{\psi}) = -\frac{1}{\lambda^2}\sin^2\bar{\psi} + \frac{2}{\mu^2}\cos\left(\bar{\psi} - \bar{\phi}\right). \tag{F.9}$$

Since the particle moves in a conservative potential, the energy E is a constant of motion. It is given by

$$E = \left(\frac{\mathrm{d}\bar{\psi}}{\mathrm{d}y}\right)^2 + V(\bar{\psi}). \tag{F.10}$$

We solve Eq. (F.10) by separation of variables:

$$\left[E - V(\bar{\psi})\right]^{-1/2}\mathrm{d}\bar{\psi} = \sigma_1\,\mathrm{d}y, \tag{F.11}$$

where we look for solutions for $\sigma_1 = -1$ and for $\sigma_1 = 1$. Note that any non-homogeneous solution to Eq. (F.11) must be a solution to Eq. (F.2) as well. This is because squaring of Eq. (F.11) yields Eq. (F.10) and subsequent derivation with respect to y yields Eq. (F.2).

Nematic coupling only

Before presenting the general solution of Eq. (F.11), we first consider the special case of nematic coupling only ($\mu \to \infty$). The solution for the case of polar coupling only ($\lambda \to \infty$) can be obtained analogously. For nematic coupling only, Eq. (F.11) becomes

$$\left[E\lambda^2 + \sin^2\bar{\psi}\right]^{-1/2} \mathrm{d}\bar{\psi} = \frac{\sigma_1}{\lambda}\,\mathrm{d}y. \tag{F.12}$$

This equation can be systematically solved by differentiating all possible types of motion of the point particle for a given energy $E\lambda^2$. In each case, Eq. (F.12) can be integrated analytically using the incomplete elliptic integral of the first kind [160]. As a result, for all cases, the integrated trajectory can be put into the form

$$\bar{\psi}(y) = N\pi + \frac{\pi}{2} + \mathrm{am}\left(\frac{y - y_0}{m\lambda}\middle|\, m\right), \tag{F.13}$$

where N is an integer and the "am" function is amplitude of the inverse of the incomplete elliptic integral of the first kind [160] and where the modulus is given by

$$m = \sigma_1\left[1 + E\lambda^2\right]^{-1/2}, \tag{F.14}$$

where y_0 and m are the integration constants. The beforementioned type of motion depends on $E\lambda^2$ and thus on m (see also Fig. 4.8).

Note that the stationary trajectories $\bar{\psi}(y) = j\pi/2$ for integer j are also solutions of Eq. (F.12), which correspond to the states of stable (odd j) and unstable (even j) mechanical equilibrium. These solutions are also captured by Eq. (F.13): For even j, these solutions correspond to $|m| = 1$ and $y_0 \to \pm\infty$; and for odd j, they correspond to $m \to \pm\infty$.

General solution

In the general case, both couplings, nematic and polar, appear. In order to simplify expressions, we define the relative strength of the polar coupling with respect to the nematic coupling by

$$b = \frac{\lambda^2}{\mu^2}, \tag{F.15}$$

from which follows that $b = |\zeta/2k|$.

Here, we integrate Eq. (F.11) for $\bar{\phi} = 0$ and for $\bar{\phi} = \pi/2$. For other values of $\bar{\phi} = z\pi/2$ with integers $z \neq 0, 1$, stationary solutions can be obtained using the invariance Eq. (4.9) of the polarity angle dynamics.

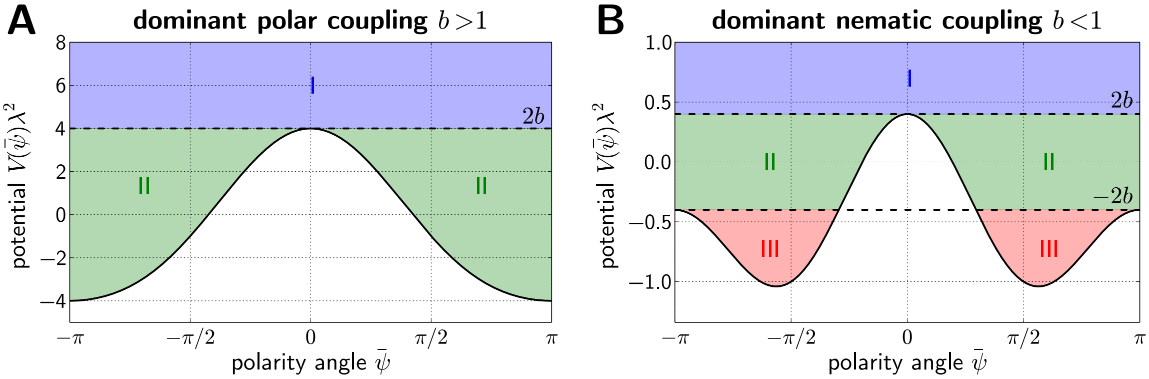

Figure F.1: Potential $V(\bar\psi)\lambda^2$ for the case $\bar\phi = 0$ (black solid lines) and energy regimes $E\lambda^2$ (hatched areas), where in different energy regimes, different analytical expressions for the solution of Eq. (F.2) apply (see also Table F.2A). Parameter values: **(A)** $b = 2$, **(B)** $b = 0.2$.

Stationary states for $\bar\phi = 0$ In order to integrate Eq. (F.11) using elliptic integrals, we have to transform it appropriately. The transformation $t = \cos\bar\psi$ yields

$$\Big[(1-t)(1+t)p(t)\Big]^{-1/2} \mathrm{d}t = -\frac{\sigma_1\sigma_2}{\lambda}\,\mathrm{d}y, \tag{F.16}$$

where the polynomial $p(t)$ is defined by

$$p(t) = -(t+b)^2 + E\lambda^2 + b^2 + 1 \tag{F.17}$$

and σ_2 denotes the sign of $\sin\bar\psi$.

The method of integration for the left hand side of Eq. (F.16) depends on the zeros of $p(t)$ [160], which depend in turn on the value of the energy $E\lambda^2$. Therefore, we differentiated three regimes for the value of $E\lambda^2$ and integrated Eq. (F.16) in each of these cases (Table F.2A). The energy regimes are illustrated in Fig. F.1, where the case of strong polar coupling ($b > 1$) is shown in Fig. F.1A and the case of strong nematic coupling ($b < 1$) is shown in Fig. F.1B. Note that these energy regimes correspond to different types of motion. In particular, for case I, the motion is unbound; for case II, the motion is bound and oscillatory; and for case III, the motion is stationary or oscillatory as well but with a smaller amplitude than in case II. At the interfaces between these regimes, motion is incoming and outgoing or stationary.

Stationary states for $\bar\phi = \pi/2$ Similar to above, we reexpress Eq. (F.11) in order to integrate it. Using the transformation $t = \sin\bar\psi$, we find

$$\Big[(1-t)(1+t)p(t)\Big]^{-1/2} \mathrm{d}t = \frac{\sigma_1\sigma_2}{\lambda}\,\mathrm{d}y, \tag{F.18}$$

Table F.2: Integrals of Eq. (F.11) for $\bar{\phi} = 0$ and for $\bar{\phi} = \pi/2$. Shown are analytical results for different regimes for the value of the energy $E\lambda^2$ and of b. For shortness of presentation, we introduce $a = (E\lambda^2 + 1 + b^2)^{1/2}$ for $\bar{\phi} = 0$; and $a = |E\lambda^2 - b^2|^{1/2}$ for $\bar{\phi} = \pi/2$. Also, we introduce other auxiliary quantities as listed in the table. The functions sn and cn denote Jacobian Elliptic Functions [160]. The integration of Eq. (F.11) creates the integration constant y_0.

Energy regime	**Auxiliary quantities**	**Modulus**	**Solution**
(A) Case: $\bar{\phi} = 0$			
(I) $2b < E\lambda^2$	$u = \mathrm{sn}^2\left(\frac{[(1-b+a)(1+b+a)]^{1/2}(y-y_0)}{2\lambda} \middle\vert m\right)$	$m^2 = \frac{4a}{(1-b+a)(1+b+a)}$	$\cos\bar{\psi} = -\frac{2(b+a)u-(1+b+a)}{2u-(1+b+a)}$
(II) $-2b < E\lambda^2 \leq 2b$	$u = \mathrm{sn}^2\left(\frac{\sqrt{a}(y-y_0)}{\lambda} \middle\vert m\right)$	$m^2 = \frac{(1-b+a)(1+b+a)}{4a}$	$\cos\bar{\psi} = -\frac{(b+a)(1-b+a)u-2a}{(1-b+a)u-2a}$
(III) $E\lambda^2 \leq -2b$	$u = \mathrm{sn}^2\left(\frac{[(1-b+a)(1+b+a)]^{1/2}(y-y_0)}{2\lambda} \middle\vert m\right)$	$m^2 = \frac{4a}{(1-b+a)(1+b+a)}$	$\cos\bar{\psi} = -\frac{2au-(b+a)(1-b+a)}{2au-(1-b+a)}$
Energy regime III exists only for $b \leq 1$.			
(B) Case: $\bar{\phi} = \pi/2$			
(I) $b^2 < E\lambda^2$	$A^2 = (1-b)^2 + a^2,\ B^2 = (1+b)^2 + a^2,$ $u = \mathrm{cn}\left(\frac{\sqrt{AB}(y-y_0)}{\lambda} \middle\vert m\right)$	$m^2 = \frac{4-(A-B)^2}{4AB}$	$\sin\bar{\psi} = \frac{B-A-(A+B)u}{A+B+(A-B)u}$
(IIa) $2b-1 < E\lambda^2 \leq b^2$, $b \geq 1$	$u = \mathrm{sn}^2\left(\frac{[(b+a-1)(1+b-a)]^{1/2}(y-y_0)}{2\lambda} \middle\vert m\right)$	$m^2 = \frac{4a}{(-1+b+a)(1+b-a)}$	$\sin\bar{\psi} = \frac{2(b+a)u+1-b-a}{2u-1+b+a}$
(IIb) $2b-1 < E\lambda^2 \leq b^2$, $b < 1$	$u = \mathrm{sn}^2\left(\frac{[(1-b+a)(1+b+a)]^{1/2}(y-y_0)}{2\lambda} \middle\vert m\right)$	$m^2 = \frac{(1-b-a)(1+b-a)}{(1-b+a)(1+b+a)}$	**(i)** $\sin\bar{\psi} = \frac{(1+b-a)u-(1-b+a)}{(1+b-a)u+(1-b+a)}$ **(ii)** $\sin\bar{\psi} = \frac{-(1-b-a)u+(1+b+a)}{(1-b-a)u+(1+b+a)}$
(III) $E\lambda^2 \leq 2b-1$	$u = \mathrm{sn}^2\left(\frac{\sqrt{a}(y-y_0)}{\lambda} \middle\vert m\right)$	$m^2 = \frac{(-1+b+a)(1+b-a)}{4a}$	$\sin\bar{\psi} = \frac{(b+a)(1+b-a)u-2a}{(1+b-a)u+2a}$

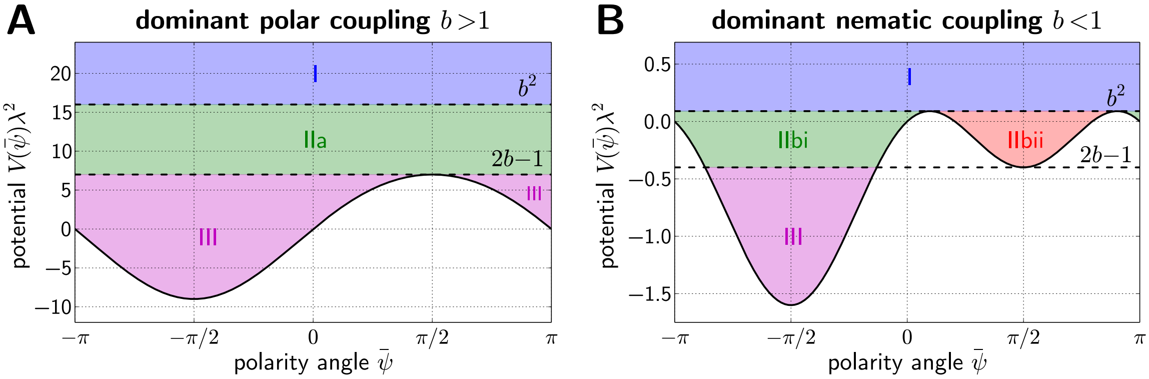

Figure F.2: Potential $V(\bar{\psi})\lambda^2$ for the case $\bar{\phi} = \pi/2$ (black solid lines) and energy regimes $E\lambda^2$ (hatched areas), where in different energy regimes, different analytical expressions for the solution of Eq. (F.2) apply (see also Table F.2B). Parameter values: **(A)** $b = 4$, **(B)** $b = 0.3$.

where the polynomial $p(t)$ is defined by

$$p(t) = (t + b)^2 + E\lambda^2 - b^2 \tag{F.19}$$

and σ_2 denotes the sign of $\cos\bar{\psi}$.

Like above, the analytical expression for the integral of Eq. (F.18) depends on the value of the energy $E\lambda^2$. The integrals for all possible energy regimes are listed in Table F.2B. The energy regimes are illustrated in Fig. F.2, where the case of strong polar coupling ($b > 1$) is shown in Fig. F.2A and the case of strong nematic coupling ($b < 1$) is shown in Fig. F.2B. Again, these energy regimes correspond to different types of motion. For cases I and IIa, the motion is unbound; whereas for cases IIb and III, the motion is bound and oscillatory. In cases IIbii and III, motion could be stationary as well. At the interfaces between these regimes, motion is incoming and outgoing, stationary, unbound (between cases I and IIa), or oscillatory (between cases IIbi and III).

Summary The integration of the second order ODE in Eq. (F.2) creates two integration constants, $E\lambda^2$ and y_0. The analytical expression that solves Eq. (F.2) depends on the value of the energy $E\lambda^2$. In Table F.2, these solutions are listed for each of the two cases $\bar{\phi} = 0$ and $\bar{\phi} = \pi/2$.

Furthermore, in Table F.2, the solution is given in terms of $\sin\bar{\psi}(y)$ and $\cos\bar{\psi}(y)$. In order to obtain a curve $\bar{\psi}(y)$, we invert these functions in regions where they are monotonous. Then, we stitch the resulting pieces of $\bar{\psi}(y)$ together so that the resulting curve is on the one hand continuous and differentiable and on the other hand, it reflects the type of motion corresponding to the energy regime (see above and Figs. F.1 and F.2).

F.2 Fits of stationary states to wing hair angle profiles

Here, we present technical details for the discussion in Section 4.3.1, where we fitted quantified wing hair angles to stationary solutions of the polarity angle dynamics. In particular, in Section F.2.1, we define the precise fit function and in Section F.2.2, we present the fitting method. Finally, in Section F.2.3, we discuss the obtained fit parameters.

F.2.1 Fit function

Here, we define the functions $\psi_{\mathrm{fit}}(y)$ with which we fitted the quantified wing hair angle profiles $\psi_{\mathrm{exp}}(y)$ in Section 4.3.1. As mentioned in the main text, we plot wing hair angles along the profile line indicated in red in Fig. 4.9A, because the observed wing hair patterns appeared to vary significantly in y, but not in x direction. Consistent with that, we assume homogeneity in x for the fit functions $\psi_{\mathrm{fit}}(y)$, which corresponds to a stationary solution of the polarity angle dynamics along the profile line. Thus, the $\psi_{\mathrm{fit}}(y)$ are solutions of

$$0 = k \sin\big(2[\psi - \theta]\big) - \zeta \sin\big(\psi - \phi\big) + \kappa \frac{\mathrm{d}^2\psi}{\mathrm{d}y^2}, \tag{F.20}$$

where we assumed the simplified angle fields for nematic coupling θ and for polar coupling ϕ as discussed in the main text (Fig. 4.9B,C). In particular, we set $\theta = 0$ everywhere and

$$\phi = \begin{cases} -\pi/2 & \text{for } y \leq y_{\mathrm{L3}} \text{ and} \\ \pi/2 & \text{for } y > y_{\mathrm{L3}}, \end{cases} \tag{F.21}$$

where y_{L3} corresponds to the position of the vein L3 on the profile line, which we measured directly.

In order to obtain solutions for Eq. (F.20), we first solved it separately for $y \leq y_{\mathrm{L3}}$ and for $y > y_{\mathrm{L3}}$, i.e. for the two cases $\phi = -\pi/2$ and $\phi = \pi/2$ following Section F.1.1. Then, the respective solutions $\psi_-(y)$ and $\psi_+(y)$ were connected by the following interface conditions:

$$\psi_-(y_{\mathrm{L3}}) = \psi_+(y_{\mathrm{L3}}) \qquad \text{and} \qquad \frac{\mathrm{d}\psi_-(y_{\mathrm{L3}})}{\mathrm{d}y} = \frac{\mathrm{d}\psi_+(y_{\mathrm{L3}})}{\mathrm{d}y}, \tag{F.22}$$

which follow from the assumption of local thermodynamic equilibrium at y_{L3}.

The stationary solutions $\psi_-(y)$ and $\psi_+(y)$ contain the length scales λ and μ as parameters, which depend on whether tissue over-expresses Sple (λ_{so} and μ_{so}) or not (λ_{wt} and μ_{wt}). However, for some of the seven experiments listed in Section 4.1.1, the genetic conditions at late times may differ between both wing compartments. In particular, in the late and permanent posterior Sple over-expression cases, the anterior compartment behaves wild-type-like whereas the posterior compartment over-expresses Sple. For these cases, we assume different stationary solutions $\psi_P(y)$ and $\psi_A(y)$ for anterior and posterior compartments, respectively. In particular, the solution $\psi_P(y)$ applies to the region $y \leq y_{AP}$ and takes λ_{so} and μ_{so} as parameters; whereas the solution $\psi_A(y)$ applies to the region $y \geq y_{AP}$ and takes λ_{wt} and μ_{wt} as parameters. The parameter y_{AP} describes the position of the AP boundary along the profile line and the interface conditions are

$$\psi_P(y_{AP}) = \psi_A(y_{AP}) \qquad \text{and} \qquad \frac{\mathrm{d}\psi_P(y_{AP})}{\mathrm{d}y} = \frac{\mathrm{d}\psi_A(y_{AP})}{\mathrm{d}y}, \tag{F.23}$$

which follows again from local thermodynamic equilibrium at y_{AP}. Thus, in these cases, there are two interface positions, y_{AP} and y_{L3}, and the solution of Eq. (F.20) is defined by three pieces, $\psi_P(y)$, $\psi_{A-}(y)$, and $\psi_{A+}(y)$, which are connected by all of the above interface conditions.

The fit functions may thus contain the length scales λ_{so}, μ_{so}, λ_{wt}, and μ_{wt} as parameters and the position y_{AP}. Moreover, there are two integration constants resulting from solving the second order ODE in Eq. (F.20). We used these integration constants as further fitting parameters.

F.2.2 Fitting procedure

In order to fit the average wing hair angle data $\psi_{\exp}(y)$ along the profile line with a fit function $\psi_{\mathrm{fit}}(y)$, we define the measure

$$\chi^2_{\mathrm{profile}} = \sum_{i=1}^{N} \frac{n(y_i)}{\sigma^2_\psi(y_i)} \left[\psi_{\exp}(y_i) - \psi_{\mathrm{fit}}(y_i)\right]^2, \tag{F.24}$$

where the sum runs over N sampling points i at positions y_i along the profile line. The value of N was $N = 165 \ldots 180$ depending on the experimental conditions. The standard deviation σ_ψ was computed according to the definition in Section E.1.2. The symbol $n(y_i)$ denotes the number of wings for which we measured the local wing hair direction at y_i and which thus enter the average $\psi_{\exp}(y)$. To minimize $\chi^2_{\mathrm{profile}}$ depending on the values of the fit parameters, the Levenberg-Marquardt method was used.[1]

F.2.3 Fit parameter values for Sple over-expression

Here, we discuss the fit parameter values obtained for late and permanent Sple over-expression conditions. For the early over-expression conditions, all relevant fit parameters are covered in the main text.

---

[1] More precisely, the Python method `scipy.optimize.leastsq` from the SciPy package was used, which is a wrapper around the `lmdif` method of the MINPACK package [167].

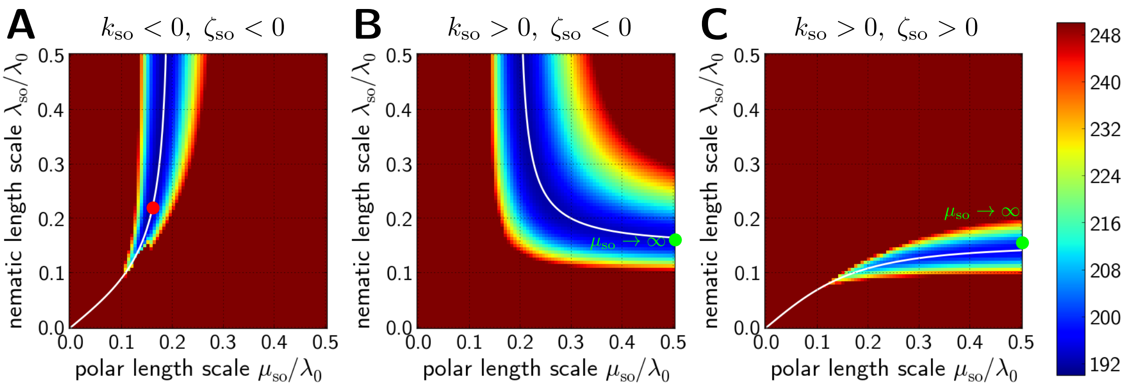

Figure F.3: Deviation measure χ^2_{profile} for fits of the wing hair data for the permanent, posterior Sple over-expression case to stationary solutions of the polarity angle dynamics. For each pair λ_{so}, μ_{so} of Sple over-expression length scales, we fitted the wing hair profile as described in Sections F.2.1 and F.2.2. The respective value for χ^2_{profile} is indicated by a color according to the color bar (left). Values $\chi^2_{\text{profile}} > 250$ are indicated in red. The white solid line indicates Eq. (F.27), which characterizes the minimum valley of χ^2_{profile} by two length parameters. Also indicated are the parameter values from the fits discussed in Section 4.3.1 (see also Table 4.1). The case of nematic coupling only ($\zeta_{\mathrm{so}} = 0$ and $\nu_{\mathrm{so}} > 0$) is indicated by green dots and the case of a dominating polar coupling ($\zeta_{\mathrm{so}} = 4k_{\mathrm{so}} < 0$) is indicated by a red dot. Different panels correspond to different signs of k_{so} and ζ_{so}: **(A)** $k < 0,\ \zeta < 0$, **(B)** $k > 0,\ \zeta < 0$, and **(C)** $k > 0,\ \zeta > 0$.

Effective length scales for Sple over-expression

Fitting wing hair angle profiles for late and permanent Sple over-expression conditions (Fig. 4.10C-F), we found that several combinations of length scales λ_{so} and μ_{so} and of the signs of k_{so} and ζ_{so} describe our observations. Here, we discuss this in more detail. Therefore, we focus on the case of permanent, posterior over-expression.

We fitted the wing hair angle profile for permanent, posterior over-expression with different parameter values for the length scales λ_{so} and μ_{so} and for different signs of k_{so} and ζ_{so}. In Fig. F.3, we plot the corresponding deviation measure χ^2_{profile} depending on the parameter values. Therefore, we consider all combinations of the signs of k_{so} and ζ_{so} except for $k_{\mathrm{so}} < 0$, $\zeta_{\mathrm{so}} > 0$, because we could not sensibly fit the data for this combination. For the other sign combinations, we scanned the λ_{so}, μ_{so} parameter space and plotted the value of $\chi^2_{\text{profile}} = 190 \ldots 250$ according to a color code. Red pixels indicate values $\chi^2_{\text{profile}} \geq 250$. We found that χ^2_{profile} is close to its absolute minimum for many parameter combinations, which resemble a one-dimensional valley.

We found that we could characterize the shape of this valley by two effective length scales $\lambda_{\mathrm{so}}^{(\mathrm{lim})}$ and $\mu_{\mathrm{so}}^{(\mathrm{lim})}$. To this end, we considered two positions y_0 and y_s within the posterior compartment along the profile line, such that the wing hair data curve

$\psi_{\exp}(y)$ attained its minimum at y_0. Furthermore, around y_s, we assumed an effective slope of the wing hair data curve of $\psi'_{\exp}(y_s) \approx s$. Now, assume that for given k_{so} and ζ_{so}, a fit function $\psi_{\mathrm{fit}}(y)$ fits the wing hair data well for the length scale parameter values λ_{so} and μ_{so}. Then, we used a relation similar to Eq. (F.10) to write

$$E = s^2 - \frac{\mathrm{sgn}(k)}{2\lambda_{\mathrm{so}}^2}\cos\left[2\psi_{\mathrm{fit}}(y_s)\right] + \frac{2\mathrm{sgn}(\zeta)}{\mu_{\mathrm{so}}^2}\cos\left[\psi_{\mathrm{fit}}(y_s) - \phi\right] \quad \text{and} \tag{F.25}$$

$$E = -\frac{\mathrm{sgn}(k)}{2\lambda_{\mathrm{so}}^2}\cos\left[2\psi_{\mathrm{fit}}(y_0)\right] + \frac{2\mathrm{sgn}(\zeta)}{\mu_{\mathrm{so}}^2}\cos\left[\psi_{\mathrm{fit}}(y_0) - \phi\right], \tag{F.26}$$

where the “sgn” function returns the sign of its argument. From these two equations follows that

$$1 = \mathrm{sgn}(k)\left(\frac{\lambda_{\mathrm{so}}^{(\mathrm{lim})}}{\lambda_{\mathrm{so}}}\right)^2 - \mathrm{sgn}(\zeta)\left(\frac{\mu_{\mathrm{so}}^{(\mathrm{lim})}}{\mu_{\mathrm{so}}}\right)^2 \tag{F.27}$$

where we defined

$$\lambda_{\mathrm{so}}^{(\mathrm{lim})2} = \frac{\sin^2\left[\psi_{\mathrm{fit}}(y_0)\right] - \sin^2\left[\psi_{\mathrm{fit}}(y_s)\right]}{s^2} \quad \text{and} \tag{F.28}$$

$$\mu_{\mathrm{so}}^{(\mathrm{lim})2} = 2\frac{\sin\left[\psi_{\mathrm{fit}}(y_0)\right] - \sin\left[\psi_{\mathrm{fit}}(y_s)\right]}{s^2}. \tag{F.29}$$

Therefore, we assumed that both expressions on the right hand sides of Eqs. (F.28) and (F.29) are positive. This is based on the observation that the wing hair data could be well fitted for $k > 0$ and $\zeta = 0$ (green dashed line in Fig. 4.10F and green dots in Fig. F.3); and for $k = 0$ and $\zeta < 0$ (not shown). From these fits, we found the “limit” length scales $\lambda_{\mathrm{so}}^{(\mathrm{lim})} = 0.152\lambda_0$ and $\mu_{\mathrm{so}}^{(\mathrm{lim})} = 0.195\lambda_0$. Using these parameters, we drew the lines corresponding to Eq. (F.27) into the plots in Fig. F.3 (white solid lines). Indeed, Eq. (F.27) described the minimum valley of $\chi^2_{\mathrm{profile}}$ very well.

Position of the compartment boundary

The position y_{AP} of the boundary between anterior and posterior compartments (AP boundary) appears only as fit parameter for the permanent and late posterior Sple over-expression conditions. The corresponding parameter values for the two cases of nematic coupling only ($\zeta_{\mathrm{so}} = 0$ and $\nu_{\mathrm{so}} > 0$) and for the case of a dominating polar coupling ($\zeta_{\mathrm{so}} = 4k_{\mathrm{so}} < 0$) are listed in Table F.3.

Comparing to the directly observed position of the AP boundary, the position of vein L4 was at $y = 0.009\lambda_0$ and the AP boundary was not more than $\approx 0.04\lambda_0$ further anterior from vein L4 such that according to our observations, $y_{AP} \approx 0.05\lambda_0$. This is coarsely consistent with the values found from the fits (Table F.3), in particular for the permanent, posterior over-expression condition assuming a dominant polar coupling.

Table F.3: Values of the fit parameter y_{AP}/λ_0 for the case of nematic coupling only ($\zeta_{\text{so}} = 0$ and $\nu_{\text{so}} > 0$) and for the case of a dominating polar coupling ($\zeta_{\text{so}} = 4k_{\text{so}} < 0$). The fit parameter y_{AP} is only relevant for the permanent posterior Sple over-expression ("permanent post.") and late posterior Sple over-expression ("late post.") conditions.

y_{AP}/λ_0	**nematic coupling only**	**dominant polar coupling**
permanent post.	0.002	0.056
late post.	-0.096	-0.079

F.3 Numerical solution of the polarity reorientation dynamics

We solved the dynamics for the polarity angle ψ given by Eq. (4.7) on a domain that was defined by a wild type wing blade at 32 hAPF. We therefore cut off the hinge by a straight line that connects the anterior indentation and the posterior indentation at the hinge blade interface. The coordinate system chosen is defined in Fig. 4.9A. Our numerical solutions covered a time interval of 16 hours corresponding to the developmental time interval from 16 hAPF to 32 hAPF at 25°C.

We numerically solved Eq. (4.7) using a first order finite difference method with Euler time steps. We used squared boxes of size $0.05\lambda_0$ and time steps of 0.1 h. In addition, we reduced the length of the time step if necessary, such that the change in ψ in any box between two steps is at most 0.01.

We used in general different parameter values for the region corresponding to the anterior compartment ($y > 0$) and for the region corresponding to the posterior compartment ($y < 0$). The values of the dynamic parameters k, ζ, and κ could always take either their respective wild type value or their Sple over-expression value depending on the genetic condition described (Table 4.2). The parameter values used are listed in Table 4.3.

As boundary condition, we used Eq. (G.10) with the parameter values for B/K and a as listed in Table G.1. In the following, we describe in detail the initial conditions used.

F.3.1 Initial conditions

We used simplified initial conditions, which were based on quantified Core PCP patterns at 16 hAPF. The initial conditions were defined by homogeneous angles ψ_P^{IC} and ψ_A^{IC} in the regions that correspond to posterior and anterior compartment, respectively. For the three initial conditions used, the values of these angles are already mentioned in the main text. However, for clarity, we list them again in Table F.4. The particular initial condition used for each of the seven genetic conditions discussed in the main

Table F.4: Initial conditions for the wild type case, the permanent, posterior Sple over-expression case ("posterior oe."), and the permanent, ubiquitous Sple over-expression case ("ubiquitous oe."). Listed are the bulk angles in the regions that correspond to posterior (ψ_P^{IC}) and anterior (ψ_A^{IC}) compartments, respectively.

Condition	**Posterior angle** ψ_P^{IC}	**Anterior angle** ψ_A^{IC}
wild type	$\pi/4$	$-\pi/4$
posterior oe.	$\pi/4$	$-5\pi/4$
ubiquitous oe.	$-3\pi/4$	$-5\pi/4$

text is listed in Table 4.2.

In between both regions of homogeneous angle ψ^{IC}, we used a cubic polynomial to smoothly interpolate. The functional form of the initial condition is given by

$$\psi^{\mathrm{IC}}(x,y) = \begin{cases} \psi_P^{\mathrm{IC}} & \text{for } \bar{y} \leq 0, \\ \psi_P^{\mathrm{IC}} + (\psi_A^{\mathrm{IC}} - \psi_P^{\mathrm{IC}})(3-2\bar{y})\bar{y}^2 & \text{for } 0 < \bar{y} \leq 1, \text{ and} \\ \psi_A^{\mathrm{IC}} & \text{for } 1 < \bar{y}, \end{cases} \tag{F.30}$$

where $\bar{y} = (y - y^{\mathrm{IC}})/w^{\mathrm{IC}} + 1/2$. The parameters y^{IC} and w^{IC} denote the center position and the width of the interpolating region, respectively. We always set $y^{\mathrm{IC}} = 0.1\lambda_0$ and $w^{\mathrm{IC}} = 0.3\lambda_0$. We found that the final states of our numerical solutions were largely independent of w^{IC} and mainly only the final state of the early, posterior Sple over-expression case depended on y^{IC}. Therefore, the value of y^{IC} was adjusted by hand such that the position of the bending region in the final state matched the position of the bending region in the quantified wing hair pattern for the early, posterior over-expression case.

F.4 Comparison to an observed PCP reorientation after 36 hAPF

In Chapter 4, we study the reorientation of Core PCP between 16 hAPF and 32 hAPF. Here, we discuss a reorientation of both PCP systems simultaneously that was observed in wild type wings after 36 hAPF. We compare this reorientation to a theory similar to the Core PCP angle dynamics assumed in Chapter 4 in order to provide an independent check for parameter values obtained there.

First, we found that the concentration of Pk suddenly decreases in wild type wings around 36 hAPF [159]. Furthermore, we observed that at the same time, the anisotropy in the cellular distribution of Core PCP proteins, which is reflected in the norm of the cellular Core PCP nematic, decreased significantly (Fig. F.4A).

In ref. [159], we provide evidence for the hypothesis that Pk counteracts Sple and

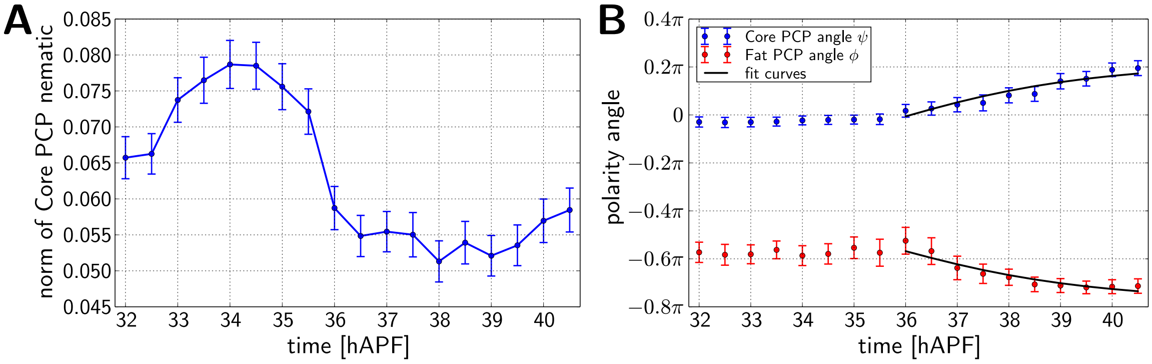

Figure F.4: Simultaneous reorientation of Core PCP and Fat PCP after 32,hAPF in a wild type wing, quantified in the region between veins L4 and L5, distal to the posterior cross vein. **(A)** Average cellular norm of the Fz nematic depending on time. **(B)** Angles of the average Fz nematic (blue circles) and of the average Ds nematic (red circles). The black line represents a fit to Eqs. (F.33) and (F.34) simultaneously, which yields the parameter values $\zeta^{\psi}_{\text{late}} = (-0.20 \pm 0.07)\,\text{h}^{-1}$ and $\zeta^{\phi}_{\text{late}} = (-0.19 \pm 0.09)\,\text{h}^{-1}$. Error bars indicate the standard error of the mean (95% confidence). PCP nematics for single cells were computed as described in Section E.3.2.

therefore, a lack of Pk could produce similar effects as an over-expression of Sple. Therefore, according to our findings in Chapter 4, we would expect that after 36 hAPF, Core PCP reorients opposite to Fat PCP. Indeed, we could experimentally confirm this late reorientation of Core PCP (Fig. F.4B). Moreover, Fat PCP reoriented as well. Here, we discuss this late simultaneous reorientation of both PCP systems.

In Chapter 4, the parameter ζ_{so} describes reorientation of Core PCP by Fat PCP for Sple over-expression conditions. Here, we compare the value of ζ_{so} used in Chapter 4 to the observed late reorientation shown in Fig. F.4B. To this end, we describe the reorientation of the Core PCP angle ψ and the Fat PCP angle ϕ after 36 hAPF by the following effective theory:

$$\frac{\mathrm{d}\psi}{\mathrm{d}t} = -\zeta^{\psi}_{\text{late}} \sin\left(\psi - \phi\right) \tag{F.31}$$

$$\frac{\mathrm{d}\phi}{\mathrm{d}t} = -\zeta^{\phi}_{\text{late}} \sin\left(\phi - \psi\right), \tag{F.32}$$

where we only consider a polar coupling between Core PCP and Fat PCP with the respective coupling coefficients $\zeta^{\psi}_{\text{late}}$ and $\zeta^{\phi}_{\text{late}}$. The solution of this coupled system of differential equations reads

$$\psi(t) = \frac{1}{\zeta^{\psi}_{\text{late}} + \zeta^{\phi}_{\text{late}}} \left[A + \zeta^{\psi}_{\text{late}} \Psi(t)\right] \tag{F.33}$$

$$\phi(t) = \frac{1}{\zeta^{\psi}_{\text{late}} + \zeta^{\phi}_{\text{late}}} \big[A - \zeta^{\phi}_{\text{late}} \Psi(t) \big], \tag{F.34}$$

where

$$\tan \big[\Psi(t)/2 \big] = B \mathrm{e}^{-(\zeta^{\psi}_{\text{late}} + \zeta^{\phi}_{\text{late}}) t} \tag{F.35}$$

and A and B are integration constants. In Fig. F.4B, we fitted this solution to the observed angles of both PCP systems simultaneously for times $t \geq 36\,\text{hAPF}$, where fit parameters are A, B, $\zeta^{\psi}_{\text{late}}$, and $\zeta^{\phi}_{\text{late}}$. We obtained from these fits $\zeta^{\psi}_{\text{late}} = (-0.20 \pm 0.07)\,\text{h}^{-1}$ and $\zeta^{\phi}_{\text{late}} = (-0.19 \pm 0.09)\,\text{h}^{-1}$. Thus, both polar coupling coefficients have similar values. Moreover, the value of $\zeta^{\psi}_{\text{late}}$, which describes reorientation of Core PCP by Fat PCP, is of the same order of magnitude as the value for Sple over-expression $\zeta_{\text{so}} = -0.4\,\text{h}^{-1}$ assumed in Chapter 4.

F.5 Comparison to the turnover rate of Core PCP clusters

In Chapter 4, we determined the parameter value $\kappa_{\text{wt}} = 10^{-2}\,\lambda_0^2\,\text{h}^{-1}$, which describes the tendency of Core PCP to align locally in wild type tissue. Here, we check its order of magnitude by comparing it to the turnover time of Core PCP clusters, which is known to be on the order of a few minutes [36, 37, 54].

In order to connect both quantities in a simplified manner, we reconsider the Core PCP vertex model described in Appendix D. There, we show that for regular hexagonal cellular packings, the coefficients describing local polarity alignment are given by

$$\kappa_{\text{splay}} = \frac{rA_0}{4\sqrt{3}} \left(3 - \frac{1}{J+1} \right) \qquad \text{(splay)} \tag{F.36}$$

$$\kappa_{\text{bend}} = \frac{rA_0}{4\sqrt{3}} \left(1 - \frac{1}{J+1} \right) \qquad \text{(bend).} \tag{F.37}$$

Here, κ_{splay} and κ_{bend} describe the relaxation of splay and bend modes in the polarity field, respectively. The coefficient r is a parameter of the Core PCP vertex model, which we consider as a proxy for the subcellular Core PCP cluster turnover rate, here. The symbol A_0 denotes the area of a hexagonal cell, which is given by $A_0 = d_0^2\sqrt{3}/2$, where d_0 is the distance of two neighboring cell centers. The parameter J describes the ratio between the intracellular interaction strength of Core PCP proteins and the inter-cellular interaction strength within Core PCP clusters.

In our hydrodynamic description in Chapter 4, we do not assume different relaxation rates for bend and splay modes. Therefore, here, we consider κ_{wt} to be the average of both. Solving for r yields:

$$r = \frac{4\kappa_{\text{wt}}\sqrt{3}}{cA_{32\text{hAPF}}}. \tag{F.38}$$

Here, we substituted the area A_0 by the average cell area in the wing blade at 32 hAPF, $A_{32\text{hAPF}}$. We measured $A_{32\text{hAPF}}$ in the segmented movies described in Section 2.3.1:

$$A_{32\text{hAPF}} = 10^{-3}\,\lambda_0^2. \tag{F.39}$$

Furthermore, the coefficient c is defined by

$$c = 2 - \frac{1}{J+1}. \tag{F.40}$$

Because $J > 0$, the coefficient c takes values between $1 \leq c \leq 2$. Taken together, we find that:

$$r \sim 1\,\text{min}^{-1}. \tag{F.41}$$

This corresponds to the measured Core PCP cluster turnover time scale of a few minutes [36, 37, 54].

F.6 Possible additional effects

Here, we study effects that could possibly influence the polarity angle dynamics and that are not taken into account by the dynamics assumed in Chapter 4 (Eq. (4.7)). In Section F.6.1, we consider alternative bulk terms. In particular, we study the effect of local tissue rotation and we discuss the scenario where the nematic coupling is entirely defined by local tissue shear. In Section F.6.2, we discuss a possible effect of wing veins. Finally, in Section F.6.3, we discuss possible effects of a gradient in Sple expression as it appears in the late and permanent posterior Sple over-expression cases.

F.6.1 Variants of the polarity angle bulk dynamics

Here, we compare variants of the polarity angle dynamics by fitting their prediction to experimental data. To this end, we numerically solved a given polarity angle dynamics with wild type parameters. Then, we applied the method from Section 4.3.2 in order to quantify the deviation χ^2 of the numerical solution from quantified time-dependent Core PCP data in a wild type wing.

As a prerequisite for this study, we measured the time-dependent flow field in a pupal wing using a particle image velocimetry method [54, 58]. In particular, we extracted space- and time-dependent local tissue rotation rate and local tissue shear rate, which are respectively represented by the antisymmetry ω and by the traceless, symmetric part $\tilde{v}_{ij}$ of the velocity gradient.

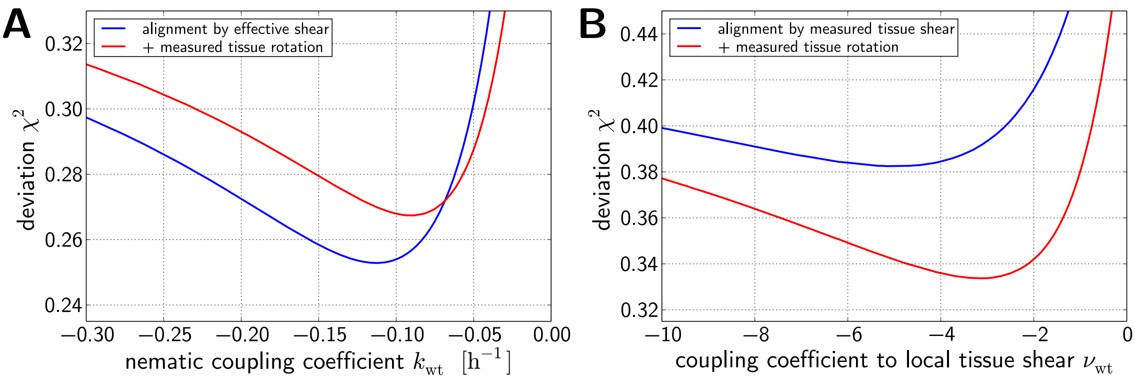

Figure F.5: Deviation χ^2 between numerical solutions of the polarity angle dynamics and quantified time-dependent Core PCP data in wild type wings. The deviation χ^2 is defined as in Eq. (4.17) and was computed for 200 times for each curve. For the numerical solutions, we chose different assumptions for the polarity angle dynamics. **(A)** As in the main text, the polarity angle ψ is reoriented by an effective shear nematic $\tilde{s}_{ij}$ towards $\theta = 0$ (blue solid line, Eq. (4.7)). For the red solid curve, we additionally considered the effect of local tissue rotation (Eq. (F.42)). **(B)** The polarity angle ψ is reoriented by the actual local shear field (blue solid line, Eq. (F.44)). For the red solid curve, we additionally considered the effect of local tissue rotation (Eq. (F.45)).

Effects of tissue rotation

Here, we take the effect of local tissue rotation into account via the corotational term in Eq. (4.2). This yields the following polarity angle dynamics

$$\frac{\partial \psi}{\partial t} = \omega + k_{\mathrm{wt}} \sin\big(2[\psi - \theta]\big) - \zeta_{\mathrm{wt}} \sin\big(\psi - \phi\big) + \kappa_{\mathrm{wt}} \partial_i \partial_i \psi, \tag{F.42}$$

where, as in the main text, we assume that the nematic coupling coefficient k_{wt} is constant and homogeneous. Also, we set $\theta = 0$, $\zeta_{\mathrm{wt}} = 0$, and $\lambda_{\mathrm{wt}} = 0.07\,\lambda_0$. For a given value of k_{wt}, the value of κ_{wt} was determined according to Eq. (4.14).

In Fig. F.5A, we plot the deviation χ^2 between experiment and numerical solutions over k_{wt}. Without local tissue rotation, we found the minimal deviation of $\chi^2_{\mathrm{min}} = 0.253$ (blue solid line; same plot as in Fig. 4.12 in the main text); whereas if we included the effect of local tissue rotation, we found $\chi^2_{\mathrm{min}} = 0.267$ (red solid line). Thus, taking local tissue rotation into account did not improve the fit. For this reason, we neglected the corresponding term in the main text.

Nematic coupling defined by quantified shear pattern

Here, we assume that the nematic coupling $k_{\mathrm{wt}}\tilde{s}_{ij}$ is entirely due to local tissue shear:

$$k_{\mathrm{wt}}\tilde{s}_{ij} = \nu_{\mathrm{wt}}\tilde{v}_{ij}, \tag{F.43}$$

where ν_{wt} is a model parameter. Therefore, we obtain the following polarity angle dynamics:

$$\frac{\partial\psi}{\partial t} = \nu_{\mathrm{wt}}|\tilde{v}|\sin\big(2[\psi-\theta_{\tilde{v}}]\big) - \zeta_{\mathrm{wt}}\sin\big(\psi-\phi\big) + \kappa_{\mathrm{wt}}\partial_i\partial_i\psi, \tag{F.44}$$

where $|\tilde{v}|$ and $\theta_{\tilde{v}}$ denote the norm and the angle of the measured local tissue shear rate $\tilde{v}_{ij}$ (both defined as in Section A.2.2). We also studied a variant of the polarity angle dynamics where we additionally included the effect of local tissue rotation:

$$\frac{\partial\psi}{\partial t} = \omega + \nu_{\mathrm{wt}}|\tilde{v}|\sin\big(2[\psi-\theta_{\tilde{v}}]\big) - \zeta_{\mathrm{wt}}\sin\big(\psi-\phi\big) + \kappa_{\mathrm{wt}}\partial_i\partial_i\psi. \tag{F.45}$$

For both variants, we set $\zeta_{\mathrm{wt}} = 0$ and $\lambda_{\mathrm{wt}} = 0.07\,\lambda_0$. For a given value of ν_{wt}, the value of κ_{wt} was determined according to Eq. (4.14) with $k_{\mathrm{wt}} = \nu_{\mathrm{wt}}|\tilde{v}|$, where we set $|\tilde{v}| = 0.01\,\mathrm{h}^{-1}$ (compare blue solid line in Fig. 2.16A).

In Fig. F.5B, we plot the deviation χ^2 between experiment and numerical solutions over ν_{wt}. For a coupling to local tissue shear but not to local tissue rotation, the minimal deviation was $\chi^2_{\mathrm{min}} = 0.382$ (blue solid line); whereas if we included local tissue rotation, we found $\chi^2_{\mathrm{min}} = 0.334$ (red solid line). For the latter case, the minimum was at $\nu_{\mathrm{wt}} = -3$ confirming the findings in refs. [54, 58].

To sum up, the fit was improved by taking local tissue rotation into account. However, the experimental Core PCP data were still significantly better described by a simplified effective shear nematic with $\theta = 0$ and constant rate k_{wt} as in the main text (Fig. F.5A, blue solid line). Because the simplified effective shear nematic resembled much more the quantified cell elongation pattern (Fig. 4.2E) than the quantified tissue shear pattern [54], this suggests that cell elongation could have a more important effect on Core PCP reorientation than tissue shear. Further evidence is given by the experimental correlations shown in Fig. 4.3.

F.6.2 Effect of wing veins

A number of observations indicated that Core PCP tends to align parallel to wing veins. For example in all wings examined, wing hairs were mostly aligned parallel to wing veins (Fig. 4.1). Furthermore, in cases where wing hairs near a wing vein were not parallel to it, the wing hair pattern appeared to be significantly deflected by the wing vein (Fig. F.6A; blue line and orange dots in Fig. F.6B). Here, we establish a description of this effect within our hydrodynamic theory.

In order to describe such an effect, we consider an additional term in the effective

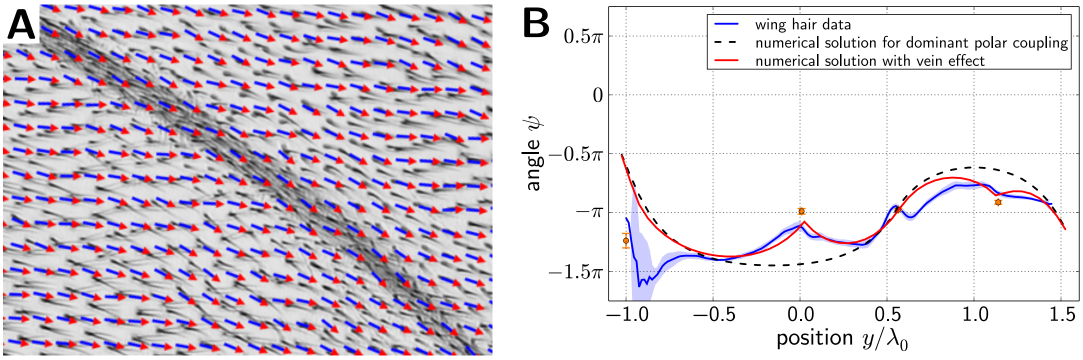

Figure F.6: (A) The direction of wing hairs (arrows) in wild type wings appeared to be deflected by wing veins (shown here: vein L5). **(B)** Including an aligning effect by wing veins into our theory (red solid line) described the observed wing hair angles for the permanent, ubiquitous Sple over-expression (blue solid line) better than without the vein effect (black dashed line). The wing hair angles are plotted along the red line in Fig. 4.9A. The parameters for the black dashed line are listed in Table 4.3B. For the red solid line, we additionally set $\lambda_V = 0.15\,\lambda_0$. Orange dots indicate vein positions and vein angles.

potential:

$$F_{\text{total}} = \dots - \frac{1}{2} K_V \sum_m \int_{\boldsymbol{r}^{(m)}} p_i \tilde{w}_{ij}^{(m)} p_j \,\mathrm{d}s, \tag{F.46}$$

where the dots indicate the contributions to F_{total} considered in Chapter 4, as given by Eqs. (4.1) and (G.1). The sum index m runs over all wing veins considered here, which are the longitudinal veins L2 to L5 and both cross veins. In our theory, each vein m is described by a curve $\boldsymbol{r}^{(m)}(s)$, which is parametrized by the arc length coordinate s (i.e. $\left|\mathrm{d}\boldsymbol{r}^{(m)}/\mathrm{d}s\right| = 1$). The local orientation of vein m at some position s is described by the nematic $\tilde{w}_{ij}^{(m)}$, which is normalized to one.[2] The coefficient K_V defines the elasticity associated with polarity alignment by veins. For $K_V > 0$, the polarity $\boldsymbol{p}$ tends to align parallel to the local vein axis. For $K_V < 0$, it aligns perpendicular.

The resulting term in the polarity angle dynamics reads

$$\frac{\partial \psi(\boldsymbol{r}, t)}{\partial t} = \dots - \frac{\kappa}{\lambda_V} \sum_m \int_{\boldsymbol{r}^{(m)}} \delta\left(\boldsymbol{r} - \boldsymbol{r}^{(m)}\right) \sin\left(2[\psi - \vartheta^{(m)}]\right) \mathrm{d}s, \tag{F.47}$$

where a characteristic length scale $\lambda_V = K/K_V$ appears. Here, we assume $K_V > 0$ and therefore, $\lambda_V > 0$. The symbol δ denotes the Dirac distribution and the angle $\vartheta^{(m)}$ is the local angle of vein m (i.e. it is the angle of $\tilde{w}_{ij}^{(m)}$). Note that this assumed effect of vein alignment corresponds to the effect of an effective shear term for $k < 0$

---

[2] I.e. $\tilde{w}_{ij}^{(m)} = 2\left(\mathrm{d}r_i^{(m)}/\mathrm{d}s\right)\left(\mathrm{d}r_j^{(m)}/\mathrm{d}s\right) - \delta_{ij}$.

that is localized to the wing veins (compare to first term in Eq. (4.7)).

First, we ask how this additional term affects the polarity angle dynamics. In order to understand this more clearly, we consider the one-dimensional dynamics along the profile line (Fig. 4.9A) assuming homogeneity of ψ in x direction:

$$\begin{aligned}\frac{\partial\psi(y,t)}{\partial t} &= k\sin\big(2[\psi-\theta]\big) - \zeta\sin\big(\psi-\phi\big) + \kappa\frac{\partial^2\psi}{\partial y^2} \\ &\quad - \frac{\kappa}{\lambda_V}\sum_m \frac{\delta\left(y-y^{(m)}\right)}{|\cos\vartheta^{(m)}|}\sin\big(2[\psi-\vartheta^{(m)}]\big),\end{aligned} \tag{F.48}$$

where $y^{(m)}$ denotes the position of vein m along the profile line (i.e. it is the y component of $\boldsymbol{r}^{(m)}$). For a given vein m, we integrate the whole equation on an interval $y^{(m)}-\varepsilon\dots y^{(m)}+\varepsilon$, which yields:

$$\frac{\partial\psi\left(y^{(m)}+\varepsilon\right)}{\partial y} - \frac{\partial\psi\left(y^{(m)}-\varepsilon\right)}{\partial y} = \frac{\sin\left(2\left[\psi(y^{(m)})-\vartheta^{(m)}\right]\right)}{\lambda_V\,|\cos\vartheta^{(m)}|} \qquad \text{for } \varepsilon\to 0, \tag{F.49}$$

where the contributions from the first two terms of Eq. (F.48) vanish for $\varepsilon\to 0$. Thus, in our hydrodynamic description, the vein effect induces discontinuities in the gradient of ψ. The magnitude of these discontinuities is higher for small length scales λ_V and for large deviations between polarity angle and vein angle.

We found that the wing hair pattern for the permanent, ubiquitous Sple over-expression case was matched better by our physical theory if we included the vein term. In Fig. F.6B, we compare the quantified wing hair angles (blue solid line) to numerical solutions of the polarity angle dynamics without the vein effect (black dashed line; same curve as the red solid line in Fig. 4.15) and to the numerical solution including the vein effect (red solid line). We found that including the vein effect helped explaining the observations. In particular, around $y=0$, the quantified wing hair angles were much better described by a discontinuity in the gradient of polarity angle field, which is in our theory created by the vein effect. Note that in very posterior regions ($y \lesssim -0.6\,\lambda_0$), there was a defect in the quantified wing hair pattern, which could not be reproduced by our numerical solutions.

F.6.3 Effect of gradients in Sple protein concentration

Here, we shortly discuss two additional terms for our hydrodynamic description, which describe possible effects of gradients in Sple protein concentration. As a first possible effect, the elastic constant characterizing the tendency of polarity to align locally K could in principle depend on Sple concentration. Indeed, we observed that the fluorescence intensity of Core PCP proteins at the membrane is increased in tissue over-expressing Sple. Therefore, we discuss the effect of inhomogeneities in K on the polarity angle dynamics, here.

Second, gradients in Sple concentration could directly bias Core PCP: Consider a cell that detects different concentrations of Sple within two opposing neighboring cells. It is plausible that the cell's Core PCP is biased by this concentration difference, since cells form complexes of Core PCP proteins across cell boundaries.[3] Indeed, such an effect could be reflected by the quantified wing hair pattern shown in Fig. 4.4D. In this wing, Sple was over-expressed in the posterior compartment, but at the same time, Fat was knocked down there as well. It is plausible that the polar coupling to Fat PCP is suppressed in these wings. Therefore, wing hair polarity should be as in wild type wings, which was indeed observed at least distally in these wings. However, in the region close to the AP boundary, wing hair polarity pointed posteriorly. This is consistent with the picture that the direction Core PCP in this region is directly influenced by the gradient of Sple concentration.

In order to describe the second effect in our hydrodynamic theory, we assume the following additional term in the effective free energy:

$$F_{\text{total}} = \cdots - \int K_{\text{sp}} p_i (\partial_i c_{\text{sp}}) \, \mathrm{d}^2 x, \tag{F.50}$$

where the dots indicate the contributions to F_{total} considered before, as given by Eqs. (4.1) and (G.1). The symbol c_{sp} denotes the local Sple concentration and K_{sp} denotes the associated elasticity. For $K_{\text{sp}} > 0$, polarity tends to point in the same direction as the Sple concentration gradient. For $K_{\text{sp}} < 0$, it tends to point antiparallel to the gradient. According to our discussion above, we would expect a positive sign of K_{sp}.

Also allowing for inhomogeneities in K, the resulting polarity angle dynamics reads

$$\begin{aligned} \frac{\partial \psi}{\partial t} &= k \sin\big(2[\psi - \theta]\big) - \zeta \sin\big(\psi - \phi\big) + \kappa \partial_i \partial_i \psi \\ &\quad + \frac{1}{\gamma_1} (\partial_i K)(\partial_i \psi) - \frac{K_{\text{sp}} |\nabla c_{\text{sp}}|}{\gamma_1} \sin\big(\psi - \phi_{\text{sp}}\big), \end{aligned} \tag{F.51}$$

where the symbol ϕ_{sp} denotes the angle of ∇c_{sp}. The first of the two additional terms tends to adapt the gradient of ψ to inhomogeneities in K. When a region with small K is close to a region with high K, this term tends to decrease the gradient of ψ where K is high and tends to increase the gradient of ψ where K is low. For positive K_{sp}, the second additional term in the ψ dynamics reorients the polarity angle towards the direction of the Sple gradient ϕ_{sp}. Because it corresponds to a polar coupling to the Sple gradient, it is formally very similar to the second term in the above equation.

Considering a gradient in Sple concentration applies in particular to the posterior Sple over-expression conditions. In these wings, Sple was over-expressed in the posterior compartment, but not in the anterior compartment. Therefore in our description, we consider the simplified Sple gradient

---

[3] This is similar to the so-called "factor X" models, compare Section 1.5.3.

$$\begin{aligned} \partial_x c_{\mathrm{sp}} &= 0 \\ \partial_y c_{\mathrm{sp}} &= -\delta(y - y_{AP})\Delta c_{\mathrm{so}}, \end{aligned} \tag{F.52}$$

where the symbol y_{AP} denotes the position of the AP boundary and $\Delta c_{\mathrm{so}} > 0$ denotes the increase in Sple protein concentration that is induced by the over-expression. Moreover, we assume inhomogeneous K according to

$$K = \begin{cases} K_P & \text{for } y \leq y_{AP} \text{ and} \\ K_A & \text{for } y > y_{AP}. \end{cases} \tag{F.53}$$

Thus, the symbol K_P denotes the value of K in the posterior compartment and K_A denotes the value in the anterior compartment. Then, assuming homogeneity in x direction, the condition of local thermodynamic equilibrium at the AP boundary yields the following interface condition at the AP boundary

$$K_A \frac{\partial \psi\,(y_{AP} + \varepsilon, t)}{\partial y} - K_P \frac{\partial \psi\,(y_{AP} - \varepsilon, t)}{\partial y} = K_{\mathrm{sp}} \Delta c_{\mathrm{so}} \sin\left[\psi(y_{AP}) - \phi_{\mathrm{sp}}\right] \quad \text{for } \varepsilon \to 0. \tag{F.54}$$

Thus, both effects do independently induce a discontinuity in the gradient of ψ. The effect of an inhomogeneous K alone creates a ratio of slopes $\partial\psi/\partial y$ that corresponds to the ratio of the values of K in both compartments. In contrast to that, the effect of alignment of polarity with the Sple gradient alone creates a jump in the slope of ψ, which is large for a large elasticity K_{sp} as compared to K, for a large Sple concentration difference created by the Sple over-expression Δc_{so}, and for a large deviation of the polarity angle from the Sple gradient direction. Therefore, this term is formally similar to the term describing the effect of wing veins. The main difference between both is the factor of two, which appears in the sine function for the vein effect, because for veins, only a local axis could be defined; whereas for the Sple gradient, a direction can be defined.

Appendix G

Boundary conditions for the polarity field in the fruit fly wing

Here, we establish boundary conditions based on quantified directions of bristles that grow out of the wing margin. Therefore, in Section G.1, we discuss quantified bristle direction profiles along the margin. Based on these observations, in Section G.2, we develop an effective physical theory for bristle directions including a coupling to Core PCP. This theory corresponds to the boundary conditions of the polarity field $\boldsymbol{p}$. Afterwards, in Section G.3, we fit our theory to experimental data in order to determine parameter values. Finally, in Section G.4, we compare our theory to quantified bristle direction profiles.

G.1 Quantification of wing margin bristle directions

We noticed that the bristles along the wing margin point in similar directions as wing hairs close to them do. Thus, to better understand the boundary conditions that affect Core PCP reorientation, we studied the direction of margin bristles. Also, we discuss a possible influence of Sple over-expression on margin bristle direction.

In order to quantify margin bristle angles, we first parametrized positions on the wing margin by the coordinate s, which varies between $s = 0$ and $s = 1$ (Fig. G.1A and Appendix E.1.3). For discrete positions s, we quantified margin bristle angles ψ_b and margin angles ψ_m, where margin angles are defined to point in clockwise direction around the wing margin.

First, we compared the bristle angles for four different conditions (conditions 1-4; see Section 4.1.1). To this end, for each wing, we plotted profiles of the bristle angles relative to the margin $\psi_b - \psi_m$ over the position coordinate s (Fig. G.1B). For each condition, we plotted the profile of at least three different wings and found that the bristle angle profile was largely reproducible. Furthermore, the profile for late ubiquitous over-expression largely resembled the wild type profile. Similarly, the profiles for early and permanent ubiquitous over-expression largely resembled each other.

We discussed two alternative explanations for these observations. According to the first explanation, the bristle direction at a given position s on the margin only depends

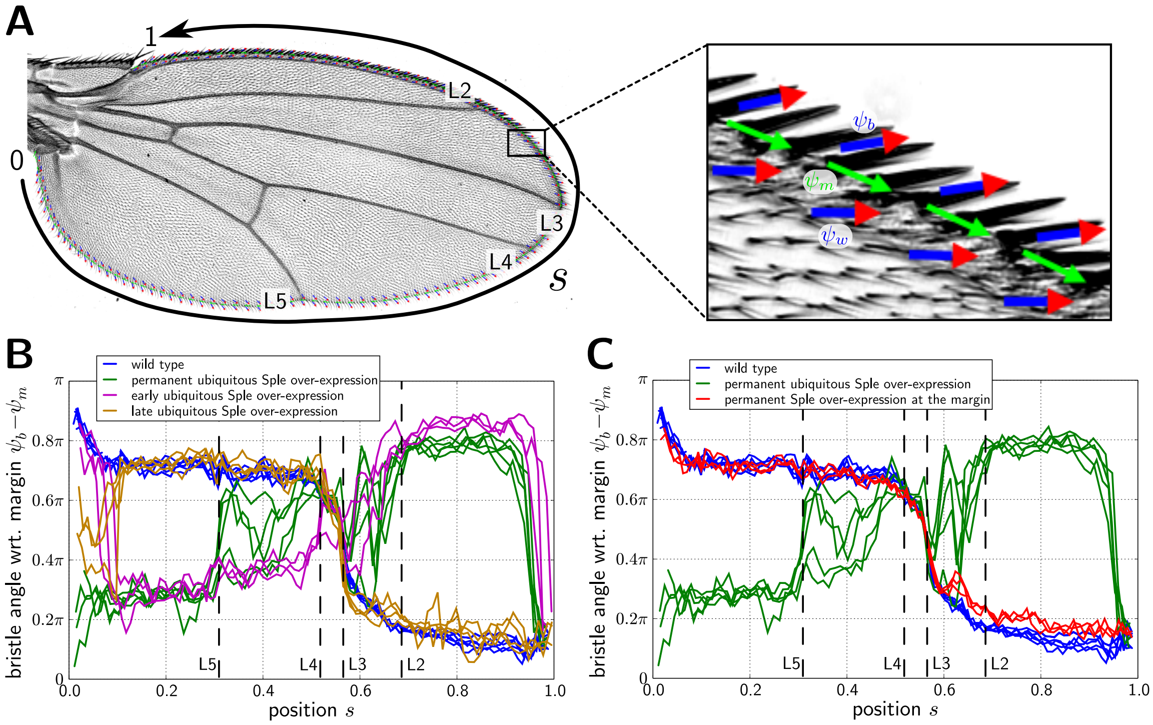

Figure G.1: Quantification of margin bristle directions in fruit fly wings. **(A)** Parametrization of the wing margin by the variable s. At discrete positions s, we define the angles ψ_b, ψ_m, and ψ_w, which correspond to margin bristle angle, margin angle, and wing hair angle at a distance w from the margin, respectively. All angles are defined to increase in counter-clockwise direction. **(B)** Margin bristle direction profile for wild type wings as well as permanent, early, and late ubiquitous Sple over-expression. **(C)** Margin bristle direction profile for wild type wings, wings permanently and ubiquitously over-expressing Sple, as well as wings permanently over-expressing Sple only at the wing margin. For each condition in panels B and C, the data of at least three wings are shown. In panels A-C, the positions of the ends of the longitudinal veins L2-L5 are marked.

on whether Sple is over-expressed at s at some critical time point or not. According to our observations (Fig. G.1B), this critical time point should be before 16 hAPF. This is because in late Sple over-expression wings, there is no over-expression before 16 hAPF. Consistent with that, we observed mainly the wild type bristle angle profile for these wings. Conversely, in early Sple over-expression wings, there is over-expression before 16 hAPF. Therefore, we observed a bristle angle profile which largely corresponded to the permanent over-expression. Another feature of such an explanation is that it has to assume that cells at the margin are aware of their position, since the bristle angles are position-dependent in a reproducible manner.

In contrast to that, the second explanation assumes that it does not matter whether Sple is over-expressed at the wing margin or not. Furthermore, the bristle direction is not fixed before bristle outgrowth; rather, bristles may merely have a few preferred angles with respect to the margin. In addition, the bristle direction is coupled to Core PCP of margin cells, which is in turn coupled to the Core PCP system in the bulk. According to this explanation, we observed different bristle angle profiles for different perturbations (Fig. G.1B), because the Core PCP system behaved differently in the bulk. Because bristles still have preferred angles, bristle directions were reproducible, even for different conditions.

In order to distinguish between both explanations, we quantified bristle angles of wings which permanently over-express Sple only within a stripe at the wing margin. According to the first explanation, the bristle angle profile in these wings should resemble that of permanent ubiquitous over-expression wings. Conversely, according to the second explanation, the over-expression only at the margin should affect the wild type margin bristle directions only little. Indeed, a comparison of the bristle angle profiles for all three conditions suggested the second explanation (Fig. G.1C).

G.2 Physical theory for the direction of wing margin bristles

G.2.1 Effective potential describing the boundary conditions

Motivated by these experimental findings, we model the boundary conditions as follows. In each point of the boundary, there is an effective potential $f_b(\psi_b - \psi_m)$ for the bristle angle ψ_b with respect to the margin angle ψ_m, where preferred angles are defined by the functional form of f_b. This effective potential is the same for wild type tissue and for tissue over-expressing Sple. Furthermore, the bristle direction is coupled by an elastic element to the local Core PCP direction at the boundary. Therefore, the boundary contributions to the total free energy read

$$F_{\text{boundary}} = \oint \Big[f_b(\psi_b - \psi_m) - C\cos(\psi_b - \psi_0) \Big] \, \mathrm{d}l, \tag{G.1}$$

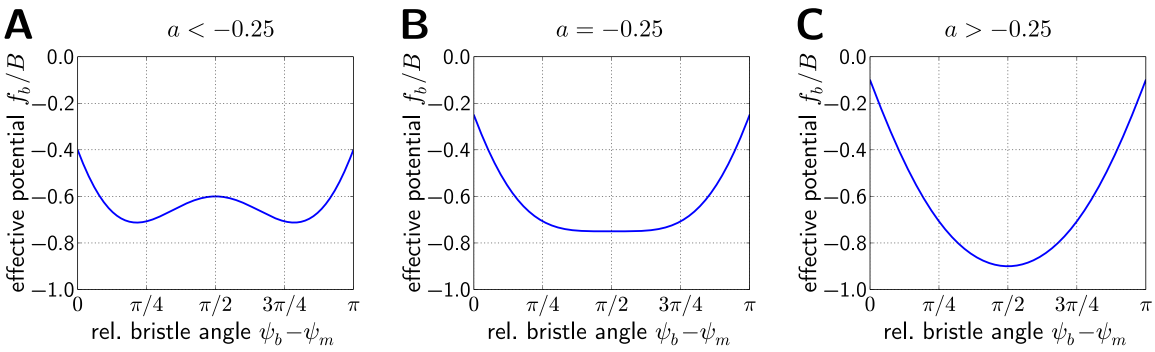

Figure G.2: The effective potential $f_b(\psi_b - \psi_m)$ for the bristle angle relative to the margin $\psi_b - \psi_m$. The parameter values are **(A)** $a = -0.40$, **(B)** $a = -0.25$, and **(C)** $a = -0.10$.

where the integral goes around the boundary. The elasticity C couples the bristle angle ψ_b to the angle ψ_0, which denotes the value of ψ at the boundary. In order to energetically favor that ψ_b and ψ_0 point in the same direction, we require $C > 0$.

We chose the functional form of the effective potential $f_b(\psi_b - \psi_m)$ by the following requirements.

1. For simplicity, $f_b(\psi_b - \psi_m)$ should be symmetric around $\psi_b - \psi_m = \pi/2$, which corresponds to the absence of chiral terms at the boundary.
2. Since all observed bristles pointed away from the wing blade, we choose to energetically favor the corresponding angle interval $\psi_b - \psi_m = 0 \dots \pi$.
3. Our observations in the previous section indicate the existence of two preferred relative bristle angles $\psi_b - \psi_m$. This is reminiscent of a double well potential.

A simple generic form of $f_b(\psi_b - \psi_m)$ that includes all three aspects is given by

$$f_b(\psi_b - \psi_m) = B\Big[- \sin\big(\psi_b - \psi_m\big) + a\cos\big(2[\psi_b - \psi_m]\big)\Big], \tag{G.2}$$

where B and a are elastic coefficients that may in general depend on position on the boundary. Because of the second requirement, B has to be positive. In Fig. G.2, the potential $f_b(\psi_b - \psi_m)$ is plotted for three different parameter values a. For $a < -0.25$, the effective potential $f_b(\psi_b - \psi_m)$ possesses two minima within the relevant angle interval $\psi_b - \psi_m = 0 \dots \pi$ (Fig. G.2A); otherwise, $f_b(\psi_b - \psi_m)$ possesses only a single minimum within this interval, which is located at $\psi_b - \psi_m = \pi/2$ (Fig. G.2B,C).

G.2.2 Effective thermodynamic equilibrium at the boundary

The general form of the boundary conditions follows from the condition of local thermodynamic equilibrium at the boundary, allowing for variations in ψ_b and ψ_0. The relevant terms of F_{total} are given by

$$F_{\text{total}} = \int \frac{K}{2}(\partial_i\psi)(\partial_i\psi)\,\mathrm{d}^2x + \oint \Big[f_b(\psi_b - \psi_m) - C\cos(\psi_b - \psi_0)\Big]\,\mathrm{d}l + \dots, \tag{G.3}$$

where we used that

$$(\partial_i p_j)(\partial_i p_j) = (\partial_i\psi)(\partial_i\psi) \tag{G.4}$$

for $\boldsymbol{p} = (\cos\psi, \sin\psi)^{\mathrm{T}}$.

Now, we compute the variation of F_{total}, where we allow for independent variations of the bristle angle ψ_b and the boundary value ψ_0 of the polarity angle field ψ. Integration by parts yield:

$$\begin{aligned}\delta F_{\text{total}} = &\oint \Big[n_i K(\partial_i\psi)\delta\psi_0 + f_b'(\psi_b - \psi_m)\delta\psi_b + C\sin(\psi_b - \psi_0)(\delta\psi_b - \delta\psi_0)\Big]\,\mathrm{d}l \\ &- \int \partial_i\big[K(\partial_i\psi)\big]\delta\psi\,\mathrm{d}^2x + \dots,\end{aligned} \tag{G.5}$$

where $\boldsymbol{n}$ denotes the unit normal vector to the boundary pointing outside and f_b' denotes the first derivative of the effective bristle potential f_b. The condition of local thermodynamic equilibrium at the boundary yields:

$$-f_b'(\psi_b - \psi_m) = C\sin(\psi_b - \psi_0) \qquad \text{from variation of } \psi_b \text{ and} \tag{G.6}$$

$$K n_i \partial_i \psi = C\sin(\psi_b - \psi_0) \qquad \text{from variation of } \psi_0. \tag{G.7}$$

These are the boundary conditions in their general form. They simultaneously describe bristle orientations ψ_b and the polarity angle ψ at the boundary, denoted by ψ_0.

G.3 Determination of parameter values

In order to find appropriate parameter values, we fit these boundary conditions to observed data of margin bristle angles ψ_b, hair angles ψ_w at a distance w from the margin, and margin angles ψ_m. To this end, we first note that from Eqs. (G.6) and (G.7) directly follows that

$$K n_i \partial_i \psi = -f_b'(\psi_b - \psi_m). \tag{G.8}$$

Because we could not determine the exact polarity angle ψ_0 at the margin, we choose an effective description assuming a strong coupling between polarity at the margin and bristle orientation, i.e. $C \gg B$ and $C \gg Ba$. Then, from Eqs. (G.6) follows

$$|\psi_b - \psi_0| \ll 1. \tag{G.9}$$

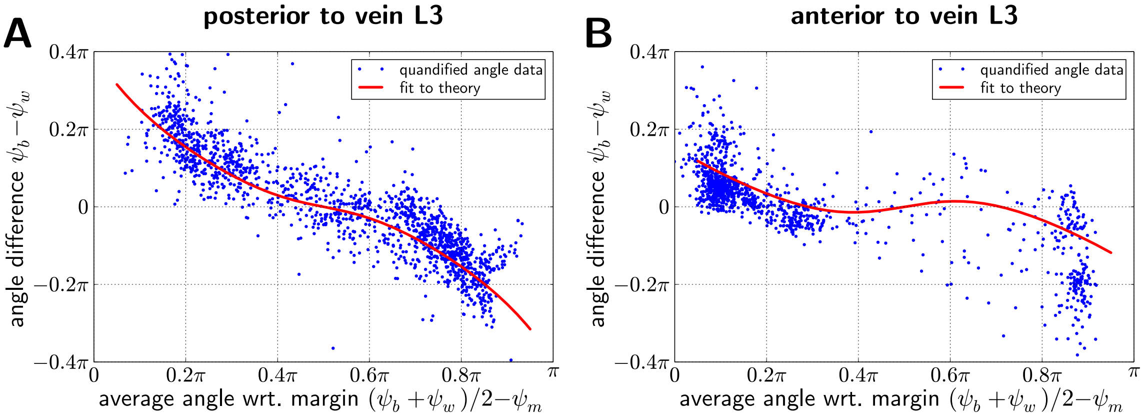

Figure G.3: Plots of quantified differences of margin bristle angles ψ_b and wing hair angles ψ_w close to the wing margin (blue dots). Also shown are fits to Eq. (G.14) (red solid lines), which reflects the theoretically assumed boundary condition Eq. (G.10). Each blue data point corresponds to a quantified pair ψ_b, ψ_w (see Fig. G.1A). The data shown include at least three wings for each of the seven genetic conditions considered. We differentiated two regions: **(A)** posterior to vein L3 ($s = 0 \ldots 0.57$) and **(B)** anterior to vein L3 ($s = 0.57 \ldots 1$), where the position coordinate s is defined in Fig. G.1A.

With Eq. (G.8) follows

$$n_i \partial_i \psi = \frac{B}{K}\Big[\cos\big(\psi_0 - \psi_m\big) + 2a \sin\big(2[\psi_0 - \psi_m]\big)\Big]. \tag{G.10}$$

This equation is used as boundary condition for the numerical solution of Eq. (4.7), where the parameters B/K and a are position-dependent.

To find the parameter values for B/K and a, we plot for each quantified pair of margin bristle angle ψ_b and wing hair angle ψ_w the difference of both angles over the average $\bar{\psi}_{bw} = (\psi_b + \psi_w)/2 - \psi_m$ of both angles with respect to the margin angle ψ_m (Fig. G.3).

Now, we derive a function to fit these data. To this end, we approximate the normal derivative $n_i \partial_i \psi$ in Eq. (G.8) using the polarity angle ψ_w at a distance w from the boundary:

$$w n_i \partial_i \psi = \psi_0 - \psi_w. \tag{G.11}$$

Then, with $|\psi_b - \psi_0| \ll 1$ follows

$$\psi_b - \psi_w = -\frac{w}{K} f_b'(\psi_b - \psi_m). \tag{G.12}$$

Table G.1: Parameter values for the boundary condition Eq. (G.10). We differentiate three regions: posterior to vein L3 (subscript "P"), anterior to vein L3 (subscript "A"), and the straight line cuts off the hinge to close the domain where we solve Eq. (4.7) (subscript "H"). Lengths are given in terms of λ_0, which is defined in Fig. 4.9A.

wing margin posterior to vein L3		**wing margin anterior to vein L3**		**straight line cutting hinge from blade**	
B_P/K	a_P	B_A/K	a_A	B_H/K	a_H
$70/\lambda_0$	-0.23	$16/\lambda_0$	-0.32	0	–

We Taylor expand f_b' around $\bar{\psi}_{bw} = (\psi_b + \psi_w)/2 - \psi_m$:

$$f_b'(\psi_b - \psi_m) = f_b'(\bar{\psi}_{bw}) - \frac{1}{2}(\psi_b - \psi_w) f_b''(\bar{\psi}_{bw}). \tag{G.13}$$

This finally yields

$$\psi_b - \psi_w = \frac{\cos\bar{\psi}_{bw} + 2a\sin\left(2\bar{\psi}_{bw}\right)}{\frac{K}{w_{\text{eff}}B} + \frac{1}{2}\Big[\sin\bar{\psi}_{bw} - 4a\cos\left(2\bar{\psi}_{bw}\right)\Big]}. \tag{G.14}$$

Here, the known distance w was substituted by an effective value w_{eff} in order to compensate for the approximation of a strong coupling C between bristle direction and polarity exactly at the margin.

We fitted the data in Fig. G.3 by Eq. (G.14), where $w_{\text{eff}}B/K$ and a were fit parameters. Therefore, we identified two regions which could be described with different parameter values. Posterior to vein L3 ($s = 0\ldots0.57$), the data were well described by $w_{\text{eff}}B/K = 2.9$ and $a = -0.227$ (Fig. G.3A); whereas anterior to vein L3 ($s = 0.57\ldots1$), the data were reasonably described by $w_{\text{eff}}B/K = 0.689$ and $a = -0.316$ (Fig. G.3B).

In order to identify the parameter values for the boundary condition Eq. (G.10), we still needed to calibrate the effective distance w_{eff}. By comparing the quantified bristle angles for the wild type case to the final boundary polarity of numerical solutions (see below), we found that $w_{\text{eff}} = 1.5w$, where $w = 0.028\lambda_0$. The resulting parameters for the boundary conditions are listed in Table G.1.

For our numerical solutions, in addition to the two above-mentioned boundary regions, we also considered the straight line which cuts the blade from the hinge. In that region, we assumed for simplicity a free boundary condition with $n_i\partial_i\psi = 0$, which results from Eq. (G.10) with $B = 0$ (see also Table G.1).

G.4 Comparison of theory and experiment

Here, we compare the boundary polarity ψ_0 of the final states of numerical solutions of Eq. (4.7) (see green arrows in the second columns in Figs. 4.13 and 4.15, respectively) to quantified bristle angle profiles (Fig. G.4). We found that both do largely agree, which is in particular true for the wild type case and the late over-expression cases (Fig. G.4A,D,E).

We find that deviations between experiment and theory of boundary angles mostly correspond to deviations in the bulk polarity (see Section 4.3.2). For instance, for both early over-expression cases, the deviations in the bulk polarity that were observed distally were also reflected in the deviations in the boundary polarity between the ends of veins L5 and L2 (Fig. G.4B,C). Similarly, the deviations that were observed proximally and posteriorly were reflected in the boundary angles for $s \lesssim 0.1$. Similarly, the deviations between experiment and theory of boundary angles that occur in both permanent over-expression cases between the ends of veins L5 and L2 coincided with defects in the bulk of the corresponding wing hair patterns.

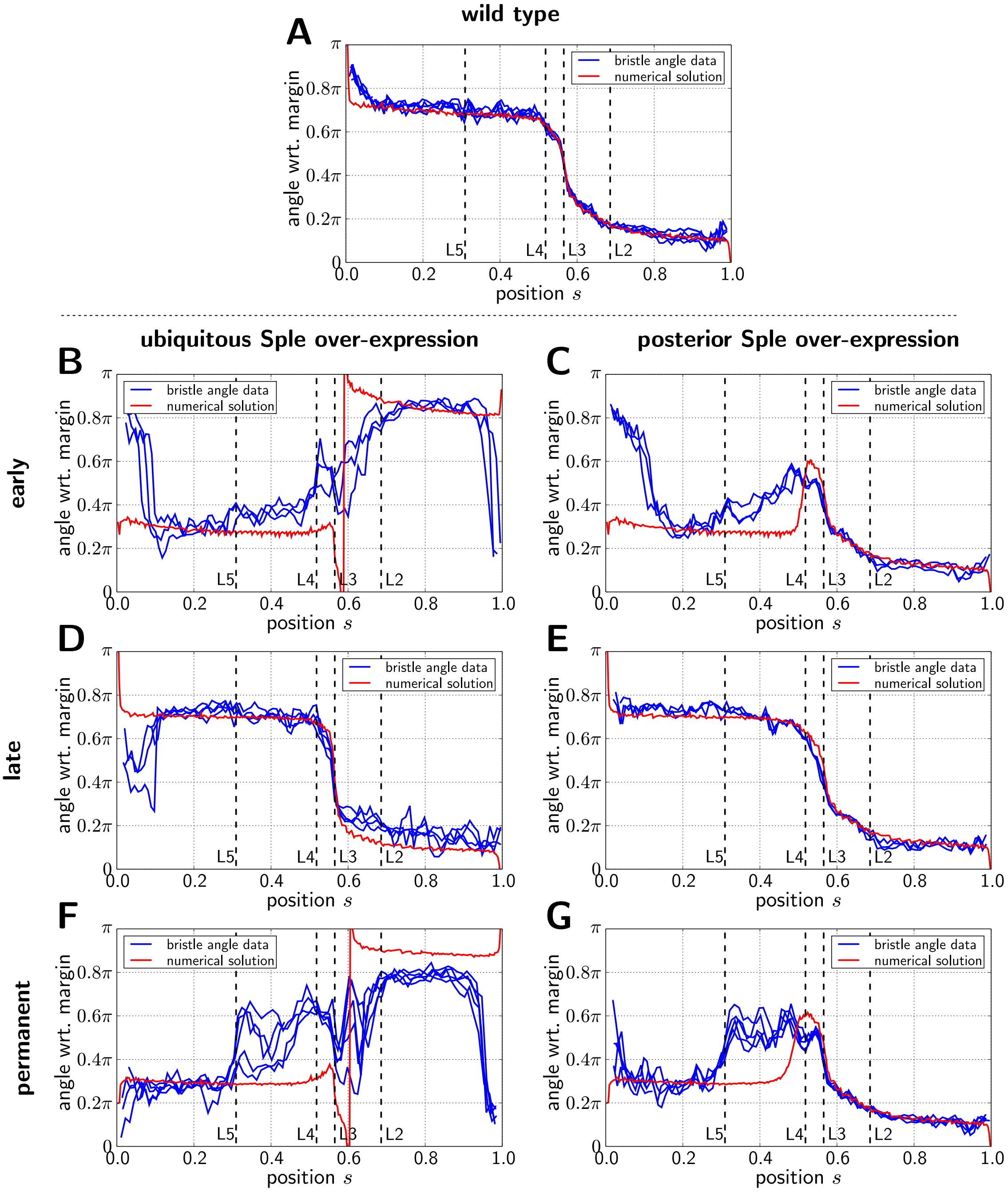

Figure G.4: Comparison of boundary polarity angles ψ_0 of the final state of numerical solutions (red solid lines) to quantified bristle angles ψ_b (blue solid lines), both with respect to the margin angle ψ_m. Each blue line represents the data of a single wing. The numerical solutions correspond to those shown in Figs. 4.13 and 4.15.

Table of symbols

Here, we list important symbols appearing in this thesis together with the place where they are defined.

Chapter 2: Tissue shear in cellular networks

	state properties of a triangle m	
S_{ij}^m	Eq. (2.6)	state tensor
A^m	Eq. (2.11)	area
Q_{ij}^m	Eq. (2.7)	symmetric shape tensor
$\tilde{Q}_{ij}^m$	Eq. (2.10)	elongation nematic; traceless, symmetric part of Q_{ij}^m
Φ^m	below Eq. (2.12)	angle of the elongation nematic $\tilde{Q}_{ij}^m$
Θ^m	Eq. (2.7)	absolute triangle orientation angle
	deformation properties of a triangle m (symbols describing an infinitesimal transformation in parentheses)	
M_{ij}^m	Eq. (2.14)	linear transformation tensor
U_{ij}^m (δU_{ij}^m)	Eq. (2.18)	discretely defined displacement gradient
$\Delta\Psi^m$ ($\delta\Psi^m$)	Eq. (2.19)	rotation angle
ΔN_{ij}^m (δN_{ij}^m)	Eq. (2.19)	symmetric deformation tensor
$\delta\tilde{U}_{ij}^m$	below Eq. (2.25)	infinitesimal shear; symmetric, traceless part of δU_{ij}^m
$\delta\tilde{J}_{ij}^m$	Eq. (2.29)	infinitesimal corotational contribution to shear
$\delta\Xi^m$	Eq. (2.30)	infinitesimal shear-induced contribution to rotation

large-scale deformation of a cellular network		
v_{ij}	Eq. (2.50)	velocity gradient
ω	Eq. (2.51)	vorticity of the velocity field
$\tilde{v}_{ij}$	Eq. (2.51)	shear rate nematic
$\tilde{J}_{ij}$	Eq. (2.55)	corotational contribution to the shear rate
$\tilde{T}_{ij}$	Eq. (2.57)	shear rate induced by T1 transitions
$\tilde{C}_{ij}$	Eq. (2.58)	shear rate induced by cell divisions
$\tilde{E}_{ij}$	Eq. (2.59)	shear rate induced by T2 transitions
$\tilde{D}_{ij}$	Eq. (2.56)	shear rate induced by correlations

Chapter 3: Mechanical behavior of shearing tissue in a vertex model

Note that in most of Chapter 3 and Appendix C, dimensionless units are used (Section 3.1.2, page 53). Here, we discuss dimenionless parameters omitting the bar.

vertex model		
W	Eq. (3.1)	work function describing force-balanced states
Γ	Eq. (3.1)	perimeter elasticity parameter
Λ^b	Eq. (3.1)	line tension of bond b
Λ_0	Eq. (3.2)	line tension offset parameter
Λ_F	Eq. (3.2)	line tension fluctuation amplitude parameter
k_Λ	Eq. (3.2)	characteristic rate of line tension fluctuations

boundary conditions		
L_x	Section 3.1.4	width of the periodic simulation box
L_y	Section 3.1.4	height of the periodic simulation box
γ	Section 3.1.4	total simple shear
$\dot{\gamma}$	Section 3.1.4	simple shear rate

observables		
$\tilde{\sigma}_{ij}$	Eq. (C.46)	mean field shear stress
$\tilde{Q}_{ij}$	Eq. (2.39)	average cell elongation
$\tilde{F}_{ij}$	Eq. (3.7)	nematic describing the relaxation of elongation

Chapter 4: Quantitative study of polarity reorientation in the fruit fly wing

vector and nematic fields		
$\boldsymbol{p}$	Section 4.2	vector field representing the Core PCP field
$\boldsymbol{q}$	Section 4.2	vector field representing the Fat PCP field
$\tilde{s}_{ij}$	Section 4.2	nematic field representing the effective shear field

angle fields		
ψ	Eq. (4.4)	angle of the vector field $\boldsymbol{p}$ representing Core PCP
ϕ	Eq. (4.4)	angle of the vector field $\boldsymbol{q}$ representing Fat PCP
θ	Eq. (4.4)	angle of the nematic field $\tilde{s}_{ij}$ representing effective shear

polarity dynamics parameter		
k	Eq. (4.5)	coupling of $\boldsymbol{p}$ to the nematic field $\tilde{s}_{ij}$
ζ	below Eq. (4.7)	coupling of $\boldsymbol{p}$ to the other vector field $\boldsymbol{q}$
κ	below Eq. (4.7)	coefficient describing the local slignment of the vector field $\boldsymbol{p}$

length scales		
λ	Eq. (4.14)	length scale comparing the local polarity alignment to the nematic coupling
μ	Eq. (4.16)	length scale comparing the local polarity alignment to the polar coupling
λ_0	Fig. 4.9A	length unit chosen for a given fly wing (corresponding to the half wing width)

Bibliography

[1] L. Wolpert, R. Beddington, T. Jessell, P. Lawrence, E. Meyerowitz, and J. Smith. *Principles of Development.* Oxford: Oxford University Press, 2001 (cited on pages 1–3, 5–6).

[2] B. Alberts, A. Johnson, J. Lewis, M. Raff, K. Roberts, and P. Walter. *Molecular Biology of the Cell.* 4th edition. New York: Garland Science, 2002 (cited on pages 1–3, 10).

[3] S. Newman and W. Comper. "'Generic' physical mechanisms of morphogenesis and pattern formation". *Development* 110.1 (1990), 1–18 (cited on pages 1, 11).

[4] T. Lecuit and P.-F. Lenne. "Cell surface mechanics and the control of cell shape, tissue patterns and morphogenesis". *Nature Reviews Molecular Cell Biology* 8.8 (2007), 633–644 (cited on page 1).

[5] T. Mammoto and D. Ingber. "Mechanical control of tissue and organ development". *Development* 137.9 (2010), 1407–1420 (cited on page 1).

[6] G. B. Blanchard and R. J. Adams. "Measuring the multi-scale integration of mechanical forces during morphogenesis". *Current Opinion in Genetics & Development* 21.5 (2011), 653–663 (cited on page 1).

[7] J. Eyckmans, T. Boudou, X. Yu, and C. Chen. "A hitchhiker's guide to mechanobiology". *Developmental Cell* 21.1 (2011), 35–47 (cited on page 1).

[8] S. Grill. "Growing up is stressful: biophysical laws of morphogenesis". *Current Opinion in Genetics and Development* 21.5 (2011), 647–652 (cited on page 1).

[9] A. Mateus, N. Gorfinkiel, and A. Arias. "Origin and function of fluctuations in cell behaviour and the emergence of patterns". *Seminars in Cell and Developmental Biology* 20.7 (2009), 877–884 (cited on page 2).

[10] A. T. L. Van Lommel. "Tissues". In: *From cells to organs.* Boston: Springer, 2003, 59–122 (cited on page 2).

[11] F. Mollica, L. Preziosi, and K. R. Rajagopal. *Modeling of biological materials.* Springer, 2007 (cited on pages 2, 11).

[12] D. R. Garrod and J. E. Collins. "Intercellular junctions and cell adhesion in epithelial cells". In: *Epithelial organization and development.* Edited by T. P. Fleming. Dordrecht: Springer, 1992, 1–52 (cited on pages 2–3).

[13] U. Tepass and G. Tanentzapf. “Epithelial cell polarity and cell junctions in drosophila”. *Annual Review of Genetics* 35 (2001), 747–784 (cited on page 3).

[14] M. Farquhar and G. Palade. “Junctional complexes in various epithelia.” *The Journal of cell biology* 17 (1963), 375–412 (cited on page 3).

[15] T. Morgan. “Sex limited inheritance in drosophila”. *Science* 32.812 (1910), 120–122 (cited on page 3).

[16] M. Adams et al. “The genome sequence of drosophila melanogaster”. *Science* 287.5461 (2000), 2185–2195 (cited on page 3).

[17] L. Hartwell, L. Hood, M. Goldberg, A. Reynolds, and L. Silver. *Genetics: From Genes to Genomes*. New York: McGraw-Hill Science/Engineering/Math, 2010 (cited on pages 3–5).

[18] C. Dahmann, A. Oates, and M. Brand. “Boundary formation and maintenance in tissue development”. *Nature Reviews Genetics* 12.1 (2011), 43–55 (cited on pages 4–5, 11).

[19] A. Classen, B. Aigouy, A. Giangrande, and S. Eaton. “Imaging drosophila pupal wing morphogenesis”. *Methods in molecular biology* 420 (2008), 265–275 (cited on pages 5, 190).

[20] S. Blair. “Wing vein patterning in drosophila and the analysis of intercellular signaling”. *Annual Review of Cell and Developmental Biology* 23 (2007), 293–319 (cited on pages 5–6).

[21] L. Abouchar, M. D. Petkova, C. R. Steinhardt, and T. Gregor. “Precision and reproducibility of macroscopic developmental patterns”. *arXiv:1309.6273 [q-bio]* (2013) (cited on pages 6, 79).

[22] Y. Wang and J. Nathans. “Tissue/planar cell polarity in vertebrates: new insights and new questions”. *Development* 134.4 (2007), 647–658 (cited on pages 6, 8).

[23] J. Seifert and M. Mlodzik. “Frizzled/pcp signalling: a conserved mechanism regulating cell polarity and directed motility”. *Nature Reviews Genetics* 8.2 (2007), 126–138 (cited on pages 6, 10).

[24] J. Zallen. “Planar polarity and tissue morphogenesis”. *Cell* 129.6 (2007), 1051–1063 (cited on pages 6, 10, 14).

[25] M. Simons and M. Mlodzik. “Planar cell polarity signaling: from fly development to human disease”. *Annual Review of Genetics* 42 (2008), 517–540 (cited on pages 6–10).

[26] D. Gubb and Garcia-Bellido. “A genetic analysis of the determination of cuticular polarity during development in drosophila melanogaster”. *Journal of Embryology and Experimental Morphology* Vol. 68 (1982), 37–57 (cited on pages 8, 10).

[27] C. Vinson and P. Adler. “Directional non-cell autonomy and the transmission of polarity information by the frizzled gene of drosophila”. *Nature* 329.6139 (1987), 549–551 (cited on pages 8, 10).

[28] N. Guo, C. Hawkins, and J. Nathans. “Frizzled6 controls hair patterning in mice”. *Proceedings of the National Academy of Sciences of the United States of America* 101.25 (2004), 9277–9281 (cited on page 8).

[29] M. Montcouquiol, R. Rachel, P. Lanford, N. Copeland, N. Jenkins, and M. Kelley. “Identification of vangl2 and scrb1 as planar polarity genes in mammals”. *Nature* 423.6936 (2003), 173–177 (cited on page 8).

[30] Y. Wang, N. Guo, and J. Nathans. “The role of frizzled3 and frizzled6 in neural tube closure and in the planar polarity of inner-ear sensory hair cells”. *Journal of Neuroscience* 26.8 (2006), 2147–2156 (cited on page 8).

[31] R. Keller. “Shaping the vertebrate body plan by polarized embryonic cell movements”. *Science* 298.5600 (2002), 1950–1954 (cited on pages 8, 96).

[32] K. Doyle, J. Hogan, M. Lester, and S. Collier. “The frizzled planar cell polarity signaling pathway controls drosophila wing topography”. *Developmental Biology* 317.1 (2008), 354–367 (cited on page 8).

[33] A.-K. Classen, K. Anderson, E. Marois, and S. Eaton. “Hexagonal packing of drosophila wing epithelial cells by the planar cell polarity pathway”. *Developmental Cell* 9.6 (2005), 805–817 (cited on page 8).

[34] L. Zheng, J. Zhang, and R. Carthew. “Frizzled regulates mirror-symmetric pattern formation in the drosophila eye”. *Development* 121.9 (1995), 3045–3055 (cited on page 8).

[35] M. Gho and F. Schweisguth. “Frizzled signalling controls orientation of asymmetric sense organ precursor cell divisions in drosophila”. *Nature* 393.6681 (1998), 178–181 (cited on page 8).

[36] A. Sagner. “Evolution of Planar Cell Polarity during wing development in Drosophila melanogaster”. PhD thesis. Technische Universität Dresden, 2011 (cited on pages 8, 92, 98, 207–208).

[37] H. Strutt, S. Warrington, and D. Strutt. “Dynamics of core planar polarity protein turnover and stable assembly into discrete membrane subdomains”. *Developmental Cell* 20.4 (2011), 511–525 (cited on pages 8–9, 92, 98, 207–208).

[38] H. Strutt and D. Strutt. “Asymmetric localisation of planar polarity proteins: mechanisms and consequences”. *Seminars in Cell and Developmental Biology* 20.8 (2009), 957–963 (cited on pages 8–10, 14).

[39] J. Sasaki, J. a. Knoblich, H. Senoo, T. Sasaki, T. Ayukawa, M. Akiyama, J. L. Mummery-Widmer, T. Stoeger, and M. Yamazaki. “Dachsous-Dependent Asymmetric Localization of Spiny-Legs Determines Planar Cell Polarity Orientation in Drosophila”. *Cell Reports* 8.2 (2014), 610–621 (cited on pages 8–9, 97).

[40] D. Gubb, C. Green, D. Huen, D. Coulson, G. Johnson, D. Tree, S. Collier, and J. Roote. “The balance between isoforms of the prickle lim domain protein is critical for planar polarity in drosophila imaginal discs”. *Genes and Development* 13.17 (1999), 2315–2327 (cited on pages 9, 92).

[41] D. Ma, C.-H. Yang, H. McNeill, M. Simon, and J. Axelrod. “Fidelity in planar cell polarity signalling”. *Nature* 421.6922 (2003), 543–547 (cited on page 9).

[42] H. Strutt and D. Strutt. “Long-range coordination of planar polarity in drosophila”. *BioEssays* 27.12 (2005), 1218–1227 (cited on page 9).

[43] C. Thomas and D. Strutt. “The roles of the cadherins fat and dachsous in planar polarity specification in drosophila”. *Developmental Dynamics* 241.1 (2012), 27–39 (cited on page 9).

[44] A. Ambegaonkar, G. Pan, M. Mani, Y. Feng, and K. Irvine. “Propagation of dachsous-fat planar cell polarity”. *Current Biology* 22.14 (2012), 1302–1308 (cited on page 9).

[45] A. Brittle, C. Thomas, and D. Strutt. “Planar polarity specification through asymmetric subcellular localization of fat and dachsous”. *Current Biology* 22.10 (2012), 907–914 (cited on page 9).

[46] P. Bryant, B. Huettner, L. Held Jr., J. Ryerse, and J. Szidonya. “Mutations at the fat locus interfere with cell proliferation control and epithelial morphogenesis in drosophila”. *Developmental Biology* 129.2 (1988), 541–554 (cited on page 9).

[47] M. Willecke, F. Hamaratoglu, L. Sansores-Garcia, C. Tao, and G. Halder. “Boundaries of dachsous cadherin activity modulate the hippo signaling pathway to induce cell proliferation”. *Proceedings of the National Academy of Sciences of the United States of America* 105.39 (2008), 14897–14902 (cited on page 9).

[48] D. Rogulja, C. Rauskolb, and K. Irvine. “Morphogen control of wing growth through the fat signaling pathway”. *Developmental Cell* 15.2 (2008), 309–321 (cited on page 9).

[49] L. Baena-López, A. Baonza, and A. García-Bellido. “The orientation of cell divisions determines the shape of drosophila organs”. *Current Biology* 15.18 (2005), 1640–1644 (cited on page 9).

[50] Y. Mao, A. Tournier, P. Bates, J. Gale, N. Tapon, and B. Thompson. “Planar polarization of the atypical myosin dachs orients cell divisions in drosophila”. *Genes and Development* 25.2 (2011), 131–136 (cited on pages 9, 13).

[51] F. Bosveld et al. “Mechanical control of morphogenesis by fat/dachsous/four-jointed planar cell polarity pathway”. *Science* 336.6082 (2012), 724–727 (cited on pages 9, 94).

[52] A. Vichas and J. Zallen. “Translating cell polarity into tissue elongation”. *Seminars in Cell and Developmental Biology* 22.8 (2011), 858–864 (cited on pages 9, 14).

[53] P. Lawrence, G. Struhl, and J. Casal. “Planar cell polarity: one or two pathways?” *Nature Reviews Genetics* 8.7 (2007), 555–563 (cited on page 9).

[54] B. Aigouy, R. Farhadifar, D. Staple, A. Sagner, J. Röper, F. Jülicher, and S. Eaton. “Cell Flow Reorients the Axis of Planar Polarity in the Wing Epithelium of Drosophila”. *Cell* 142.5 (2010), 773–786 (cited on pages 9–10, 13–15, 45, 48, 65, 72–73, 84, 92, 94, 96, 98, 163–164, 186, 188, 207–208, 210).

[55] A. Sagner, M. Merkel, B. Aigouy, J. Gaebel, M. Brankatschk, F. Jülicher, and S. Eaton. “Establishment of global patterns of planar polarity during growth of the drosophila wing epithelium”. *Current Biology* 22.14 (2012), 1296–1301 (cited on pages 9–10, 179, 185, 188).

[56] S. Blair. “Cell polarity: overdosing on pcps”. *Current Biology* 22.14 (2012), R567–R569 (cited on page 9).

[57] M. Matis, D. A. Russler-Germain, Q. Hu, C. J. Tomlin, and J. D. Axelrod. “Microtubules provide directional information for core PCP function.” *eLife* 3 (2014), e02893 (cited on pages 9, 14, 97).

[58] D. B. Staple. “Understanding Mechanics and Polarity in Two-Dimensional Tissues”. PhD thesis. Technische Universität Dresden, 2012 (cited on pages 10, 13–14, 52, 56, 64–65, 72–73, 92, 95–96, 147–150, 188, 190, 208, 210).

[59] K. Kruse, J. Joanny, F. Jülicher, J. Prost, and K. Sekimoto. “Generic theory of active polar gels: A paradigm for cytoskeletal dynamics”. *European Physical Journal E* 16.1 (2005), 5–16 (cited on pages 11–12, 96, 175).

[60] J. Joanny, F. Jülicher, K. Kruse, and J. Prost. “Hydrodynamic theory for multi-component active polar gels”. *New Journal of Physics* 9 (2007) (cited on pages 11–12).

[61] G. Salbreux, J. Prost, and J. Joanny. “Hydrodynamics of cellular cortical flows and the formation of contractile rings”. *Physical Review Letters* 103.5 (2009) (cited on pages 11, 96).

[62] S. Ramaswamy. “The mechanics and statistics of active matter”. *Annual Review of Condensed Matter Physics* 1 (2010), 323–345 (cited on pages 11–12).

[63] A. Callan-Jones and F. Jülicher. “Hydrodynamics of active permeating gels”. *New Journal of Physics* 13 (2011) (cited on pages 11–12, 65, 74, 96).

[64] M. Marchetti, J. Joanny, S. Ramaswamy, T. Liverpool, J. Prost, M. Rao, and R. Simha. “Hydrodynamics of soft active matter”. *Reviews of Modern Physics* 85.3 (2013), 1143–1189 (cited on pages 11–12).

[65] J. Howard. *Mechanics of motor proteins and the cytoskeleton.* Sunderland: Palgrave Macmillan, 2005 (cited on page 11).

[66] S. de Groot and P. Mazur. *Non-equilibrium thermodynamics.* Dover Books on Physics Series. New York: Dover Publications, 1984 (cited on pages 11, 175).

[67] Y. C. Fung. *Biomechanics: mechanical properties of living tissues.* New York: Springer, 1993 (cited on page 11).

[68] C. Verdier, J. Etienne, A. Duperray, and L. Preziosi. “Review: rheological properties of biological materials”. *Comptes Rendus Physique* 10.8 (2009), 790–811 (cited on pages 11–12).

[69] C. Verdier. “Rheological properties of living materials. from cells to tissues”. *Journal of Theoretical Medicine* 5.2 (2003), 67–91 (cited on page 11).

[70] J. Holtfreter. “Gewebeaffinität, ein Mittel der embryonalen Formbildung”. *Archiv Für Experimentelle Zellforschung* 23 (1939), 169–209 (cited on page 11).

[71] J. Holtfreter. “Experimental studies on the development of the pronephros”. *Revue Canadienne de Biologie* 3 (1944), 220–250 (cited on page 11).

[72] M. Steinberg. “Reconstruction of tissues by dissociated cells”. *Science* 141.3579 (1963), 401–408 (cited on page 11).

[73] R. Foty, C. Pfleger, G. Forgacs, and M. Steinberg. “Surface tensions of embryonic tissues predict their mutual envelopment behavior”. *Development* 122.5 (1996), 1611–1620 (cited on page 11).

[74] D. Beysens, G. Forgacs, and J. Glazier. “Cell sorting is analogous to phase ordering in fluids”. *Proceedings of the National Academy of Sciences of the United States of America* 97.17 (2000), 9467–9471 (cited on page 11).

[75] M. Steinberg. “Differential adhesion in morphogenesis: a modern view”. *Current Opinion in Genetics and Development* 17.4 (2007), 281–286 (cited on page 11).

[76] A. Harris. “Is cell sorting caused by differences in the work of intercellular adhesion? a critique of the steinberg hypothesis”. *Journal of Theoretical Biology* 61.2 (1976), 267–285 (cited on page 11).

[77] G. Brodland. “The differential interfacial tension hypothesis (dith): a comprehensive theory for the self-rearrangement of embryonic cells and tissues”. *Journal of Biomechanical Engineering* 124.2 (2002), 188–197 (cited on page 11).

[78] M. Manning, R. Foty, M. Steinberg, and E.-M. Schoetz. “Coaction of intercellular adhesion and cortical tension specifies tissue surface tension”. *Proceedings of the National Academy of Sciences of the United States of America* 107.28 (2010), 12517–12522 (cited on pages 11, 13).

[79] J.-L. Maître, H. Berthoumieux, S. Krens, G. Salbreux, F. Jülicher, E. Paluch, and C.-P. Heisenberg. “Adhesion functions in cell sorting by mechanically coupling the cortices of adhering cells”. *Science* 338.6104 (2012), 253–256 (cited on page 11).

[80] K. Landsberg, R. Farhadifar, J. Ranft, D. Umetsu, T. Widmann, T. Bittig, A. Said, F. Jülicher, and C. Dahmann. “Increased cell bond tension governs cell sorting at the drosophila anteroposterior compartment boundary”. *Current Biology* 19.22 (2009), 1950–1955 (cited on pages 11, 13).

[81] M. Aliee, J.-C. Röper, K. Landsberg, C. Pentzold, T. Widmann, F. Jülicher, and C. Dahmann. “Physical mechanisms shaping the drosophila dorsoventral compartment boundary”. *Current Biology* 22.11 (2012), 967–976 (cited on pages 11, 13, 95).

[82] M. Aliee. “Dynamics and mechanics of compartment boundaries in developing tissues”. PhD thesis. Technische Universität Dresden, 2013 (cited on pages 11, 13, 52, 56, 147).

[83] D. Weaire and S. Hutzler. *The Physics of Foams*. Oxford, New York: Oxford University Press, 2001 (cited on page 11).

[84] R. Höhler and S. Cohen-Addad. “Rheology of liquid foam”. *Journal of Physics Condensed Matter* 17.41 (2005), R1041–R1069 (cited on page 11).

[85] P. Marmottant, C. Raufaste, and F. Graner. “Discrete rearranging disordered patterns, part ii: 2d plasticity, elasticity and flow of a foam”. *European Physical Journal E* 25.4 (2008), 371–384 (cited on pages 11–12, 49, 93–94).

[86] R. Gordon, N. Goel, M. Steinberg, and L. Wiseman. “A rheological mechanism sufficient to explain the kinetics of cell sorting”. *Journal of Theoretical Biology* 37.1 (1972), 43–73 (cited on page 11).

[87] H. Phillips and M. Steinberg. “Embryonic tissues as elasticoviscous liquids. i. rapid and slow shape changes in centrifuged cell aggregates”. *Journal of Cell Science* Vol. 30 (1978), 1–20 (cited on page 12).

[88] H. Phillips, M. Steinberg, and B. Lipton. “Embryonic tissues as elasticoviscous liquids. ii. direct evidence for cell slippage in centrifuged aggregates”. *Developmental Biology* 59.2 (1977), 124–134 (cited on page 12).

[89] G. Forgacs, R. Foty, Y. Shafrir, and M. Steinberg. “Viscoelastic properties of living embryonic tissues: a quantitative study”. *Biophysical Journal* 74.5 (1998), 2227–2234 (cited on page 12).

[90] W. Malik, S. Prasad, K. Rajagopal, and L. Preziosi. “On the modeling of the viscoelastic response of embryonic tissues”. *Mathematics and Mechanics of Solids* 13.1 (2008), 81–91 (cited on page 12).

[91] L. Preziosi, D. Ambrosi, and C. Verdier. “An elasto-visco-plastic model of cell aggregates”. *Journal of Theoretical Biology* 262.1 (2010), 35–47 (cited on page 12).

[92] P. Marmottant, A. Mgharbel, J. Käfer, B. Audren, J.-P. Rieu, J.-C. Vial, B. Van Der Sanden, A. Marée, F. Graner, and H. Delanoë-Ayari. “The role of fluctuations and stress on the effective viscosity of cell aggregates”. *Proceedings of the National Academy of Sciences of the United States of America* 106.41 (2009), 17271–17275 (cited on pages 12–13, 64).

[93] T. Bittig, O. Wartlick, A. Kicheva, M. González-Gaitárr, and F. Jülicher. “Dynamics of anisotropic tissue growth”. *New Journal of Physics* 10 (2008) (cited on pages 12–13).

[94] T. Bittig. “Morphogenetic signaling in growing tissues”. PhD thesis. Technische Universität Dresden, 2008 (cited on pages 12–13).

[95] J. Ranft, M. Basan, J. Elgeti, J. Joanny, J. Prost, and F. Jülicher. “Fluidization of Tissues by Cell Division and Apoptosis”. *Proceedings of the National Academy of Sciences* 107.49 (2010), 20863–20868 (cited on pages 12–13).

[96] J. Ranft. “Mechanics of Growing Tissues: A Continuum Description Approach”. PhD thesis. Université Pierre et Marie Curie and Technische Universität Dresden, 2012 (cited on page 12).

[97] M. Behrndt, G. Salbreux, P. Campinho, R. Hauschild, F. Oswald, J. Roensch, S. Grill, and C.-P. Heisenberg. “Forces driving epithelial spreading in zebrafish gastrulation”. *Science* 338.6104 (2012), 257–260 (cited on page 12).

[98] K. Rajagopal and A. Srinivasa. “Mechanics of the inelastic behavior of materials - part 1, theoretical underpinnings”. *International journal of plasticity* 14.10-11 (1998), 945–967 (cited on page 12).

[99] K. Rajagopal and A. Srinivasa. “Mechanics of the inelastic behavior of materials. part ii: inelastic response”. *International journal of plasticity* 14.10-11 (1998), 969–995 (cited on page 12).

[100] K. Rajagopal and A. Srinivasa. “A thermodynamic frame work for rate type fluid models”. *Journal of Non-Newtonian Fluid Mechanics* 88.3 (2000), 207–227 (cited on page 12).

[101] C. Truesdell and K. R. Rajagopal. *An Introduction to the Mechanics of Fluids.* Modern Birkhäuser Classics. Boston: Birkhäuser, 2008 (cited on pages 12, 49).

[102] P. Marmottant and F. Graner. “An elastic, plastic, viscous model for slow shear of a liquid foam”. *European Physical Journal E* 23.4 (2007), 337–347 (cited on page 12).

[103] J. Humphrey and K. Rajagopal. “A constrained mixture model for growth and remodeling of soft tissues”. *Mathematical Models and Methods in Applied Sciences* 12.3 (2002), 407–430 (cited on page 12).

[104] A. Anderson and K. Rejniak. *Single-cell-based models in biology and medicine.* Basel, Boston: Birkhäuser, 2007 (cited on pages 12–13).

[105] R. Smallwood. “Computational modeling of epithelial tissues”. *Wiley Interdisciplinary Reviews: Systems Biology and Medicine* 1.2 (2009), 191–201 (cited on pages 12–13).

[106] D. Drasdo, R. Kree, and J. McCaskill. “Monte carlo approach to tissue-cell populations”. *Physical Review E* 52.6 (1995), 6635–6657 (cited on pages 12–13).

[107] D. Drasdo and S. Höhme. “A single-cell-based model of tumor growth in vitro: monolayers and spheroids”. *Physical Biology* 2.3 (2005), 133–147 (cited on pages 12–13).

[108] J. Galle, G. Aust, G. Schaller, T. Beyer, and D. Drasdo. “Individual cell-based models of the spatial-temporal organization of multicellular systems - achievements and limitations”. *Cytometry Part A* 69.7 (2006), 704–710 (cited on pages 12–13).

[109] H. Byrne and D. Drasdo. “Individual-based and continuum models of growing cell populations: a comparison”. *Journal of Mathematical Biology* 58.4-5 (2009), 657–687 (cited on pages 12–13).

[110] P. Pathmanathan, J. Cooper, A. Fletcher, G. Mirams, P. Murray, J. Osborne, J. Pitt-Francis, A. Walter, and S. Chapman. “A computational study of discrete mechanical tissue models”. *Physical Biology* 6.3 (2009) (cited on pages 12–13).

[111] M. Basan, J. Prost, J.-F. Joanny, and J. Elgeti. “Dissipative particle dynamics simulations for biological tissues: rheology and competition”. *Physical Biology* 8.2 (2011) (cited on pages 12–13).

[112] F. Graner and J. Glazier. “Simulation of biological cell sorting using a two-dimensional extended potts model”. *Physical Review Letters* 69.13 (1992), 2013–2016 (cited on page 13).

[113] J. Glazier and F. Graner. “Simulation of the differential adhesion driven rearrangement of biological cells”. *Physical Review E* 47.3 (1993), 2128–2154 (cited on page 13).

[114] P. Hogeweg. “Evolving mechanisms of morphogenesis: on the interplay between differential adhesion and cell differentiation”. *Journal of Theoretical Biology* 203.4 (2000), 317–333 (cited on page 13).

[115] R. Merks and J. Glazier. “A cell-centered approach to developmental biology”. *Physica A: Statistical Mechanics and its Applications* 352.1 (2005), 113–130 (cited on page 13).

[116] E. Ising. “Beitrag zur Theorie des Ferromagnetismus”. *Zeitschrift für Physik* 31.1 (1925), 253–258 (cited on page 13).

[117] F. Wu. “The potts model”. *Reviews of Modern Physics* 54.1 (1982), 235–268 (cited on page 13).

[118] R. Farhadifar, J. Röper, B. Aigouy, S. Eaton, and F. Jülicher. “The Influence of Cell Mechanics, Cell-Cell Interactions, and Proliferation on Epithelial Packing”. *Current Biology* 17.24 (2007), 2095–2104 (cited on pages 13, 51–54, 95).

[119] M. Weliky and G. Oster. “The mechanical basis of cell rearrangement. i. epithelial morphogenesis during fundulus epiboly”. *Development* 109.2 (1990), 373–386 (cited on page 13).

[120] L. Hufnagel, A. Teleman, H. Rouault, S. Cohen, and B. Shraiman. “On the mechanism of wing size determination in fly development”. *Proceedings of the National Academy of Sciences of the United States of America* 104.10 (2007), 3835–3840 (cited on page 13).

[121] R. Farhadifar. “Dynamics of Cell Packing and Polar Order in Developing Epithelia”. PhD thesis. Technische Universität Dresden, 2009 (cited on pages 13–15, 52, 54, 56, 95, 147, 163–164).

[122] D. B. Staple, R. Farhadifar, J. Röper, B. Aigouy, S. Eaton, and F. Jülicher. “Mechanics and remodelling of cell packings in epithelia”. *European Physical Journal E* 33.2 (2010), 117–127 (cited on pages 13, 53–54, 58, 95–96).

[123] P. Mumcu. “Self-organized Growth in Developing Epithelia”. PhD thesis. Technische Universität Dresden, 2011 (cited on pages 13, 52, 56, 95, 147).

[124] O. Wartlick, P. Mumcu, A. Kicheva, T. Bittig, C. Seum, F. Jülicher, and M. González-Gaitán. “Dynamics of dpp signaling and proliferation control”. *Science* 331.6021 (2011), 1154–1159 (cited on page 13).

[125] G. Salbreux, L. Barthel, P. Raymond, and D. Lubensky. “Coupling mechanical deformations and planar cell polarity to create regular patterns in the zebrafish retina”. *PLoS Computational Biology* 8.8 (2012) (cited on pages 13–14).

[126] E. Hannezo, J. Prost, and J.-F. Joanny. “Theory of epithelial sheet morphology in three dimensions”. *Proceedings of the National Academy of Sciences* 111.1 (2014), 27–32 (cited on page 13).

[127] A. G. Fletcher, M. Osterfield, R. E. Baker, and S. Y. Shvartsman. “Vertex models of epithelial morphogenesis”. *Biophysical Journal* 106.11 (2014), 2291–2304 (cited on page 13).

[128] M. Rauzi, P. Verant, T. Lecuit, and P.-F. Lenne. “Nature and anisotropy of cortical forces orienting drosophila tissue morphogenesis”. *Nature Cell Biology* 10.12 (2008), 1401–1410 (cited on pages 13, 93–94, 96).

[129] R. Bayly and J. Axelrod. “Pointing in the right direction: new developments in the field of planar cell polarity”. *Nature Reviews Genetics* (2011) (cited on page 14).

[130] P. Lawrence, J. Casal, and G. Struhl. “Cell interactions and planar polarity in the abdominal epidermis of drosophila”. *Development* 131.19 (2004), 4651–4664 (cited on page 14).

[131] K. Amonlirdviman, N. Khare, D. Tree, W.-S. Chen, J. Axelrod, and C. Tomlin. “Mathematical modeling of planar cell polarity to understand domineering nonautonomy”. *Science* 307.5708 (2005), 423–426 (cited on page 14).

[132] J.-F. Le Garrec, P. Lopez, and M. Kerszberg. “Establishment and maintenance of planar epithelial cell polarity by asymmetric cadherin bridges: A computer model”. *Developmental Dynamics* 235.1 (2006), 235–246 (cited on page 14).

[133] J. Axelrod and C. Tomlin. “Modeling the control of planar cell polarity”. *Wiley Interdisciplinary Reviews: Systems Biology and Medicine* 3.5 (2011), 588–605 (cited on page 14).

[134] P. G. de Gennes and J. Prost. *The Physics of Liquid Crystals.* 2nd edition. Oxford, New York: Oxford University Press, 1995 (cited on pages 14, 65, 73–74, 96–97, 163, 175).

[135] S. Cortès, N. Glade, I. Chartier, and J. Tabony. “Microtubule self-organisation by reaction-diffusion processes in miniature cell-sized containers and phospholipid vesicles”. *Biophysical Chemistry* 120.3 (2006), 168–177 (cited on page 14).

[136] S. Haase and D. Lew. “Microtubule organization: cell shape is destiny”. *Current Biology* 17.7 (2007), R249–R251 (cited on page 14).

[137] R. Daga and P. Nurse. “Interphase microtubule bundles use global cell shape to guide spindle alignment in fission yeast”. *Journal of Cell Science* 121.12 (2008), 1973–1980 (cited on page 14).

[138] T. Harumoto, M. Ito, Y. Shimada, T. Kobayashi, H. Ueda, B. Lu, and T. Uemura. “Atypical cadherins dachsous and fat control dynamics of noncentrosomal microtubules in planar cell polarity”. *Developmental Cell* 19.3 (2010), 389–401 (cited on page 14).

[139] Y. Shimada, S. Yonemura, H. Ohkura, D. Strutt, and T. Uemura. “Polarized transport of frizzled along the planar microtubule arrays in drosophila wing epithelium”. *Developmental Cell* 10.2 (2006), 209–222 (cited on page 14).

[140] J. Olofsson, K. A. Sharp, M. Matis, B. Cho, and J. D. Axelrod. “Prickle/spiny-legs isoforms control the polarity of the apical microtubule network in planar cell polarity.” *Development (Cambridge, England)* 141.14 (2014), 2866–74 (cited on pages 14, 97).

[141] S. N. Ehaideb et al. “Prickle modulates microtubule polarity and axonal transport to ameliorate seizures in flies.” *Proceedings of the National Academy of Sciences of the United States of America* 111.30 (2014), 11187–92 (cited on pages 14, 97).

[142] S. Fischer, P. Houston, N. Monk, and M. Owen. “Is a persistent global bias necessary for the establishment of planar cell polarity?” *PLoS ONE* 8.4 (2013) (cited on page 14).

[143] Y. Burak and B. Shraiman. “Order and stochastic dynamics in drosophila planar cell polarity”. *PLoS Computational Biology* 5.12 (2009) (cited on page 14).

[144] H. Meinhardt. “Computational modelling of epithelial patterning”. *Current Opinion in Genetics and Development* 17.4 (2007), 272–280 (cited on page 14).

[145] H. Zhu. “Is anisotropic propagation of polarized molecular distribution the common mechanism of swirling patterns of planar cell polarization?” *Journal of Theoretical Biology* 256.3 (2009), 315–325 (cited on page 14).

[146] S. Schamberg, P. Houston, N. Monk, and M. Owen. “Modelling and analysis of planar cell polarity”. *Bulletin of Mathematical Biology* 72.3 (2010), 645–680 (cited on page 14).

[147] M. Mani, S. Goyal, K. Irvine, and B. Shraiman. “Collective polarization model for gradient sensing via dachsous-fat intercellular signaling”. *Proceedings of the National Academy of Sciences of the United States of America* 110.51 (2013), 20420–20425 (cited on page 14).

[148] W. Kaballo. *Aufbaukurs Funktionalanalysis und Operatortheorie. Distributionen - lokalkonvexe Methoden - Spektraltheorie.* Berlin: Springer Spektrum, 2013 (cited on page 22).

[149] P. M. Chaikin and T. C. Lubensky. *Principles of Condensed Matter Physics.* Cambridge, New York: Cambridge University Press, 2000 (cited on pages 49, 73, 163, 175).

[150] M. Aubouy, Y. Jiang, J. Glazier, and F. Graner. “A texture tensor to quantify deformations”. *Granular Matter* 5.2 (2003), 67–70 (cited on pages 49, 93–94).

[151] M. Asipauskas, M. Aubouy, J. Glazier, F. Graner, and Y. Jiang. “A texture tensor to quantify deformations: the example of two-dimensional flowing foams”. *Granular Matter* 5.2 (2003), 71–74 (cited on pages 49, 93–94).

[152] B. Dollet and F. Graner. “Two-dimensional flow of foam around a circular obstacle: local measurements of elasticity, plasticity and flow”. *Journal of Fluid Mechanics* 585 (2007), 181–211 (cited on pages 49, 93–94).

[153] F. Graner, B. Dollet, C. Raufaste, and P. Marmottant. “Discrete rearranging disordered patterns, part I: Robust statistical tools in two or three dimensions”. *The European Physical Journal E* 25.4 (2008), 349–369 (cited on pages 49, 93–94).

[154] G. Blanchard, A. Kabla, N. Schultz, L. Butler, B. Sanson, N. Gorfinkiel, L. Mahadevan, and R. Adams. “Tissue tectonics: morphogenetic strain rates, cell shape change and intercalation”. *Nature Methods* 6.6 (2009), 458–464 (cited on pages 49, 93–94).

[155] E. Polak and G. Ribiere. “Note sur la convergence de méthodes de directions conjuguées”. *Revue Française d’Informatique et de Recherche Opérationnelle* 16 (1969), 35–43 (cited on pages 52, 147).

[156] A. Lees and S. Edwards. “The computer study of transport processes under extreme conditions”. *Journal of Physics C: Solid State Physics* 5.15 (1972), 1921–1928 (cited on pages 56, 95).

[157] R. B. Bird and O. Hassager. *Dynamics of Polymer Liquids.* Volume 1. New York: Wiley-Interscience, 1987 (cited on page 63).

[158] R. Larson. *Constitutive Equations for Polymer Melts and Solutions.* Butterworth’s Series in Chemical Engineering. Boston: Butterworth-Heinemann, 1988 (cited on page 63).

[159] M. Merkel, A. Sagner, F. Gruber, R. Etournay, C. Blasse, E. Myers, F. Jülicher, and S. Eaton. “The balance of Prickle/Spiny-legs isoforms controls the amount of coupling between Core and Fat PCP systems”. 2014. In preparation. (Cited on pages 65–66, 68, 91–92, 179, 185, 190, 205).

[160] P. F. Byrd and M. D. Friedman. *Handbook of elliptic integrals for engineers and scientists.* Berlin, New York: Springer-Verlag, 1971 (cited on pages 77–78, 196–198).

[161] A. Economou, L. Brock, M. Cobourne, and J. Green. “Whole population cell analysis of a landmark-rich mammalian epithelium reveals multiple elongation mechanisms”. *Development* 140.23 (2013), 4740–4750 (cited on pages 93–94).

[162] J. Blankenship, S. Backovic, J. S. Sanny, O. Weitz, and J. Zallen. “Multicellular rosette formation links planar cell polarity to tissue morphogenesis”. *Developmental Cell* 11.4 (2006), 459–470 (cited on page 96).

[163] W. Kung, M. C. Marchetti, and K. Saunders. “Hydrodynamics of polar liquid crystals”. *Physical Review E* 73.3 (2006) (cited on page 97).

[164] N. Fisher. *Statistical Analysis of Circular Data*. Statistical Analysis of Circular Data. Cambridge, New York: Cambridge University Press, 1995 (cited on page 185).

[165] K. Mardia and P. Jupp. *Directional Statistics*. Wiley Series in Probability and Statistics. Chichester, New York: Wiley, 2009 (cited on page 185).

[166] S. McGuire, P. Le, A. Osborn, K. Matsumoto, and R. Davis. “Spatiotemporal Rescue of Memory Dysfunction in Drosophila”. *Science* 302.5651 (2003), 1765–1768 (cited on page 190).

[167] J. More, B. Garbow, and K. Hillstrom. *User Guide for MINPACK-1*. Technical report. Argonne National Laboratory, 1980. Technical Report ANL-80-74 (cited on page 201).

Versicherung

Hiermit versichere ich, dass ich die vorliegende Arbeit ohne unzulässige Hilfe Dritter und ohne Benutzung anderer als der angegebenen Hilfsmittel angefertigt habe; die aus fremden Quellen direkt oder indirekt übernommenen Gedanken sind als solche kenntlich gemacht. Die Arbeit wurde bisher weder im Inland noch im Ausland in gleicher oder ähnlicher Form einer anderen Prüfungsbehörde vorgelegt. Diese Abreit wurde unter der wissenschaftlichen Betreuung von Prof. Dr. Frank Jülicher am Max-Planck-Institut für Physik komplexer Systeme in Dresden angefertigt. Ich erkläre hiermit, dass keine früheren erfolglosen Promotionsverfahren stattgefunden haben. Ich erkenne die Promotionsordnung der Fakultät für Mathematik und Naturwissenschaften der Technische Universität Dresden an.

……………………
Dresden, der 2. Juli 2014, Matthias Merkel